Contribution of advanced orientation microscopy techniques for the analysis of phase transformation microstructures in steels

Tomas Martinez Ostormujof

LABORATOIRE D'ÉTUDE DES MICROSTRUCTURES ET DE MÉCANIQUE DES MATÉRIAUX

UNIVERSITÉ DE LORRAINE

C2MP

Thèse

Présentée et soutenue publiquement pour l'obtention du titre de

DOCTEUR DE l'UNIVERSITE DE LORRAINE

Mention : **SCIENCE DES MATERIAUX**

Apport des approches avancées en microscopie d'orientation pour l'analyse des microstructures de transformation de phase dans les aciers

Contribution of advanced orientation microscopy techniques for the analysis of phase transformation microstructures in steels

Par **Tomas MARTINEZ OSTORMUJOF**

13 décembre 2022

Membres du jury :

Directeur de thèse :	**M. Lionel GERMAIN**	**Professeur à l'Université de Lorraine, France**
Co-directrice de these :	**Mme. Nathalie GEY**	**Chargé de Recherche au CNRS, LEM3, France**
Président du jury :	**M. Sébastien ALLAIN**	**Professeur à l'Université de Lorraine, France**
Rapporteurs :	**Mme. Anne Françoise GOURGUES-LORENZON**	**Professeur au Centre des Matériaux Mines ParisTech, France**
	M. Alexis DESCHAMPS	**Professeur à l'Institut polytechnique de Grenoble, France**
Examinateurs :	**M. Marc De GRAEF**	**Professeur à l'Université de Carnegie Mellon, Etats Unis**
	M. Ali GHOLINIA	**Chercheur à l'Université de Manchester, Royaume Uni**
Membres invités :	**M. Matthieu SALIB**	**ArcelorMittal Global R&D (Maizières - les-Metz), France**
	Mme. Audrey COUTURIER	**ArcelorMittal, Industeel France, Creusot**
	M. Philippe CHAROBERT	**ArcelorMittal, Industeel France, Creusot**

Acknowledgments

First of all, I would like to thank my supervisors M. Lionel GERMAIN and Mme. Nathalie GEY for having trusted me to carry out this project and for having supported me throughout these years not only from an academic point of view but also from a personal one. All the discussions and exchanges we have had have allowed me to advance not only in my thesis but also to grow as a researcher. I am proud and happy of the working team we have formed and the experiences we have had together will remain etched in my memory.

In addition, I would like to thank the reviewers Mme. Anne Françoise GOURGUES-LORENZON and M. Alexis DESCHAMPS, the president of the committee M. Sébastien ALLAIN and the examiners M. Marc De GRAEF and M. Ali GHOLINIA for accepting the responsibility of being part of my thesis defense committee and devoting their time and dedication to provide their critical point of view and enrich my thesis work. My thanks also to M. Matthieu SALIB, Mme. Audrey COUTURIER and M. Philippe CHAROBERT for being part of the thesis defense.

A very special thanks to M. Simon BREUMIER, M. Ravi PURUSHOTTAM RAJ PUROHIT and M. Julien GUYON with whom I have had the pleasure of working and collaborating at different stages of the thesis. We have helped each other and the exchanges have been very enriching and productive.

I am grateful to all the members of the LEM3, PhD students, technicians, researchers, with whom I have formed both a professional and personal relationship and that have made me enjoy precious moments over these years.

Last, but not least, I would like to dedicate this work to my loved ones, my girlfriend, my family and my friends who have always supported and motivated me to move forward in difficult times.

Abstract

This thesis focuses on some of the latest progress in EBSD-based orientation microscopy to improve the analysis of complex steel microstructures and to contribute to a better understanding of the genesis of phase transformation induced microstructures. This is of key importance to optimize the thermomechanical processing route of steels and to improve mechanical properties.

The first issue to progress in the understanding of phase transformation induced microstructures in steels was to capture the formation of high temperature austenite before complete ferrite/bainite or martensite transformation during cooling. For this purpose, in-situ EBSD heat treatments have been implemented in a SEM in complement with the well-known indirect crystallographic reconstruction. A heating module with an optimized design for the EBSD set-up has been coupled with a state-of-art EBSD camera. The result shows that high quality patterns can be acquired at temperatures around 1000°C with an indexing speed of more than 1000Hz. This allows to capture the dynamic microstructure evolution induced by phase transformation and austenite grain growth. Different cases of studies carried out with different industrial partners illustrate the performance of HT EBSD analysis, with a special focus on the analysis of the austenite grain refinement due to austempering treatments.

The second issue was to apply advanced EBSD pattern analysis to complex and multiphase steel microstructures to improve the acquired orientation data in terms of indexing rate and phase discrimination (especially for phases with cubic crystal symmetry). For the classical Hough Transform (HT) based indexing approach, optimizing the reflector list per phase is the most important feature for reliable phase discrimination. The recently proposed "Refined Accuracy" (RA) approach is sensitive to difference in Kikuchi Band Width and is found to be able to discriminate cubic phases with a difference in the lattice parameter of 0.73Å. Finally, Pattern Matching approaches that compare experimental patterns to a dictionary of dynamically simulated patterns was found to offer the best performance to (1) index poor quality patterns often found in martensite/austenite islands and (2) discriminate cubic-based phases corresponding to inclusions or minor precipitates in a ferrite/austenite matrix. The best metric to compare experimental and simulated patterns is the Normalized Cross Correlation (NCC).

Finally, the last issue was to progress in the automated EBSD-based discrimination of ferrite/bainite/martensite transformation products. Those phases are all indexed as ferrite-cubic phase in an EBSD map. Additional EBSD-based parameters like pattern quality and/or KAM can be leveraged to highlight differences between those phases. However, user defined threshold criteria to identify those phases is often subjective and the procedure can be time consuming. In the search of an objective and effortless approach, we have implemented Artificial Intelligence models to discriminate the phase transformation products based on pattern quality and KAM. A supervised learning method was developed using the U-Net CNN architecture to separate ferrite/upper bainite/martensite. High accuracies were reached for microstructures with similar features to those shown to the model during training, thus it is a good option for repetitive tasks. To avoid labeling, unsupervised approaches were also tested. A k-means clustering approach demonstrated a relatively good ability to discriminate upper and lower bainite using features extracted from indirect crystallographic reconstruction. On the other hand, a method called unsupervised CNN showed an excellent ability to discriminate ferrite and martensite from DP steels but it struggled with multiphase microstructures. Both unsupervised approaches provided promising results and may be used as a pre-labeling step to ease the process.

Résumé

Cette thèse se concentre sur certains des derniers progrès réalisés en microscopie d'orientation (EBSD) afin d'améliorer l'analyse des microstructures complexes de l'acier et de contribuer à une meilleure compréhension de la genèse des microstructures héritées par transformation de phase. Ceci est d'une importance capitale pour optimiser les traitements thermomécaniques et les propriétés mécaniques.

La première question était de capturer la formation d'austénite à haute température avant la transformation complète en ferrite/bainite ou martensite pendant le refroidissement. Dans ce but, des traitements thermiques EBSD in-situ ont été mis en œuvre dans un MEB en complément de la reconstruction cristallographique indirecte. Un module de chauffage au design optimisé pour l'EBSD a été couplé à une caméra EBSD dernière génération. Le résultat montre que des clichés de haute qualité peuvent être acquis à des températures d'environ 1000°C avec une vitesse d'indexation de plus de 1000Hz. Cela permet de capturer l'évolution dynamique de la microstructure héritée par transformation de phase et la croissance des grains d'austénite. Différents cas d'études réalisées avec différents partenaires industriels illustrent les performances de l'analyse EBSD à haute température, avec un accent particulier sur l'analyse de l'affinement du grain d'austénite dû aux traitements de trempe.

La deuxième question était d'appliquer l'analyse avancée des clichés EBSD à des microstructures d'acier complexes et multiphases afin d'améliorer les données d'orientation acquises en termes de taux d'indexation et de discrimination des phases (en particulier pour les phases à symétrie cristalline cubique). Pour l'approche classique d'indexation par Transformée de Hough (HT), l'optimisation de la liste de réflecteurs par phase est la caractéristique la plus importante pour une discrimination de phase fiable. L'approche "Refined Accuracy" (RA) récemment proposée est sensible à la différence de largeur de bande de Kikuchi et s'avère capable de discriminer les phases cubiques avec une différence de paramètre de réseau de 0.73Å. Les approches Pattern Matching qui comparent les clichés expérimentaux à un dictionnaire de cliches simulés dynamiquement se sont avérées les plus performantes pour (1) indexer les clichés de mauvaise qualité souvent trouvés dans les îlots de Martensite/Austenite et (2) discriminer les phases cubiques correspondant à des inclusions ou des précipités mineurs dans une matrice de ferrite/austenite. La meilleure métrique pour comparer les clichés expérimentaux et simulés est la Normalized Cross Correlation (NCC).

Enfin, la dernière question était de progresser dans la discrimination automatisée des produits de transformation (ferrite/bainite/martensite) en utilisant données de l'EBSD. Ces phases sont toutes indexées comme phase ferrite-cubique mais des paramètres comme la qualité du cliché ou le KAM, peuvent être utilisés pour les différencier. Cependant, les critères définis par l'utilisateur pour identifier ces phases sont souvent subjectifs et la procédure peut prendre beaucoup de temps. Pour ces raisons nous avons mis en place des modèles d'IA basés sur la qualité du cliché et le KAM. Une méthode d'apprentissage supervisé a été développée en utilisant l'architecture U-Net CNN pour séparer ferrite/bainite supérieure/martensite. Des précisions élevées ont été atteintes pour les microstructures ayant des caractéristiques similaires à celles montrées au modèle pendant l'entrainement, ce qui en fait une bonne option pour les tâches répétitives. Pour éviter l'étiquetage, des approches non supervisées ont également été testées. Une approche de clustering k-means a démontré une capacité relativement bonne à discriminer la bainite supérieure et inférieure en utilisant des caractéristiques extraites de la reconstruction cristallographique indirecte. D'autre part, les CNN non supervisées ont montré une excellente capacité à discriminer la ferrite et la martensite des aciers DP, mais elle a eu des difficultés avec les microstructures multiphases. Les deux approches non supervisées ont fourni des résultats prometteurs et peuvent être utilisées comme une étape de pré-étiquetage pour faciliter le processus.

Résumé étendu

Pour répondre aux enjeux des transitions énergétique et carbone, les matériaux se doivent d'être de plus en plus performants, durables et avec une empreinte carbone limitée. Dans ce contexte, les aciers de haute performance sont en constant développement avec des microstructures de plus en plus complexes. Ces dernières sont souvent multi-phasées avec des constituants de tailles parfois nanométriques, dont la distribution topologique et cristallographique influence fortement le comportement mécanique. Pour optimiser ces microstructures et améliorer les propriétés en service et la durabilité des produits, il est essentiel de bénéficier des récents avancements en microcopie électronique à balayage couplée aux techniques d'analyse. L'objectif de la présente thèse s'inscrit dans ce contexte et explore l'apport d'innovation en microscopie d'orientation (EBSD) assistée par ses approches en Intelligence Artificielle (IA) pour lever des verrous dans la compréhension des microstructures d'acier héritées par transformation de phase. Trois axes de recherche où il y a encore des questions ouvertes et des défis à relever ont été investigués :

1. Le suivi in situ des transformations de phases par EBSD à haute température
2. Les nouvelles stratégies d'indexation pour l'analyse des matériaux multiphasés et nanométriques et la discrimination des phases de symétrie cubique
3. L'IA pour l'exploitation automatisée des données d'orientations comme la segmentation de la ferrite, bainite et martensite

1. Suivi in situ des transformations de phases par EBSD à haute température

Pour comprendre la genèse des microstructures induites par la transformation de phase, la connaissance de la microstructure de la phase se développant à haute température est essentielle pour optimiser un traitement thermique ou thermomécanique. Dans le cas des aciers bas-carbone, il est cependant impossible de figer l'état métallurgique de l'austénite par trempe. Au fil des années, de nombreux chercheurs ont utilisé des techniques de reconstruction cristallographique indirecte pour simuler la microstructure austénitique à haute température en exploitant la relation d'orientation qui la relie aux phases à température ambiante. Néanmoins, ces approches sont limitées lorsque les grains parents d'austénite sont de petites tailles et ne contiennent pas assez de variants cristallographiques après transformation de phase pour identifier leurs orientations de façon fiable. C'est pourtant la tendance dans le développement des aciers de dernière génération pour améliorer les propriétés en service. De plus par reconstruction indirecte, l'évolution dynamique de la microstructure en cours de transformation n'est pas accessible. Cette information est pourtant essentielle pour comprendre les mécanismes en jeu. Pour ces raisons, nous avons exploré la faisabilité de l'EBSD in-situ à haute température en développant un dispositif optimisé et en évaluant son apport dans trois études conduites avec des partenaires industriels et universitaires :

- Analyse de la réduction de la taille de grains austénitiques par traitement d'austénitisation (Société Vallourec)
- Formation de l'austénite a haute température dans les aciers carbonitrurés – effet des nitrures (Institut Jean Lamour, IRT M2P)
- Mobilité des interfaces γ/α lors du refroidissement (Le Groupe de Physique des Matériaux (GPM))

Pour réaliser les expériences in situ, nous avons développé avec Kammrath & Weiss (représenté en France par la société EDEN Instruments) une platine chauffante à géométrie optimisée aux conditions d'acquisition EBSD et avec une capacité de chauffage adaptée à l'étude de notre problématique (température jusqu'à 1050°C, et variation de la vitesse de chauffage et de refroidissement jusqu'à 45°C/s et 3°C/s respectivement). Le module de chauffage a été couplé à une caméra CMOS EBSD de dernière génération pour l'acquisition de clichés EBSD de haute qualité à des vitesses élevées, essentiel pour suivre les évolutions en température de la microstructure.

La Figure 1 illustre de potentiel des acquisitions EBDS in situ et leurs complémentarités face aux reconstructions indirects. Le schéma de la Figure 1 (a) montre la stratégie originale mise en œuvre pour analyser l'évolution de la taille de grains austénitiques par deux traitements d'austénitisation successifs. A partir de la carte EBSD acquise à température ambiante sur l'état A (résultant d'une première austénitisation), la reconstruction indirecte donne la carte d'orientation de la phase austénitique suite au premier chauffage (Figure 1 (b)). L'analyse in situ au chauffage par palier de très courte durée permet de suivre sur la même zone, la précipitation et la croissance de l'austénite au chauffage. La Figure 1 (c) montre la microstructure entièrement austénitique (890°C), afin d'analyser l'évolution de la taille des grains.

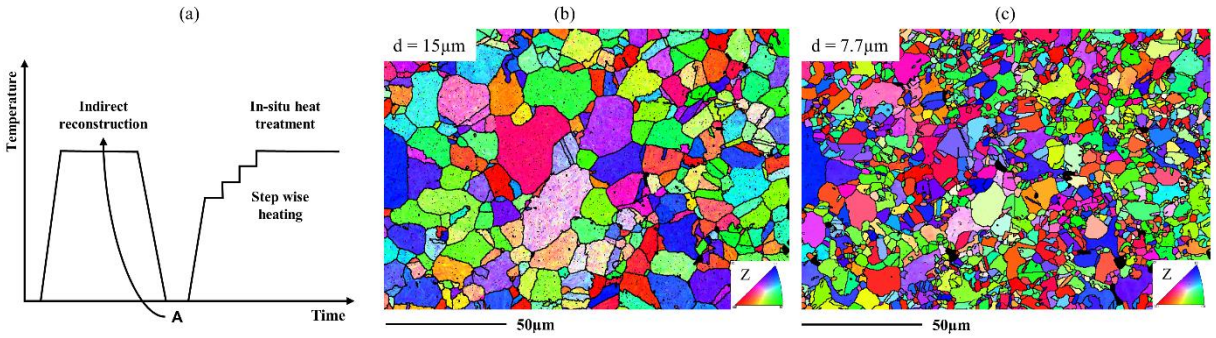

Figure 1. Analyse d'un acier faiblement allié 23MnCrMo5 (a) Schéma de la stratégie expérimentale, (b) reconstruction indirecte de l'austénite à HT à partir de la carte A et (c) carte EBSD acquise à 890°C sur la même zone après un chauffage par paliers.

Plus largement, notre expérience en EBSD in situ prouve que notre configuration est idéale pour acquérir des cartes EBSD de qualité à ces hautes températures. En particulier, la carte EBSD Figure 1 (c) couvre 170×120µm pour un temps d'acquisition de moins de 2mn. Avec ici une résolution de 0.3µm, elle permet d'identifier les grains les plus petits tout en balayant de grandes zones pour visualiser les

hétérogénéités de microstructure. De plus, des événements dynamiques ont pu être suivis pendant le chauffage pour détecter les sites préférentiels de germination de l'austénite et d'analyser les mécanismes à l'origine de la réduction du grain.

2. Les nouvelles stratégies d'indexation pour l'analyse des matériaux multiphasés et nanométriques et la discrimination des phases de symétrie cubique

L'EBSD est largement appliquée pour effectuer la discrimination des phases sur la base des différences cristallographiques. Cependant, lorsque deux phases appartiennent à la même structure cristalline, la géométrie de leurs diagrammes de diffraction est très similaire et leur discrimination devient compliquée. Les microstructures de l'acier représentent un excellent défi pour la discrimination de phase EBSD : (1) la grande majorité des phases mineures appartiennent au même réseau de Bravais FCC que l'austénite et (2) les contraintes induites par les transformations déplacées (bainite et martensite) réduisent la qualité du cliché et compliquent encore la discrimination des phases. Par conséquent, dans cet axe, nous avons voulu évaluer comment les avancées en matière d'acquisition et d'indexation EBSD peuvent nous aider à atteindre un pourcentage plus élevé et plus fiable d'indexation des phases et en même temps une meilleure identification et discrimination des phases de symétrie similaire.

Il a été démontré que pour les approches d'indexation basées sur la détection des bandes de la Transformée de Hough (HT), il est essentiel d'optimiser la liste des réflecteurs considérés par phase puisque l'intensité des bandes détectées dans l'EBSP ne correspond pas aux intensités des réflecteurs. Une optimisation correcte des réflecteurs considérés peut améliorer le résultat de la discrimination de phase montré sur la Figure 2 (b) en celui de la Figure 2 (c) pour une microstructure d'acier présentant une matrice bainitique, de l'austénite résiduelle et du MnS comme phases mineures.

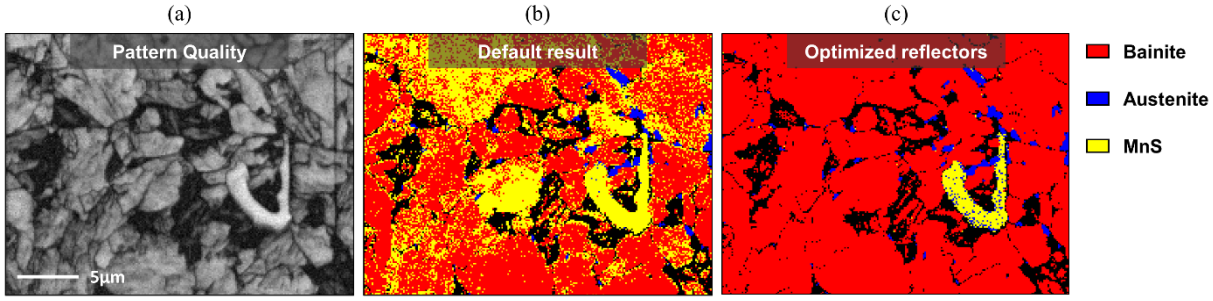

Figure 2. (a) Qualité du cliché, (b) résultat de la discrimination de phase par défaut et (c) résultat de la discrimination de phase après optimisation de la liste des réflecteurs.

Dans certains cas, la liste des réflecteurs des phases à discriminer est équivalente et il n'y a pas d'optimisation possible. Dans ce cas, des méthodes d'indexation avancées telles que Refined Accuracy (RA) et Pattern Matching (PM) ont été employées car elles sont capables de s'appuyer sur la différence du paramètre de réseau des phases à discriminer. Pour ce faire, RA simule la forme hyperbolique réelle des bandes dans l'EBSP tandis que PM compare pixel par pixel les clichés expérimentaux et un dictionnaire de clichés simulés dynamiquement. Les deux approches ont montré un potentiel pour

discriminer l'austénite du $(TiNb)C_2$, deux phases avec une liste équivalente de réflecteurs et une différence de paramètre de réseau de 0.73Å.

La PM s'est avérée la plus performante pour (1) indexer les clichés de mauvaise qualité souvent trouvés dans les îlots de Martensite/Austenite et (2) discriminer les phases à base cubique correspondant à des inclusions ou des précipités mineurs dans une matrice de ferrite/austenite. Ceci grâce à l'exploitation de toute l'information contenue dans le cliché et pas seulement dans les bandes de Kikuchi. Pour comparer les clichés simulés et expérimentaux, la Normalized Cross Correlation (NCC) est la meilleure métrique.

3. L'IA pour l'exploitation automatisée des données d'orientations comme la segmentation de la ferrite, bainite et martensite

Ces dernières années, les approches de l'IA ont gagné en popularité pour aider à l'analyse microstructurale. De plus en plus de travaux proposent d'exploiter les approches en IA pour identifier les constituants d'une microstructure. Dans le cas des aciers, il s'agit par exemple de classer les phases secondaires (perlite, bainite et martensite) d'aciers à matrice ferritique par une approche d'apprentissage automatique. Ce type d'approche a été appliqué à des données issues de différentes techniques telles que la microscopie optique (MO), la microscopie électronique à balayage (MEB) mais beaucoup plus rarement la diffraction des électrons rétrodiffusés (EBSD).

Distinguer directement dans une microstructure les différents produits de transformation comme la ferrite, les bainites et la martensite est souvent au cœur des demandes de industrielles de la sidérurgique. L'EBSD ne permet pas aujourd'hui de distinguer directement ces différents produits de transformation, tous indexés en Ferrite α de structure Cubique Centrée. Toutefois, le signal EBSD est sensible à certaines caractéristiques qui distinguent ces phases : la présence de défauts cristallins, l'existence et le type de relation d'orientation avec le voisinage, la distribution spatiale de micro-constituants. Aujourd'hui cette information est extraite manuellement ou semi-automatiquement par un utilisateur expert. Les procédures mises en œuvre sont complexes, chronophages et surtout très subjectives.

C'est dans ce contexte que nous avons proposé des solutions pour exploiter l'apport de l'IA dans l'analyse des données EBSD acquises sur des microstructures héritées par transformation de phase dans les aciers. Deux approches ont été explorés : l'apprentissage supervisé et les approches non-supervisées.

Discrimination des phases par réseaux de neurones convolutifs (RNC)

Un premier travail a été réalisé en utilisant les réseaux neuronaux convolutifs (RNC) avec une architecture de type U-Net afin de classer automatiquement les phases présentes dans la microstructure d'un acier (Figure 3). Les données d'entrée du modèle ayant permis la meilleure classification se sont avérées être la qualité de la diffraction et de désorientation locale (Kernel Average Misorientation (KAM)). Ce type d'architecture s'appuie sur un apprentissage supervisé. Il faut donc se donner les

moyens de créer un jeu de données labellisées pour l'entrainement du modèle. Par conséquent une procédure « semi-automatique » de labellisation des cartes EBSD a été mise en place.

Pour pallier à la difficulté de labelliser l'ensemble d'une carte EBSD, nous avons introduit une classe « Unknown » pour les configurations difficiles à labelliser même par un expert. Cette classe est alors exclue de l'entrainement. Par ailleurs, pour permettre au modèle de généraliser indépendamment des conditions d'acquisition (en particulier de la taille du pixel de la carte EBSD), la valeur du pas d'acquisition a été intégré aux données d'entrées. Le résultat montre que les performances du modèle sont significativement améliorées pour des cartes EBSD de résolutions différentes de celles utilisées lors de la phase d'entrainement.

Sur une microstructure assez simple d'un acier dualphase, le modèle discrimine les deux phases – ferrite et martensite – automatiquement en quelques secondes et avec une précision de l'ordre de 98.5% [1]. La même approche a été appliquée à des microstructures d'aciers plus complexes en intégrant comme troisième phase la bainite supérieure, en collaboration avec Simon Breumier post-doctorant LEM3/IRT-M2P. Ainsi de nouvelles données EBSD ont été acquises sur des échantillons de deux nuances d'aciers bas-carbone mis à disposition par Industeel et ayant subi différents chemins thermiques pour varier les proportions de ferrite/bainite supérieure/martensite. Là aussi, les résultats sont significativement meilleurs, en qualité de la classification et avec une rapidité de quelques secondes [2].

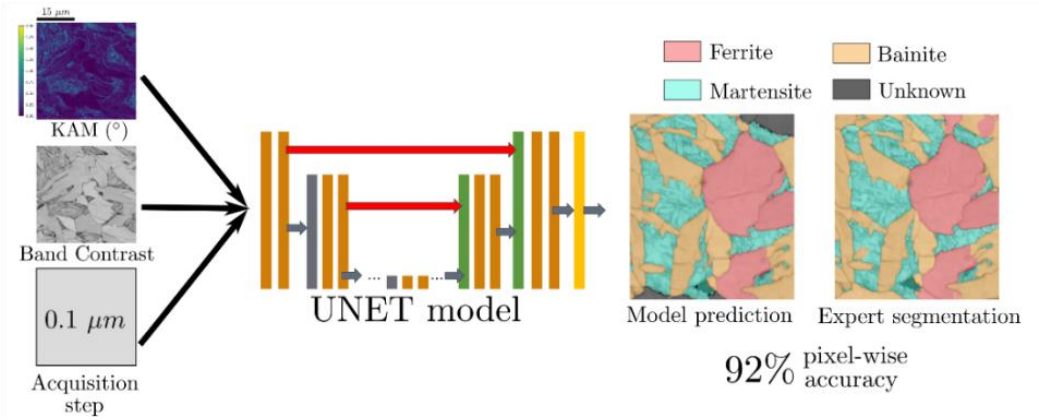

Figure 3. Illustration de l'application des réseaux de neurones convolutifs de type UNET à la discrimination automatique de la ferrite/bainite supérieure/martensite.

Vers des approches non-supervisées

Le principal inconvénient des approches d'apprentissage supervisé est la nécessité de labelliser afin de guider le modèle vers la bonne réponse pendant le processus d'apprentissage. Comme cette tâche est chronophage et très laborieuse, nous avons également testé des approches d'apprentissage non supervisées qui ne nécessitent pas de labellisation.

La première approche testée était un algorithme de clustering *k*-means pour effectuer la discrimination de la bainite supérieure et inférieure (UB et LB : upper bainite, lower bainite). Dans ce type d'approche, le point clé concerne la préparation des données d'entrée pour permettre à l'algorithme de classer les

données efficacement (communément appelé « Feature Engineering »). Différentes caractéristiques ont été extraites des données EBSD avec des complexités croissantes. Notre expérience montre que la distinction entre UB/LB se fait au niveau de l'organisation des variants au sein des paquets (ensemble de variants partageant le même plan d'habitat au sein du grain parent). L'extraction de ce type de caractéristique des données EBSD a été une clé pour classer efficacement les domaines cristallins à l'aide du *k*-means. Les caractéristiques des interfaces – UB/UB, LB/UB, LB/LB – sont également des données importantes (désorientation, tortuosité…) en particulier pour élargir l'approche à des microstructures plus complexes pour prendre en compte l'écart à un plan d'habitat par exemple.

Ainsi la méthode que nous avons développée classifie d'abord l'interface entre deux domaines cristallins (UB/UB, LB/UB, LB/LB) à partir de caractéristiques cristallines associées à chaque domaine et à l'interface. Elle attribue la phase à chaque domaine cristallin à partir de la classification de ces différentes interfaces par vote. La Figure 4 (d) présente le résultat de la segmentation comparé à la labélisation manuelle (Figure 4 (b)). Le résultat est relativement bon compte tenu de la nature non supervisée de l'approche ; les régions de bainite supérieure et inférieure sont bien localisées. Les pixels classés comme ambigus (en violet) correspondent aux grains pour lesquels le mécanisme de vote n'a pas conduit à l'identification d'une phase majoritaire.

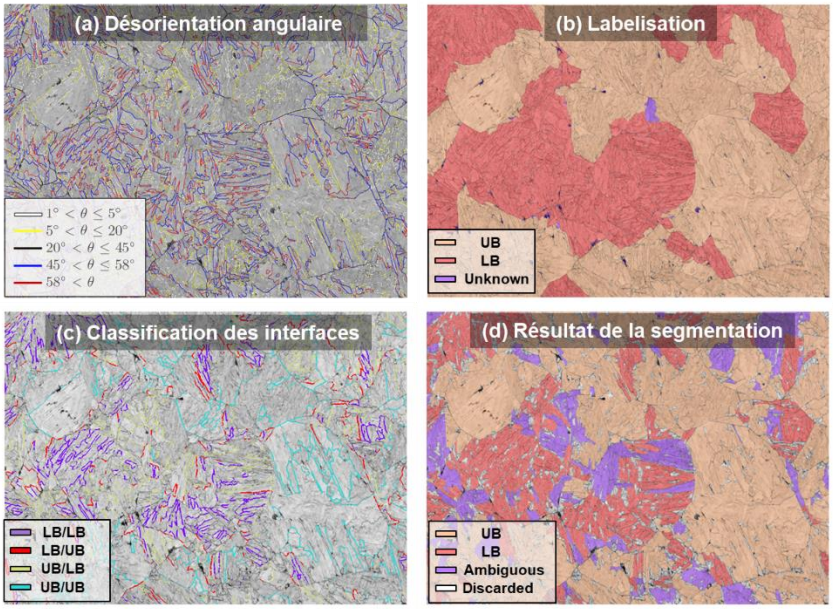

Figure 4. Analyse non supervisée d'une microstructure contenant de la bainite supérieure (UB) et bainite inférieure (LB). (a) Données EBSD visualisées sous forme de carte de désorientations angulaires et (b) labélisation manuelle. Prédiction obtenue avec le modèle k-means : (c) Classification des interfaces, (d) résultat de la segmentation.

La deuxième approche d'apprentissage non supervisé consiste en un RNC couplé à un algorithme de segmentation par superpixels pour obtenir la segmentation de différentes microstructures d'acier. Le modèle a été alimenté par l'indice de qualité des clichés et le KAM et a démontré une très grande précision pour discriminer la ferrite et la martensite des aciers biphasés (Figure 5 (a)). La qualité des résultats pour séparer la ferrite, la bainite supérieure et la martensite dépend de la complexité des

microstructures et du contraste des images de qualité de cliché ou KAM pour discriminer les phases (Figure 5 (b)).

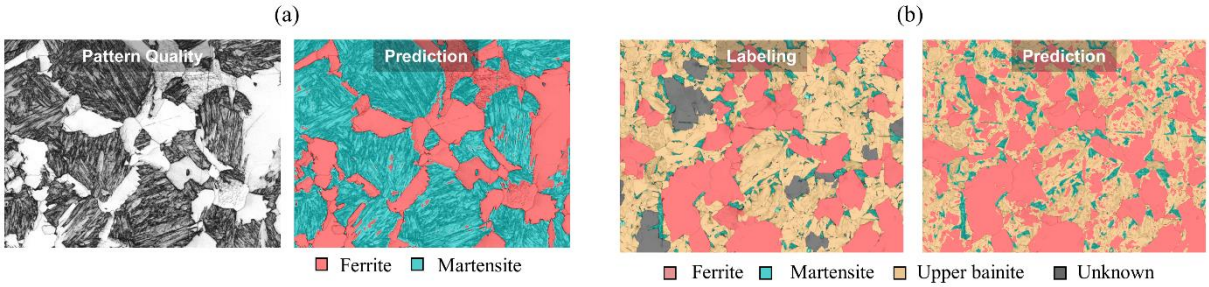

Figure 5. (a) Cas d'une microstructure biphasée ferrite/martensite : carte de la qualité du cliché et prédiction du modèle CNN non supervisé. (b) Cas d'une microstructure plus complexe contenant de la ferrite, de la bainite supérieure et de la martensite : Labélisation manuelle et résultat obtenu par le modèle CNN non supervisé. (Les pixels gris correspondent aux régions que le spécialiste n'était pas sûr de classer).

Les deux approches non supervisées ont fourni des résultats prometteurs et peuvent être utilisées comme une étape de pré-étiquetage pour faciliter le processus.

Publications :

1. Martinez Ostormujof T., Purushottam Raj Purohit R., Breumier S., Gey N., Salib M., Germain L. (2021). "Deep Learning for automated phase segmentation in EBSD maps. A case study in Dual Phase steel microstructures". Materials Characterization, 184:111638. Réf. HAL: hal-03450484
2. Breumier S., Martinez Ostormujof T., Frincu B., Gey N. E., Couturier A., Loukachenko N., Aba-Perea P. E., Germain L. (2022). "Leveraging EBSD data by deep learning for bainite, ferrite and martensite segmentation". Materials Characterization, 186. DOI: https://doi.org/10.1016/j.matchar.2022.111805. Réf. HAL: hal-03480629

Conférences internationales :

1. Martinez Ostormujof T., Purushottam Raj Purohit R., Gey N., Purohit R., Salib M., Germain L. (2021). "Applying Deep Learning to EBSD data for the discrimination of phase transformation products in Steels", MMC2021, 5 juillet 2021, Virtual (États-Unis). Réf. HAL: hal-03442897
2. Martinez Ostormujof T., Purushottam Raj Purohit R., Gey N., Salib M., Germain L. (2021). "Can Convolutional Neural Networks be trained on EBSD data to classify phase transformation products in Steels?" Virtual EBSD 2021, 20-22 Avril 2021, Sheffield (Royaume-Uni). URL: https://www.rms.org.uk/rms-event-calendar/2021-events/ebsd-2021.html. Réf. HAL: hal-03205416
3. Breumier S., Martinez Ostormujof T., Gey N., Frincu B., Couturier A., Loukachenko N., Aba-Perea P., Germain L. (2022). "Assessing the robustness of an EBSD-data-based U-Net model to classify phase transformation products in Steels", 1st World Congress on Artificial

Intelligence in Materials and Manufacturing, 6 Avril 2022, Pittsburgh (États-Unis). Réf. HAL: hal-03788345

4. Breumier S., Martinez Ostormujof T., Gey N. E., Germain L., Frincu B., Loukachenko N., Couturier A., Aba-Perea P. E. (2022). "Leveraging EBSD data for phase transformation product quantification in low carbon steels by deep learning", TMS 2022, 27 février-3 mars 2022, Anaheim, California (États-Unis). Réf. HAL: hal-03611998
5. Germain L., Martinez Ostormujof T., Salib M., Frincu B., Gey N. (2022). "Advanced EBSD and Machine Learning to identify phase transformation products in Steels", RMS EBSD 2022, 12 avril 2022, London (virtual) (Royaume-Uni). INVITED CONFERENCE. Réf. HAL: hal-03788370

Table of content

General introduction and context

To limit climate change, the European Community aims to achieve zero net greenhouse gas emissions by 2050. This perspective places the metallurgical industry under pressure as it is one of the largest contributors to fossil CO_2 emissions.

In this context, steel plays a major role since it is the most widely used metallic material worldwide in many structural applications such as construction, transport and energy. One of the advantages of steel is the abundance and even distribution of most of its base minerals. Additionally, it shows a high versatility in terms of performance as a wide range of mechanical properties can be achieved by tuning its composition and thermomechanical processing (Figure 6). Finally, it is easy to recycle because it can be sorted out from waste through magnetic separation. For all these reasons, steel is a fundamental pillar for present and future structural developments of efficient and sustainable products that need to meet the challenges of the ecological transition.

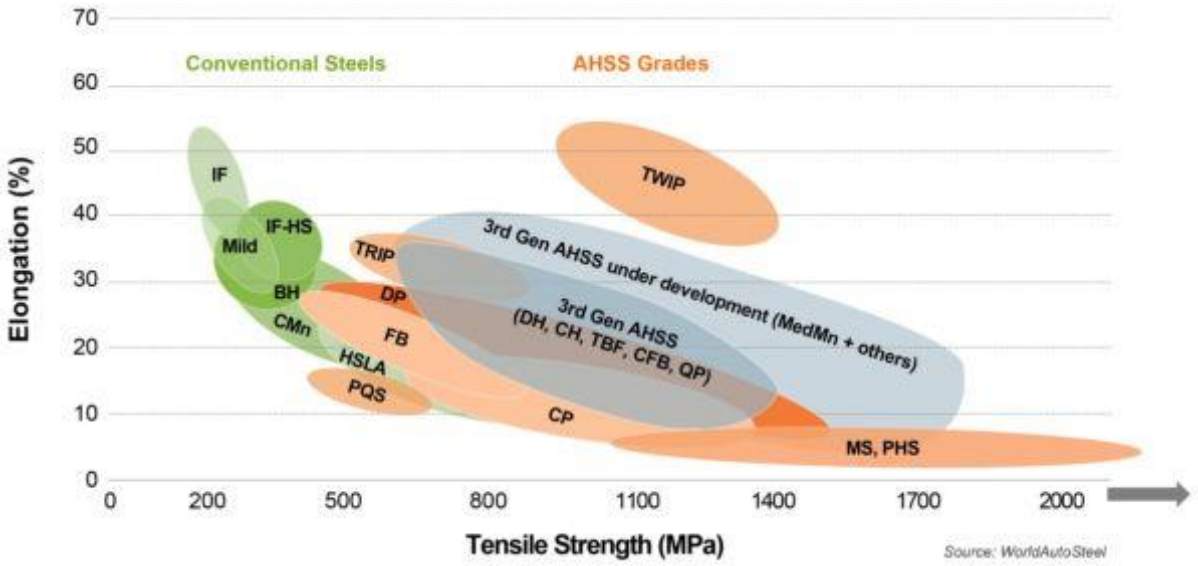

Figure 6. Global Formability Diagram (2021) comparing strength and elongation of current and emerging steel grades [3].

The in-service properties and durability of steel products are strongly linked to their microstructures, inherited from thermomechanical treatments. Therefore, the understanding and optimization of the microstructural evolution are key topics. Modern high-performance steel grades present increasingly complex microstructures inherited by phase transformation: they are multiphase, with constituents of nanometric size, whose topological and crystallographic distribution strongly impacts the mechanical behavior.

For this reason, their characterization by conventional microcopy is more and more challenging. Nowadays there exists many open questions for scanning electron (SE) based microscopy to understand the microstructure of steels in depth: to discriminate with confidence the phase transformation products,

to identify and quantify with accuracy minor phases (especially retained austenite), to know the parent high temperature microstructure that gave rise to the microstructure at room temperature, are some of them.

Recently, great progresses have been made to push the limits of SE-based microscopy including an outstanding evolution of the Electron Backscattering Diffraction (EBSD) technique, widely used for the study of steel microstructures. We can list some progresses below:

- Last generation of EBSD cameras [4] allow the acquisition of high-quality patterns in short times.
- New indexing strategies for EBSD patterns such as improved Hough-based [5] and Pattern Matching [6] have been developed.
- Methods for indirect reconstruction of the parent microtexture [7]–[9] have widely been proposed.
- In-situ heating experiments have started to be coupled with EBSD [10], [11].
- Artificial Intelligence (AI) has started to be applied to interpret the microstructures [12], [13].
- Also complimentary techniques such as chemistry analysis coupled with EBSD [14], High Resolution EBSD (HR-EBS) [15], Electron Contrast Channeling Imaging (ECCI) [16]–[18], Transmission Kikuchi Diffraction (TKD) [19], [20] and 3D-EBSD [21], [22] have been developed to gain more insights about complex microstructures.

Thus, the aim of the present thesis is to evaluate and assess how recent developments in orientation-based microscopy (EBSD) contribute to the analysis and characterization of steel microstructures inherited by phase transformation. The manuscript is organized in two main sections:

1. Application of advanced EBSD-based orientation microscopy for the analysis of steel microstructures.
2. Contribution of AI algorithms for the discrimination of phase transformation products in steels.

Section 1 includes three chapters:

Chapter I is dedicated to a general literature review, initially focused on steel microstructures inherited by phase transformation. Both microstructural and crystallographic features characterizing the different phases like ferrite/bainite/martensite are detailed. Secondly, a review of EBSD as a powerful characterization tool for steel microstructures is presented. The focus is on the discrimination of main phase transformation products and minor phases with close crystal symmetry. Approaches of indirect parent reconstruction and EBSD in-situ heat treatments are also reviewed.

Chapter II focuses on the contribution of last generation EBSD cameras and new pattern indexing methods (Hough-based and Pattern Matching) to improve the characterization of multiphase steels. The aim is to evaluate their performance for improved reliable phase indexing. In particular we are interested

in the correct identification of retained austenite; its small size and the high density of defects in its neighborhood (martensite) complicate the acquisition of clean patterns. Additionally, its discrimination from minor phases such as carbides, nitrides and sulfides with close crystal structure is a great challenge. Tips for optimizing and increasing confidence in phase indexing are provided, together with algorithms to improve data postprocessing.

Chapter III focuses on the contribution of high temperature EBSD experiments to analyze the transformation mechanisms and inherited microstructure while heating and cooling, in complementarity with indirect parent reconstruction. For this purpose, a heating module with a maximum temperature of 1000°C and an optimized geometry has been implemented in a FEG-SEM equipped with a last generation CMOS EBSD camera. We discuss the performance and limitations of the module (and the technique in general) for a better understanding of the microstructure inheritance by phase transformation. From this first feedback, we have conducted three preliminary studies to evaluate the contribution of in-situ EBSD experiments: 1) the effect of austempering cycles (in collaboration with our industrial partner Vallourec) and 2) the effect of nitrides (in collaboration with Institute Jean Lamour) on the austenite microstructure refinement at high temperature, 3) ferrite nucleation and growth during cooling from the austenite domain (in collaboration with University of Rouen).

Section 2 is also divided in three chapters:

Chapter IV presents theoretical background about AI where the main concepts of this field are explained, followed by a detailed literature review about AI approaches devoted to the characterization of steel microstructures.

Chapter V is dedicated to the discrimination of phase transformation products in steels microstructures by means of supervised learning methods. A semantic segmentation (pixel-wise classification) approach based on EBSD-derived parameters fed to a Convolutional Neural Network (CNNs) called U-Net is proposed for the characterization of dual-phase (ferrite and martensite) and multiphase (ferrite, martensite and upper bainite) steel microstructures. These studies have been performed in collaboration with ArcelorMittal (Global R&D, Maizières and Industeel France, Creusot).

Chapter VI aims to work on unsupervised learning approaches to reduce the time, effort and human input needed. Synthetic EBSD maps are generated to reduce the need of experimental data to train a model. Additionally, we propose two segmentation approaches: a *k*-means clustering to segment the microstructures proposed in Chapter V and an unsupervised CNN coupled with superpixel segmentation to discriminate upper and lower bainite.

Chapter I**: Literature review**

I.1 Introduction

This chapter is dedicated to the general literature review of the main topics addressed by this thesis and it is separated in three main parts.

Initially, an introduction to low-carbon steels is provided, where we detail how the main steel phases are formed and which are the most relevant microstructural features characterizing each of them. Additionally, a section addresses the role of alloying elements that are prone to precipitate minor phases such as carbides, nitrides and sulfides that are usually difficult to discriminate from austenite by EBSD.

In a second instance, we describe the crystallographic features such as orientation relationships, hierarchal organization of variants, misorientation angle distributions, among others, that may help in the characterization of the different phase transformation products such as ferrite, martensite and bainite.

Finally, an extensive literature review about the potential and limits of EBSD as a characterization technique applied to inherited steel's microstructures is provided. A section is dedicated to detail the state of the art in automatic or semiautomatic discrimination of ferrite, bainite and martensite based on EBSD-derived features. This is followed by a review about EBSD-based studies dedicated to the discrimination of minor phases present in steel sharing similar crystal structures. Lastly, we focus on the studies related to austenitic parent microstructures, reviewing both indirect reconstruction methods and also in-situ heating EBSD experiments.

I.2 Introduction to low carbon steels

Steel is an alloy principally made up of iron (Fe) and carbon (C) as alloying element. C acts as an interstitial solute to improve the steel's mechanical properties such as tensile strength, hardness, and yield strength. On the contrary, the ductility and toughness of the steel get reduced. Steels have a C concentration between 0.02 and 2.11% by weight, but low-carbon steels are limited to 0.3%. Apart from C, many other alloying elements are added to improve important properties of the steel (see I.2.2).

The microstructure of a steel is controlled by heat treatments, where many different phases (presented in I.2.1) can precipitate. Each of these phases presents different mechanical properties and their combination is a way to optimize the alloys. Therefore, steels' microstructures are often very complex, showing a mix of inherited phases, residual parent phase that may not have been transformed and several precipitates like carbides, nitrides and sulfides obtained from the alloying elements.

I.2.1 Main phases and transformation mechanisms

Low-carbon steels present the same allotropic transformations as pure Fe as can be observed on the left-hand side of the Fe-C equilibrium diagram in Figure I.1. Fe can adapt different crystal structures depending on the temperature. From room temperature and up to 912°C, pure Fe is called α-Fe or ferrite and presents a Body Centered Cubic (BCC) crystal structure. In the range between 912°C and 1394°C,

the stable phase is called γ-Fe or austenite and shows a Face Centered Cubic (FCC) crystal structure. Above these temperatures, between 1394°C and 1538°C pure iron is called δ-Fe and once again its structure is BCC.

The compactness of the FCC crystal structure is higher than that of the BCC. The lattice constant parameter for ferrite is equals to 0.286nm at 20°C while for austenite it is 0.358nm at 912°C. Solubility in ferrite is very low (its maximum reaches 0.022% by weight at 727°C) because the shape and size of the interstitial sites in the BCC structure make it difficult to position the C atoms. Austenite, on the other hand, has a much higher solubility (2.11% at 1148°C).

In Figure I.1, steel is localized in concentrations between 0.02 and 2.11% by weight of C. Depending on the C content, steels can be classified in hypoeutectoid (from 0.08 to 0.76%), eutectoid (0.77%) and hypereutectoid (from 0.78% to 2.11%).

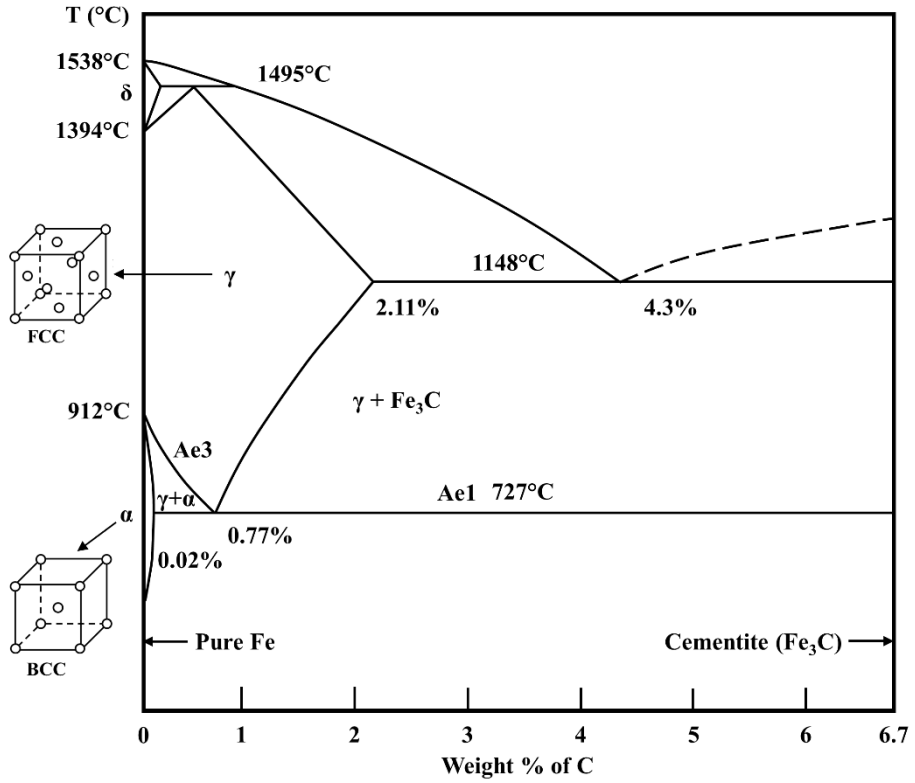

Figure I.1. Fe-C equilibrium diagram.

As shown in the schematic continuous cooling transformation (CCT) diagram in Figure I.2 (a), high temperature parent austenite phase can transform in different inherited phases: ferrite, pearlite, bainite and martensite. All these transformations can be classified into two main groups: diffusional and displacive (Figure I.2 (b)). Diffusional transformations occur thanks to the thermally activated movement of C atoms across the interface between austenite and the new phase that is transforming (child phase). This transformation respects equilibrium as the atoms have enough time to diffuse and get rearranged in their new crystal structure. On the other hand, displacive transformations occur when the cooling rates are higher and diffusion is hindered. Only a small and correlated movement of atoms

is allowed (shear and volume change), what introduces a lattice deformation by keeping an invariant plane so that their atomic positions and orientation do not change during the transformation. This plane is called habit plane and it is better detailed in I.3.3.

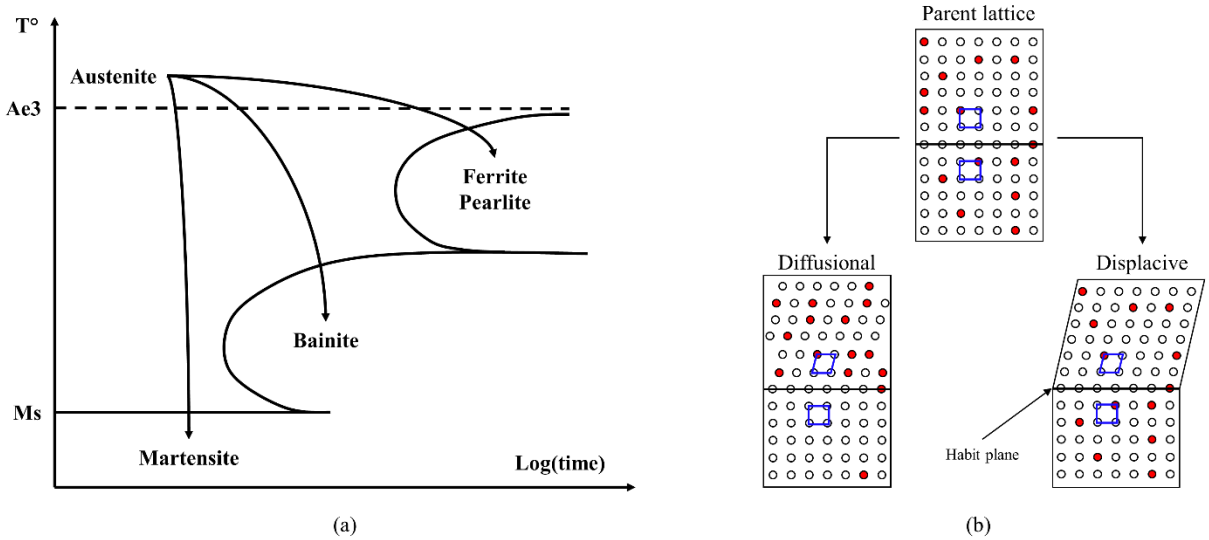

Figure I.2.(a) Scheme of the CCT diagram of a steel and (b) illustration of the diffusional and displacive transformations.

In the following sections we detail how the different transformations presented in the CCT diagram of Figure I.2 (a) occur and the corresponding microstructures are described.

I.2.1.1 Ferritic-pearlitic transformation

During cooling from the high temperature austenitic field, if the cooling rate is slow, equilibrium is respected and austenite transforms into ferrite and pearlite through a diffusional transformation. Upon contact with the Ac3 line, proeutectoid ferrite starts to nucleate at the austenitic grain boundaries and grows into the austenitic grain thanks to the C diffusion from ferrite to austenite. The resulting ferrite mainly presents an equiaxed and polygonal shape and it is known as allotriomorph ferrite.

Once temperature reaches Ac1, the nucleation and growth of ferrite and cementite (Fe_3C) in the remaining austenite grains occurs giving rise to a pearlitic microstructure. The pearlite is then a product of two laminar phases of eutectoid decomposition given by a cooperative and synchronized growth. The alternate arrangement of ferrite and Fe_3C is created as C diffuses towards Fe_3C.

If the cooling rate is increased, the diffusional transformation of allotriomorph ferrite is hindered and gives place to a different ferrite type called Widmanstätten, which is thought to be a displacive transformation, although it is still the subject of study. It shows a needle like structure and nucleates in the allotriomorph ferrite.

Examples of both ferrite types are shown in Figure I.3.

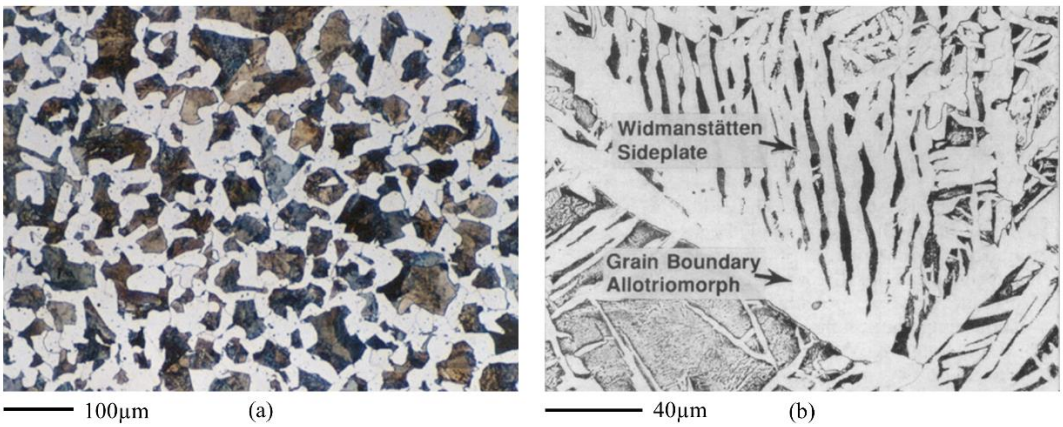

Figure I.3. Optical micrographs of (a) allotriomorph ferrite (bright) and pearlite (dark) [23] *and (b) Widmanstätten ferrite that precipitated from the allotriomorph ferrite* [24].

I.2.1.2 Martensitic transformation

Martensite precipitates from the parent austenite phase as a result of a quick cooling (quenching) after reaching the martensite start (Ms) temperature where the first martensitic domain is formed. As a displacive transformation, it occurs thanks to a shear mechanism. As the temperature keeps decreasing, the transformation continues by forming new martensitic domains and not growing the preformed ones. This process is repeated until martensite finish (Mf) temperature, where transformation stops. In some cases, austenite does not totally transform into martensite leaving retained austenite in the final microstructure.

The resulting martensite is a solid solution of Fe presenting a Body Centered Tetragonal (BCT) crystal structure saturated in C as the C atoms have no time to diffuse from ferrite to austenite. For this reason, the chemical composition of martensite is equal to that of its parent austenite. Although there exists a crystal structure difference between ferrite and martensite (BCC and BCT respectively), for low-carbon steels their lattice parameter remains close as there is not a high amount of C to induce a large degree of deformation.

The morphology of martensite strongly depends on the C content. For steels with a C content by weight below 0.6%, martensite precipitates with the shape of laths which are grouped in packets whose laths are parallel. For higher C contents (but low fraction of alloying elements), the microstructure changes from a lath to a roughly plate-like product. In this case, a first plate divides the entire Prior Austenite Grain (PAG) and the following plates precipitate in the remaining PAG by further subdividing it. Thus, the size of the plates decreases as the transformation progresses. The plates contain a high density of dislocations and twins. If the steel has both high C and high alloying content the plates precipitate with a lenticular shape.

Examples of lath-like and plate-like martensite are shown in Figure I.4.

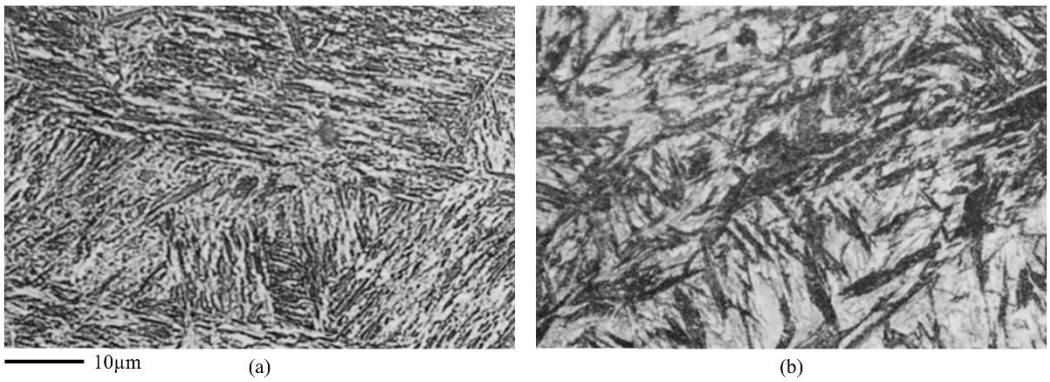

Figure I.4. Optical micrographs of (a) lath-like martensite for a steel 0.3%C, 4%Ni, 1.4%Cr and (b) plate-like martensite (dark) with residual austenite (bright) on a steel 0.8%C, 4%Ni, 1.6%Cr, 0.4%Mo [25].

I.2.1.3 Bainitic transformation

At intermediate cooling rates between ferrite-pearlite and martensite, the bainitic transformation occurs. From its first observation, the formation of bainite is still a subject of discussion. There exist two main theories, the displacive [26] and the diffusional [27]. According to the displacive theory, the bainitic transformation is assumed to occur without diffusion of Fe or substitutional atoms as for the martensitic transformation. However, the growth rate of bainite is controlled by the rate at which C can diffuse away from the interface, whereas martensite plates are able to advance without any C diffusion. In the diffusional theory, bainite growth occurs by a short-range diffusion mechanism of lattice atoms, i.e., Fe and substitutional atoms.

Bainite is a mixture of ferrite and Fe_3C or retained austenite. The microstructure of bainite depends mainly on the temperature at which it forms. At high temperature (350-550°C) bainite consists of needles or laths of ferrite with Fe_3C precipitates between the laths. This bainite type is called upper bainite. At sufficiently low temperature (200-400°C) the microstructure of bainite changes from laths into plates and the carbide dispersion becomes much finer appearing both between plates and in the ferrite plate. This is the so-called lower bainite [28]. Examples of lower and upper bainite are shown in Figure I.5.

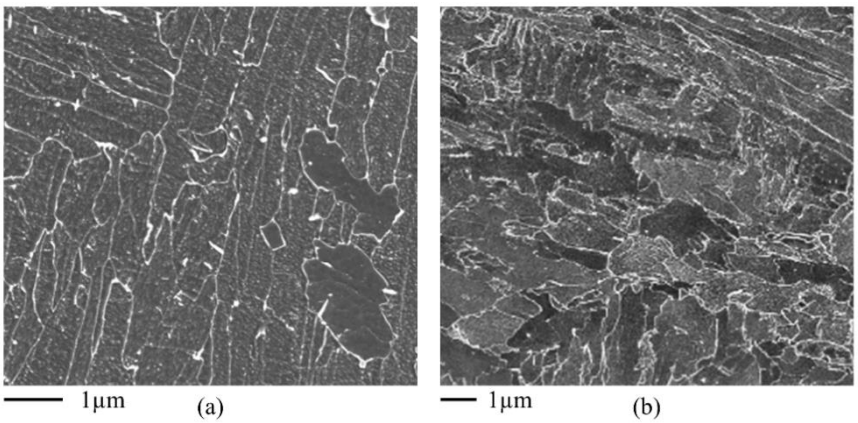

Figure I.5. SEM micrographs of (a) lower bainite and (b) upper bainite [28].

I.2.2 Minor phases: alloying elements and precipitates

Apart from C, other alloying elements may be present in the steel composition as they can influence and modify the precipitation of the different phase transformation products. One very important aim of alloying elements is to increase the hardenability of steel in order to optimize mechanical properties and toughness after heat treatment. To increase the hardenability means delaying the time required for the decomposition into ferrite and pearlite in order to produce a fully martensitic microstructure [29].

The alloying elements are usually classified in two main types: those that expand the austenite field and favor the formation of austenite over wider compositional limits such as Mn, Ni or Cu (called austenite stabilizers) and those that contract the austenite field and encourage the formation of ferrite over wider compositional limits such as Cr, Mo or Si (called ferrite stabilizers).

Among the mentioned alloying elements, there are some that have higher affinity with oxygen than Fe (e.g. Al, Ti or V) and are used to form oxides during the steelmaking in order to deoxidize the steel. Other elements are prone to form carbides or nitrides since they have a higher affinity with C and N than with Fe, e.g. Cr, Mo, Mn, Nb, Ti or V [30]. Both carbides and nitrides are known to increase the hardness of steels by precipitation hardening.

In this context, the final, microstructure of a steel may present certain precipitates such as MC, M_3C, $M_{23}C_6$, M_2C, M_7C_3, M_6C, MN or M_2N depending on the alloy's composition (being M the alloying element). In addition to carbides and nitrides, sulfides can be also found within the microstructure in particular MnS. Mn has a high affinity for S what transforms it in a strong sulfide former (MnS). Mn is used to avoid the formation of Fe-sulfides at the grain boundaries that results in the fragilization of the steel. Instead, MnS mainly presents an intragranular nucleation that avoids this fragilization effect [31].

I.3 Crystallographic features of low-carbon steels

Microstructural characterization is achieved with conventional microscopic analysis techniques such as light optical (LOM) or scanning electron (SEM) microscopy on a sample etched with an appropriate chemical agent. However, since the advent of EBSD as a crystallographic characterization technique, a large number of new and significant features can be obtained in a reasonable time, allowing to shed more light on the identification of the different phase transformation products. Along this section, several important crystallographic concepts are explained in order to understand how crystallographic orientations can provide meaningful information for microstructural characterization.

I.3.1 Individual orientation and misorientation

EBSD is a characterization technique that enables the determination of the crystallographic orientation at a measured point in a microstructure [32]. A crystallographic orientation is defined as the rotation *g* that allows the macroscopic reference frame (K_A), linked to the sample, to coincide with one crystallographic reference frame (K_B) linked to the considered crystal lattice (all translations ignored)

(Figure I.6) [33]. K_A is usually chosen according to the geometry of the sample or the manufacturing process while K_B follows the symmetry of the crystal lattice.

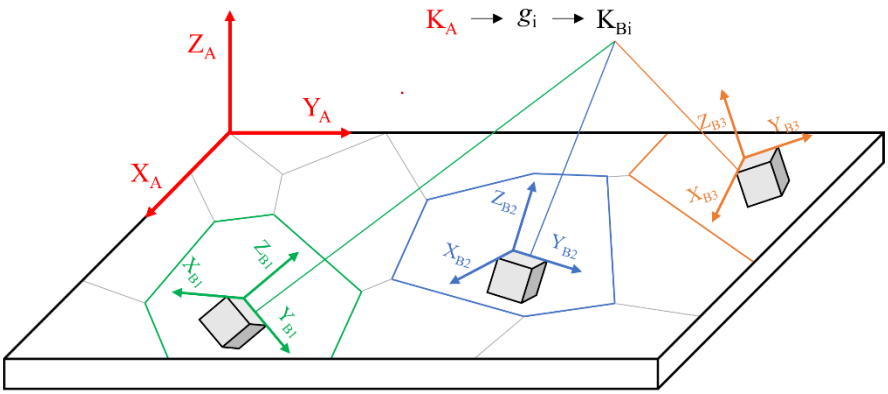

Figure I.6. Sample's reference axes K_A and the crystallographic reference axes K_{Bi} for each individual grain.

In a cubic crystal, the reference axes of the K_B frame are chosen parallel to the <100>, <010> and <001> crystallographic directions. Since there are twenty-four physically indistinguishable ways to choose K_B for a cubic crystal [34], there are twenty-four equivalent rotations that characterize the same orientation:

$$S_i * g \equiv g$$

S_i being any of the twenty-four symmetry elements of the cubic group.

A misorientation between two crystals is defined as a rotation g necessary to put into coincidence the axes of two different crystal reference frames (for example K_{B1} and K_{B2}):

$$g_2^{-1} * g_1 \equiv (S_j * g_2)^{-1} * (S_i * g_1)$$

Since there are 24×24 cubic-cubic misorientations, conventionally the misorientation space is reduced by choosing among all possibilities, the rotation of minimum angle around a rotation axis falling in the fundamental space (standard triangle).

Rotations can be expressed in several different ways:

Euler angles. It has been the most commonly used representation. A rotation g is broken into three elementary rotations described by a Euler angles triplet (φ_1, Φ, φ_2) as shown in Figure I.7. First, a rotation of an angle φ_1 around the axis z of K_A transforms K_A into K' = (x', y', z). A second rotation of an angle Φ around the axis x' of K' transforms K' into K'' = (x', y'', z'). Finally, a rotation of an angle φ_2 around the axis z' of K'' transforms K'' into K_B = (x'', y''', z') [33].

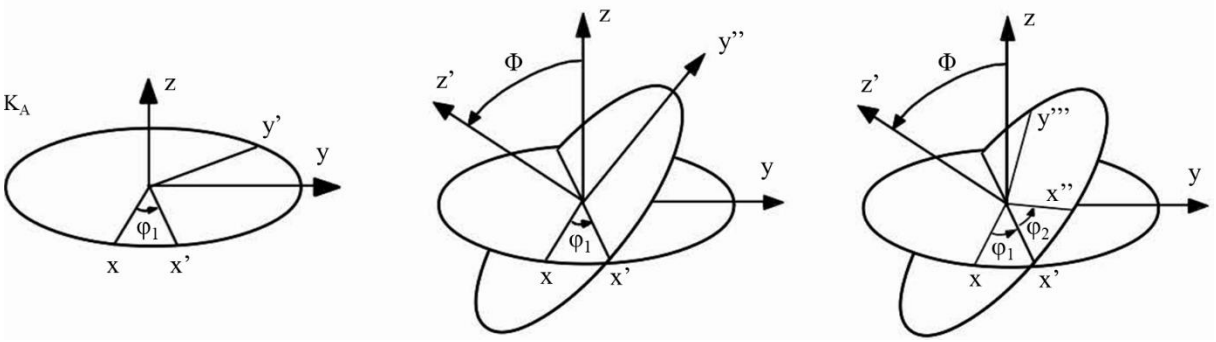

Figure I.7. Definition of the Euler angles.

Matrices. A rotation g can also be defined by a matrix M(g) that allows the calculation of a vector components defined in the K_B frame, into the K_A frame:

$$K_A \rightarrow K_B$$

$$V_{K_A} = M(g).V_{K_B}$$

Decomposing the rotation according to the three rotations described above:

$$M(g) = \begin{pmatrix} c_1c_2 - s_1s_2c & c_1c_2 - s_1s_2c & s_1s \\ s_1c_2 + c_1s_2c & -s_1s_2 + c_1c_2c & -c_1s \\ s_2s & c_2s & c \end{pmatrix}$$

where $c = cos\phi,\ c_1 = cos\varphi_1,\ c_2 = cos\varphi_2,\ s = sin\phi,\ s_1 = sin\varphi_1,\ s_2 = sin\varphi_2$

Axis-angle. A rotation g can be described as a rotation of an angle ω about a unit axis $\vec{d}$:

$$\omega = \left(\arccos\left(\frac{Trace\big(M(g)\big) - 1}{2}\right)\right)$$

$$\vec{d} = \begin{pmatrix} d_1/N \\ d_2/N \\ d_3/N \end{pmatrix}, with \begin{array}{l} d_1 = M(2,3) - M(3,2) \\ d_2 = M(3,1) - M(1,3) \\ d_3 = M(1,2) - M(2,1) \end{array} and\ \ N = \sqrt{{d_1}^2 + {d_2}^2 + {d_3}^2}$$

Quaternions. A quaternion is defined as $\mathrm{q} = q_1 + q_2 * \mathrm{i} + q_3 * \mathrm{j} + q_4 * \mathrm{k}$, where q_1 represents the rotation angle (called scalar part) and $q_2 * \mathrm{i} + q_3 * \mathrm{j} + q_4 * \mathrm{k}$ stands for the axis about the rotation is performed (called vector part). Its practical to manipulate rotations. A rotation g of an angle ω around a unit axis $\vec{d}$ can be expressed as a quaternion as:

$$q_1 = \cos\left(\frac{\omega}{2}\right) \quad q_2 = \sin\left(\frac{\omega}{2}\right).\frac{d_1}{N} \quad q_3 = \cos\left(\frac{\omega}{2}\right).\frac{d_2}{N} \quad q_4 = \cos\left(\frac{\omega}{2}\right).\frac{d_3}{N}$$

A rotation can be defined by two equivalent quaternions (q_1, q_2, q_3, q_4) and $(-q_1, -q_2, -q_3, -q_4)$. Therefore when necessary, to avoid this ambiguity, it is possible to only use the equivalent with $q_n > 0$, with n being the lowest index where $q_n \neq 0\ and\ n \in [1,2,3,4]$.

Other representations. There are other mathematical concepts that can be used to represent rotations. A review can be found in [35].

I.3.2 Orientation relationship between austenite and inherited phases

The parent austenite phase presents a non-random crystallographic relationship with the inherited phase called orientation relationship (OR), associated to the existence of coherent interfaces between the crystal lattices of both phases. A particular OR can be characterized by the coincidences between a plane and a direction of the parent austenite and the inherited phase and can be summarized as follows:

$$(hkl)_\gamma \parallel (hkl)_\alpha \; and \; [uvw]_\gamma \parallel [uvw]_\alpha$$

This OR can be expressed as a rotation Δg that puts into coincidence the crystallographic reference frame of parent austenite with that of the inherited phase. Since austenite has a cubic structure, it presents twenty-four symmetry elements $\{S_i^\gamma; i = 1, 2, \dots, 24\}$ that result in twenty-four different rotations that express all twenty-four possible orientations of inherited phase in relationship with the parent phase. These orientations are called crystallographic variants and the particular orientation of a variant (g_i^α) can be calculated from the OR knowing the orientation of the parent austenite g_p and it is expressed as the product of the following rotations:

$$g_i^\alpha = \Delta g . S_i^\gamma . g_p$$

As the inherited phases also present a cubic lattice $\{S_j^\alpha; i = 1, 2, \dots, 24\}$ the rotations representing the orientation of a variant (g_i^α) can be described equivalently by one of the twenty-four following rotations:

$$S_j^\alpha . g_i^\alpha = S_j^\alpha . \Delta g . S_i^\gamma . g_p$$

I.3.2.1 Orientation relationships applied to steels

In 1924, Bain [36] proposed a structural transformation of austenite (FCC) into martensite (BCC) occurring by an homogeneous deformation of the austenite lattice illustrated in Figure I.8. The OR proposed by Bain, presented in Table I.1, consists in a 45° rotation about the <100>$_\gamma$ axis to go from FCC to BCC. With this rotation, the twenty-four variants result in only three distinct variants being confused by groups of eight.

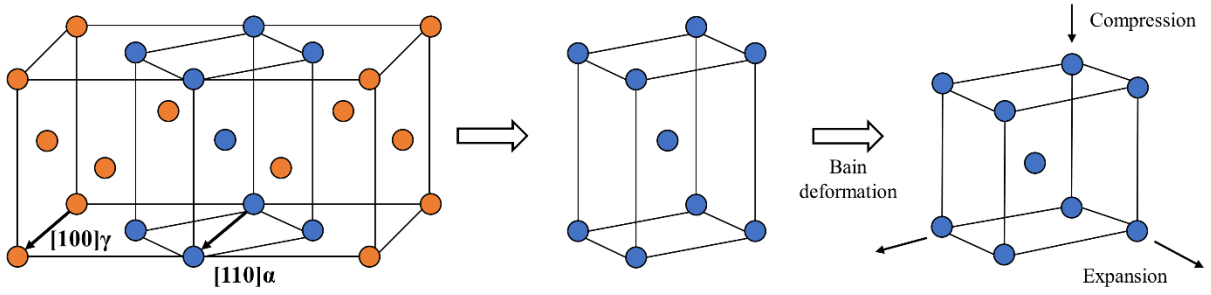

Figure I.8. Bain transformation.

Following Bain's work, several studies have been performed in order to propose more elaborated ORs that enable a better description of phase transformations from austenite. The most commonly used are those of Kurdjumov-Sachs (KS) [37], Nishiyama-Wassermann (NW) [38], Pitsch [39] and Greninger-Troiano (GT) [40] (Table I.1). It must be noted that these ORs are based on different directions and crystallographic planes, and thus lead to a different number of possible variants.

Table I.1. Orientation relationships (ORs) most commonly used to describe the correlation between FCC and BCC lattices.

Orientation relationships	Parallel planes	Parallel directions	Number of variants
Bain	$\{100\}_\gamma$ // $\{100\}_\alpha$	$<100>_\gamma$ // $<110>_\alpha$	3
Kurdjumov-Sachs (KS)	$\{111\}_\gamma$ // $\{110\}_\alpha$	$<100>_\gamma$ // $<111>_\alpha$	24
Nishiyama-Wassermann (NW)	$\{111\}_\gamma$ // $\{110\}_\alpha$	$<211>_\gamma$ // $<110>_\alpha$	12
Pitsch	$\{100\}_\gamma$ // $\{110\}_\alpha$	$<110>_\gamma$ // $<111>_\alpha$	12
Greninger-Troiano (GT)	$\{111\}_\gamma$ 1° from $\{110\}_\alpha$	$<211>_\gamma$ 2.5° from $<110>_\alpha$	24

Although the proposed ORs in Table I.1 are respected in several cases, it has been repeatedly found that a single OR is apparently never strictly followed for a given material. These OR dispersions can be due to different factors such as differential expansion during cooling, evolution of the microstructure (relaxation) after transformation and local residual stresses resulting in plastic rotations [41]. In the case of bainite and martensite, the orientations of the different observed variants are usually located within the Bain region [42].

I.3.2.2 Measured orientation relationships in steels

As mentioned, the OR between the parent and inherited phases in steels does rarely correspond exactly to those presented in Table I.1. One speaks of an irrational OR when it cannot be expressed by a parallelism between close packed planes and directions. The OR can be directly measured in presence of retained parent phase, or indirectly using only martensite variant orientation coming from a single parent grain [43]–[45]. Unfortunately, in the literature most studies report KS or NW as representative ORs because of the complexity of the measure.

Irrational ORs are then often represented in a biaxial plot where the angles between close packed planes and close packed direction are represented (Figure I.9). Martensite OR is often very close to GT but can be influenced by composition and by grain size [46]. Bainite OR spans from GT towards larger angles between closed packed planes. It is sensitive to the composition [44], to cooling speed and prior austenite state (deformed/recrystallized) [46].

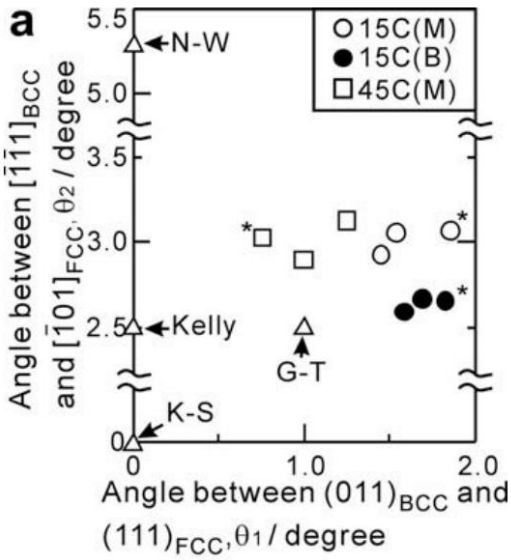

Figure I.9. Angles between $[\bar{1}01]_{fcc}$ *and* $[\overline{11}1]_{bcc}$ *(θ2) of ORs obtained by fitting as a function of angles between* $(111)_{fcc}$ *and* $(001)_{bcc}$ *(θ1) for martensite and bainite with respect to reference ORs (KS, NW, GT and Kelly). White and black circles: OR of martensite and bainite obtained for a 0.15%C-1.5%Mn-0.2%Si steel. White squares: OR of martensite obtained for a steel 0.45%C-0.86%Mn-0.26%Si* [44].

For ferrite it has been observed that the eutectoid ferrite forming pearlite nucleates at the PAG boundaries (PAGBs) with a KS OR [47]. In the case of proeutectoid ferrite, the allotriomorph type is known to nucleate in the PAGB with which it shears a KS or NW OR, but grows into the PAG with which there does not exists an OR [41]. For the specific case of Widmanstätten ferrite, it has been observed that the needles within the packet are weakly misoriented between them and nucleate in KS or NS-OR with austenite, but grow into the PAG with which they present an OR [48].

I.3.3 Habit plane

As described in I.2, displacive (martensitic) transformations present an invariant plane called habit plane where its orientation and its relative atomic positions remain unchanged during transformation. This is the plane at the interface between the parent austenite and the inherited phase. The crystallographic characteristics of the habit plane depend on the transformation mechanism and the ability of the parent and inherited phases to accommodate the induced deformation by shear or twinning. The habit plane varies according to the chemical composition of the steel and the transformation temperature.

For lath-like martensite (<0.5% by weight of C), the OR found with the parent austenite is close to KS showing a habit plane of type $\{111\}_\gamma$ [49]. As the C content increases to 1.4% it has been found that the habit plan changes to the $\{225\}_\gamma$ [50] and above 1.4% it corresponds to the $\{259\}_\gamma$ [37]. The bainitic transformation shows as well a habit plane which also depends on the composition and transformation temperature. Considering low-carbon steels, the habit plane for upper bainite is close to $\{223\}_\gamma$ or $\{557\}_\gamma$ [51] whereas for lower bainite is close to $\{335\}_\gamma$ (0.38% by weight of C) [52].

I.3.4 Inherited variants: spatial distribution and hierarchical organization

It has been observed that for certain transformations such as martensitic or bainitic, not all the possible twenty-four variants appear randomly in the inherited microstructure and there exists a selection of some particular variants. In [41] three variant configurations have been described: 1) No variant selection: the variants are spatially random distributed and all appear with the same probability, 2) Spatial variant selection: locally some variant pairs are favored (usually called variant pairing) and 3) Volumetric variant selection: at the sample scale, some variant are favored influencing the inherited texture of the material. A combination of spatial and volumetric variant selection is also possible.

Spatial variant selection has been evidenced for martensite within the PAGs by Morito et al. [53]. Table I.2 lists the twenty-four possible variants in the case of the KS-OR. A PAG is divided in packets (CP) whose laths have the same plane parallel relationship between close-packed planes (e.g. V1 to V6). This gives raise to four crystallographically different packets within the PAG. For one couple of parallel close-packed planes within a packet, there exist a maximum of six variants with different direction parallel relationships.

Table I.2. Twenty-four variants of the K–S OR and their values for the CP groups.

Variant no.	Plane parallel	Direction parallel	CP group	Misorientation from V1 (°)
V1	$(1\,1\,1)_\gamma//(0\,1\,1)_\alpha$	$[\bar{1}\,0\,1]_\gamma//[\bar{1}\,\bar{1}\,1]_\alpha$	CP1	–
V2		$[\bar{1}\,0\,1]_\gamma//[1\,1\,\bar{1}]_\alpha$		60.0
V3		$[0\,1\,\bar{1}]_\gamma//[\bar{1}\,\bar{1}\,1]_\alpha$		60.0
V4		$[0\,1\,\bar{1}]_\gamma//[1\,1\,\bar{1}]_\alpha$		10.5
V5		$[1\,\bar{1}\,0]_\gamma//[\bar{1}\,\bar{1}\,1]_\alpha$		60.0
V6		$[1\,\bar{1}\,0]_\gamma//[\bar{1}\,1\,\bar{1}]_\alpha$		49.5
V7	$(1\,\bar{1}\,1)_\gamma//(0\,1\,1)_\alpha$	$[1\,0\,\bar{1}]_\gamma//[\bar{1}\,\bar{1}\,1]_\alpha$	CP2	49.5
V8		$[1\,0\,\bar{1}]_\gamma//[\bar{1}\,1\,\bar{1}]_\alpha$		10.5
V9		$[\bar{1}\,\bar{1}\,0]_\gamma//[\bar{1}\,\bar{1}\,1]_\alpha$		50.5
V10		$[\bar{1}\,\bar{1}\,0]_\gamma//[\bar{1}\,1\,\bar{1}]_\alpha$		50.5
V11		$[0\,1\,1]_\gamma//[\bar{1}\,\bar{1}\,1]_\alpha$		14.9
V12		$[0\,1\,1]_\gamma//[\bar{1}\,1\,\bar{1}]_\alpha$		57.2
V13	$(\bar{1}\,1\,1)_\gamma//(0\,1\,1)_\alpha$	$[0\,\bar{1}\,1]_\gamma//[\bar{1}\,\bar{1}\,1]_\alpha$	CP3	14.9
V14		$[0\,\bar{1}\,1]_\gamma//[\bar{1}\,1\,\bar{1}]_\alpha$		50.5
V15		$[\bar{1}\,0\,\bar{1}]_\gamma//[\bar{1}\,\bar{1}\,1]_\alpha$		57.2
V16		$[\bar{1}\,0\,\bar{1}]_\gamma//[\bar{1}\,1\,\bar{1}]_\alpha$		20.6
V17		$[1\,1\,0]_\gamma//[\bar{1}\,\bar{1}\,1]_\alpha$		51.7
V18		$[1\,1\,0]_\gamma//[\bar{1}\,1\,\bar{1}]_\alpha$		47.1
V19	$(1\,1\,1)_\gamma//(0\,1\,1)_\alpha$	$[\bar{1}\,1\,0]_\gamma//[\bar{1}\,\bar{1}\,1]_\alpha$	CP4	50.5
V20		$[\bar{1}\,1\,0]_\gamma//[\bar{1}\,1\,\bar{1}]_\alpha$		57.2
V21		$[0\,\bar{1}\,\bar{1}]_\gamma//[\bar{1}\,\bar{1}\,1]_\alpha$		20.6
V22		$[\bar{1}\,\bar{1}\,0]_\gamma//[\bar{1}\,1\,\bar{1}]_\alpha$		47.1
V23		$[1\,0\,1]_\gamma//[\bar{1}\,\bar{1}\,1]_\alpha$		57.2
V24		$[1\,0\,1]_\gamma//[\bar{1}\,1\,\bar{1}]_\alpha$		21.1

Figure I.10 shows the resulting organization within a PAG. The PAG is divided in packets whose laths are parallel and share the same habit plane $\{111\}_\gamma$. Within each packet, blocks corresponding to a group of laths with the same variant or with weakly misoriented variants can be found. Upon the C content, alloys with less than 0.4% by weight of C (Figure I.10 (a)) present blocks containing laths corresponding to two weakly misoriented variants (10.53° around the $<110>_\alpha$ direction according to KS) but a single

variant for those containing more than 0.6% (Figure I.10 (b)). The blocks are highly misoriented between them, presenting misorientation angles higher than 45° (mainly 60°). The group of adjacent laths within a block with a weak misorientation between variants is called sub-block.

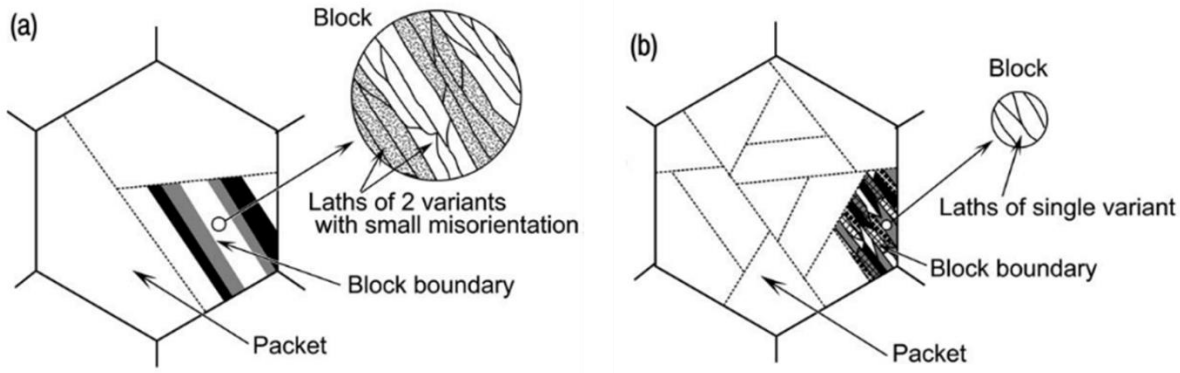

Figure I.10. Schematic illustrations showing lath martensite structure in (a) low carbon (0–0.4%C) and (b) high carbon (0.6%C) alloys [53].

Bainite has been studied presenting a similar organization than that proposed for martensite. Furuhara et al. [54] separates upper bainite formed at high temperature (type A 450°C), upper bainite formed at low temperature (type B 400-350°C) and lath martensite (type C) according to the arrangement of the substructures shown in Figure I.11.

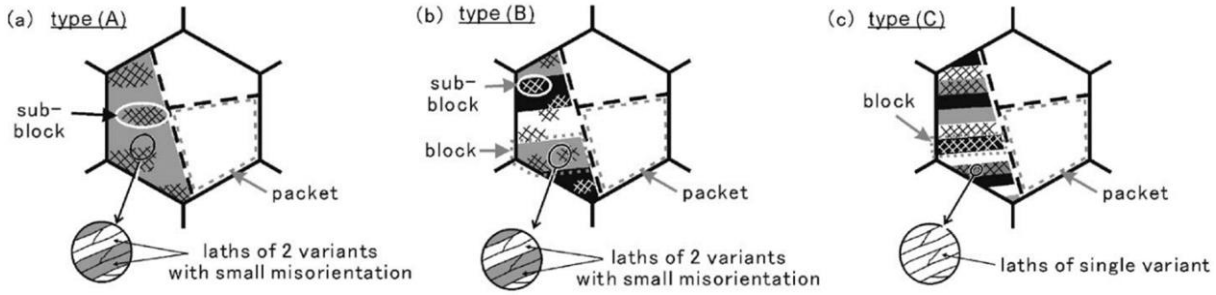

Figure I.11. Schematic illustration describing the crystallographic characteristics of upper bainite and lath martensite substructures in Fe–9Ni–C alloys [54].

In Takayama et al. [55] the concept of Bain groups was included: K–S variants are also grouped according to three distinctive variants of the Bain correspondence ([001]γ//[001]α, [100]γ//[110]α and [010]γ//[110]α). They tried to separate bainite formed at 540°C, bainite formed at 450°C and lath martensite with EBSD and arrived to a similar classification to that proposed by [54]. In Figure I.12 the region formed by variants belonging to the same Bain group is represented by the same color and a packet is characterized as a region of the same elongated direction for boundaries between different Bain groups.

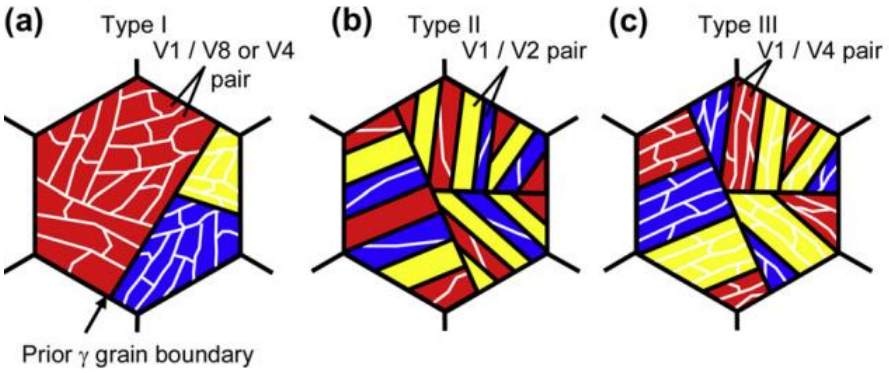

Figure I.12. Schematic illustrations of variant paring in (a) bainite formed at 540°C, (b) bainite formed at 450°C, and (c) lath martensite. White and black lines represent low- and high-angle boundaries, respectively. Only the most frequently occurring variant pairs are indicated [55].

They found a predominance of specific variant pairs depending on the microstructure. For Type 1, V1/V8 or V4 predominantly appears within the same Bain group, while V1/V2 in mainly observed between Bain groups within the packet. As the V1/V8 or V4 misorientation is 10° and the V1/V2 is 60°, this confirms that upper bainite (Type I) can be characterized by a peak at low angle misorientations and lower bainite (Type II) by a peak at high angle misorientations. This misorientation angle distribution had already been evidenced years ago in [56] and confirmed in [28] as shown in Figure I.13.

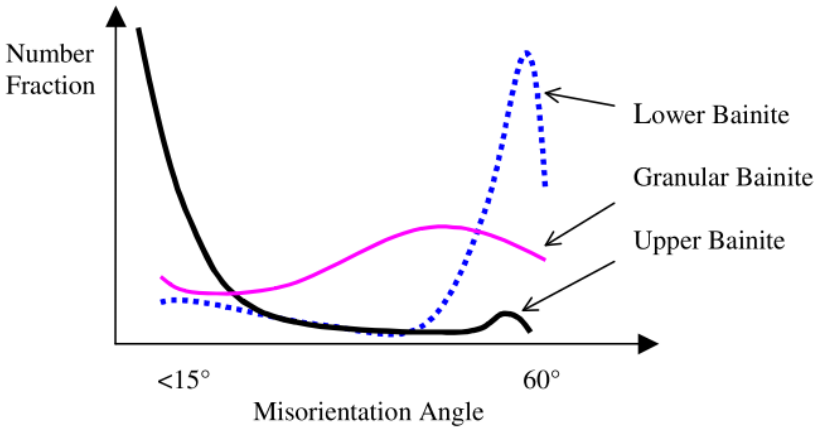

Figure I.13. Schematic histograms of misorientation angle distributions for different types of bainites.

I.4 EBSD: potential and limits to study phase transformation inheritance in steel

I.4.1 Discrimination of ferrite, bainite and martensite

It is very well known that EBSD indexing alone cannot differentiate between different phase transformation products since they all share the same BCC crystal structure. However, as explained along I.3, it has been possible to access very rich information to distinguish the phases in steels: the existence and type of ORs with the neighborhood, the spatial distribution of variants in packets/blocks, among others. In this respect, several authors have tried to implement advanced data processing approaches to automatically (or semi automatically) discriminate steels transformation products.

In Ryde [57] a round robin test has been proposed to different laboratories in order to automatically discriminate ferrite and martensite from dual phase microstructures. Three main strategies where proposed in order to find a threshold to separate both phases: 1) grain size: since martensite is obtained from a displacive transformation, many new boundaries are created what results in a smaller grain size than that of polygonal ferrite, 2) an average quality measure of the Kikuchi diffraction patterns per detected grain: the diffraction pattern quality is lower for martensite than for ferrite due to its high density of dislocations and 3) the Band Slope (BS) of the Kikuchi pattern, which is the slope of the intensity change between the background of the pattern and the band: as expected the BS is lower for martensite than ferrite.

In Zaefferer et al. [58], the separation between bainite and ferrite was based on the difference in transformation induced geometrically necessary dislocations (GNDs) in bainite. To determine the areas with larger GNDs density, the authors proposed to work with pattern quality maps, grain reference orientation deviation maps and Kernel Average Misorientation (KAM) maps. They conclude that the best parameter to find a threshold and enable a good separation is the KAM.

Kang et al. [59], [60] proposed the separation of ferrite and martensite within dual-phase steels using both grain averaged Band Contrast (BC) and BS. In [59] they also suggested to identify bainite by filtering through the Grain Average Misorientation (GAM), which has higher values for bainite than ferrite. Zhu et al. [61] implemented a multi parameter method by considering mean grain BS, Grain Internal Mean Misorientation (GIMM), grain size and shape to dissociate different ferritic phases, especially ferrite from bainite. Shrestha et al. [62] proposed the separation of bainite, acicular ferrite and polygonal ferrite based on grain boundary misorientation, aspect ratio and mean misorientation at the grain scale.

Although each of the cited studies found the most suitable parameters to discriminate the different phases in steels, the approaches are in most of the cases restricted to the particular studied sample and the threshold should be readjusted for new cases. Additionally, it must be noted that there exists a huge number of ambiguous configurations where it is very difficult to ensure with certainty which is the correct phase, even manually.

Microstructural characterization requires expertise, time and effort, and still may carry a certain degree of subjectivity depending on the person that looks at the microstructure to characterize. In the search for alternatives, AI-based techniques are worth to be explored as they may potentially enable a quicker and effortless classification by unifying a criterion to reduce subjectivity. A detailed literature review of AI applied to the microstructural characterization of steels is given in Chapter IV.

I.4.2 Discrimination of phases with close crystal symmetry

EBSD is widely applied to perform phase discrimination based on the crystallographic differences between the present phases of the microstructure. However, when two phases belong to the same crystal structure, e.g. cubic, the geometry of their diffraction patterns looks very similar and it is necessary to look at the difference between their diffracting planes (reflectors). For instance, ferrite (iron BCC) and austenite (FCC) can be distinguished by the differences in the list of reflectors.

The discrimination becomes still more complex when both phases belong not only to the same crystal structure but also to the same Bravais lattice, e.g. FCC. In this case, the most intense reflectors are equivalent between both phases and the difference appears in the lower intensity diffracting planes. If the quality of the acquired patterns is high enough to identify the lower reflectors, then EBSD indexing may be able to find differences between both phases and select the best matching phase.

Nevertheless, there exist some cases where the list of reflectors for both phases is equivalent and the only difference remains in their lattice parameter. Conventional EBSD indexing is not able to measure this difference and phase discrimination is hindered. Thus, the probability of a pattern to be indexed as of both phases is roughly equal.

Steel microstructures present an excellent challenge for EBSD phase discrimination as they show all the issues presented above. As described in I.2.2, during cooling, a large variety of minor phases such as carbides, nitrides and sulfides may precipitate in the steel microstructure. The great majority of these minor phases belong to the same FCC Bravais lattice as well as one of the main phases appearing in steel such as austenite. This is problematic since the minor phases can be indexed as austenite, resulting in a wrong phase fraction calculation during characterization. Due to the stresses induced by the displacive transformations (bainite and martensite), the obtained diffraction patterns over such structures may present a low quality that can further complicate phase discrimination.

I.4.2.1 Approaches combining EBSD with other techniques

Nowell et al. [14] proposed to couple EBSD with X-ray energy-dispersive spectroscopy (XEDS) in order to collect both crystallographic and chemical information from the microstructure. With this strategy the authors were able to discriminate 3 FCC phases such as Ni, Cu and austenite that share exactly the same list of reflectors and present very close lattice parameters (3.52, 3.61 and 3.66 Å respectively).

On this base, several studies have been performed to carry out a complete characterization of steel microstructures. Laigo et al. [63] evaluated the combination of EBSD and EDS to characterize the microstructure of centrifugally cast heat resistant steel by discriminating MC, M_7C_3 and $M_{23}C_6$ carbides from an austenitic matrix. Crystallographic differences between M_7C_3 and $M_{23}C_6$ enabled their discrimination by EBSD but the similarities between MC and austenite should be resolved by EDS.

Fazarinc et al. [64] studied the transformation kinetic of a duplex stainless-steel containing ferrite, austenite, sigma phase, $M_{23}C_6$ and MC carbides. They were able to distinguish ferrite, sigma and $M_{23}C_6$ by EBSD but other techniques such as XEDS and X-ray diffraction (XRD), were needed to separate austenite from MC. Goran [65] applied EBSD coupled with EDS to achieve the full characterization of a tool steel microstructure with a ferritic matrix and MC and M_6C carbides as minor phases. He firstly indexed the map by adding only ferrite and austenite as candidate phases and detected that several particles with a low pattern quality where indexed as austenite. The EDS analysis showed the presence of W and V what resulted in two different carbides VC and W_3Fe_3C, that once they have been added as candidates could be discriminated by EBSD. This study highlights the importance of considering the minor phases to avoid wrong phase fraction calculations.

Other materials such as Ni-based super alloys have also been studied by EBSD and EDS in order to distinguish the γ matrix (Ni) from TiN and NbC, that present the same list of reflectors and close lattice parameter [66]. In addition, they tried to separate γ matrix from γ' (Ni_3(Ti,Al)) precipitates with no success since γ' size is in the order of the EDS resolution. This last study highlights the major problematic of coupling EBSD with other techniques: spatial resolution disagreement.

Other authors have tried different strategies to obtain significant information from a single EBSD acquisition instead of using several different characterization techniques. Payton et al. [67] implemented forward scattering detectors (FSD) mounted in the EBSD camera to obtain the backscatter electron signal (BSE). The intensity of this signal is sensitive to the variations in the atomic number (Z) of the elements and can be used to confirm if the indexed phase composition correlates well with the BSE map. Later, due to the small size of the mounted detectors (diodes) and their position outside the main intensity maximum, Wright et al. [68] reported the use of an EBSD detector as an imaging device similar to a backscatter (or forward-scatter) detector. Based on these advances, Afshar [69] proposed a new Pattern Overall Intensity Based (POIB) method for phase discrimination. Since the pattern overall intensity varies with Z, the discrimination of the phases with a similar atomic number remains an issue.

I.4.2.2 EBSD as a single tool for phase discrimination

Phase discrimination has been greatly enhanced by the advances and progresses made over the last few years in EBSD. The possibility to acquire high quality patterns in short times enables the possibility to identify and measure a larger number of Kikuchi bands more accurately. In addition, innovative indexing methods have appeared by pushing the limits of band detection and are able to measure band widths to improve phase discrimination.

Thomsen et al. [5] and Oxford Instruments developed an innovative indexing approach called Refined Accuracy (RA) based on classic Hough Transform (HT) indexing but performing a refinement step to better measure the hyperbolic shape of the bands and extract important information at the level of the band width (the method is detailed in II.2.3.2). This approach has been recently used by Sharma et al.

[70] in order to separate two phases (Ni_3Nb and Ni_3Ti) of Ni-based superalloys. Although both phases belong to different crystal structures (orthorhombic and hexagonal respectively) the arrangement of the atoms along the crystal is exactly equivalent and only slight differences in the lattice parameters are found. Using RA, they were able to correctly index the main part of the pixels contained in the minor phases, however some misidexed pixels have been evidenced.

As an alternative to HT-based indexing, the Pattern Matching (PM) approach has been proposed by different authors [6], [71], [72] in order to improve the quality of the orientation determination and therefore phase discrimination. Briefly, it compares pixel by pixel the acquired pattern with a dictionary of simulated patterns for the candidate phase and selects the best matching simulated pattern by using an image similarity metric, i.e. the simulated pattern that matches the experimental pattern with the highest similarity defines the orientation and the phase indexing (the method is better described in II.2.3.3).

In the work of Sharma presented above [70], they also applied PM to discriminate both Ni-superalloy minor phases and got better results than those obtained by RA. Ram et al. [73] used PM to distinguish three similar FCC phases such as Ag, Cu and Ni with 0.4086, 0.3615 and 0.35236 nm lattice parameters respectively. Initially they were able to discriminate all three phases based on their simulated patterns. In second instance they validated the results on an experimental EBSD map from a monophasic Cu sample where all three phases were added as candidate phases. PM has also been used to separate ferrite from martensite due to the difference in lattice parameter introduced by the martensitic transformation that results in a tetragonal structure [74], [75].

A recent approach based on AI has been recently presented for the discrimination of patterns belonging to different symmetry groups and phases [76], [77]. Although it appears to be a promising approach with high potential, its development is still recent and it has not been considered along this thesis.

I.4.3 Indirect reconstruction of parent austenite

In order to reconstruct the parent austenite phase, the easiest way is to compare the orientation of a crystal belonging to the inherited phase with a neighbor crystal of the parent austenite phase [44], [78]. However, after phase transformation of low-carbon steels there exists a very low amount of residual austenite, therefore an indirect reconstruction method is needed.

The main part of the indirect methods is based on the study of Humbert et al. [79]. As mentioned in I.3.2, if the orientation of a parent grain g_p and the OR are known, the orientation of the ith variant $g_{v_i}^{\alpha}$ is described by:

$$g_{v_i}^{\alpha} = g_p . P_i . \Delta g$$

Where P_i is the ith symmetry element of the parent phase. Equally, the orientation of a potential parent g_{p_i} of the variant g_v^α is expressed by:

$$g_{p_i} = g_v^\alpha . {C_i}^{-1} . \Delta g^{-1}$$

If several variants inherited from the same PAG are known, then it is possible to deduce the orientation of the PAG. As the variants are considered without knowing the parent boundary, it often happens that the selected set overlaps more than one parent grain. Thus, the purpose is to find the unique parent orientation shared by most selected variants and exclude the few variants not consistent with this parent.

Some authors proposed to manually select the variants [80]–[82] but for a large number of grains, it becomes impractical and automatic methods are needed. To automate reconstruction, it is accepted that variants inherited from the same PAG are adjacent and thus it is necessary to define a neighborhood. Some methods [83], [84] have defined the neighborhoods at the pixel scale while others opted to look at the crystallographic domains. The first case needs a sufficient number of variants to be contained in the defined kernel of pixels to determine the parent grain orientation. It may work well in fine structures. On the other hand, approaches considering the crystallographic domains need a first grain detection but overall, they are less computer intensive. We will focus on these last approaches.

First automatic method has been published by Gey et al. [85] and later improved by Germain et al. [86] to reconstruct the high temperature β-phase in the allotropic transformation of titanium. However, the austenite transformation of steels presents some particular issues that makes it more complicated than the β-titanium reconstruction: 1) the OR is only approximately known as there exists many possible ORs to adopt and the reality has shown that in many cases the experimental OR falls in between theoretical ORs, 2) the inherited orientations of the crystallographic domains are highly spread and the characteristic misorientations are not always observed and 3) there exist a high fraction of special grain boundaries such as twins that complicates the correct identification of the PAG.

I.4.3.1 Available approaches to reconstruct parent austenite in steels

Cayron et al. [87] were the first to perform the indirect reconstruction of austenite in steels. They proposed to use the groupoid theory to cluster neighboring variants and to establish the contour of the PAGs. Germain et al. [7] addressed the reconstruction of the austenitic parent phase based on the criteria proposed in [86] to determine the crystallographic domains belonging to the same PAG. As the OR is only roughly known for steels, the authors demonstrated that an average OR improves the reconstruction result.

Both [7], [87] approaches are local neighbor level voting algorithms, i.e. they identify local groups of child grains that have a common parent orientation variant and propagate to the surrounding parent phase. The determination of the parent orientation variant is performed by a voting mechanism of the

participating child grains. In [88] they proposed a voting mechanism performed on the grains belonging to a predefined square grid.

More recently, Gomes de Araujo et al. [89], proposed a different approach called the grain graph algorithm, which is a mathematical description of the adjacency relationships of the grains. It calculates a scalar probability to know if two adjacent grains may belong to the same PAG. Then, these probabilities are extended to higher order neighboring grains by a random walk clustering technique.

Hielscher et al. [9] summarized the advantages and weaknesses of both types of approaches: local neighbor level voting and grain graph. They state that although the first one is relatively robust it may happen that some microstructures do not have enough local groups of child grains that have a common parent orientation variant to cover all parent orientations. On the other hand, the grain graph method is computationally efficient and considers all grains within the microstructure, but it uses scalar probabilities to describe the likelihood of having a common parent orientation. These probabilities are extended to higher order neighboring grains without checking whether or not they apply to the same parent orientation variant. Thus, the authors propose a method called hybrid variant graph to combine the advantages of both aforementioned methods.

Huge advances have been obtained in the field of indirect parent phase reconstruction that help on shedding more light to the nature of phase transformations. However, researchers have always looked for experimental approaches to study dynamic processes in real time and this is why indirect reconstruction can be coupled with in-situ heating experiments to validate the reconstruction results and be able to observe the intermediate stages of the microstructure between room and high temperature.

I.4.4 In-situ high temperature EBSD

Phase transformations have been studied with in-situ heating SEM-EBSD along the years. A breakthrough study was performed by Seward et al. [90] in which the transformation from α to β phase in commercially pure titanium during heating was analyzed. They were able to heat up a Ti sample up to 900°C and detect intergranular and grain boundary β (allotriomorph) nucleation and confirmed that both β types nucleate with a Burgers-OR with the α-phase. At that time, the acquisition speed of the EBSD camera was in the order of 10 points per second, far from the thousands of points per second that are possible to obtain today with the last generation CMOS-based detectors in normal acquisition conditions.

On the other hand, numerous authors put the focus on the study of phase transformation in steels. A great number of these studies have been focused on studying the nucleation and growth of austenite and ferrite during heating and cooling respectively. For instance, it has been found that both the forward and backward nucleation of γ and α respectively occur mainly at triple junctions by holding the KS-OR in the majority of the nucleating grains [91]–[95]. Initial growth occurs by wetting the grain boundaries

[94] followed by interface migration (growth into the PAG), an interface deviated from KS between the nucleating grain and the PAG is needed, i.e. random grain boundaries have a higher mobility than those with a specific OR [91], [93], [95], [96]. Some authors also found that the transformation during cooling has faster kinetics than during heating [91], [94], although in [96] not a clear difference was evidenced.

In the studies detailed above, the transformations were close to equilibrium as the heating and cooling speeds are relatively low. Up to date, the only study in the literature that proposed the phase transformation of austenite to martensite has been recently presented by Taniyama et al. [11]. They were able to observe such transformation in-situ thanks to the special design of the heating stage they used, that allows a fast-enough cooling rate to induce the martensitic transformation. They discovered that the martensite variants were related with the PAG with a near KS-OR. They also compared for the first time a real austenitic microstructure at high temperature with an indirect reconstruction and, although there was a relatively good agreement, they evidenced problems to reconstruct small grains and twin boundaries.

Although very interesting results have been published, few authors have mentioned the difficulties or drawbacks that may carry such a complex technique. For instance, Tomota et al. [97] found that the austenite formation of a 1.5Mn-1.5Si-0.2C steel was starting at much higher temperatures than those expected. Such discrepancy was attributed to the change in chemical compositions near the surface of a specimen heated to elevated temperatures in vacuum, resulting in Mn and C concentrations drop with heating. Pham et al. [95] warned about the special care that must be taken on the interpretation of the in-situ observation, as the heating rate should be kept low in order to maintain a low transformation rate sufficient for EBSD data acquisition. Despite the great advances in acquisition speeds, the highest acquisition rate reported for in-situ EBSD heating experiments has been 870 patterns per second [10]. As one can imagine, high acquisition speeds are necessary when thinking about capturing dynamic events occurring very quickly.

I.5 Conclusion

Along this chapter, the most important points about the microstructural and crystallographic aspects of steel microstructures obtained by phase transformation have been reviewed.

From the studies that have been focused on the discrimination of phases with similar crystal structures we can conclude that to the best of our knowledge, there are no studies that assess the ability and reliability of EBSD as a single tool to perform this task for the microstructure of steels.

The review about in-situ heating EBSD showed that the focus was mainly on observing the nucleation and growing behavior of both ferrite and austenite during cooling and heating respectively. Although these results are very interesting and we dedicate a part of our studies to such issues, our focus is on the analysis of the parent austenite microstructure refinement after heating and cooling cycles. This topic

has never been addressed in the literature by in-situ heating EBSD and it is also an important opportunity to compare the in-situ observed microstructures with the indirect reconstructions.

Chapter II: **EBSD for the discrimination of phases with cubic crystal structures in steels**

II.1 Introduction

EBSD struggles to discriminate phases sharing the same space group or the same symmetry. Several strategies have been developed along the years to overcome such issue, also coupling EBSD with other characterization techniques. Thanks to the advances in quality acquisition together with new and powerful indexing methods some of the issues initially presented by EBSD to discriminate similar phases have started to been solved without the need of complementary techniques. However, there still remain issues to address.

In this chapter, we want to assess the contribution of such advances in EBSD as a single tool for the phase discrimination of steel microstructures. The goal is to evaluate how we can reach a higher and better percentage of phase indexing and at the same time a better identification and discrimination of phases with similar symmetry. We aim to perform more reliable phase discrimination, with a critical eye on the final result.

Initially, a brief introduction about EBSD and the most important related concepts is addressed followed by the presentation of challenging multiphase steel microstructures that are used as testing examples. Phase discrimination has been performed by three indexing methods: Hough Transform (HT), Refined Accuracy (RA) and Pattern Matching (PM) and their performance is assessed. The effect of the pattern quality over the final results has been also considered. In the cases where the phase discrimination result is not satisfactory, several possible solutions are provided in order to improve it.

II.2 Electron Backscattering Diffraction (EBSD)

II.2.1 Measuring an individual orientation with EBSD

The principle of the EBSD technique is schematically presented in Figure II.1. EBSD is performed in a Scanning Electron Microscope (SEM) [98]. The incident electron beam is focalized at a point of interest on a perfectly polished sample tilted in order to form an angle of 70° between the sample's normal and the incident electron beam. The backscattered electrons that fulfill the Bragg's law with the lattice planes of the sample are diffracted, giving rise to two diffraction cones (called Kossel cones). The intensity of the diffracting lattice planes varies depending on the incident Bragg angle; the higher the angle, the lower the intensity. Both Kossel cones intersect a phosphor screen as hyperbolas forming a band called Kikuchi band [99]. Each diffracted pair of cones generates a band on the detector and the width of the band is related to the lattice constant (d_{hkl}) of the analyzed crystal structure. The ensemble of these bands gives rise to the so-called Kikuchi diffraction pattern or Electron Backscattering Pattern (EBSP) [100]. The resulting EBSP is imaged by a camera in real time. CCD cameras have been used for several years before faster CMOS cameras were introduced [4]. Once the image of the EBSP is acquired it is possible to automatically measure the orientation with a dedicated software through a process called indexing [101]. This requires providing the system with the crystal structure of the phases present in the material. The different types of indexing methods are detailed in II.2.3.

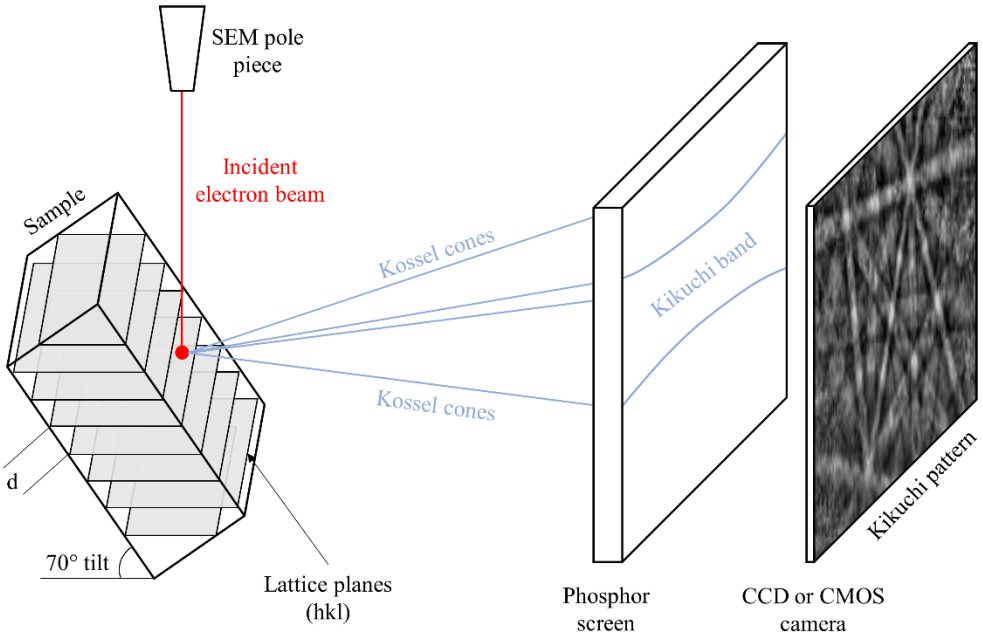

Figure II.1. Scheme of the EBSD working principle and experimental setup.

II.2.2 Representing EBSD data

In an EBSD map, the crystallographic orientation is measured at each point of a sampling grid. The step size, i.e., the separation between each point of the grid, defines the spatial resolution of the EBSD map. The smallest achievable spatial resolution depends on the size of the incident beam and the interaction volume and can reach down to 20-50nm in a Field Emission Gun-SEM (FEG-SEM). The relative angular resolution (the smallest measurable misorientation) is usually of 0.5° but can be reduced down to 0.01° when large EBSPs are acquired and dedicated post processing techniques are used [15].

The collected data forms an EBSD map in which each pixel contains the orientation, the corresponding phase and several indicators related to the quality of the EBSP such as Band Contrast (BC), Band Slope (BS) and other indicators that depend on the method used to index the pattern (see II.2.3). The BC corresponds to the brightness of the bands and the BS evaluates the gradient of intensity at the edge of the bands [102].

There are many different ways to represent EBSD data among which the most used are described below and presented in Figure II.2:

(a) Pattern quality maps. The quality indicators of an EBSP are scalars that can be plotted on a gray scale and reveal the microstructure (grain boundaries or phases). Additionally, they are sensitive to deformation (high dislocation density) and scratches what provides darker pixels in the map.

(b) Phase maps. In multiphase microstructures, several phases can be added to the candidates list to perform indexing. The phase is then determined simultaneously with the orientation based on the best matching phase from the list. In a phase map, each pixel is colored according to its phase.

(c) Inverse Pole Figure (IPF) maps. This is the most common representation of an orientation. Each pixel of the map is assigned with a color based on its orientation and on a chosen macroscopic direction. The color is determined by the crystallographic axis pointing in the chosen direction according to the key given in the standard triangle.

(d) Misorientation maps. The main idea of misorientation maps is to calculate the misorientation angle between two neighboring pixels. This scalar value is then plotted at the interface between pixels according to a predefined color scale by highlighting grain boundaries.

(e) Grain maps. The set of pixels belonging to the same grain is obtained by grouping the neighboring pixels whose misorientation angle does not exceed the selected threshold. In grain maps, each grain is plot in a randomly selected color.

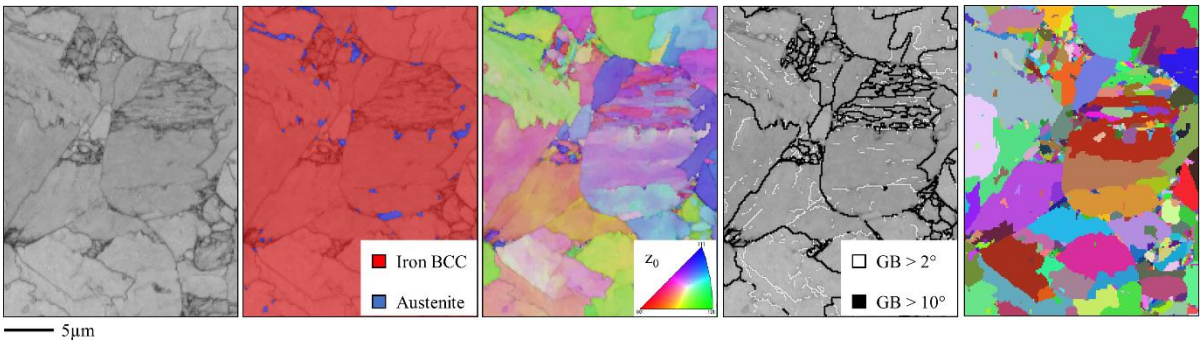

Figure II.2. (a) Pattern quality map, (b) phase discrimination map showing an iron BCC matrix in red with retained austenite in blue overlapped on the pattern quality map, (c) orientation map plotted with the IPF color code relative to the z direction, (d) misorientation map showing grain boundaries between 2° and 10° in white and greater than 10° in black, (e) grain map presenting each detected grain at 3° with a random color.

It may happen that if the quality of the EBSP is not sufficient to clearly identify the Kikuchi bands, the corresponding pixel is not indexed and thus it does not contain any phase or orientation. These pixels are called non-indexed pixels and can be corrected by assigning the orientation of their nearest neighboring pixels.

On the other hand, it can happen that although the EBSP is of good quality, the orientation is not assigned correctly due to pseudosymmetry problems (orientation misindexing) or the phase is confused due to two candidate phases with similar crystal structures (phase misindexing).

II.2.3 Indexing methods

Indexing consists in assigning the orientation to a measured point based to the acquired EBSP. There exist different methods to perform this task. The different indexing methods used in this work are described below.

II.2.3.1 Hough Transform based indexing

This is the most conventional and widely used indexing method. It has been presented for the first time in [103]. First, the Kikuchi bands are detected using the Hough transform which converts the bands into points or peaks on the Hough space using the following equation:

$$\rho = x * \cos(\theta) + y * \sin(\theta)$$

where *x* and *y* are the coordinates of a pixel in the EBSP, ρ is the perpendicular distance to the origin of the image (usually the pixel at the center of the EBSP) and θ is the angle between ρ and the x-axis. A point in the image space is represented by a cosine in the Hough space. All the points aligned on a same line in the image space result on several cosines that intersect altogether in a single point (ρ, θ) of the Hough space (Figure II.3). It must be remarked that Kikuchi bands having a certain thickness, they transform, in the Hough space, into elliptical peaks with their long axis aligned in the ρ direction.

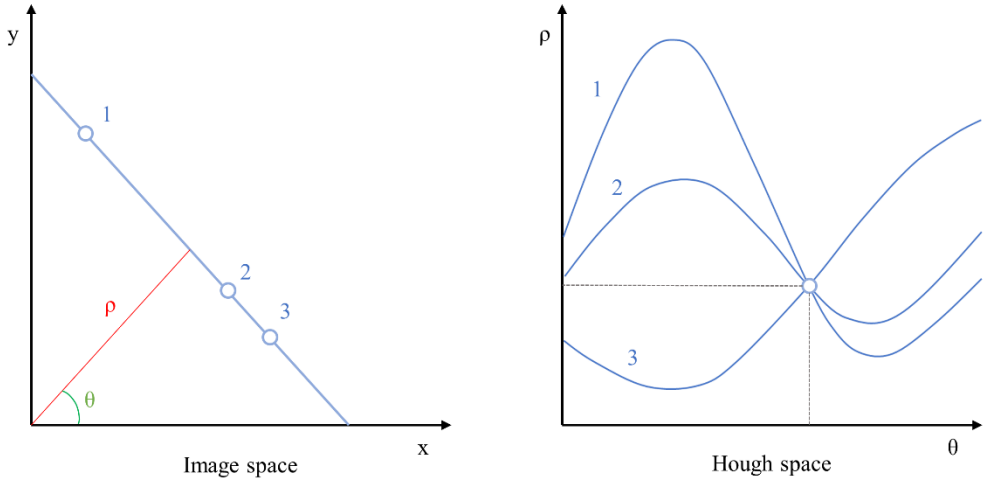

Figure II.3. A line in the image space is converted into a point in the Hough space through the Hough transform.

The position of the peaks in the Hough space can be easily detected and the positions of the Kikuchi bands deduced. From the bands' positions, the angular relationships between these bands can be compared with those theoretically calculated in advance for the analyzed crystal structure for selected reflecting planes (reflectors). The solution that best fits the experimental EBSP is kept, and the orientation is assigned.

When it comes to phase discrimination, the best solutions for all candidate phases are compared based on different parameters such as number of matching bands, the misfit between the experimental bands and the solution (for example with the Mean Angular Deviation (MAD)), etc. These parameters depend on the EBSD manufacturer that developed the indexing algorithm. The phase in the list that matches the higher number of bands or best fits the experimental pattern is kept (phase indexing) and its orientation is assigned.

II.2.3.2 Refined Accuracy

This approach has been developed by Oxford Instruments and presented in Thomsen et al. [5]. It is based on the same principle as classic HT-based indexing but the difference remains in its ability to recognize the varying width and hyperbolic edges of the Kikuchi bands while classic HT-based assumes them as parallel straight lines. RA performs two steps: a first guess of the orientations by classical HT-based and a band refinement step where the real hyperbolic shape of the bands is simulated constrained by the ρ and θ calculated beforehand.

It is expected that thanks to this refinement step, the band widths are accurately measured what can help in the discrimination of two phases presenting a similar list of reflectors but different lattice parameter (translated into band width within an EBSD pattern). However, in order to exploit the full potential of this approach it is necessary to acquire high resolution and high-quality patterns.

II.2.3.3 Pattern matching

As an alternative to classic HT-based indexing, PM has been proposed by different authors [6], [71], [72] in order to improve the quality of the orientation determination since it considers the entire information inside the pattern and not only the Kikuchi bands and their angular relationships. In this study in particular, the Dictionary Indexing (DI) approach presented in [6] has been used and it is described below.

By using the physics-based forward model proposed in [104], a set (dictionary) of simulated patterns sampling all the orientation space with an angular step of ~1.4° is generated for the considered crystal structure. This dictionary must be adapted to the microscope parameters and acquisition conditions of the EBSD map to index. Each experimental pattern is matched against every pattern in the generated dictionary by using an image correlation metric such as Normalized Dot Product (NDP) which is defined as follows:

$$NDP(f,t) = \frac{f}{\|f\|}.\frac{t}{\|t\|}$$

Where f is the experimental EBSP and t are simulated patterns belonging to the dictionary. An NDP value of 1 means perfect matching. The indexing of an EBSP is then obtained by the simulated pattern with the highest image correlation (NDP).

For phase discrimination, a dictionary of simulated patterns must be generated for all candidate phases. The best solutions for all the candidate phases are compared based on the highest NDP and the best match provides the phase indexing and its corresponding orientation.

With such approach, both orientation and phase indexing are normally more accurately measured than using classic HT-based indexing or even RA since all the pixel information contained in the pattern is used to calculate the image correlation metric. However, it is necessary to save the experimental patterns

for re-indexing since this approach is not implemented as an automatic online indexing method during acquisition. DI has been performed in the open source software *EMsoft* [105].

II.3 Materials and experimental

II.3.1 Materials

Two different steels (Table II.1) presenting challenging configurations have been selected for EBSD analysis and in particular for phase discrimination. They both show minor phases belonging to the same space group that may be potentially misindexed with the main steel phases as their reflectors list are very similar.

S1 has been provided by Ascometal and presents a bainitic matrix with a typical lath-like structure with the presence of Martensite/Austenite (M/A) islands what results in a significant degradation of the diffraction signal due to the high dislocation content. Two minor phases such as MnS and $(TiNb)C_2$ are also present, both with an FCC structure. S2 is a sample that's has been used during the PhD thesis of Arnold Tellier at the Université Bourgogne Franche-Comté [106] and presents a large fraction of hard $Cr_{23}C_6$ carbides embedded in a soft austenite FCC matrix. Moreover, S2 sample preparation was complicated what affects the surface quality and reduces the pattern quality. These two samples are therefore a very good example of those cases where the quality of the signals of the main phase impact their discrimination with minor phases.

The crystallographic information of the concerned phases is shown in Table II.2. The relative diffraction intensities are given by the AZtec software and could be calculated from the structure factor of each phase and ranked in descending order. Both ferrite and bainite were considered as iron BCC phase for indexing.

Table II.1. Materials used in this study with their respective phases and compositions.

Sample	Main phase	Minor phases	Composition (% by weight)
S1	Bainite	Austenite, MnS and $TiNbC_2$	0.345C-0.2Si-1.24Mn-0.21Ni-0.707Cr-0.029Ti-0.021Al-0.038Nb
S2	Austenite	Ferrite and $Cr_{23}C_6$	1.23C-24.8Cr-4.6Mn-3.5Ni-2.1Mo-3Si-0.027O

Table II.2. Crystallographic information for all the phases in this chapter (default reflectors in AZtec are in bold). {hkl} stands for the families of planes, I their relative intensities and N° is the accumulative number of planes forming the family.

Phase	Austenite			Iron BCC			MnS			$(TiNb)C_2$			$Cr_{23}C_6$		
Lattice parameter	3.66Å			2.86Å			5.22Å			4.39Å			10.65Å		
Space group	225 Fm-3m			229 Im-3m			225 Fm-3m			225 Fm-3m			225 Fm-3m		
Families of diffracting planes	N°	{hkl}	I	N°	{hkl}	I	N°	{hkl}	I	N°	{hkl}	I	N°	{hkl}	I
	4	**{111}**	**100**	**6**	**{110}**	**100**	**3**	**{200}**	**100**	**3**	**{200}**	**100**	**4**	**{333}**	**100**
	7	**{200}**	**76**	**9**	**{200}**	**51**	**9**	**{220}**	**51**	**7**	**{111}**	**67**	**10**	**{660}**	**38**
	13	**{220}**	**37**	**21**	**{211}**	**32**	**13**	**{222}**	**32**	**13**	**{220}**	**48**	**16**	**{440}**	**32**
	25	**{311}**	**26**	**27**	**{220}**	**23**	**16**	**{400}**	**22**	**16**	**{222}**	**29**	**19**	**{600}**	**27**
	29	**{222}**	**23**	**39**	**{310}**	**17**	**28**	**{420}**	**17**	**19**	**{400}**	**20**	**22**	**{800}**	**26**
	32	**{400}**	**16**	**43**	**{222}**	**13**	**40**	**{422}**	**13**	**32**	**{311}**	**18**	**34**	**{511}**	**21**
	44	{331}	13	67	{321}	10	46	{440}	8	44	{420}	14	46	{844}	20

II.3.2 EBSD acquisition

S1 sample was mechanically polished with SiC grit papers followed by successive steps of 9 and 3µm diamond suspension while the final step was performed with colloidal silica suspension OP-S. S2 had an additional ionic polishing step since the large fraction of hard $Cr_{23}C_6$ carbides hindered mechanical polishing to obtain a satisfactory surface to perform EBSD.

EBSD data was acquired on a ZEISS Auriga 40 FIB–SEM microscope, AZtec acquisition software and the Oxford-instruments' CMOS Symmetry camera with a maximum resolution of 1244×1024 pixels. The step size was set for all maps at 0.1µm and the acquisition conditions for each map are detailed in Table II.3.

Table II.3. Acquired EBSD maps with their respective acquisition conditions and present phases.

Sample	Map	Pattern size (pixels)	Accelerating voltage [kV]	Indexed phases
S1	M1	156x128	20	Iron BCC, austenite and MnS
S1	M1-HR	622x512	20	Iron BCC, austenite and MnS
S1	M1-2	1244x1024	10	Iron BCC, austenite and $(TiNb)C_2$
S2	M2	1244x1024	10	Iron BCC, austenite and $Cr_{23}C_6$

Online indexing has been performed with the option called "Optimized TKD" available in AZtec, with a maximum of detected bands set to twelve and the minimum being automatically fixed to six. Thus, if

the indexing algorithm is not able to match 6 bands or more with the candidate solutions, the EBSP is not indexed and appears as a non-indexed point in the EBSD map. All the background corrected EBSPs have been saved for reindexing with the other indexing methods described in II.2.3.

Figure II.4 shows the pattern quality image (BS) and a reference phase image of the maps listed in Table II.3. The reference phase images have been obtained after several steps of data cleaning and post processing and are considered as the ground truth indexing (explained in II.3.3). The phase fractions obtained from the reference phase image of each map are given. M1 and M1-HR were acquired at exactly the same region of interest but with different camera binning to analyze how the pattern resolution affects the quality of the result. Only the M1 map is presented in Figure II.4 but a reference phase map has been also obtained for M1-HR. Some regions in M2 have a pattern quality that is not enough to correctly assign a phase even after post processing. The corresponding pixels are labeled as "Unknown" and drawn in black in Figure II.4 (c).

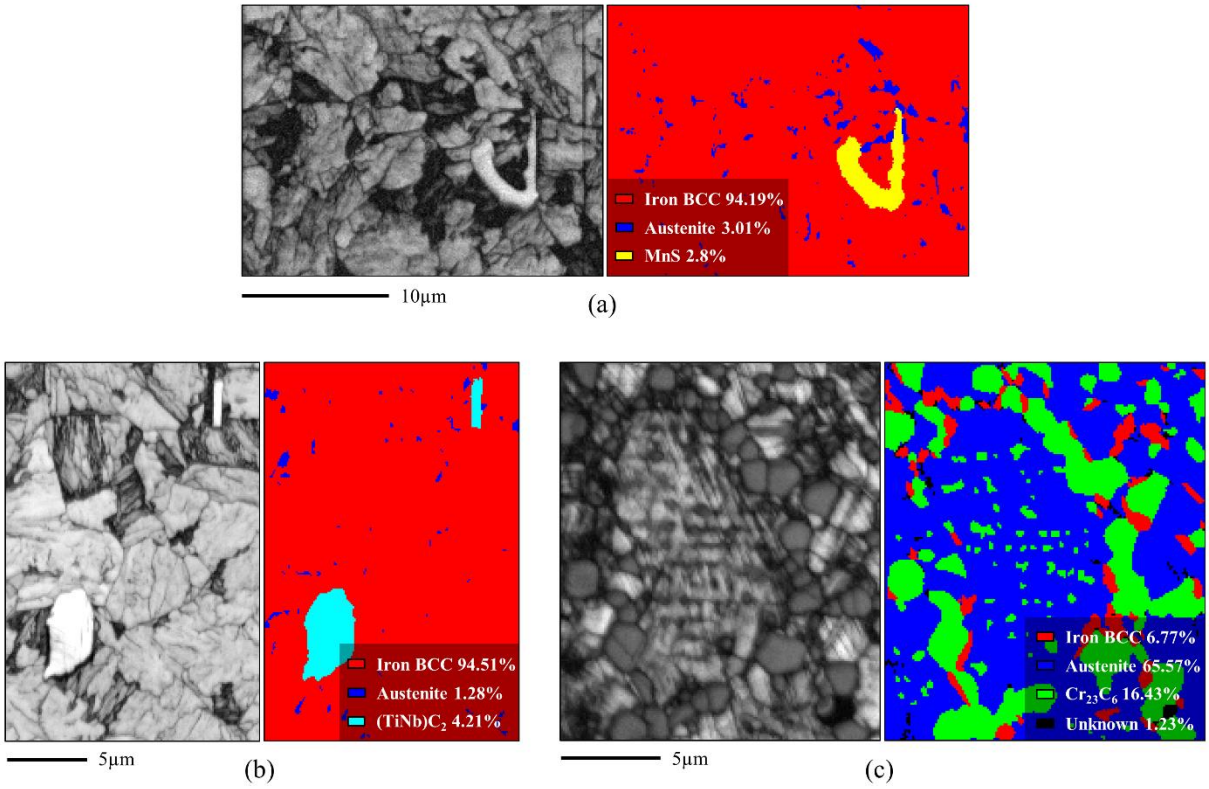

Figure II.4. Pattern quality (BS) and phase image reference for (a) M1, (b) M1-2 and (c) M2 maps with their respective phase fractions.

II.3.3 Reference phase maps

Reference phase maps were obtained combining the results obtained with the different indexing methods and then corrections have been manually performed by checking that:

- Adjacent pixels with a close orientation should not be indexed in different phases. The only exception is for the small $Cr_{23}C_6$ in S2 which are coherent with the austenite matrix.
- Austenite should be in a near KS-OR with adjacent iron BCC.

- Single pixels with a different orientation from their eight first neighbors were considered as errors except when they were in martensite and KS-related with their neighbors.
- The quality of the final map was checked at neighbor to neighbor misorientation distribution looking for spikes for common pseudo symmetries (i.e at 30°, 45°, 60° intraphase plus 0° interphase).

Additionally, for the M1-2 map an EDS analysis has been carried out to confirm the presence of both Ti and Nb and assure that the second phase precipitate is $(TiNb)C_2$ (Figure II.5 (a)). In the case of M2, a BSE micrograph was acquired at 0° tilt after the EBSD measurements (Figure II.5 (b)). In there, the $Cr_{23}C_6$ appears brighter than the austenite matrix because of a higher average atomic number. The BSE micrograph also better displays the small carbides with a nanometric size dispersed in the austenitic matrix. These carbides are coherent with the neighboring austenite and it was difficult to distinguish them through misorientation analysis. Furthermore, it is possible that the step size used to acquire this map (0.1µm) was a bit too large to accurately define the smallest $Cr_{23}C_6$ particles.

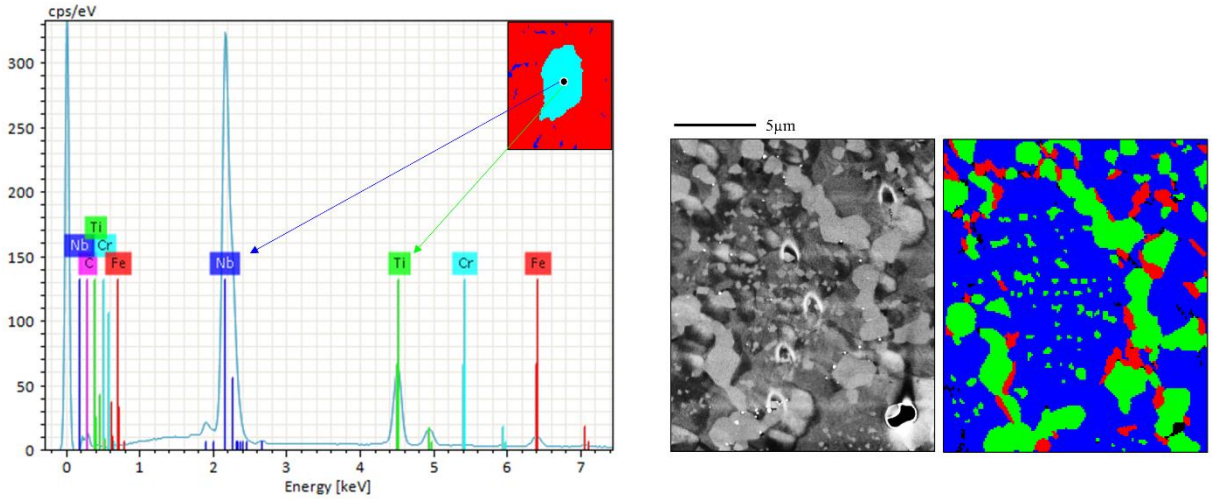

(a) (b)

Figure II.5. (a) EDS analysis over the (TiNb)C2 precipitate in map M1-2 to confirm the presence of Ti and Nb as main elements and (b) BSE micrograph of map M2.

II.3.4 Quality evaluation metrics

The phase fraction accuracy after indexing has been calculated for each phase through the well-known F1 score defined as:

$$F1(P) = 2 \times \frac{precision(P) \times recall(P)}{precision(P) + recall(P)}$$

Where *precision* is the fraction of correctly indexed pixels of phase *P* among all *P* pixels in the reference map and *recall* is the fraction of correctly indexed pixels of phase *P* among all the pixels indexed as *P*.

In addition, the confusion matrix has been presented in certain cases to have a detailed insight in the nature of misindexing. A confusion matrix applied to a binary phase discrimination problem where the possible phases are A and B is defined by:

- True A: pixels of phase A in the reference map and indexed as A.
- True B: pixels of phase B in the reference map and indexed as B.
- False A: pixels of phase B in the reference map and indexed as A.
- False B: pixels of phase A in the reference map and indexed as B.

Both F1 scores and confusion matrices have been calculated only over the indexed pixels neglecting the non-indexed ones.

II.4 Phase discrimination results

II.4.1 Evidence of phase misindexing with classic HT-based indexing

Phase misindexing with classic HT-based indexing has been evidenced for the multiphase steel microstructures presented in Table II.3. Figure II.6 (a) and (b) show the pattern quality and phase reference map of M1 respectively, together with the resulting phase discrimination map (Figure II.6 (c)) using the default list of reflectors proposed by AZtec (highlighted in bold in Table II.2). A large amount of iron BCC pixels has been misindexed as MnS phase. Both the phase fractions and the F1 score per phase are greatly affected by this misindexing.

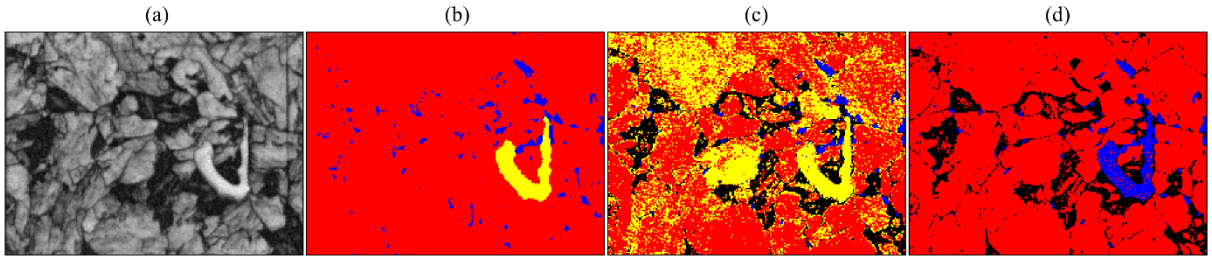

	Phase fractions	Phase fractions	F1 score	Phase fractions	F1 score
Iron BCC	94.19	54.08	0.79	84.37	0.99
Austenite	3.01	1.7	0.89	4.23	0.57
MnS	2.8	30.97	0.15	0	0
Non-indexed	-	13.24		14.4	

Figure II.6. (a) Pattern quality and (b) phase reference image of the M1 map. Phase discrimination result obtained with default parameters considering (c) iron BCC, austenite and MnS and (d) removing MnS from the candidates list.

Figure II.7 presents the (a) pattern quality and (b) reference phase map of M2 together with the resulting phase discrimination map using as default list of reflectors (c). In this case, the misindexing is observed between iron BCC and $Cr_{23}C_6$ phases. Once again, the phase fractions do not match those of the reference phase map and the F1 scores are low. Only the austenitic matrix is mainly well indexed and keeps a high accuracy.

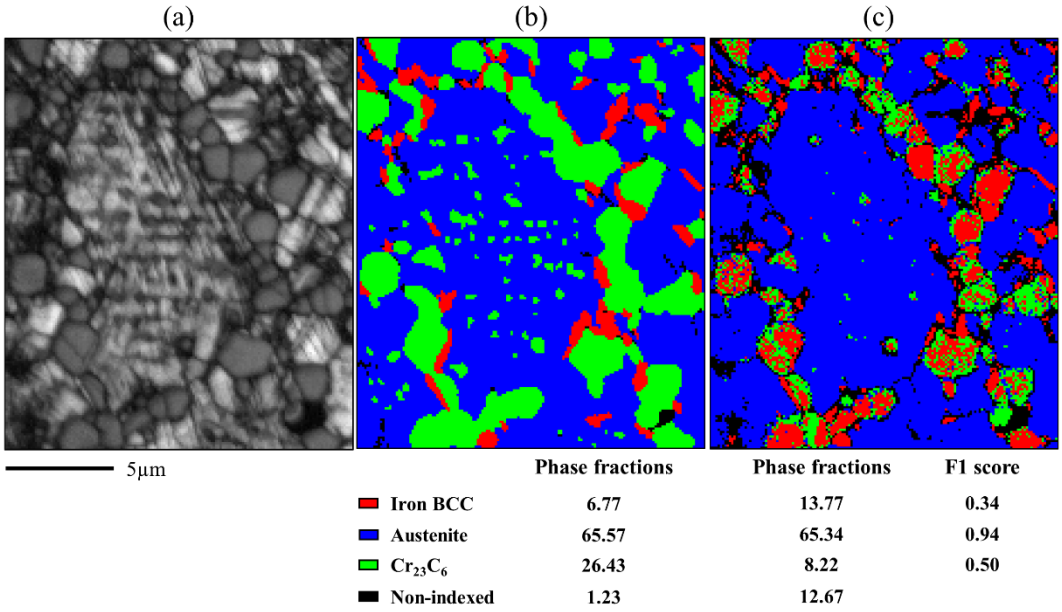

Figure II.7. (a) Pattern quality, (b) phase reference image and (c) phase discrimination result obtained with default parameters for the M2 map.

Both presented cases show that classic HT-based indexing had issues to discriminate phases beyond the fact that these phases belong to different space groups, have different diffracting plane families in their reflectors list and present large differences in their lattice parameter. This situation leads to avoid including minor phases in the list of candidate phases, but it does not solve the problem as shown in Figure II.6 (d), where only iron BCC and austenite are considered but the obtained austenite phase fraction is overestimated. In this case, the iron BCC/MnS confusion is avoided but at the expense of MnS being index as austenite (Figure II.6 (c)). This shows that complex cases require a careful adjustment of the indexing parameters.

II.4.2 How to optimize the HT-based phase discrimination?

II.4.2.1 Reflectors list optimization

One key parameter that greatly affects the quality of the phase discrimination is the considered reflectors list. In the following, the M1 and M2 maps are both improved by optimizing the reflectors list length.

With the default reflectors list (Figure II.6 (c)), the MnS precipitate in M1 was largely misindexed as iron BCC leading to a F1=0.15 for MnS. Specifically, the reflectors list of the considered phases was set to 32, 39 and 40 for austenite, iron BCC and MnS respectively. In Table II.2, the lowest diffracting intensity family considered for MnS is {422}, which is equivalent to the 3rd diffracting intensity family for iron BCC {211} resulting in MnS being confused with iron BCC. Limiting the number of reflectors of MnS to 28, excludes the family {422}, improving significantly the phase discrimination with F1 > 0.8 for all phases (Figure II.8 (b)).

Figure II.8 (c) presents the resulting confusion matrix corresponding to Figure II.8 (b). From the remaining errors, the larger portion comes from true MnS indexed as false austenite. This is because

these two phases share their three most intense families of diffracting planes. The first different family is the {311} ranked 4th in austenite. It may happen that, if the pattern quality is not enough to detect these lower intensity bands, the discrimination becomes more difficult. In this example, removing low intensity diffracting planes common with another phase, gives more relevance to high intensity ones and hinders misindexing.

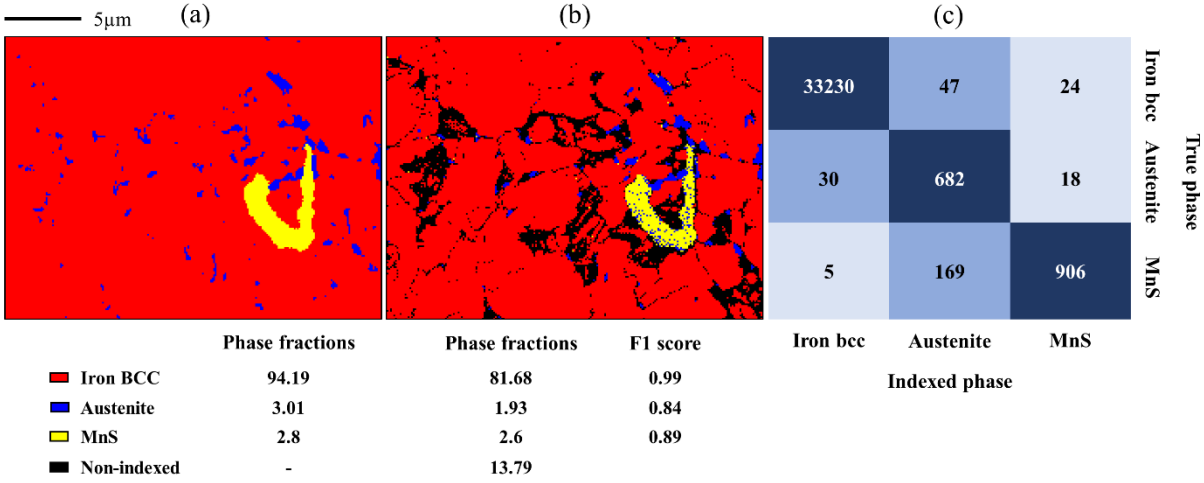

Figure II.8. (a) Phase reference image, (b) phase discrimination result after reflectors list optimization and (c) its corresponding confusion matrix for the M1 map.

Another situation appears in M2 when indexing with the default number of reflectors 32, 39 and 34 for austenite, iron BCC and carbide respectively (Figure II.7 (c)). Here, the confusion is between iron BCC and $Cr_{23}C_6$ with F1 of 0.34 and 0.5 respectively.

Looking at the list of reflectors, the 3rd diffracting intensity family of planes {211} of iron BCC overlaps with the low intensity family {844} of $Cr_{23}C_6$ that was not initially considered for indexing. Figure II.9 (b) shows the result by including the {844} family of $Cr_{23}C_6$ what provides a better phase fraction match and higher F1 scores for the $Cr_{23}C_6$ phase.

Contrary to the previous example, including a low intensity diffraction that is in common with another phase improves indexing with F1 for $Cr_{23}C_6$ increasing to 0.8 while F1 for iron BCC remains the same.

The low F1 score of iron BCC is clearly evidenced by the confusion matrix presented in Figure II.9 (c) corresponding to the phase discrimination result obtained in Figure II.9 (b). There is a large fraction of true iron BCC pixels that have been misindexed as false $Cr_{23}C_6$. This $Cr_{23}C_6$ overestimation may come from the fact that true iron BCC is located in low pattern quality regions and normally contoured by $Cr_{23}C_6$ grains, resulting in low quality patterns also affected by overlapping effects. The remaining errors mainly concern the confusion between austenite and $Cr_{23}C_6$, as seen in the confusion matrix, a large fraction of true austenite is indexed as false $Cr_{23}C_6$ and vice versa. This is coherent as both phases belong to the same space group and the first five families of diffracting planes of $Cr_{23}C_6$ are equivalent to the first three of austenite. It must be noted that a fraction of true $Cr_{23}C_6$ indexed as false austenite comes

from the small carbides in the center of the austenitic grain. It is possible that due to their nanometric size, the selected step size of 0.1µm was not ideal to acquire clean $Cr_{23}C_6$ patterns.

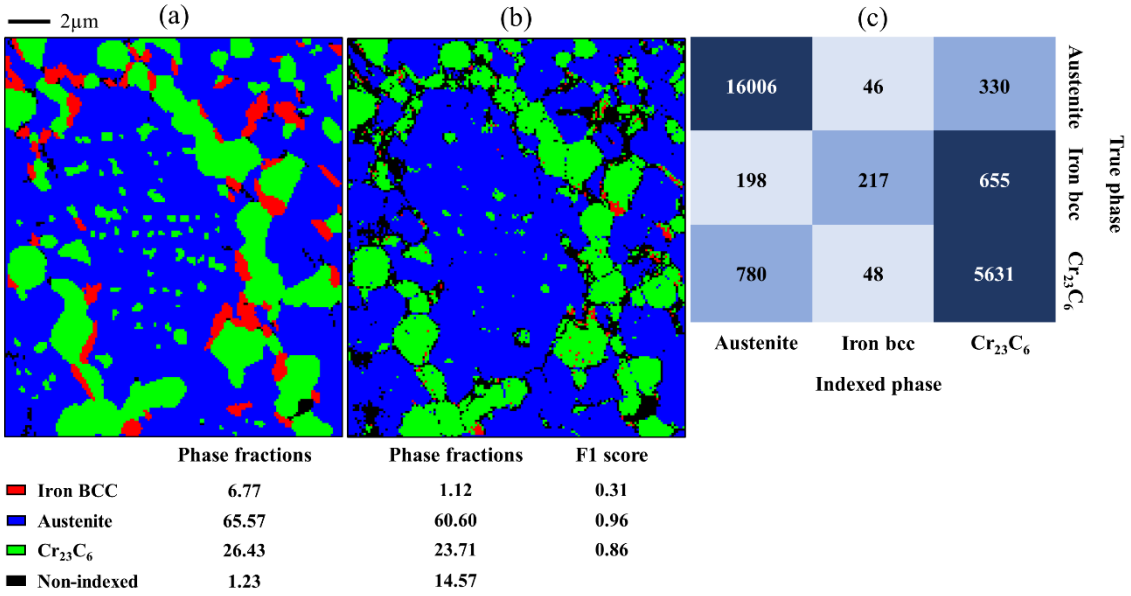

Figure II.9. (a) Phase reference image, (b) phase discrimination result after reflectors list optimization and (c) its corresponding confusion matrix for the M2 map.

Inversely to the improvement reached for M1, in M2 a better phase discrimination was found by adding a lower intensity family of diffracting planes what do not match with the fact that most intense bands should have more relevance than low intensity ones. Figure II.10 shows an example pattern from an actual $Cr_{23}C_6$ carbide with the indexing solutions overlaid of (a) iron BCC, (b) $Cr_{23}C_6$ without the {844} family and (c) $Cr_{23}C_6$ with the {844} family. When using the by-default reflectors list, iron BCC is selected as the correct solution as 10 bands are matching with the experimental pattern (Figure II.10 (a)) while only 8 are matched for $Cr_{23}C_6$ (Figure II.10 (b)). The highlighted bands in white represent those bands that have been detected by the Hough transform but which have not been matched with the indexing solution. Both white lines in Figure II.10 (a) are the most intense bands detected by the Hough transform whereas for Figure II.10 (b) the unmatched bands are ranked as 9^{th}, 10^{th}, 11^{th} and 12^{th} in terms of detected intensity. This is a clear evidence that iron BCC is not the correct phase. Adding the {844} family to the reflectors list, provides 12 bands matching with the experimental pattern. This is coherent as low intensity detected bands are matched with low intensity diffracting planes in the reflectors list.

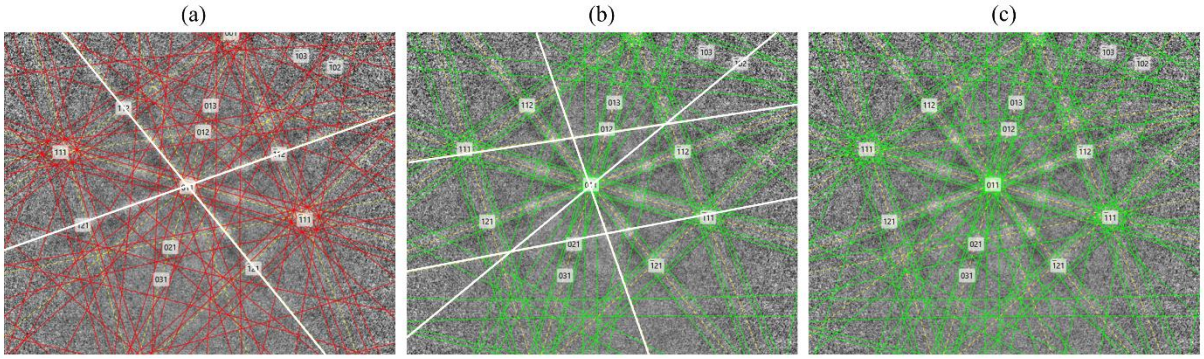

Figure II.10. Indexing solution for an experimental pattern from M2 with (a) iron BCC, (b) $Cr_{23}C_6$ without the {844} family and (c) $Cr_{23}C_6$ with the {844} family. White lines indicate the detected bands unmatched by the respective solution.

These two examples show that classic HT-based indexing does not correlate the intensity of the detected bands with the intensity of the theoretically calculated diffracting planes. In other words, a family of planes that appears last in the reflectors list has the same relevance to match the experimental pattern than a family at the top. To our knowledge, there exists no HT-based indexing available in the market that considers the intensity of the bands as a relevant parameter to find the most suitable solution. Therefore, the list of reflectors must be empirically adjusted for the specific map and candidate phases.

A rule of the thumb that can be applied to discriminate the phases presented in Table II.2 using a classic HT-based indexing approach is based on the number of reflectors and their intensity. Firstly, we choose the number to have at least 25 reflectors belonging to independent families. For instance, in austenite the first 25 reflectors belong to families {111}, {200}, {220} and {311}, thus is does not make sense to consider families {222} and {400} as they are equivalent to {111} and {200} and do not provide any additional information to improve discrimination. Since the detector-sample distance is about half of the detector size, about a quarter of the Kikuchi sphere is expected to be visible on the screen[1]. Therefore 25 reflectors should allow at least 12 bands to intersect the screen for indexing. Secondly, we have empirically observed that including bands with an intensity below 16 (Oxford Instruments calculated intensities) had a detrimental effect in the phase discrimination quality result.

II.4.2.2 Pattern resolution effect

Although significant improvements could be obtained by optimizing the reflectors list, there is still room for further improvement. Increasing the acquired pattern resolution results in longer acquisition times but a more precise EBSD analysis is expected.

Figure II.8 (b) shows a certain number of pixels belonging to MnS that were misindexed with austenite. Probably, the quality of the acquired pattern was not enough to detect the low intensity bands that may help in the discrimination between both phases. For this reason, the M1-HR map was acquired with

[1] The surface of the Kikuchi sphere situated at the distance d, from the source point is 4πd^2. The surface intersected by a detector of height, h and a circular mask is (πh^2)/4. Since all Kikuchi bands pass through the center of the Kikuchi sphere, all of them are visible on a half of it. In a first approximation, we assumed that the fraction of intersected bands is proportional to the intersected surface of the Kikuchi sphere.

higher resolution patterns to evaluate the potential improvement on the phase discrimination (Figure II.11 (b)). Higher F1 scores of MnS and austenite are obtained in addition to a reduction in the fraction of non-indexed pixels since the higher the quality, the higher the probability that the indexing algorithm detects more than 6 bands to index.

Figure II.11 (c) presents the confusion matrix for the phase discrimination result obtained in Figure II.11 (b), where it can be observed that true MnS is misindexed with austenite to a much lesser extent than in Figure II.8 (c). The larger fraction of true austenite misindexing comes from false iron BCC that results from patterns located at low pattern quality regions contoured by true iron BCC.

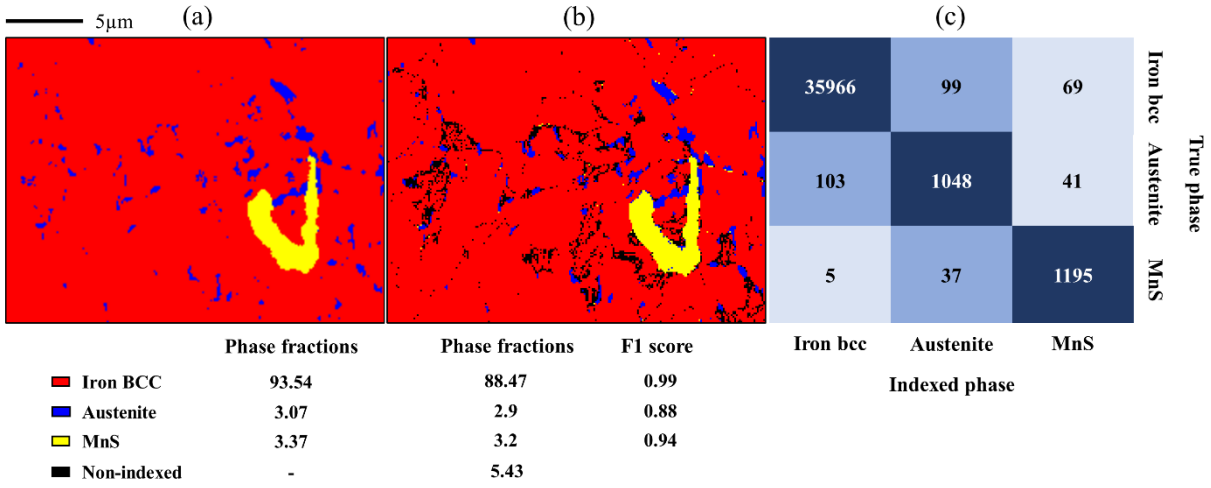

Figure II.11. (a) Phase reference image, (b) phase discrimination result (reflectors list optimized) and (c) its corresponding confusion matrix for the M1-HR map.

II.4.2.3 Indexing with Refined Accuracy

There exist certain cases where no matter the reflectors list optimization or the pattern resolution, some phases cannot be discriminated by classic HT-based indexing. This is the case of M1-2 map where austenite and $(TiNb)C_2$ belong to the same space group and both show equivalent diffracting families down to very low intensities. The only remaining difference resides in the lattice parameter where there is a difference of 0.73 Å (Table II.2). Figure II.12 (c) shows the phase map result with classic HT-based indexing where the iron BCC matrix is well indexed, but all the austenite is misindexed as $(TiNb)C_2$. Both indexing solutions are compared in Figure II.13 and are equivalent. In this case, all FCC phases are indexed as $(TiNb)C_2$ phase because of an arbitrary choice of the AZtec software; when two solutions are exactly equivalent, AZtec keeps the phase that was added last in the candidates' phase list. The reverse situation, $(TiNb)C_2$ misindexed as austenite would happen if austenite was added last in the list of candidate phases.

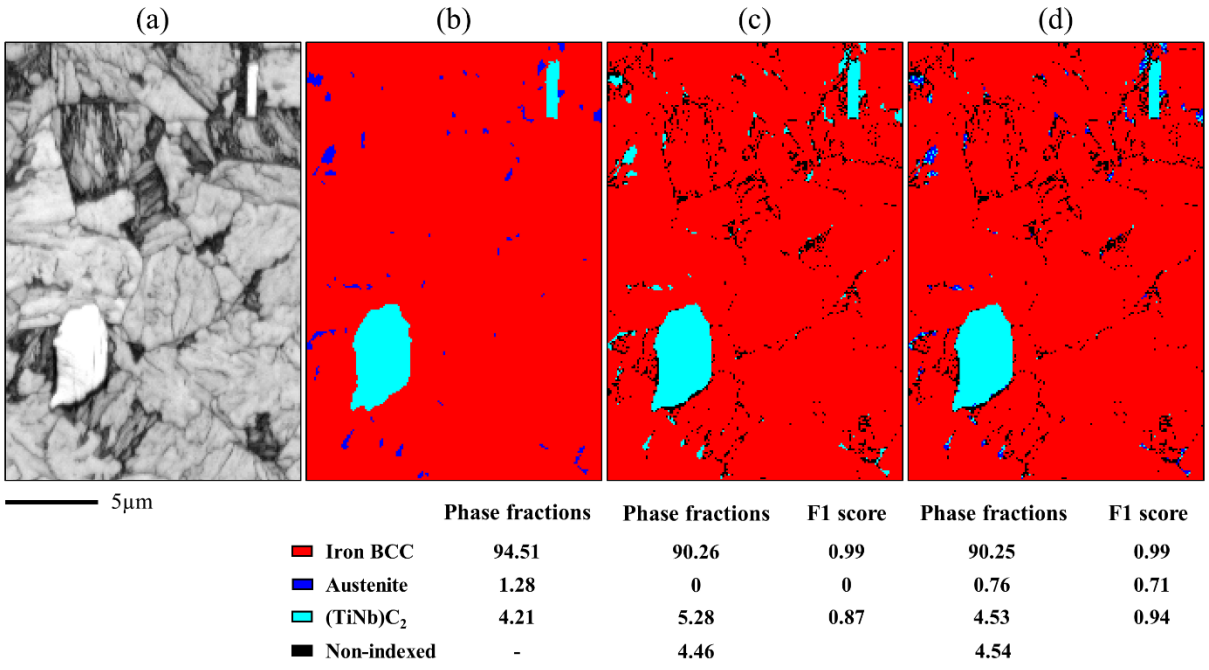

	Phase fractions	Phase fractions	F1 score	Phase fractions	F1 score
Iron BCC	94.51	90.26	0.99	90.25	0.99
Austenite	1.28	0	0	0.76	0.71
$(TiNb)C_2$	4.21	5.28	0.87	4.53	0.94
Non-indexed	-	4.46		4.54	

Figure II.12. (a) Pattern quality, (b) phase reference image, (c) classic HT-based phase discrimination result and (d) RA phase discrimination result for the map M1-2.

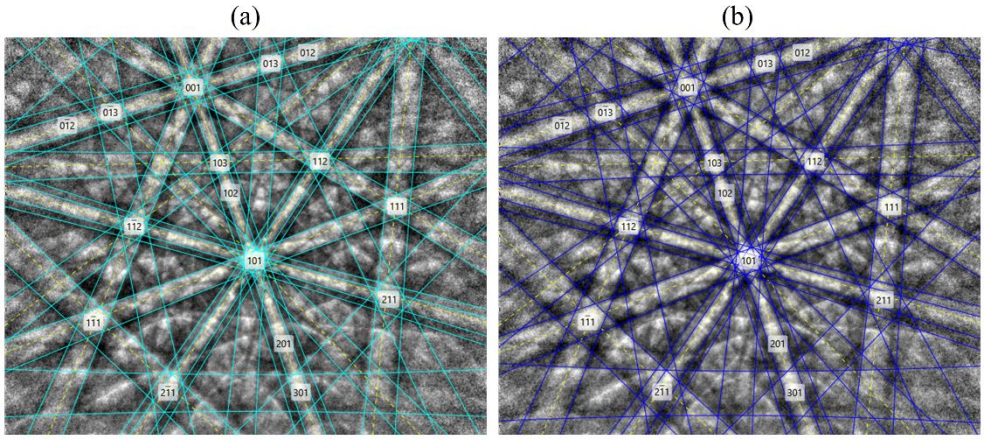

Figure II.13. Indexing solution for an experimental pattern from M1-2 with (a) $(TiNb)C_2$ and (b) austenite.

To improve phase discrimination, RA has been applied as it considers band width for indexing and it could help since lattice parameters between both phases are different. The result is shown in Figure II.12 (d). Both phase fractions and F1 scores per phase are improved since retained austenite is mainly well indexed. However, the phase map still shows some misindexed pixels in the true austenite grains, where RA could not find a clear difference in both solutions and kept indexing by the last in the list. This is clearly evidenced in the confusion matrix presented in Figure II.14 for the phase discrimination result of Figure II.12 (d). The larger fraction of errors comes from true austenite indexed as false $(TiNb)C_2$, while the rest of the errors are negligible.

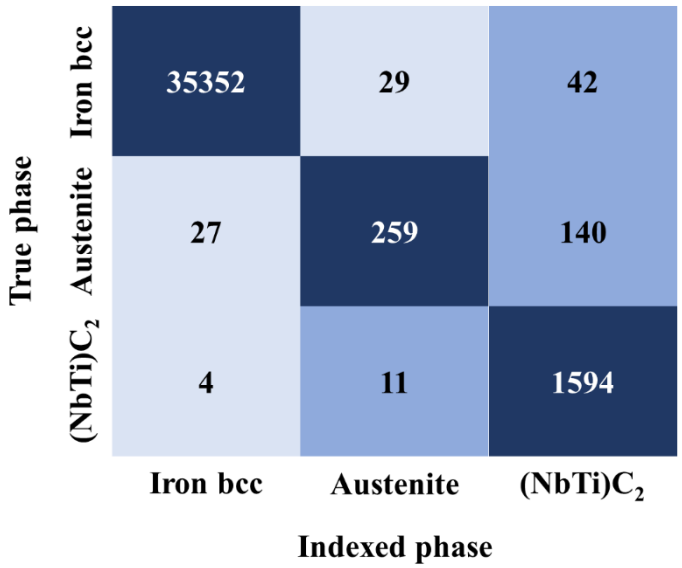

Figure II.14. Confusion matrix for the phase discrimination obtained for M1-2 map in Figure II.12 (d).

This example clearly shows that classic HT-based methods are not able to discriminate phases with equivalent reflectors whose only difference resides in their lattice parameters. Although RA enables a better phase discrimination in this case, the result is still far from being perfect.

II.4.3 Phase discrimination with Dictionary Indexing

As described in II.2.3.3, DI utilizes the entire information contained in the pattern to carry out indexing and this is the reason why it should be able to outperform the results provided by classic HT-based and RA indexing.

The three maps (M1, M1-2 and M2) have been indexed with DI in order to assess its phase discrimination performance compared with both classic HT-based and RA. For both M1-2 and M1, whose pattern sizes are 1244×1024 pixels, an 8×8 pixels binning has been applied to obtain 156×128 pixels and enable indexing to be done in a reasonable time. For M1, a dictionary per phase has been generated with 20kV accelerating voltage while for M1-2 and M2 10kV was used (Table II.1). It is worth reminding that DI indexes the whole EBSD map with each of the phases (number of phases = number of indexed maps) and then performs a merging according to the highest NDP value per pixel to obtain the final map.

Map M1

Figure II.15 (b) shows the phase discrimination result for M1 using NDP as the image similarity metric. Both phase fractions and F1 scores per phase are high, however a little accuracy drop is observed for the MnS phase. This is due to the presence of false MnS clusters appearing in the iron BCC matrix.

In DI, the whole map is indexed and no non-indexed points are displayed. It is up to the user to define a threshold to filter out unreliable results. The regions where these false MnS clusters are located, match with low pattern quality EBSPs. Figure II.15 (c) shows an example pattern that has been indexed as

MnS with an NDP value of 0.8 but little clear Kikuchi bands can be detected. Therefore, certain indexed pixels showing a low pattern quality should be filtered in order to improve the reliability of the phase discrimination.

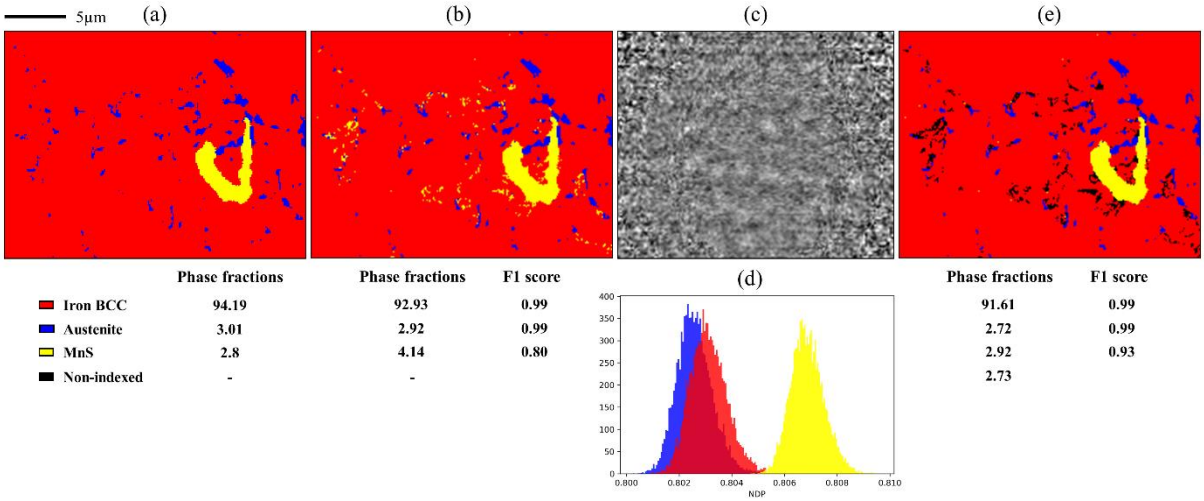

Figure II.15. (a) Phase reference map and (b) DI phase discrimination result for the M1 map. (c) Experimental pattern extracted from a pixel indexed as MnS located in a low BC region, (d) NDP histograms obtained after indexing the generated dictionaries of each phase against 10000 noise patterns and (e) DI phase discrimination result for the M1 map after thresholding low NDP pixels.

For two images with values ranging from 0 to 255, the NDP theoretically ranges from 0 to 1. Therefore, the obtained value of 0.8 for the pattern shown in Figure II.15 (c) seems high. However, obtaining NDPs close to 0 is rare since many pixels with a value of 0 should be present in the images to correlate and this is not the case of EBSPs. Thus, to estimate the lower NDP values that could be obtained during indexing, we have generated 10000 random noise patterns that have been indexed against the dictionaries for all the concerned phases. The plot in Figure II.15 (d) shows the histograms of NDP values obtained per phase against these noisy patterns. The values range from 0.8 to 0.81, therefore NDP around these values should be trusted only with caution. Additionally, the NDP distributions are different depending on the phase: MnS phase gets higher NDP values against noise than both iron bcc and austenite. This may explain the overestimation of MnS indexing shown in Figure II.15 (b), since a noisy pattern will have systematically a higher NDP when indexed against MnS than against the other two phases.

In order to filter the potential misindexed pixels, the mean NDP (M) and its standard deviation (σ) against noise for each phase has been calculated. Any pixel that has been indexed with $NDP < M + 3\sigma$ of its corresponding phase histogram against noise was assigned as non-indexed pixel. Figure II.15 (e) shows the phase discrimination map after thresholding where it can be seen how the false MnS clusters have been removed and are now assigned as non-indexed pixels, what provides a significative improvement in the F1 score of MnS. It should be noted that due to thresholding, some correctly indexed pixels of austenite or iron BCC have been assigned to non-indexed pixels. However, although the indexing matched the good phase, the reliability of the result was very low as the image correlation

value was below the threshold noise. Even if Figure II.15 (e) presents a higher fraction of non-indexed pixels than Figure II.15 (b), the result is more reliable.

Map M1-2

Figure II.16 (b) shows the phase discrimination result for M1-2, where the obtained phase fractions matched the reference and high accuracies per phase were achieved. A little lower accuracy can be seen in austenite and this may be due to the fact that it is normally located in M/A islands were the pattern quality is not optimal and it could result in iron BCC misindexing.

Once again, the dictionaries for all the concerned phases were indexed against 10000 noise patterns and the histograms are shown in Figure II.16 (c) (iron bcc and austenite histograms overlap). Applying the described thresholding strategy, the phase discrimination result remains unchanged, meaning that all the patterns of the map have been indexed with higher NDP values than the noise level. The NDP of the phases indexed against noisy patterns shows also a shift of the distribution relative to each other, with the $(TiNb)C_2$ being much lower than the other two. Also, when comparing this distribution with the one of M1, a slight shift of the ferrite/austenite can be seen towards the lower values. This means that the signal to noise ratio has been improved. Here it can be linked to the higher resolution of the patterns but also to the lower accelerating voltage.

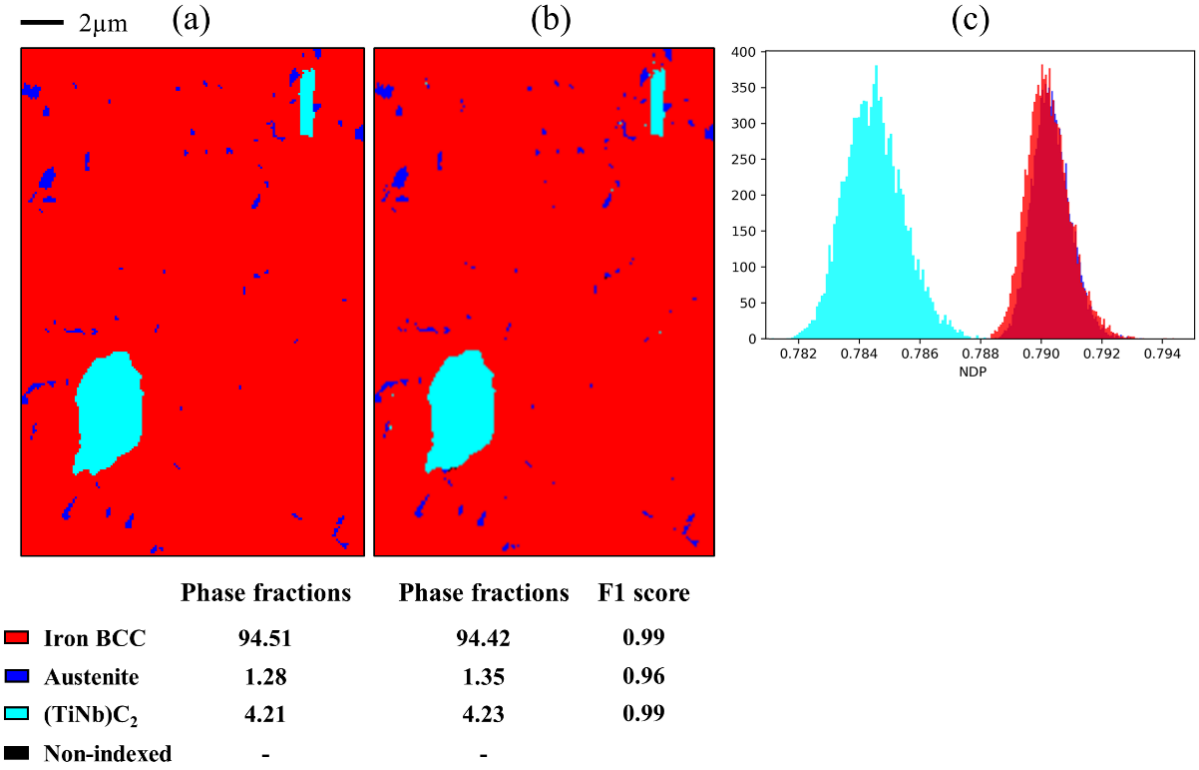

	Phase fractions	Phase fractions	F1 score
Iron BCC	**94.51**	**94.42**	**0.99**
Austenite	**1.28**	**1.35**	**0.96**
$(TiNb)C_2$	**4.21**	**4.23**	**0.99**
Non-indexed	**-**	**-**	

Figure II.16. (a) Phase reference map and (b) DI phase discrimination result for the M1-2 map. (c) NDP histograms obtained after indexing the generated dictionaries of each phase against 10000 noise patterns.

Another point to consider, as done for classic HT-based indexing with RA, is the ability of DI to discriminate austenite from $(TiNb)C_2$ based on their lattice parameter difference. For DI the misindexing

between austenite and $(TiNb)C_2$ is very low. Figure II.17 shows a scatter plot of the points that have been indexed as one of these two phases from Figure II.16 (b). The red line represents the criteria that DI uses to index the corresponding phase by the highest NDP value: if a point falls to the left of the red line is indexed as $(TiNb)C_2$ and if it falls to the right it is indexed as austenite. Both distributions can be very well separated although in the lower NDP range some particular points fall close to the red line. This indicates that the reliability of the result is reduced as these patterns could be almost equally indexed as austenite or $(TiNb)C_2$. This situation mainly happens in austenite since it is located in low pattern quality regions on the map what reduces the obtained NDP values.

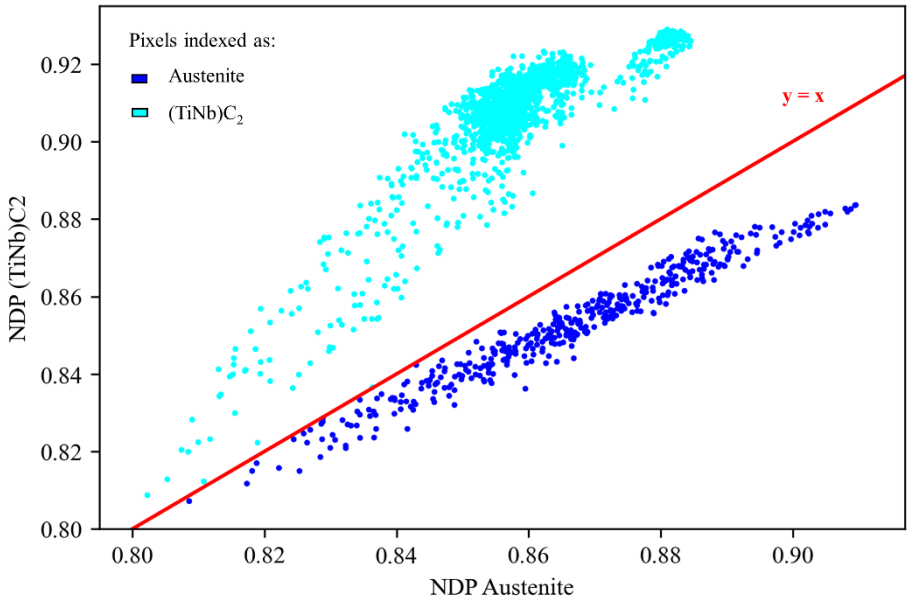

Figure II.17. NDP scatter plot of the pixels of map M1-2 that have been indexed as $(TiNb)C_2$ or austenite. The red line represents the indexing criteria used by DI.

Map M2

Phase discrimination result for M2 is shown in Figure II.18 (b). The determined phase fractions are not accurate and F1 scores per phase are low for the two minor phases. Although the austenite matrix is relatively well indexed, there is a clear overestimation of the $Cr_{23}C_6$ fraction what reduces its accuracy and those of iron BCC and austenite.

The NDP histograms against noise for the concerned phases (Figure II.18 (c)) show a flagrant difference between $Cr_{23}C_6$ and both austenite and iron bcc (these two overlaps in the plot). Once noisy indexing is eliminated and converted into non-indexed pixels as performed beforehand, the obtained result (Figure II.18 (d)) shows a tiny improvement in the accuracies but the $Cr_{23}C_6$ overestimation remains high. In this case, the difference in the NDP values obtained per phase not only affects the misindexing of noisy patterns but also good quality ones that could be indexed as austenite or iron BCC but get systematically indexed as $Cr_{23}C_6$. It is important to remark that, although the shapes do not exactly match the reference phase map, DI is able to index a portion of the small carbides located in the center of the austenitic grain.

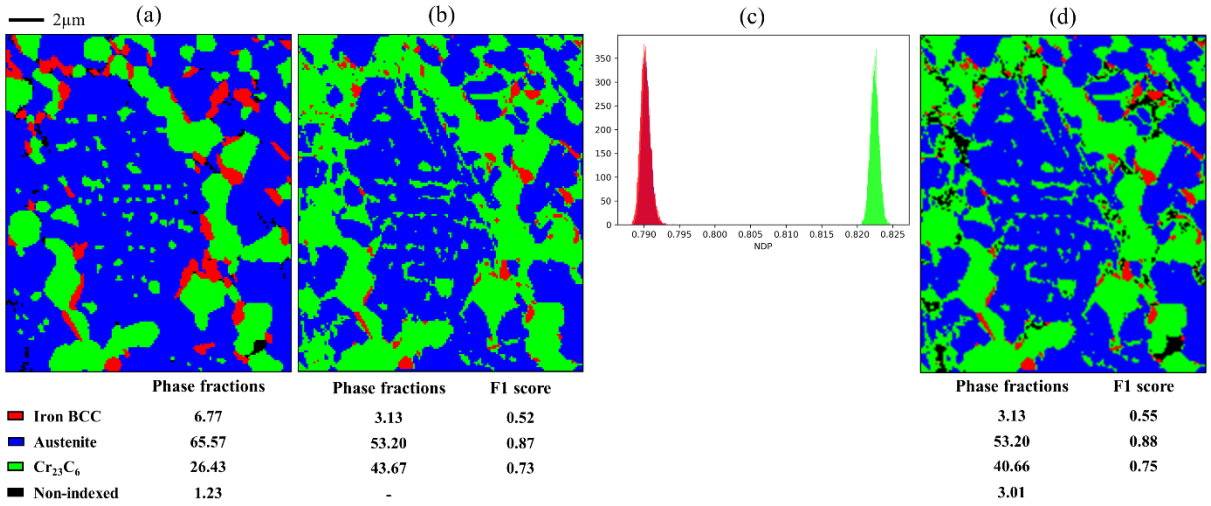

	Phase fractions	Phase fractions	F1 score	Phase fractions	F1 score
Iron BCC	6.77	3.13	0.52	3.13	0.55
Austenite	65.57	53.20	0.87	53.20	0.88
$Cr_{23}C_6$	26.43	43.67	0.73	40.66	0.75
Non-indexed	1.23	-		3.01	

Figure II.18. (a) Phase reference map and (b) DI phase discrimination result for the M2 map. (c) NDP histograms obtained after indexing the generated dictionaries of each phase against 10000 noise patterns and (e) DI phase discrimination result for the M2 map after thresholding low NDP pixels.

To explain the large overestimation of $Cr_{23}C_6$ we can have a look at Figure II.19. Figure II.19 (a) shows a scatter plot of the NDP values obtained for the patterns indexed as austenite or iron BCC and the red line explains the highest NDP merging criteria as described above. It can be seen that there are two clear distributions that could be correctly separated by the red line. This explains why austenite and iron BCC are correctly discriminated. However, once $Cr_{23}C_6$ is considered (Figure II.19 (b) and (c)) the distributions are shifted and the red line cannot separate them anymore, making highest NDP criteria non-applicable for such cases.

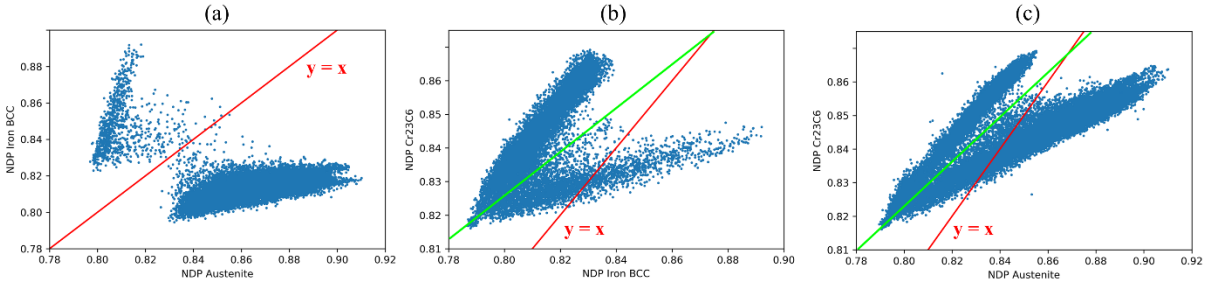

Figure II.19. NDP values of the pixels that have been indexed as (a) iron BCC or austenite, (b) $Cr_{23}C_6$ or iron BCC and (c) $Cr_{23}C_6$ or austenite.

If a custom line was traced to better separate the distributions (green lines in Figure II.19 (b) and (c)) a result as shown in Figure II.20 (b) is obtained. A clear improvement compared to Figure II.18 (d) for all phases is obtained. Only iron BCC shows an overestimation, where the main source of this error comes from true austenite being indexed as iron BCC. To filter the non-indexed points, the same criteria as for map M1 has been used, nevertheless, it does not appear to be adapted to this map. The circle in the bottom right of Figure II.20 (b) highlights a region that could not be indexed even in the reference map and it should be entirely filtered. Therefore, the threshold value needs to be selected by the user depending on the specific map.

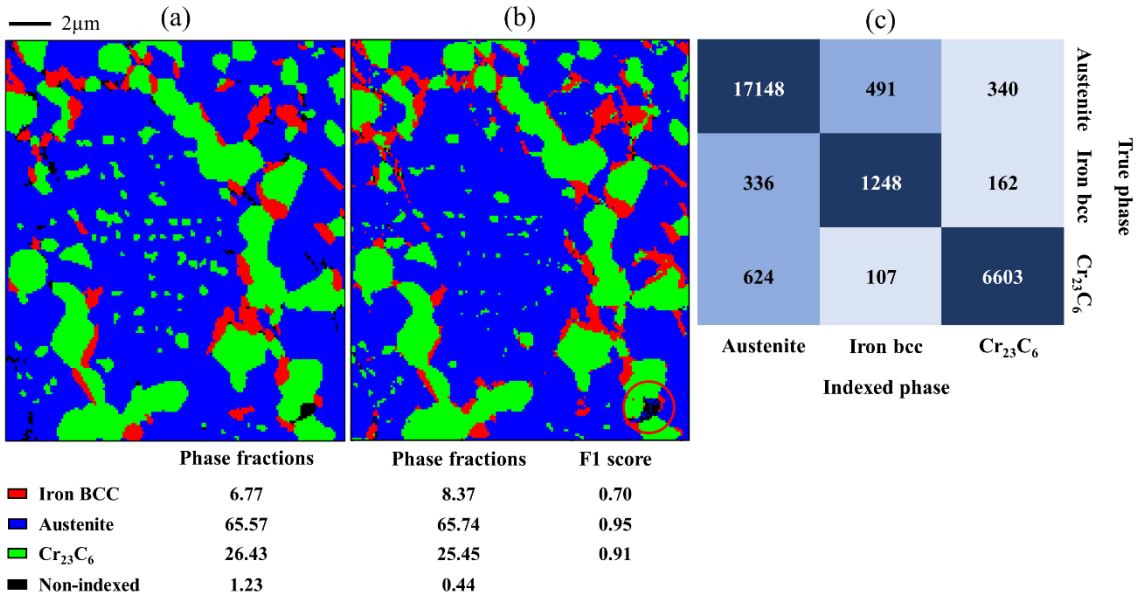

Figure II.20. (a) Phase reference image, (b) optimized phase discrimination result with DI and (c) its corresponding confusion matrix for the M2 map.

II.4.4 DI optimization: Normalized Cross-Correlation metric

As described in II.4.3, the NDP image similarity metric used by default in DI has some limitations. It provides high values (around 0.8) when matching the simulated patterns against random noise and it is sensitive to the specific phase. Some authors have proposed a different image similarity metric called Normalize Cross-Correlation (NCC) to perform DI [71]. This metric is defined as follows:

$$NCC = \frac{1}{n_x * n_y} * \sum_{x,y} \frac{(f(x,y) - \bar{f})}{\sigma_f} * \frac{(t(x,y) - \bar{t})}{\sigma_t}$$

Where n_x and n_y are the dimensions of the EBSP, f is the experimental pattern and t is the simulation.

New indexing has been performed using this metric on the M2 map as it is the one that provided the lower quality results using NDP. This indexing has been carried out with the open source code *kikuchipy* [107]. The histogram in Figure II.21, shows the NCC values obtained after indexing 10000 random noise patterns against the simulated dictionary of patterns of austenite, iron BCC and $Cr_{23}C_6$. The correlation found is very low (around 0.029 mean) and shows the same value for all phases. This is advantageous compared to NDP where we obtained high correlations and different for each phase when indexing noisy patterns.

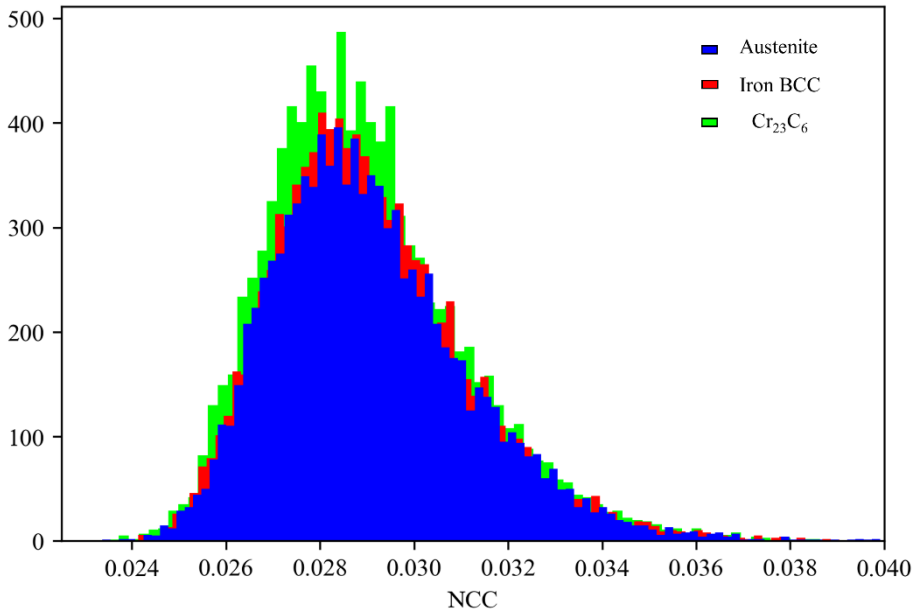

Figure II.21. NCC histograms obtained after indexing the generated dictionaries of each phase of map M2 against 10000 noise patterns

Figure II.22 (b) shows the phase discrimination result obtained after indexing by the maximum NCC value criteria. Good results have been obtained in terms of phase fractions and F1 scores per phase without the need of any further optimization as in Figure II.19 and Figure II.20. However, there is a little accuracy drop, mainly due to the overestimation of Cr23C6 and iron BCC in true austenite pixels (confusion matrix on Figure II.22 (c)).

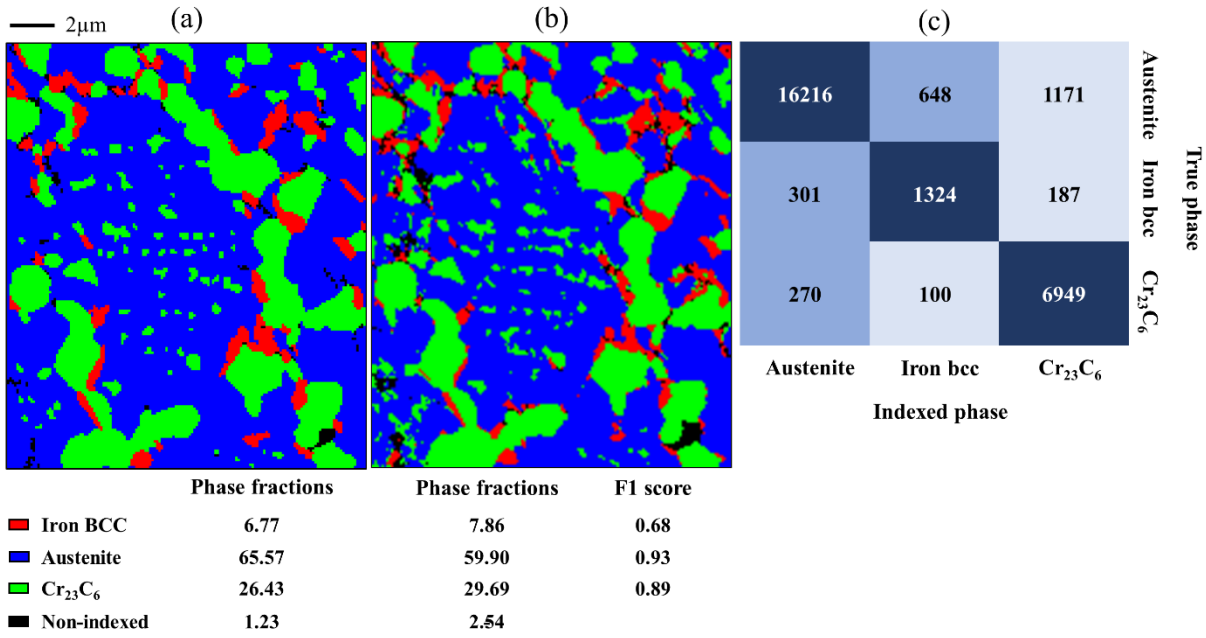

Figure II.22. (a) Phase reference image, (b) phase discrimination result with DI using the NCC metric and (c) its corresponding confusion matrix for the M2 map.

Although good results were obtained for map M2, some issues were encountered when indexing map M1. Figure II.23 (b) shows the highest NCC phase discrimination result. Here the entire MnS precipitate got misindexed with austenite and has the lowest F1 score for MnS among all indexed maps (except

when MnS was not considered as a candidate phase when indexing with classic HT-based in Figure II.6 (d)).

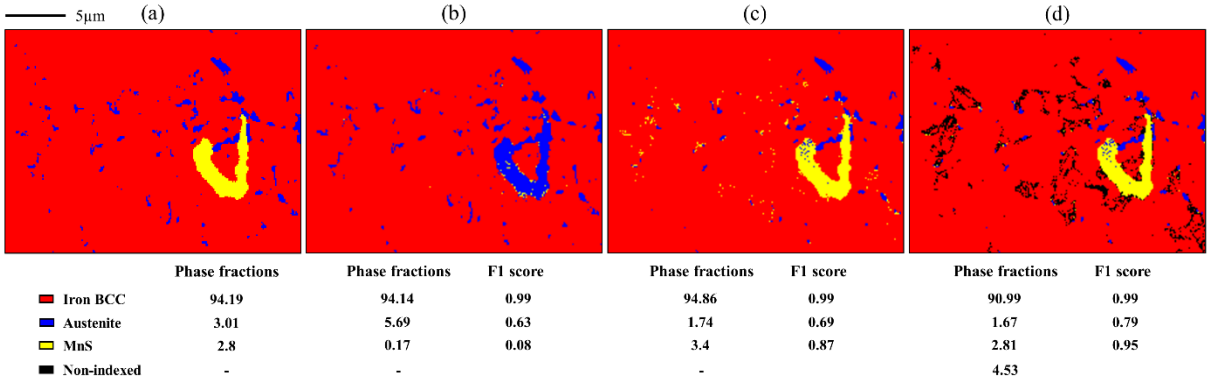

	(a) Phase fractions	(b) Phase fractions	(b) F1 score	(c) Phase fractions	(c) F1 score	(d) Phase fractions	(d) F1 score
Iron BCC	94.19	94.14	0.99	94.86	0.99	90.99	0.99
Austenite	3.01	5.69	0.63	1.74	0.69	1.67	0.79
MnS	2.8	0.17	0.08	3.4	0.87	2.81	0.95
Non-indexed	-	-		-		4.53	

Figure II.23. (a) Phase reference image, (b) phase discrimination result with DI using the NCC metric, (c) phase discrimination result with DI using the NCC metric and a mask and (d) phase discrimination result obtained in (c) after thresholding low NCC values.

During indexing with DI, it is possible to enable an option where a mask is overlaid on the pattern avoiding the matching of the pixels located at the corners where the quality is worse (Figure II.24). After applying such mask, the obtained result is presented in Figure II.23 (c) where a high improvement in the MnS precipitate indexing can be evidenced. However, some false pixels MnS indexed in the iron BCC matrix appear and also certain false austenite pixels remain indexed in the MnS precipitate. The first can be eliminated by thresholding the low NCC values (Figure II.23 (d)) as they appear in the low quality EBSPs areas but the austenite misindexed within MnS would need post-processing.

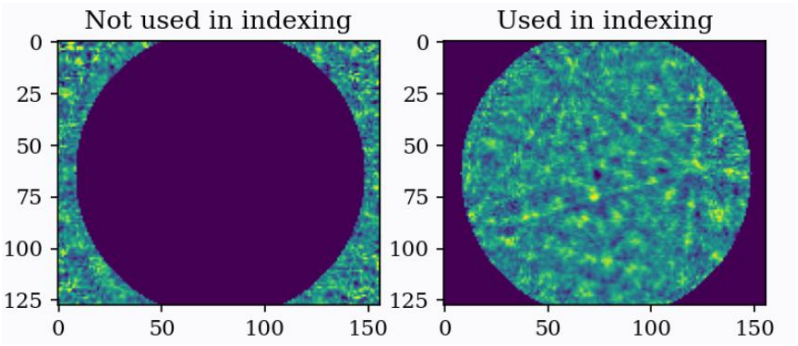

Figure II.24. Applied mask during DI to avoid matching pixels at the corners of the EBSP.

We suspect that the unexpected result obtained in Figure II.23 (b) it is not related to the similarity metric but to the particular way that the dictionary of patterns of each phase is generated by *kikuchipy*. While *kikuchipy* uses a single energy to generate the dictionary of simulated patterns, *EMsoft* interpolates several energies based on a weighting found from Monte Carlo simulations [104]. This difference may hinder the discrimination between austenite and MnS.

II.4.5 Maps postprocessing

As it has been described all along II.4, there exists no indexing method that provides a perfect result for all the addressed microstructures. In the particular case of multiphase steel microstructures containing

retained austenite and several precipitates, carbides, sulfides or nitrides were misindexed with austenite leading to a wrong retained austenite fraction calculation. Although several possible optimizations have been proposed, there is still room for further improvements.

The method described in II.3.3 to obtain the reference maps can be always used to correct phase misindexing and improve the reliability of any phase discrimination map but it involves manual corrections. When only a small amount of corrections must be done, other strategies can be employed. Classically, data cleaning consists in removing single pixels or small clusters from the dataset. However, this strategy has two drawbacks. First, assuming that only the phase was wrongly indexed, it would be interesting to correct phase misindexing while keeping measured orientation. Second, when large misindexed clusters (around 3-4 pixels) are removed it is possible that correctly indexed grains are discarded. These two problems can be addressed by adapted methods.

Often, different phases have different orientations, therefore misindexed phases can be recognized by their small misorientation angle with their neighbors. There is one noticeable exception, the presence of coherent precipitates which intrinsically share the same orientation as the matrix (like $C_{23}C_6$ precipitates in S2). When low angle misorientations can be used to trace misindexing, the following method can be used: it consists in clustering together pixels of cubic symmetry (disregarding their phase) if their misorientation is smaller than 2°. Here a floodfill algorithm is used similarly as in grain detection. Then for each cluster, the majority phase is determined and assigned to the whole cluster.

Another way to prevent removing too many small clusters is to check the OR:

1. Retained austenite must be in a near-KS OR with the matrix.
2. Martensite grains are likely to have at least one neighbor with which they share a common austenite parent.

Thus, while removing clusters, these two conditions are checked and only the clusters that do not respect one of those are removed, while the other ones are considered as correctly indexed.

These two data cleaning methods are illustrated on the example of map M1 in Figure II.6 (d) where only iron BCC and austenite where considered for indexing. The histogram below the orientation map shows the distribution of austenite to ferrite misorientations with respect to the average OR of the map. Small misorientations mean that the ferrite is in OR with austenite and a peak at 45° corresponds to ferrite/ austenite pixels with close orientations. After the phase reallocation procedure, most single austenite pixels are reallocated as ferrite and the 45° peak disappears (Figure II.25 (b)). Removing all non-orientation related clusters (without any size threshold) removes the MnS particle from the dataset. Then the difference between Figure II.25 (b) and Figure II.25 (c) could also be used to identify misindexed secondary phases for example.

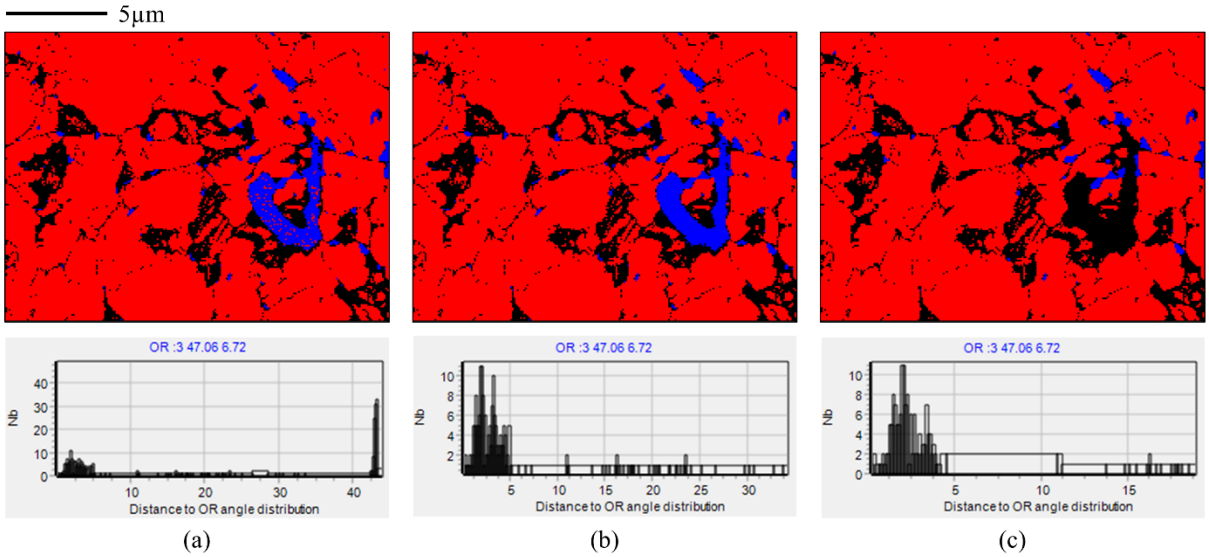

(a) (b) (c)

Figure II.25. Effect of the automatic data cleaning procedure proposed in Merengue2 for the M1 map. (a) Raw phase discrimination result considering iron BCC and austenite only, (b) result after cubic symmetry pixels clustering and (c) result after removing the clusters respect the expected OR conditions with their parents.

II.5 Conclusions and perspectives

The ability of EBSD to discriminate phases in multiphase steels has been extensively tested. Different indexing methods have been evaluated for different microstructures and the following conclusions can be drawn:

- A reflectors list optimization is needed to obtain the best possible results with HT-based indexing since the intensity of the detected bands is not matched with the intensities of the simulated bands of the solution.
- When two phases with a similar list of reflectors need to be separated with classic HT-based indexing, the acquisition of higher resolution patterns is beneficial.
- In certain cases where the reflectors list of the phases to discriminate are equivalent, classic HT-based indexing is not able to provide a correct result. In this case, RA or DI appear as alternatives since they are able to rely on the lattice parameter difference to perform the discrimination.
- For the presented cases, DI provided in general better results than both classic HT-based and RA. However, DI demands the user to save the patterns and since the indexing is performed pixel by pixel by comparing all the simulated patterns is computationally expensive and time consuming. On the contrary, classic HT-based and RA can be performed automatically during indexing saving time and storage capacity. The selection of one or another indexing method will depend on the particular map to index as in some cases classic HT-based is enough to get a good result but sometimes a more precise approach is needed.
- It has been shown that a way to save storage capacity and time while indexing with DI is to bin the patterns. This is an advantage compared to RA as the pattern quality and resolution must be high to exploit the full potential of the band indexing refinement.

- Although NDP has been conventionally used by DI, some weaknesses about this image similarity metric have been highlighted. The use of the NCC metric appears to provide more reliable results during indexing and outperforms NDP in certain phase discrimination tasks.

We also present some perspectives:

- Using Hough-based indexing, we have compared the results obtained in terms of indexing rate and phase discrimination quality by varying the size of the EBSP. It would also be interesting to vary other acquisition conditions such as accelerating voltage, number of bands to index, Hough space, tilt angle, etc. as recently proposed in [108] for the indexing of β phase in α + β titanium alloys.
- In order to better compare the results obtained with NDP and NCC, it would be important to consider the same algorithm to avoid differences in the dictionary generation. In our case, *kikuchipy* has been used for NCC metric as it was not initially implemented in *EMsoft*.
- In order to combine both indexing methods HT-based and DI, Wright et al [109] proposed to work with an hybrid indexing taking advantage of both. Here all the patterns are indexed with classic HT-based but only the lower quality ones are kept for re-indexing by DI in a second step. In this line, Oxford Instruments has recently developed an application in which it is possible to perform on-the-fly PM [110], which would save the post-processing time needed nowadays. Its performance should be tested for the discrimination of phases in steels.

Chapter III: **EBSD in-situ heat treatments**

III.1 Introduction

Within the framework of this thesis, our objective was to purchase a SEM heating module compatible with the EBSD operating conditions in order to evaluate the potential of this equipment for the in-situ study of phase transformations and its complementarity with indirect crystallographic parent phase reconstruction methodologies.

This chapter contains three main parts:

Initially we provide all the details concerning the implementation of the purchased heating module. We describe the main specifications such as the heating and temperature control devices, the sample geometry, the considerations related to the SEM chamber and EBSD analysis, etc.

In second instance, the first feasibility tests on our heating module are presented, where we have been able to define which are the main strengths and limitations of such experiments for the analysis of phase transformation.

Last, we present three preliminary studies that have been carried out on different steel samples. Two of them are related to the parent austenite microstructure refinement after successive heating and cooling cycles. The remaining study concerns the ferritic nucleation and growth during cooling from its austenite parent microstructure, where the OR is monitored.

III.2 In-situ EBSD heat treatment implementation

As mentioned in the introduction, our objective was to purchase an SEM heating module compatible with the operating conditions in EBSD to evaluate the potential of this equipment for the in-situ study of phase transformations. This led us to establish the main specifications required for our future experiments. In this respect, we considered the maximum temperature that could be attained (minimum 1000°C), the ability to heat up and cool down quickly (minimum heating speed of 10°C/s), the possibility of programming heating cycles, the accurate monitoring of the sample's temperature, the compactness of the module in order to work in ideal EBSD conditions (maximum working distance (WD) of 15mm for the FEG SEM-EBSD were it has been implemented), among others.

In the context of the purchase procedure, we tested different heating modules. Finally, we decided to propose to Kammrath & Weiss (represented in France by the company EDEN Instruments) to make evolve their device (Figure III.1 (a)) towards a stage with an optimized geometry and performances in terms of improved heating speed. The version which is currently installed at LEM3 and which results from these exchanges with Kammrath & Weiss is given in Figure III.1 (b).

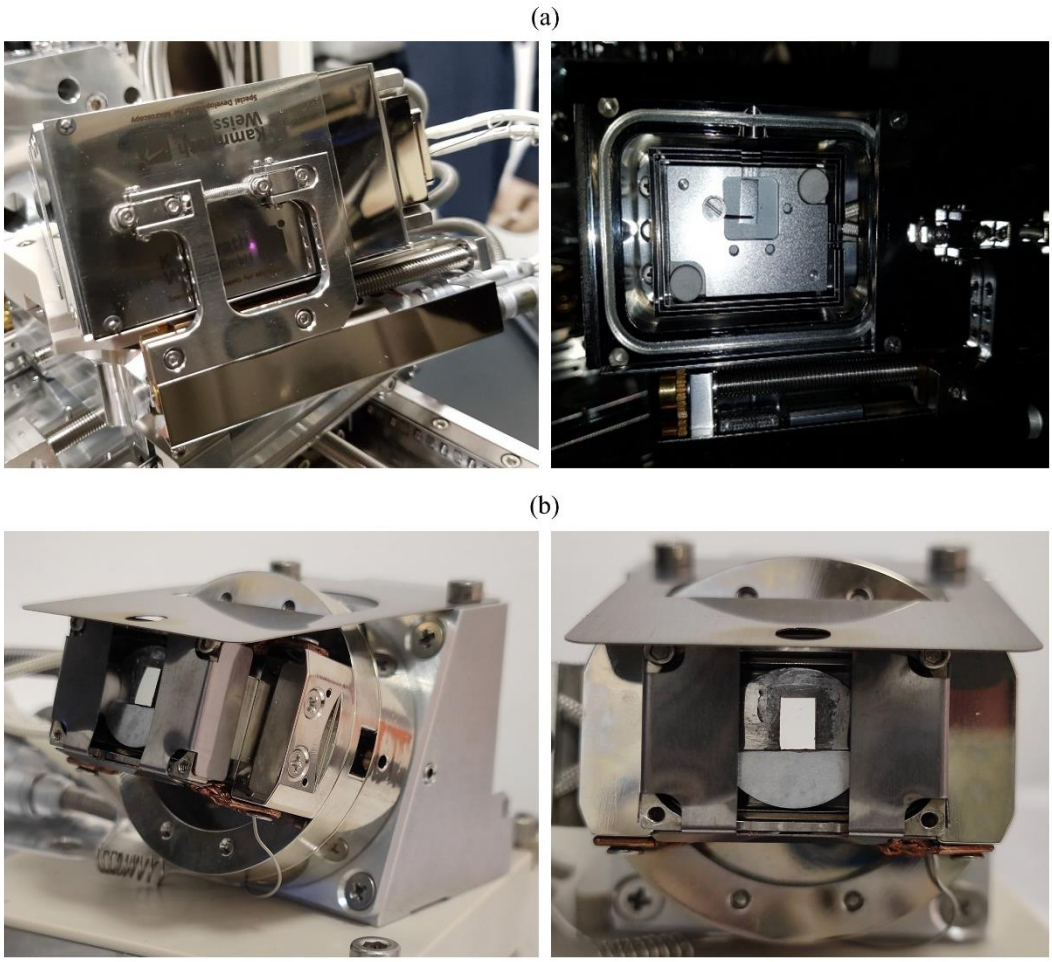

Figure III.1. Heating modules developed by Kammrath & Weiss. (a) Shows the original version where the right-hand photo shows the module with the window open. (b) Presents the optimized version purchased and installed at LEM3.

III.2.1 Heating device

A detailed view of our heating module developed by Kammrath & Weiss is given in Figure III.2. The heating principle of the presented module is based on a classic ceramic resistive element with a round shape and a diameter of 14mm (indicated with number 1 in Figure III.2 (a)) which is able to easily reach a temperature of 1050°C. The heating element is covered by a molybdenum (Mo) cap (indicated with number 3 in Figure III.2 (b)) where the sample is placed. Between the heating element and the Mo cap a thin graphite layer is placed to improve the surface contact and therefore the thermal conductivity. The Mo cap is clamped with two tungsten clamps (indicated with number 5 in Figure III.2 (b)) in order to apply pressure and further optimize the surface contact. The surface contact of the round heating element is kept low in order to keep the heat flow at the surface of the sample. To increase the heat transfer efficiency, the sample could be placed directly in contact with the ceramic heating element.

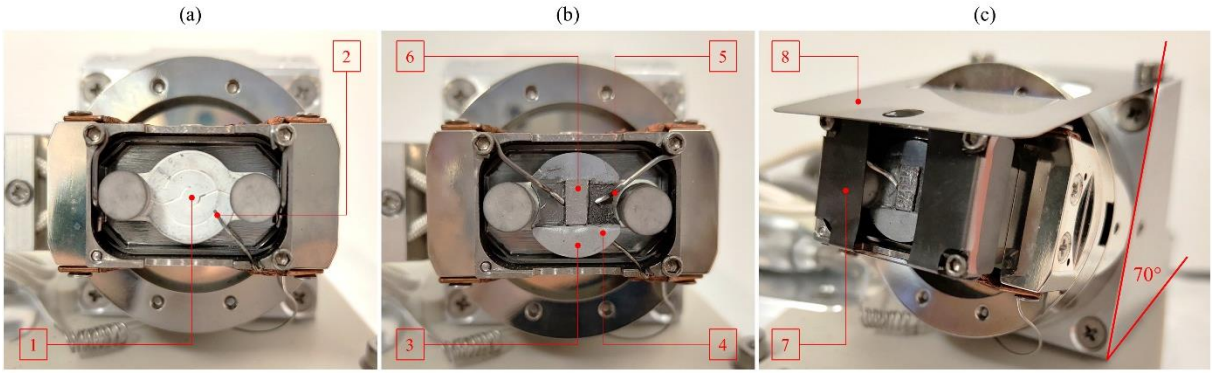

Figure III.2. Heating module developed by Kammrath & Weiss. (a) Highlights (1) the ceramic heating element and (2) the thermocouple. (b) Shows (3) the Mo cap, (4) the measuring position of the thermocouple, (5) the tungsten clamps and (6) the sample. (c) Indicates (7/8) the radiation shields and the 70°C pre-tilted stage

The main idea behind the well-known resistive heating is based on applying a current to a material with a high electrical resistance (e.g. ceramics) and as the material hinders electricity flow it generates heat. One of the main advantages of heating with ceramics is the high heating speed, although special attention must be taken to the possible temperature overshooting due to the heating inertia of the ceramic. Another positive point of such technology is the efficiency, as the entire amount of power supplied to the heating element is transformed into heat. However, ceramics are prone to suffer from thermal shocks, hence their main weakness is their slow cooling ability. They cannot be cooled in any other way than by cutting off the power supply and letting them lose their temperature naturally; any external agent used to accelerate their cooling may result in their cracking. It must be noted that the body of the heating module is actively water cooled to avoid high temperatures inside the SEM chamber. Additionally, two protective thermal shields are placed as indicated with numbers 7 and 8 in Figure III.2 (c).

III.2.2 Temperature regulation and measurement

The temperature of the heating device is regulated with a PID controller. Two specific modes with different PID settings have been configured by Kammrath & Weiss, named “PID control” and “Rapid Heating”, although other settings can be adapted by the user. The former prioritizes a precise control of the temperature set by the user, where the power supply to the heating element is regulated by the PID values and guarantees no overshoot. Inversely, the latter prioritizes the highest possible heating rate, where initially the full power is supplied to the heating element and once the thermocouple measure is close to the user-set intermediate-temperature, the power supply is regulated with the set PID values to reach the expected high temperature, although a significant overshoot and stabilization time is expected. Kammrath & Weiss claims maximum heating speed of 3°C/s for the “PID control” mode and 50°C/s for the “Rapid Heating” mode. In any mode, the highest cooling speed declared by the developers is 7°C/s.

The temperature measurements are performed with a thermocouple type NiCr-Ni (indicated with number 2 in Figure III.2 (a)). The thermocouple is inserted through a little hole that has been drilled in the bottom right of the Mo cap and reaches a position close to the bottom right of the sample as indicated

by number 4 in Figure III.2 (b). This configuration probably induces a temperature gradient between the thermocouple measure and the actual temperature of the sample, as there exist a millimetric distance between the measuring point and the bottom part of the sample. The thermocouple can also be brought closer to the sample by clamping it with one of the tungsten clamps on the Mo cap or directly on the sample. Although the temperature measurement is more realistic in this case, Kammrath & Weiss warned us from their experience that a thorough knowledge of the composition of both the sample and the thermocouple is necessary. It is possible that any unexpected chemical reactions that may occur at high temperatures and result in uncontrolled heat treatment in the microscope chamber. An intermediate ceramic layer between the sample and the thermocouple could be recommended. In our heating module, there exists also the possibility to measure the temperature with a second thermocouple to check the temperature at other locations.

III.2.3 Sample specifications

The maximum size of the sample's surface to analyze is limited by the available size over the Mo cap. However, it is important to keep the sample thickness as thin as possible (<1mm) in order to avoid the temperature gradient between the underneath face of the sample (that is being heated) and the top face we want to analyze. If all sample dimensions are kept small, then the temperature of the sample is more evenly distributed. The sample shown in number 6 Figure III.2 (b) presents a dimension of $8\times4\times1mm^3$.

In order to improve the surface contact between the sample and the Mo cap we considered two factors. 1) The bottom face of the sample has also been polished. It is important to note that a manual polishing avoiding resin embedding is recommended for this kind of high temperature applications since any resin residue remaining on the sample may evaporate inside the microscope chamber during heat treatment. 2) Although the recommendation of the manufacturer was to mechanically hold the sample with a tungsten clamp, we have found that this solution is not optimal in terms of surface contact. Additionally, if the sample is small there is not much room available to place the clamp and this can generate a shadowing effect in the acquisition of Kikuchi patterns. We have found that the best solution to improve the surface contact and get rid of any kind of shadowing effect was to glue the sample to the Mo cap. For this, we used a high temperature carbon paste consisting on a dispersion of carbon flakes in an inorganic silicate aqueous solution. Once the sample is glued, the paste needs to be dried for at least 1h at 100°C.

III.2.4 Considerations concerning SEM and EBSD

The size and shape of the module have been adapted to match the specifications of the microscope where it has been installed: ZEISS Auriga 40 FIB–SEM equipped with Oxford Instruments CMOS Symmetry EBSD camera. Its approximate dimensions are 50mm of diameter and 35mm thickness. As shown in Figure III.2 (c), the heating module is placed over a 70° pre-tilted stage in order to work in optimal EBSD conditions. The WD at the bottom part of the sample (the closest to the thermocouple as possible)

reaches 15mm. This WD is enough to detect high quality Kikuchi patterns with the CMOS Symmetry camera tilted to its lowest position.

Even if the module is designed for high temperature EBSD experiments, it is also possible to acquire SEM images during the experiments. In-situ high temperature experiments in a SEM must fulfill special recommendations to protect all the chamber components from damage induced by the increasing temperature. Also, the infrared (IR) radiation generated at high temperature may perturb the proper operation of certain detectors.

For SEM imaging, it must be noted that the BSD detector starts to be blinded between 400-600°C and it could be damaged at 800°C. On our ZEISS SEM, the In-Lens SE and Energy selective Backscattered (EsB) detectors have an IR filter and can be used up to 1000°C.

In the case of EBSD acquisition, the hot sample surface is directly facing the EBSD camera which receives strong IR radiation. This can not only damage the phosphor camera screen but it can also worsen the quality of the detected patterns. The solution proposed to reduce this effect is based on adding an extra-thick metal coating on the surface of the phosphor screen. This is the solution we have been working with during our experiments. However, the coating may reduce the detector's sensitivity and additionally any surface damage on the phosphor (such as small scratches or pin-holes) would severely limit the effectiveness of the screen. A recent approach is based on using an optical interference filter which is placed behind the phosphor screen and blocks out the IR signal without compromising the detector's sensitivity, and is unaffected by imperfections in the phosphor screen. Additionally, it must be noted that the diodes above and below the phosphor screen are blinded due to the IR radiation and no imaging can be performed with them.

III.3 Preliminary feasibility tests

The heating module has been initially tested in different conditions to establish its limitations and to know what kind of experiments can be carried out.

III.3.1 Measuring safety temperatures inside the SEM chamber

To ensure the safety of the in-situ heating experiments, we have initially measured the temperatures of the surrounding components of the chamber. Four different thermocouples have been installed: on the pole piece, close to the FIB micromanipulator, on the EBSD camera (all shown in Figure III.3 (a)) and on top of the heating module. Figure III.3 (b) presents the temperature curves of the different components as the heating evolves from room temperature to 1000°C. None of the components surpasses a temperature above 60°C, what means that the conditions to perform in-situ heating are safe.

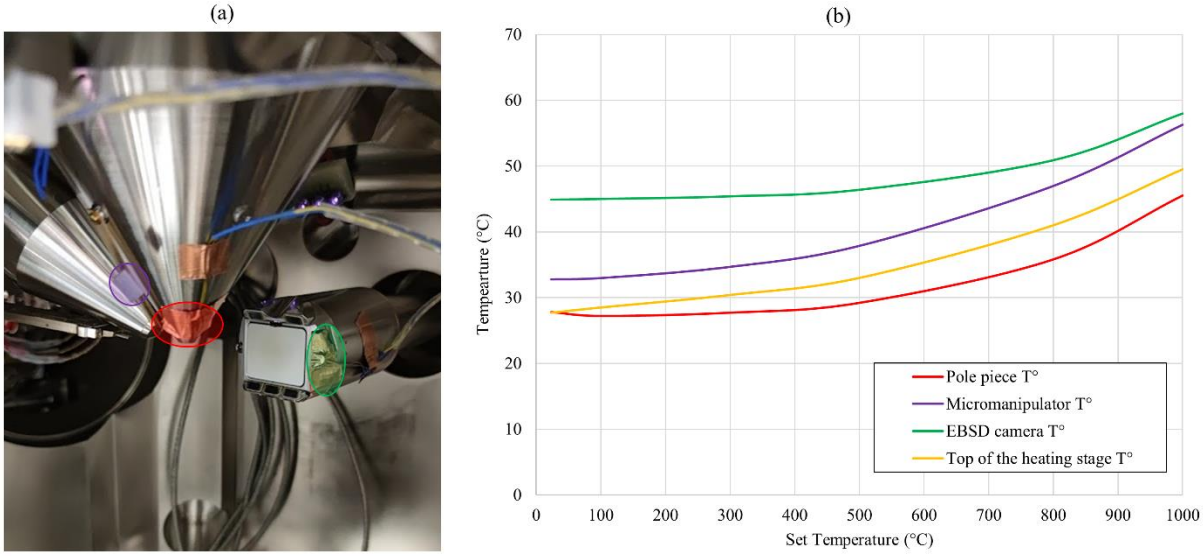

Figure III.3. (a) View of the thermocouples installed in different components of the SEM chamber before installing the heating module and (b) measured temperature curves of the components against the heating temperature with the heating module installed.

It must be noted that the EBSD camera has not been fully inserted for this test. It was inserted until 192mm, while its final position is 198.3mm. Thus, the temperature attained by the EBSD camera during in-situ experiments is of course higher than the one presented here.

III.3.2 Heating and cooling ability

As mentioned in III.2.2, the temperature is regulated with a PID controller and two different modes ("PID control" and "Rapid heating") have been provided by Kammrath & Weiss. The choice of one or the other depends on the kind of experiment we want to carry out.

Heating with "PID control" mode. Figure III.4 (a) shows a standard heating/cooling experiment performed in a model sample steel (Fe-0.12 wt%C-2 wt% Mn) that has been entirely regulated by the PID. In this case, the heating starts from room temperature to 900°C where a smooth curve shape is obtained with no overshoot. This heating takes in total ~300s for a ΔT of 870°C (~3°C/s). However, the heating up to 700°C takes only around ~90s (ΔT of 670°C with ~7.4°C/s) but the regulation from 700° to 900°C takes ~200s (ΔT of 200°C with ~1°C/s). Once the plateau at 900°C is reached, the temperature is well-regulated without any unexpected oscillation.

Heating with "Rapid heating" mode. Figure III.4 (b) shows the fast heating of the same steel sample presented above. In this case, for a heating from room temperature to 900°C, the first stage of the heating path is performed with a full power supply that is not regulated by the PID values. The idea is to heat up as quick as possible. The second stage starts once the temperature reaches 780°C (user-defined), where the heating starts to be regulated by the PID values, making it a bit slower in order to reach 900°C as smoothly as possible. In this case, 900°C are reached in ~20s (ΔT of 870°C with ~45°C/s) but with an overshooting of some tens of °C and a needed stabilization time of more than 4 minutes.

Cooling rate: The end of the curve in Figure III.4 (a) shows the cooling ability of the heating module by cutting the power supply and letting the module to naturally cool down. This is the quickest way to cool down the module and therefore the sample. It takes ~160s for a ΔT of 500°C from 900°C to 400°C (~3.1°C/s). When the cooling starts from lower temperatures, the cooling speed gets reduced.

Apart from the presented heating cycles where large ΔTs are applied, it is possible to carry out stepwise heating or cooling as we performed in some of our in-situ experiments presented in III.4.

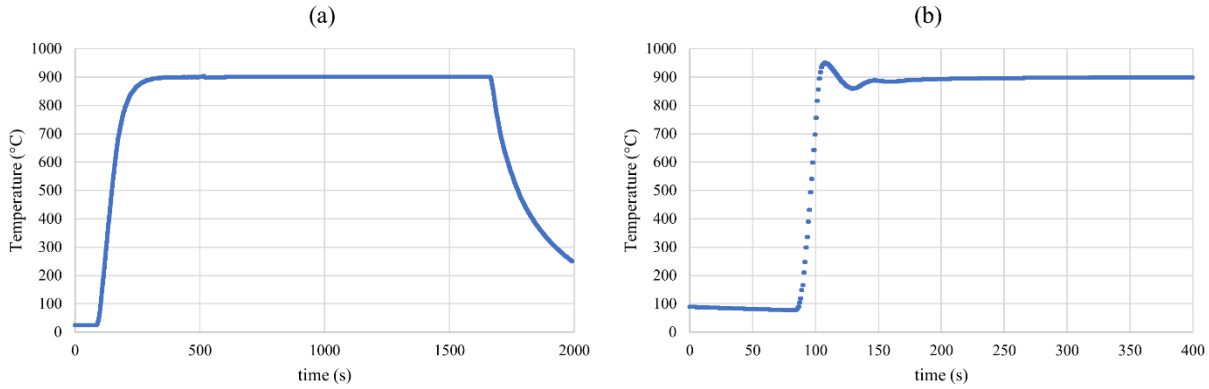

Figure III.4. (a) Standard heating and cooling cycle for a steel sample regulated by the PID values set. (b) Full power heating.

Along the literature, other heating technologies have been applied to in-situ heating experiments. Laser-powered heating has been proposed in [11], [91], [111] and it is based on a radiation and absorption heating principle. With this technique, the maximum heating speed can be very high. In [11], the authors also propose a special cooling system in which a metal block contacts on the sample holder from back side face and remove heat of the sample by conduction, what provides a high cooling rate. One of the main drawbacks is the small laser incident area that may rise the temperature locally and could result in an uneven temperature distribution. Additionally, these lasers are very expensive. Other solutions, propose a metallic heating element to avoid the thermal shock during cooling and be able to cool down quickly with an external agent as described in [11].

III.3.3 EBSD acquisition

Figure III.5 shows both raw (a) BC and (b) IPF-Z maps of the austenite parent phase of a model steel sample at 900°C. This map has been acquired with an accelerating voltage of 20kV, no frame averaging and 0.5ms exposure time. The quality of the map is remarkable as it reached an indexing rate of 87% and an acquisition speed of 1725Hz (1725 patterns per second). As the size of the maps is 111×85µm^2 and the selected step size was set to 0.5µm, the entire map took 21s to be acquired. This proves that it is possible to acquire high quality maps with high acquisition speeds at high temperatures. To the best of our knowledge, this is the first time that such high speeds are reached during in-situ analysis and this is due to the advances in terms of acquisition speed and quality of the last generation of EBSD cameras. In [10] the authors reported an acquisition speed of 870Hz while in [95] 403Hz.

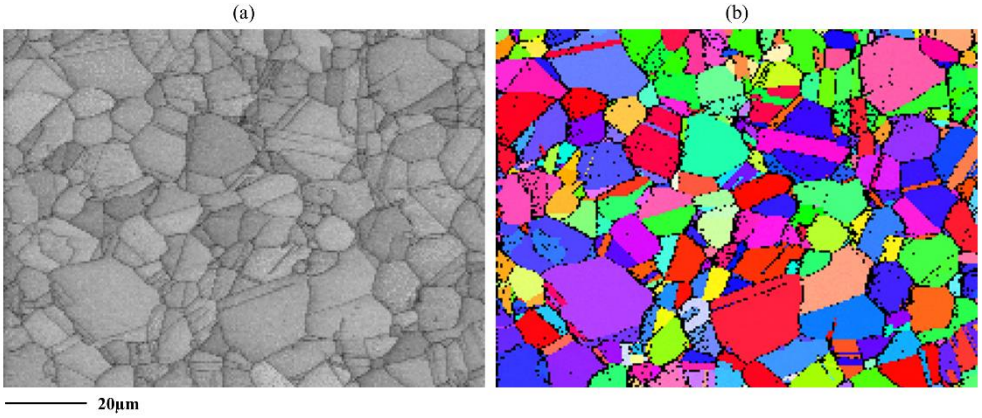

Figure III.5. (a) BC and (b) IPF-Z maps of the austenitic microstructure during plateau at 900°C.

Different trials have been also performed to acquire EBSD maps during continuous heating or cooling. Figure III.6 shows both raw (a) BC with phase map overlaid and (b) IPF-Z map acquired during continuous cooling, once the transformation from austenite to ferrite has already started. A prominent image drift can be observed generating a vertical elongation of the grains. Although the quality (85% indexing rate) and speed of the acquired map (1363Hz, 39s the entire map) are more than correct, it becomes very difficult to keep track of a region of interest during continuous heating or cooling and avoid image drift. For this reason, in order to capture dynamic processes such as grain nucleation or grain boundary motion it is better to select a strategy where the temperature is changed stepwise being possible to acquire high quality EBSD maps with no drift during a short-time plateau. Of course, such experiment does not exactly represent the real processes that a sample undergoes in an industrial context but still serves to better understand the nature of phase transformations.

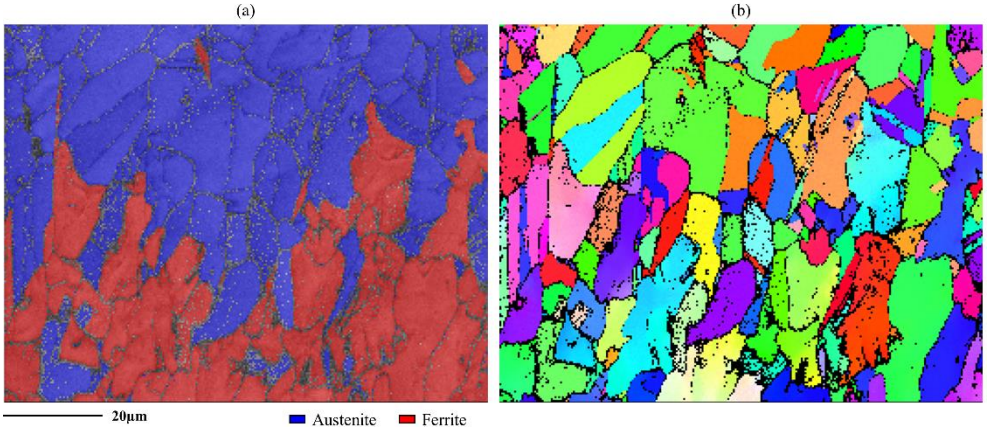

Figure III.6. (a) BC with phase map overlaid and (b) IPF-Z map of the austenite to ferrite transformation during continuous cooling.

III.3.4 Temperature gradients

Thanks to the ability of EBSD to discriminate phases, we can know with relatively good accuracy at what temperature the sample is at the beginning of a phase transformation. In this context, we have evidenced a temperature gradient of some tens of °C between the expected transformation temperature and the one indicted by the thermocouple in certain heat treatments (details given for each particular

case in III.4). However, this temperature gradient may vary with the experiment as it is not only due to the distance between the sample and the thermocouple but also to the sample dimensions and thermal conductivity and the optimization of the contact surfaces to improve the general thermal conductivity.

III.3.5 Sample's free surface effects

When conducting an in-situ heat treatment experiment, the observations are performed on the sample's free- surface in contact with the environment what may induce phenomena different from those occurring at the material bulk. Therefore, it is essential to complement in-situ heating EBSD with indirect reconstruction to verify that the observed microstructure at the sample's surface is representative of that inside the bulk.

One of the free surface effects we have observed is related to the change in the local chemistry of the sample's surface. A strong decarburization effect has been evidenced after several heat treatments from room temperature to 900°C on a model steel sample (Fe-0.12 wt%C-2wt%Mn). Figure III.7 shows the transversal section of the treated sample. The C depletion at the sample's surface resulted in the precipitation of a 20µm thick ferrite layer. This is a strong limitation for the study of phase transformation in steels, especially during cooling. A reliable interpretation of the observed phenomenon must be coupled with an additional chemistry analysis of the sample top surface. To our knowledge, coupling in-situ EBSD with chemistry analysis has not been implemented in the literature yet.

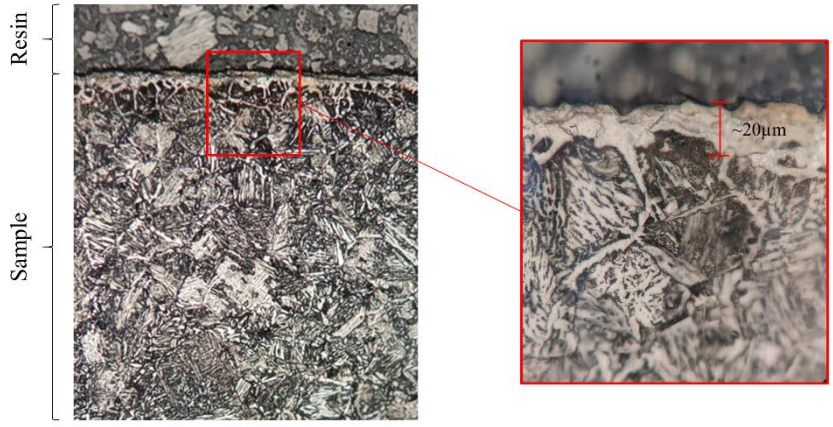

Figure III.7. Optical micrograph of the transversal section of a steel sample after performing in-situ heating.

III.4 Phase transformation studies on steels

Three different studies could be addressed in the framework of the thesis, all related to the analysis of phase transformation in steels. It should be noted that, the purchase of the heating module has started in 2020 but the acceptance of the delivered final version was in July 2022. Thus, the presented results were mostly obtained during September 2022.

III.4.1 Study 1: Austenite grain size evolution with increasing number austempering cycles

III.4.1.1 Material and context

This study (partially confidential) is part of a collaboration between our laboratory and the industrial partner Vallourec. The analyzed material is a medium-carbon steel whose composition and theoretical transformation temperatures are presented in Table III.1. The microstructure of this steel at room temperature is martensitic and it is produced for Oil Country Tubular Goods (OCTG).

Table III.1. Nominal composition [weight %] and transformation temperatures [°C] of the concerned material.

Nominal composition				Transformation temperatures			
C	Cr	Mo	V	Ac1	Ac3	Ms	Mf
0.4	1	1.3	0.2	775	850	310	120

Our purpose is to investigate the effect of the number of austempering cycles on the high temperature austenite grain size. The final objective is to confirm the austenite grain size refinement with the increasing number of cycles and consequently the refinement of the different martensite constituents (packets, blocks and sub-blocks) [112]. The general framework is motivated by the fact of improving the sulfide stress cracking (SSC) performance with microstructure refinement. Indeed, previous studies have shown evidences of hydrogen-assisted fracture happening at martensite boundaries [113]–[115].

Three samples that have been submitted to different industrial Quenching/Tempering (Q/T) treatments have been provided (Table III.2). The austenitization temperature (T_{aus}) of 880°C has been determined as Ac3+30°C. Sample A undergone a single Q/T, sample B two successive Q/Ts while sample C three successive Q/Ts.

Table III.2. Heat treatments undergone by the different studied samples.

Sample	Q/T_1		Q/T_2		Q/T_3	
	Austenitization	Tempering	Austenitization	Tempering	Austenitization	Tempering
A	880°C / 10min	715° / 30min	-	-	-	-
B	880°C / 10min	700° / 20min	880°C / 15min	715°C / 30min	-	-
C	880°C / 10min	700° / 20min	880°C / 10min	700°C / 20min	880°C / 15min	715°C / 30min

III.4.1.2 Experimental procedure

Our strategy to address the problem is to determine the austenite grain size in two steps. First, we want to perform the indirect reconstruction of the parent phase from the martensitic microstructure and then we measure the real austenitic microstructure at high temperature with in-situ heating EBSD experiments.

Sample preparation

Figure III.8 shows the sample extraction scheme from the tube. The sample highlighted with number 1 in Figure III.8 has been extracted to be analyzed under EBSD and then perform the indirect reconstruction. This sample portion has been mechanically polished with SiC grit papers followed by successive steps of 9 and 3µm diamond suspension while the final step was performed with colloidal silica suspension OP-S. This has been performed for all A, B and C samples presented in Table III.2.

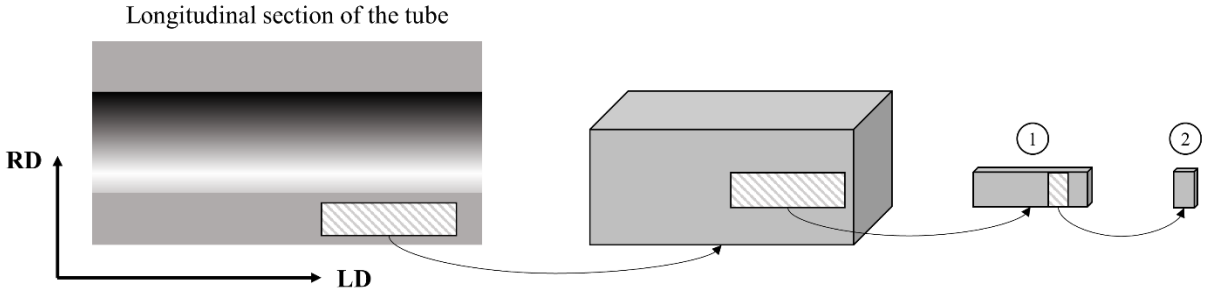

Figure III.8. Scheme of the tube section provided by Vallourec where (1) shows the sample that has been extracted to acquire the maps to perform indirect reconstruction and (2) shows the sample that has been extracted to perform in-situ heating EBSD. LD stands for the longitudinal direction and RD for the radial direction of the tube.

In a second step, the initial sample portion was further cut into smaller samples as highlighted with number 2 in Figure III.8. These samples were used for the in-situ heating EBSD experiments. We have selected samples A and B to perform the second and third austenitizations respectively. Like this, the real austenitic microstructure of A can be compared with the reconstruction of B, and the real austenitic microstructure of B can be compared with the reconstruction of C.

In-situ heating

Figure III.9 (a) and (b) show the heat treatments that have been performed to both A and B samples respectively. Knowing that the theoretical Ac1 temperature is 775°C, the temperature was initially raised from room temperature to 800°C. For both samples, it took around 300s to reach 800°C, thus a heating speed around 2.5°C/s (in "PID control" mode). An EBSD map was acquired for both samples at this temperature and the phase maps confirmed that the ferrite to austenite transformation had already begun. From this point, the temperature has been slowly increased step-wise to reach a fully austenitic microstructure. This happened when the temperature indicated by the thermocouple was 840°C for sample A and 810°C for sample B. Considering that the theoretical Ac3 is 850°C, we can estimate a ΔT of a few tens of °C between the temperature measured by the thermocouple and the real temperature of the sample. The fact that both samples reached a fully austenitic microstructures at different temperatures indicates that from one experiment to the other, the surface contact or the distance from the sample to the thermocouple may change and affect the measurement of the actual temperature of the sample. Once a fully austenitic microstructure was reached, the temperature was further increased by 30°C to simulate the heat treatments presented in Table III.2, where the T_{aus} was obtained as Ac3+30°C.

T_{aus} was 870°C for sample A and 840°C for sample B. To reach T_{aus} from room temperature, it took around 18min for sample A and 13min for sample B.

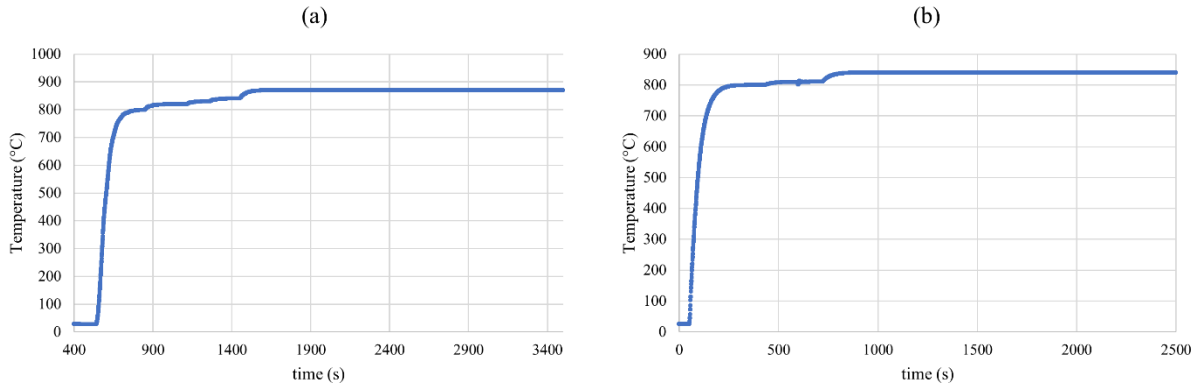

Figure III.9. Heating curved applied to samples (a) A and (b) B.

EBSD acquisition and maps processing

The acquisition conditions that are common to all the EBSD maps acquired and presented in III.4.1 are shown in Table III.3. The remaining conditions such as step size, maps size, indexing rate, acquisition time per map and acquisition speed are presented for each map along the section.

Table III.3. Acquisition conditions of the EBSD maps presented in section III.4.1 (Oxford Symmetry Camera + AZtec software)

Acquisition conditions	
Camera resolution (pixels)	156×128
Accelerating voltage [kV]	20
Exposure time [ms]	1
Pattern averaging	-
Indexing method	Optimized TKD

All maps have been corrected with conventional data cleaning procedures such as wild spikes correction and nearest neighbor orientation assignment. For all the austenitic maps acquired at high temperature, grain detection has been performed at 5° and twin boundaries (60° about <111>) have not been considered as grain fraction. To calculate grain size statistics, we have calculated the equivalent diameter of the grains by weighting the grain sizes by the grain surface. All indirect reconstructions presented along this Chapter have been performed with Merengue2 [7].

III.4.1.3 Results

Determination of the austenitic grain size evolution by indirect reconstruction

EBSD maps have been acquired over all three samples A, B and C on two different sites in order to measure a better statistic of the microstructure. These maps have been acquired with an acquisition step size of 0.1µm and a map size of 170×130µm. The corresponding parent austenite microstructure for each of the acquired maps obtained by indirect reconstruction can be observed in Figure III.10. Each

reconstructed map is presented with the average value of the equivalent diameter of the measured grains and Figure III.11 shows the statistics of the grain size distribution.

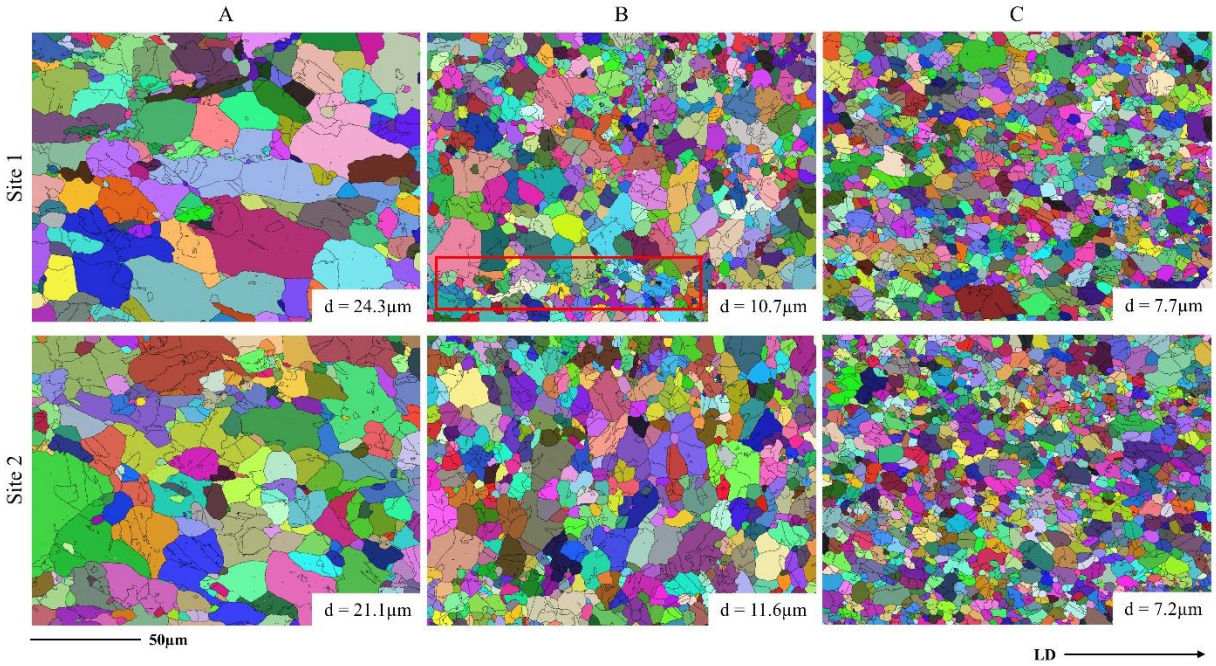

Figure III.10. Indirect parent microstructure reconstruction of the three samples A, B and C in two different acquisition sites. The austenitic grains are colored in random colors. The scale bar is the same for all maps and LD indicates the direction along which the sample has been extracted related to Figure III.8. Black lines indicate austenite grain boundaries higher than 15° (inside the random colored grains, these lines correspond to twin boundaries).

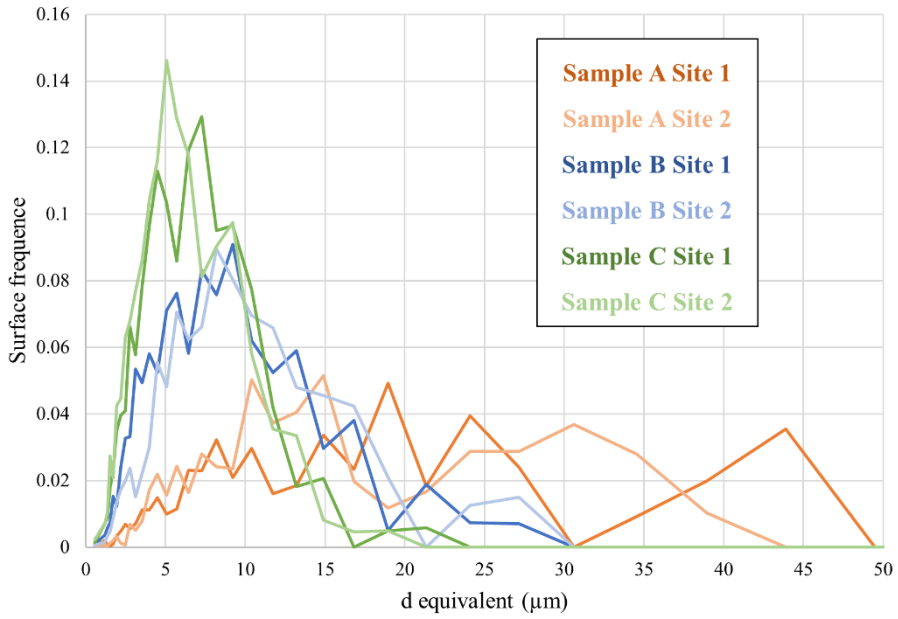

Figure III.11. Statistics of the grain size distribution (equivalent diameter) for the EBSD maps acquired over samples A, B and C on sites 1 and 2.

Indirect reconstruction confirms that the multiplication of Q/Ts drives to an austenitic grain size refinement. In average, the equivalent diameter reduces ~15µm after two successive Q/Ts. Additionally, it evidences the presence of grain size heterogeneities as elongated bands following the LD direction, highlighted by the red box in Figure III.10 for sample B in Site 1 (probably induced by local chemical

heterogeneities). These grain size heterogeneities seem to slightly disappear with the multiplication of Q/Ts, as the grain size looks more homogeneous in Figure III.10 for sample C in Site 1.

Although the indirect reconstruction provides interesting results it may encounter some difficulties that can affect the measurement of the grain size. If the initial martensitic microstructure presents regions with very small prior austenite grains, it is possible that the reconstruction algorithm does not find enough inherited variants to reconstruct a unique orientation of the parent grain. Additionally, in order to analyze the heterogeneities distribution, large maps must be acquired. As the maps are martensitic, it is necessary to optimize the acquisition to obtain high quality data and such acquisition may take long time. Thus, our point was to evaluate the possibilities offered by in-situ experiment at high temperature where large and high-quality maps could be obtained with fast speeds.

Determination of the austenitic grain size evolution by in-situ heating EBSD

Following the heating curves presented in Figure III.9, EBSD maps have been acquired for both samples A and B at T_{aus} (sample A 870°C and sample B 840°C) at the beginning of the plateau (t_0) and after fifteen minutes (t_{15}). Figure III.12 (a) and (d) show the acquired EBSD maps at t_0, while (b) and (e) show the acquired EBSD maps at t_{15} for samples A and B respectively. Each map is presented with the average value of the equivalent diameter of the measured grains. These maps have been acquired with a step size of 0.3µm, a map size of 180×130µm and a speed of 970Hz resulting in a total acquisition time per map of 4min. The average indexing rate of the maps is above 91%. Figure III.12 (c) and (f) present the statistic of the grain size distribution at both t_0 and t_{15} for samples A and B respectively.

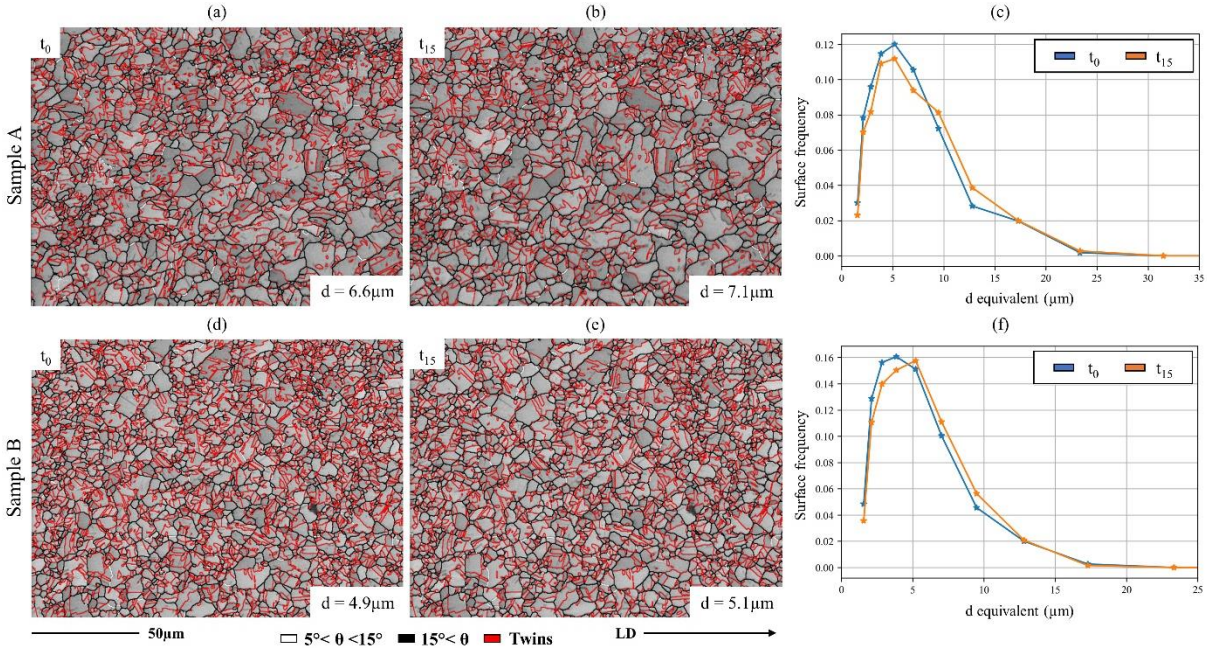

Figure III.12. (a) and (d) acquired EBSD maps at t_0 (plateau start at T_{aus}) and (b) and (e) acquired EBSD maps at t_{15} (after 15min in the plateau at T_{aus}) for samples A and B respectively. The grain boundaries disoriented between 5° and 15° are plotted in white, boundaries disoriented higher than 15° in black and twin boundaries in red. (c) and (f) statistic of the grain size distribution (equivalent diameter) at t_0 and t_{15} for samples A and B respectively. The scale bar is the same for all maps and LD indicates the direction along which the sample has been extracted related to Figure III.8

For both t_0 and t_{15} maps, the average grain size of sample B is smaller than that of sample A by a difference of ~2µm. This confirms the hypothesis that successive Q/Ts have a refinement effect on the parent austenite microstructure. It can be also noted that there exists a very slight grain growth at t_{15} for both samples, an increment of 0.5µm for sample A and 0.2µm for sample B. Although some grain size heterogeneities can be observed in the maps, the magnification (x650) seems to be too high to correctly determine if there is a difference in this respect between both samples.

To look at the heterogeneities, an EBSD map with a larger field of view (x400) has been acquired on each sample at t_{20}, and they are presented in Figure III.13 (a) and (b) for sample A and B respectively. Each map is presented with the average value of the equivalent diameter of the measured grains. These maps have been acquired with a step size of 0.5µm, a map size of 290×210µm and a speed of 970Hz resulting in a total acquisition time per map of 4min. The average indexing rate of the maps is above 88%. Figure III.13 (c) shows the statistical distribution of the grain size for samples A and B. The grain refinement from sample A to sample B is confirmed, showing a difference of 1.5µm. However, the presence of heterogeneities is not reduced by repeated austempering cylces, as we can see a strong presence of heterogeneities in sample B in a perpendicular direction to LD. This direction of the heterogeneities was not expected since sample A shows them mainly along the LD direction. It is possible that at the moment of extracting the samples from the initial sample block provided by Vallourec we inverted the directions.

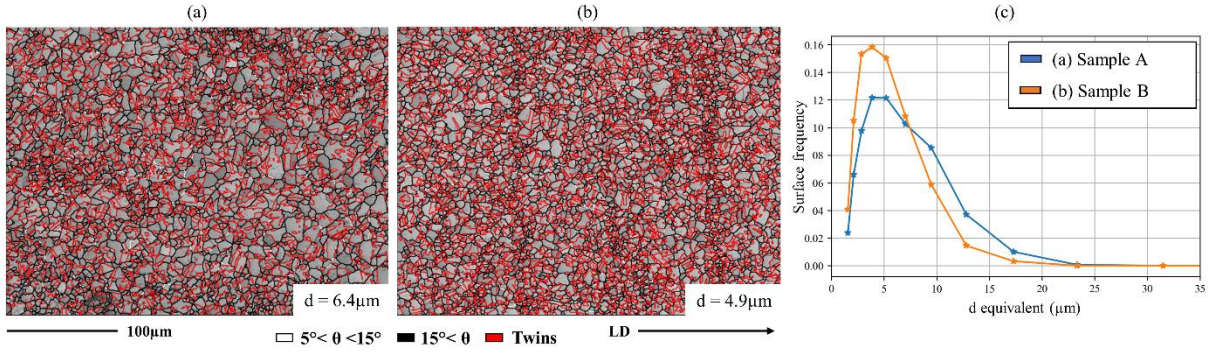

Figure III.13. (a) and (d) acquired EBSD maps at t_{20} (20min in the plateau at T_{aus}). The grain boundaries between 5° and 15° are plotted in white, boundaries higher than 15° in black and twin boundaries in red. (c) Statistic of the grain size distribution (equivalent diameter) for samples A and B. The scale bar is the same for all maps and LD indicates the direction along which the sample has been extracted related to Figure III.8.

III.4.1.4 Discussion

It has been shown that the results obtained by reconstruction are comparable to those obtained with in-situ heating EBSD as both presented an austenitic grain size reduction with the multiplication of Q/Ts. However, the heterogeneity reduction that was evidenced during reconstruction with the Q/Ts multiplication has not been observed during in-situ heating, where we observed a clear difference between large and small grains. It may be possible that, as mentioned above, if the initial martensitic microstructure presents regions with very small prior austenite grains, the reconstruction algorithm does not find enough inherited variants to reconstruct a unique orientation of the parent grain. This produces

that the smaller austenite grains cannot be reconstructed. This may be one of the reasons why the grain size found for in-situ experiments was smaller than that of the indirect reconstruction. In addition, as larger areas can be scanned during in-situ experiments, the statistics of the grain size may also be affected when compared to indirect reconstruction results.

In order to assess how well an indirect reconstruction tool such as Merengue2 [7] performs, a region of interest in sample B was selected in the austenitic field at 900°C and an EBSD map was acquired. Another EBSD map at the same region was acquired at room temperature after cooling in order to be reconstructed and compared with the real microstructure. It must be noted that for this alloy, the maximum cooling speed of our heating module allows to observe the transformation into martensite without showing any previous ferritic or bainitic transformation. We have identified the Ms temperature when the thermocouple indicated 420°C and the cooling speed was ~3°C/s.

Figure III.14 (a) shows the EBSD map acquired at room temperature, Figure III.14 (b) presents the IPF-Z map acquired in the austenitic field and Figure III.14 (c) displays the IPF-Z map of the indirect reconstruction of the austenite microstructure. It can be seen a very good agreement between both maps in terms of orientations, grains size and shape. In certain grains, as those indicated by the stars in Figure III.14 (b) and (c), the reconstruction did not find certain twins that can be observed in the real microstructure. This is a well-known limitation of reconstruction. Although this little discrepancy, the reconstruction provides realistic results that can be trusted.

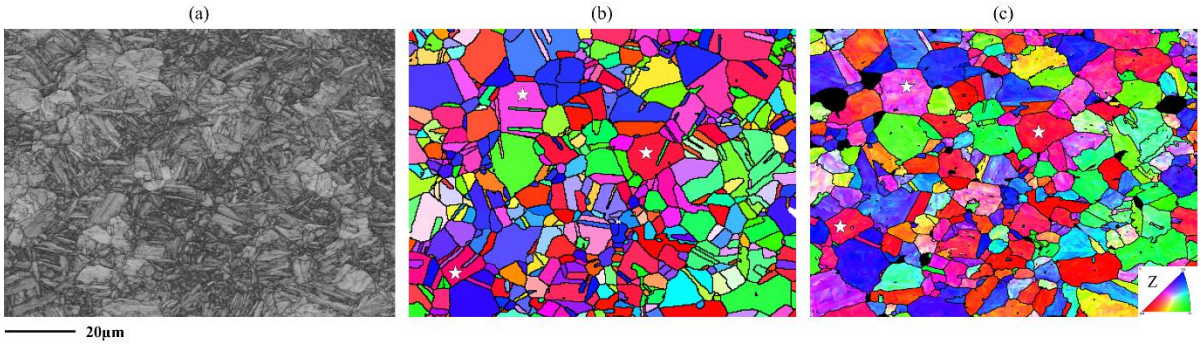

Figure III.14. (a) BC map of the martensitic microstructure at room temperature after in-situ heating and cooling at 3°C/s, (b) IPF-Z map of the austenitic microstructure acquired during plateau at 900°C and (c) IPF-Z map of the indirect reconstruction. The scale bar is the same for all maps.

III.4.2 Study 2: Austenite grain size evolution for carbonitrided steels. Effect of nitrides.

III.4.2.1 Material and context

The present study completes the research work conducted during the post-doc of Dr. Madhumanti Mandal in collaboration with our laboratory, the Institut Jean Lamour (IJL) and the Institut de Recherche Technologique Matériaux, Métallurgie, Procédés (IRT-M2P). The investigated material is a 23MnCrMo5 low-alloy steel with the composition detailed in Table III.4. This steel is used as a base composition to perform case-hardening treatments such as carbonitriding for gear applications.

Table III.4. Nominal composition [weight %] and transformation temperatures [°C] of the concerned material.

Nominal composition						Transformation temperatures		
C	Mn	Cr	Si	Ni	Mo, Al and V	Ac1	Ac3	Ms
0.246	1.21	1.31	0.237	0.184	<0.1	730	810	370

The project conducted by Dr. Madhumanti Mandal aims to improve thermochemical carbonitriding treatments. The objective is to study the effect of carbon and nitrogen enrichment (0.4 - 0.7 wt.% C, 0.2 - 0.4 wt.% N) in the austenite phase during austenitic decomposition upon cooling in low alloy steels. Previous studies on the 23MnCrMo5 steel [116]–[118] showed two main effects of N: (1) the decomposition kinetics of austenite are greatly accelerated despite the austenite stabilizing nature of N, (2) the resulting microstructures are very complex, with a grain refinement of the ferrite and bainite matrix, the presence of various nitrides (mainly CrN) and cementite. These microstructures are associated with higher hardness. The presented conclusions were obtained on enriched samples followed by a re-austenitization in order to be able to analyze by in-situ HR-XRD the enriched austenite transformation kinetics and by SEM/EBSD as well as TEM the resulting microstructure at room temperature.

A part of the post-doctoral work of Dr. Madhumanti Mandal was focused on the role of CrN nitrides (found both at the austenite grain boundaries and inside the grains) in the faster austenite decomposition and the refinement of the microstructure. For this, lamellar-shaped dilatometry samples (30mm length and 1mm thickness) with homogeneous compositions in carbon and nitrogen were elaborated at IJL. Enrichments were done in the austenite domain of stability at 900°C for durations up to 6 h, at ambient pressure, in a furnace with the thermobalance developed at IJL. Along with the base steel (0.246wt.%C), three compositions were considered: carburized (0.4-0.5 wt.%C), nitrided (0.1-0.3 wt.%C, 0.2-0.5 wt.%N) and carbonitrided (0.4-0.5 wt.%C, 0.2-0.5 wt.%N). After enrichment, the samples were oil quenched and re-austenitized at 900°C for 10min followed by water quenching to room temperature (Figure III.15). The heating speed to reach the re-austenitization plateau was 10°C/s.

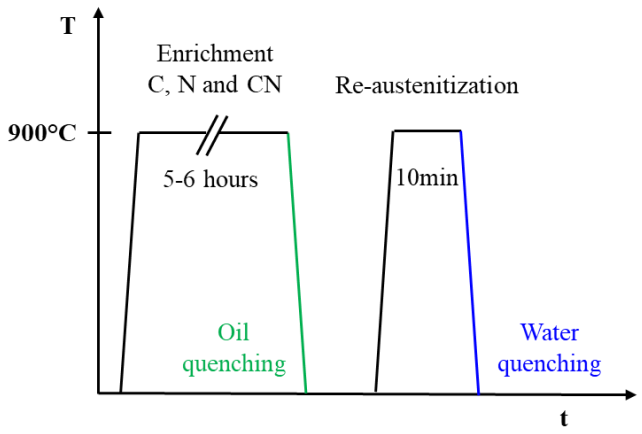

Figure III.15. Enrichment treatments at 900°C (carburizing, nitriding and carbonitriding) for 5-6h, followed by oil quenching, re-austenitization at 900°C for 10min and water quenching.

EBSD maps have been acquired after oil-quenching and after re-austenitization for all three enrichments. The corresponding parent austenite microstructure for each of the acquired maps obtained by indirect reconstruction is presented in Figure III.16 [119]. It has been shown that the enrichment treatment has no significant effect on the austenite grain size, as the grain size distributions are comparable for all enrichments (Figure III.16 (a), (b) and (c)). However, after re-austenitization it has been shown that both the CN and N samples showed a clear refinement of the austenite grains while the C sample remained unchanged (Figure III.16 (d), (e) and (f)). This refinement has been ascribed to the nitrides (CrN, $MnSiN_2$), which may hinder the grain boundaries motion and provide nucleation sites.

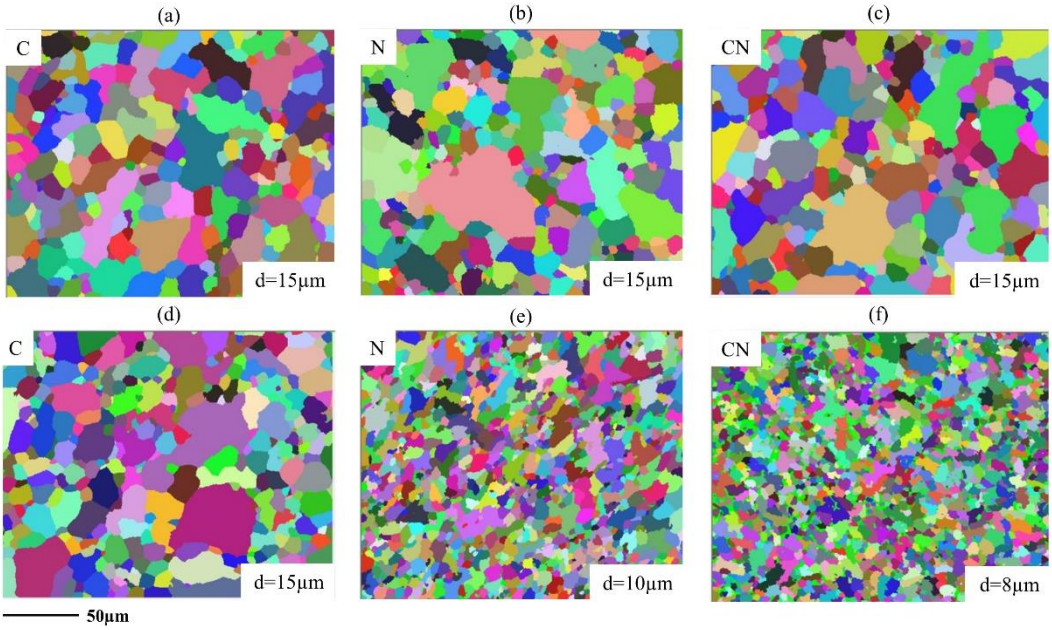

*Figure III.16. Top row presents the indirect reconstruction of the (a) C, (b) N and (c) CN samples during enrichment while bottom row shows the indirect reconstruction of the (d) C, (e) N and (f) CN samples during re-*austenitization [119]. *The scale bar is the same for all maps. Random colored prior austenite grains (including twins)*

III.4.2.2 Experimental procedure

Our strategy is to evaluate the validity of the presented findings in two steps. First, we want to study the austenite parent phase refinement by performing in-situ heating to simulate the re-austenitization after enrichment and observe the real parent austenite microstructure in order to compare it with the one obtained by indirect reconstruction. Second, we want to follow the transformation during heating in a region where CrN nitrides can be clearly detected in order to assess their role in the refinement of the austenitic microstructure. To perform both tasks, we have selected to work only with the carbonitrided sample (CN).

Sample preparation

CN samples have been cut with the same dimensions (6x4x0.5mm) and have been metallographically prepared as has been detailed in III.4.1.2 *Sample preparation*.

In-situ heating

Figure III.17 shows the heating curves that have been applied on two CN samples in order to study (a) the austenite parent phase refinement and (b) the influence of the CrN nitrides that have precipitated during enrichment in the austenite precipitation during heating.

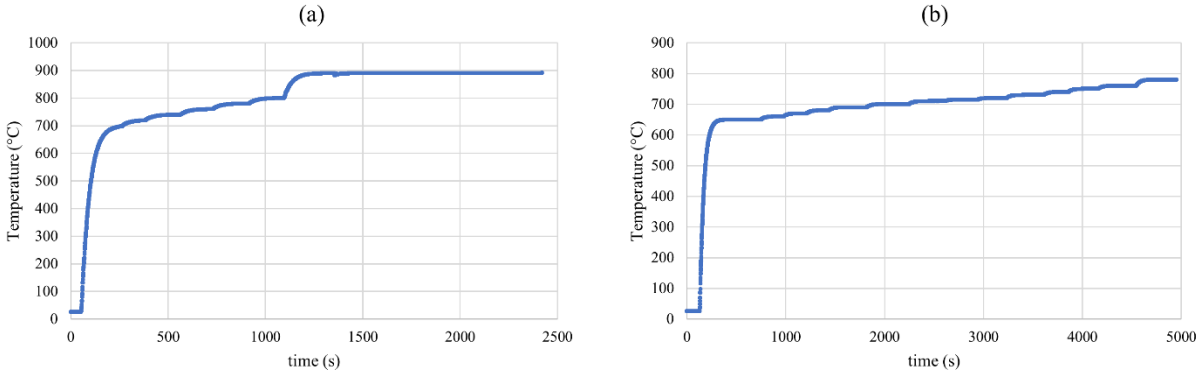

Figure III.17. Heating cycles performed to analyze (a) the austenite refinement and (b) the effect of the CrN on the austenite precipitation during heating.

In the heating curve of Figure III.17 (a), the temperature was first increased from room temperature to 720°C. It took around 200s to reach 700°C, thus a heating speed around 3.3°C/s. An EBSD map confirmed that at 720°C the austenitic precipitation had already begun and a fully austenitic microstructure was achieved when the thermocouple indicated 800°C. As the theoretical Ac3 is 810°C and the austenitization was performed at 900°C, we have performed the 10min plateau at 890°C since our experimental Ac3 measured by the thermocouple was 10°C lower than the theoretical one.

Instead, in the heating curve of Figure III.17 (b) we wanted to capture the first austenite nucleation and thus the temperature was raised from room temperature to 650°C. It took around 260s to reach 650°C, thus a heating speed around 2.4°C/s. Then, the temperature was slowly increased by steps of 10°C until we found the experimental Ac1 when the thermocouple indicated 690°C (40°C lower than the theoretical one). From this point, we continued increasing the temperature by steps of 10°C until 780°C where the microstructure was fully austenitic. After each 10°C increment, we performed a plateau of 3 to 10min in order to acquire EBSD maps and follow the austenitic nucleation during heating. From 690°C to 780°C it took around 50min, thus a heating speed around 0.8°C/min. It is worth to mention that the heating speed in the transformation temperature range is of importance as it influence the transformation mechanism.

EBSD acquisition and maps post-processing

In this particular section, only two conditions were common to every acquired EBSD map: 20kV accelerating voltage and Optimized TKD as indexing method. The remaining acquisition conditions are detailed for each map in particular along the section.

EBSD maps post-processing has been performed exactly as presented in III.4.1.2 *EBSD acquisition and maps post-processing.*

III.4.2.3 Results

Parent austenite grain refinement analysis

Figure III.18 presents the BC map acquired at room temperature after being enriched at 900°C and oil quenched for the sample that has been later re-austenized with the heat treatment of Figure III.17 (a). This map has been acquired with a camera resolution of 622×512 pixels, an exposure time of 2ms, pattern averaging equals to two, step size of 0.2µm, a map size of 180×120µm and a speed of 246Hz resulting in a total acquisition time per map of 36min. The indexing rate of the map is 73.5%. The observed microstructure is fully martensitic and presents the mentioned CrN (green) and $MnSiN_2$ (yellow) nitrides precipitated during enrichment; blue pixels represent retained austenite. The minor phases are particularly complicated to index in this microstructure since austenite and CrN belong to FCC, and CrN nitrides are usually indexed as austenite. In addition to conventional map cleaning, this map has been corrected using the algorithm explained in II.4.5, to identify those clusters of pixels that have been indexed as austenite but that do not share a KS-OR with the neighboring martensite. The black regions (as that encircled in Figure III.18) correspond to non-indexed pixels resulting from a shadowing effect of the nitrides emerging from the sample surface after sample polishing (amplified by the 70°tilt in EBSD condition).

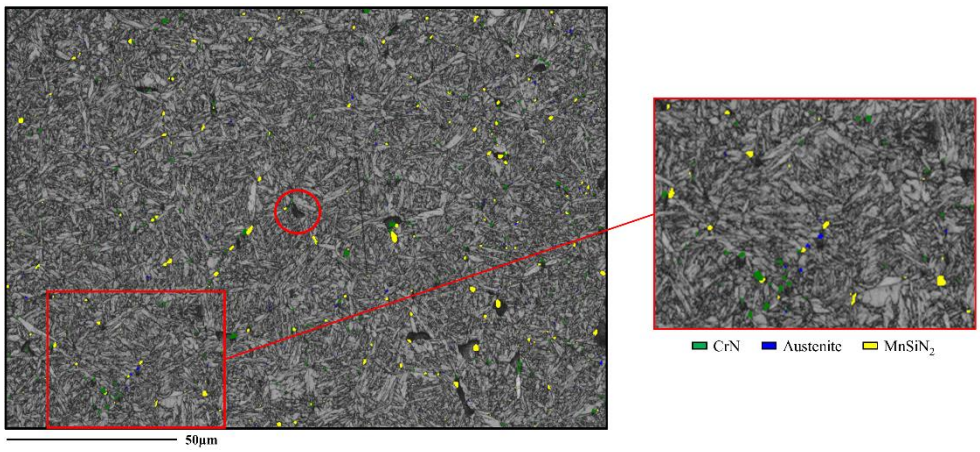

Figure III.18. BC map of the martensitic microstructure after being enriched and oil quenched.

Figure III.19 (a) shows the IPF-Z map of the indirect reconstruction of the map shown in Figure III.18, what simulates the microstructure during enrichment. Figure III.19 (b) presents the IPF-Z map of the austenitic microstructure after 10min in the plateau at 890°C on the same region where the map at room temperature has been acquired. This map has been acquired with a camera resolution of 156×128 pixels, an exposure time of 0.5ms, no pattern averaging, step size of 0.3µm, a map size of 170×120µm and a speed of 1715Hz resulting in a total acquisition time per map of 2min. The indexing rate is 86.8%. Each

map is presented with the average value of the equivalent diameter of the measured grains. Figure III.19 (c) shows statistic of the grain size distribution.

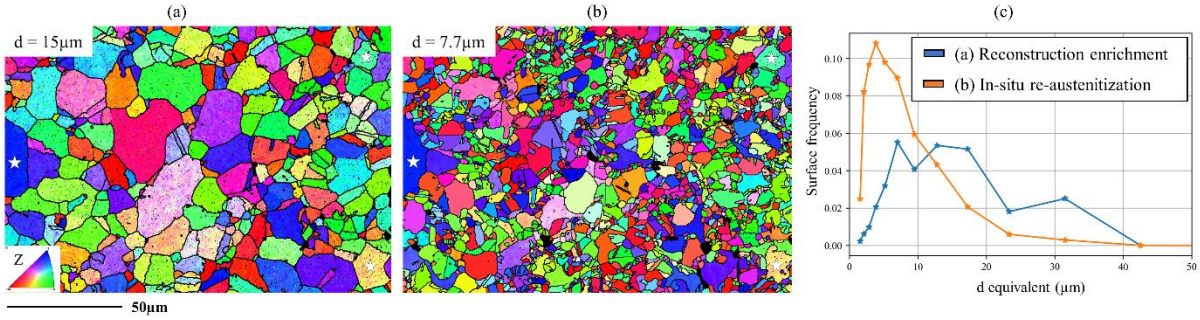

Figure III.19. (a) IPF-Z map of the indirect reconstruction of the map shown in Figure III.18, (b) IPF-Z map of the austenitic microstructure after 10 minutes in the plateau at 890°C and (c) statistics of the grain size distribution (equivalent diameter) of austenitic microstructures in (a) and (b). The scale bar is the same for all maps.

Comparing both Figure III.19 (a) and (b) we can clearly observe a microstructure refinement, where grain size reduction to the half has been evidenced. The obtained equivalent diameters are in the order of those found in previous studies presented in [119]. However, looking at Figure III.19 (b) and its corresponding curve in Figure III.19 (c) we can observe a clear heterogeneous grain size distribution showing both small and large grains. This heterogeneity has not been evidenced before and could be due to the difference in the heating curve to reach the re-austenitization plateau. While we have heat up with a speed of 3.3°C/s up to 700°C and then we performed step-wise heating, in [119] the heating speed was 10°C/s directly to austenitization.

Another important point to consider from Figure III.19 (a) and (b) is related to the nucleation of new austenitic grains with the same orientation of their PAG. Although both microstructures are different, there are certain grains in Figure III.19 (b) whose orientation is exactly the same as the one shown by the old austenite grain in the same position in Figure III.19 (a). Three examples are indicated by stars, but many more can be found.

Influence of the CrN nitrides on the nucleation of austenite

In this section we want to assess what is the role of the CrN nitrides in the austenite grain refinement and evaluate where does the more heterogeneous austenite microstructure after enrichment and re-austenitization comes from. To do this, we have worked with a second CN sample that has undergone the re-austenitization presented in Figure III.17 (b). Before that, a large EBSD map has been acquired and we selected a small region of interest where certain CrN nitrides have been indexed. On this region, several EBSD maps have been acquired once heating reached 650°C, and the first austenitic nucleation was evidenced when the thermocouple indicated 690°C. From that point on, we began to acquire EBSD maps as we raised the temperature stepwise in order to measure the austenitic evolution during heating.

Figure III.20 presents the EBSD maps that have been acquired at 700°C, 720°C and 740°C. These maps have been acquired with a camera resolution of 156×128 pixels, an exposure time of 1ms, no pattern

averaging, step size of 0.05µm, a map size of 24×19.3µm and a speed of 970Hz resulting in a total acquisition time per map of 3min. The average indexing rate for the three maps is above 70%, being higher for the maps at higher temperature as there is an increasing presence of austenite.

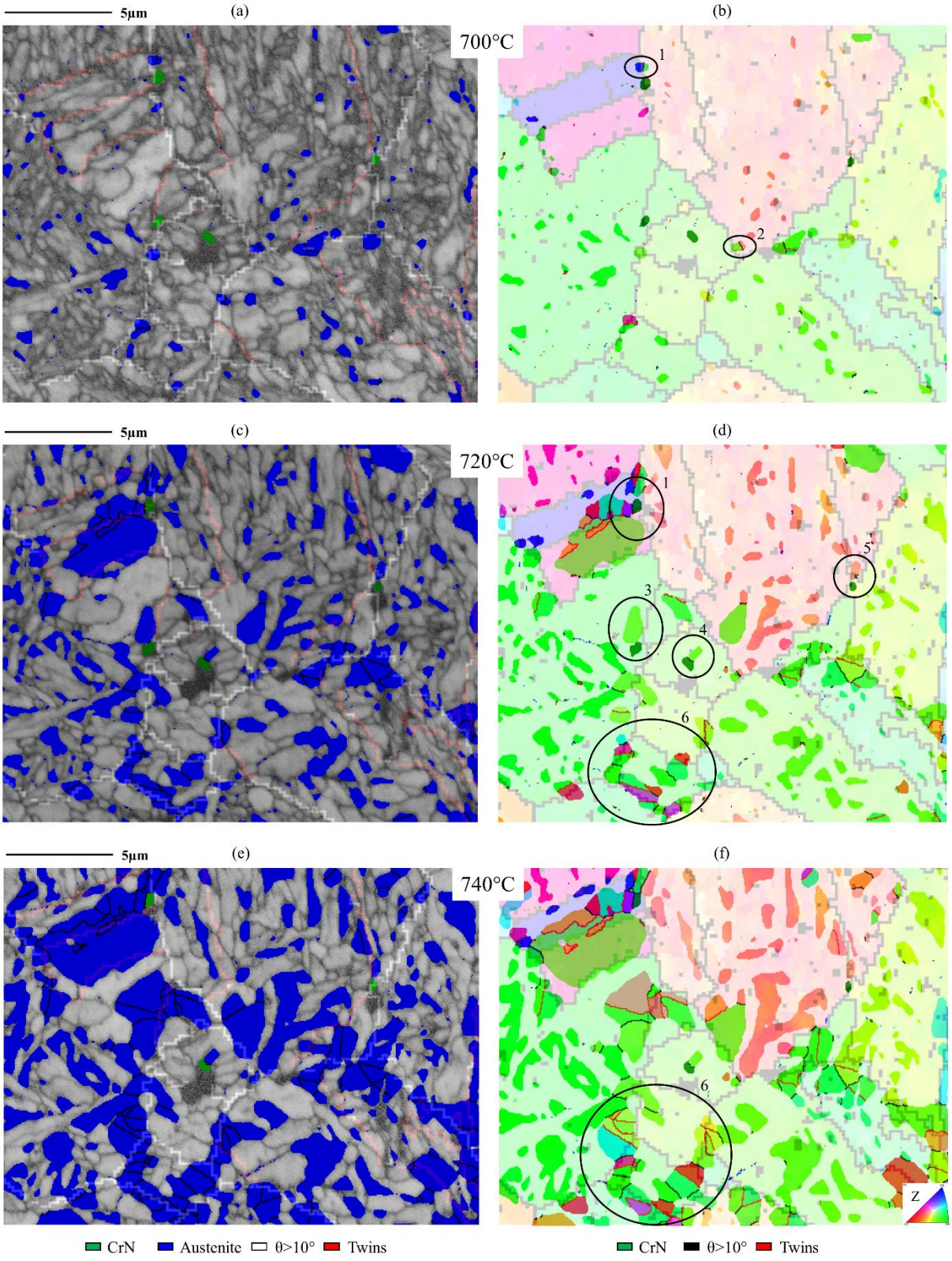

Figure III.20. EBSD maps acquired during step-wise heating at (a) and (b) 700°C, (c) and (d) 720°C and (e) and (f) 740°C. On the left column it is presented the BC map with the nucleating and growing austenite in blue and CrN nitrides in green. Overlaid on top we present the PAGBs obtained by indirect parent phase reconstruction. The white boundaries are higher

than 10° and those in red represent the twin boundaries. On the right column we present the IPF-Z map of the nucleating and growing austenitic grains and overlaid on top of it, the IPF-Z map obtained by indirect reconstruction. The black boundaries on the nucleating and growing austenite are higher than 10° and those in red represent the twin boundaries.

The left column of Figure III.20 presents the BC map with the austenite grains nucleating and growing in blue and the CrN nitrides in green. Overlaid on top of the BC map, we present the PAGBs obtained by indirect parent phase reconstruction. The white boundaries are higher than 10° and those in red represent the twin boundaries. On the right column of Figure III.20, we present the IPF-Z map of the nucleating and growing austenitic grains and overlaid on top of it, the IPF-Z map obtained by indirect reconstruction. It must be noted that overlaying is not perfect and certain boundaries may not exactly coincide.

In Figure III.20 at 700°C we can observe the first austenitic grains appearing in the martensitic matrix. The main part nucleated inside the PAGs and some of them at the PAGBs. Looking at Figure III.20 (b), it is clear that those grains that nucleate inside the PAGs, share the same orientation of the PAG. Instead, those grains nucleating at the PAGBs, do not show such a clear behavior. There are some cases, as the one highlighted with number 1 in Figure III.20 (b), where the grain at the left side grows with the same orientation as the PAG but the one growing to the right does it with a different one. In other cases, (number 2) both grains grow with the same orientation as their PAGs. At this stage of the transformation, only one grain nucleated close to one of the CrNs and is the one highlighted with number 1 in Figure III.20 (b)).

At 720°C, Figure III.20 shows that the nucleated grains keep growing and some new grains appear. At this point, all the CrN nitrides experienced a close austenite nucleation and growth. The one indicated with number 1 in Figure III.20 (d) presents the higher number of nucleated grains, but these look to be nucleating from the twin boundary at that position. The other CrN (highlighted with numbers 3, 4 and 5) show only one neighbor austenitic grain. Considering that at this point, the amount of austenite is already high, and the largest number of nucleation points appear inside the PAGs and some at the PAGBs, we cannot confirm a predominant role of nitrides in the nucleation of austenite. It is possible that at the magnification and step-size the map has been acquired, we did not capture all the present nitrides, thus we cannot be sure if there is a real effect or not.

From those grains nucleating at the PAGBs (number 6 in Figure III.20 (d)), we can see that they nucleate with different orientations and some of them present twin boundaries. If the temperature is further increased to 740°C, Figure III.20 (f) clearly shows that new grains nucleating at the PAGBs provide new orientations and are responsible for the grain size heterogeneity.

Finally, to have a global overview of the microstructure, Figure III.21 (a) presents the indirect reconstruction of the entire martensitic map that has been acquired at room temperature before in-situ heating and Figure III.21 (b) shows the full austenitic microstructure acquired at 780°C during in-situ

experiment. Here we can clearly see how the small grains are located at the PAGBs and many large PAGs are recovered with a roughly similar shape and identic orientation.

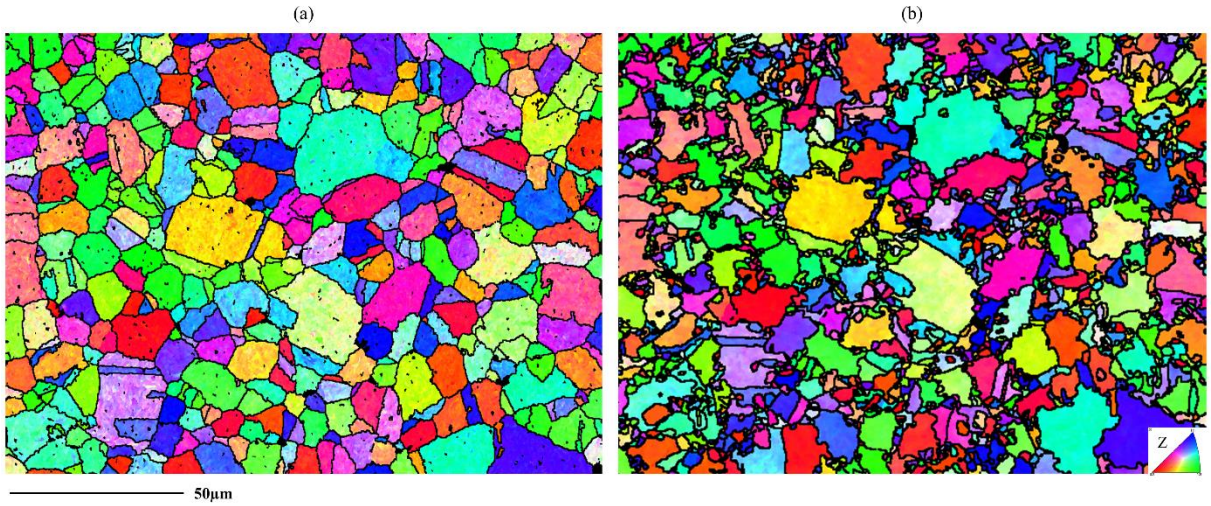

Figure III.21. (a) Indirect reconstruction of the entire martensitic map that has been acquired at room temperature before in-situ heating and Figure III.21(b) full austenitic microstructure acquired at 780°C during in-situ experiment. The scale bar is the same for both maps.

Orientation relationship during nucleation and growth

As we could follow the nucleation and growth of austenite during heating, we can confirm the existence of an OR between austenite and neighboring martensite. Figure III.22 shows the maps at (a) 700°C and (b) 720°C where the deviation from KS-OR is plotted. White interfaces indicate a deviation lower than 5° from KS, yellow between 5° and 10° and green above 10°. The main part of interphases nucleating inside the PAG in Figure III.22 (a) is white/yellow indicating that austenite nucleates with a KS-OR with respect to the neighboring martensite. On the other hand, those grains nucleating at the PAGBs show at least one green boundary that indicates that there does not exist a KS-OR (some examples encircled in Figure III.22 (a)). In Figure III.22 (b) we can see an increment of the green interfaces as the austenitic growth of those grains nucleated at the PAGB is predilected into those martensitic grains with which it does not share an OR. Inversely, the grains nucleated inside the PAG grow and always keep the KS-OR boundaries as they grow along the martensitic grain boundaries.

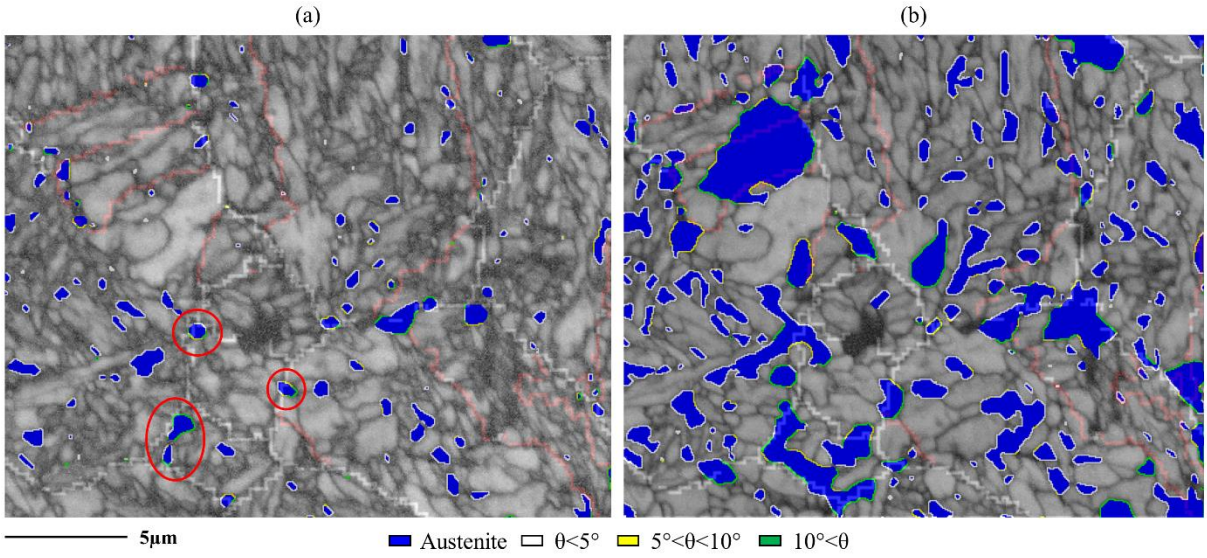

Figure III.22. BC maps with the nucleating and growing austenite in blue acquired at (a) 700°C and (b) 720°C. Overlaid on top we present the PAGBs obtained by indirect parent phase reconstruction. Deviation from KS-OR is plotted at the interfaces. The scale bar is the same for both maps.

III.4.2.4 Discussion

In-situ heating EBSD experiments have confirmed the austenitic grain size refinement on the CN sample during re-austenitization found by indirect reconstruction in [119]. Although the calculated grain size value for the reconstruction matches that obtained by in-situ measurements (d equivalent ~7µm), the austenitic microstructures were different. The in-situ measurements evidenced a clear heterogeneity on the austenitic grain size while the indirect reconstruction showed a more homogeneous microstructure. This could be due to the difference in heating speed; faster heating may favor the nucleation of new grains what results in a more homogeneous microstructure.

The indirect reconstructions have shown that the austenitic microstructure of the carburized sample during re-austenitization did not present any grain refinement. Thus, it would be very interesting to carry out the same in-situ heating measurements that we have done on the CN sample, also on the C and N samples in order to confirm the validity of the findings by indirect reconstruction.

Our heating module coupled with the CMOS Symmetry camera allowed us to measure the nucleation and growth of austenite during heating. Not a clear role could be assigned to the CrN nitrides in the refinement of the austenitic microstructure. It is possible that there exist a nanometric distribution of CrN nitrides that we could not capture with EBSD but that could play a role. This could be analyzed with in-situ TEM analysis for example. We have seen that the austenitic grains nucleate both inside the PAGs and at the PAGBs and the latter contribute to the heterogeneity of the microstructure.

III.4.3 Study 3: Mobility of γ/α interfaces during cooling

III.4.3.1 Material and context

This study is part of an on-going collaboration with Frédéric Danoix (Laboratoire GMP - University of Rouen) in the framework of the PhD thesis of Olha Nakonechna [120], that focuses on the interactions

between alloying elements (Fe-C-Mn) and the mobility of γ/α interfaces analyzed by post-mortem methods.

It has been shown using Atom Probe Tomography (APT) and Energy Dispersive X-Ray Spectroscopy (EDX) at the nanoscale on a model Fe-0.12 wt%C-2 wt%Mn steel, that there exists a strong co-segregation of both carbon and manganese at the α/γ interface during ferrite growth at 680 °C. This was determined from dilatometry samples that were first austenitized at 1100°C (for homogenization) and then quenched to 680°C, where the temperature was held for different durations. For the post-mortem APT and EDX analysis, nanometric samples were extracted at the level of the PAGBs (where there existed the α/γ interface during transformation) that have been obtained by indirect reconstruction with Merengue2 [7].

However, with post-mortem analysis, it impossible to determine the velocities of the interfaces. Therefore in-situ ferrite growth analysis could help to better study the migrating α/γ interface during ferrite growth.

III.4.3.2 Experimental procedure

Sample preparation

The samples have been cut with the same dimensions (6x4x0.5mm) and have been metallographically prepared as has been detailed in III.4.1.2 *Sample preparation*.

In-situ cooling

Considering the specifications of our heating module and the feasibility tests performed, we have adapted the in-situ heat treatment in order to conduct a feasibility study to monitor the migration of the α/γ interface. Indeed, it is impossible with our heating module to cool down as fast as it has been done in the dilatometer in [121] to reach the plateau at 680°C. Therefore, we have adopted a heat treatment as the one shown in Figure III.23. Initially, we have performed an austenitization to 900°C during 15min (not shown in Figure III.23) and then the cooling was performed in steps of 10°C, where a plateau was maintained at each temperature during around 8min in order to be able to carry out the EBSD maps acquisition. The first ferritic grain was identified when the thermocouple indicated 850°C and once we reached 820°C (almost fully ferritic microstructure), the power supply was turned off. From 860°C to 820°C it took around 45min, thus a cooling speed of around 0.9°C/min.

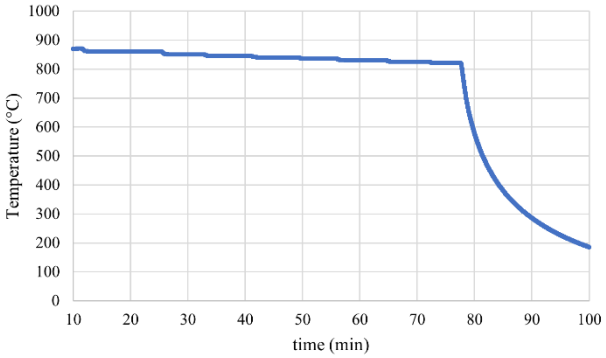

Figure III.23. Step-wise cooling curve to capture the α/γ interface migration.

EBSD acquisition and maps processing

The acquisition conditions that are common to all the EBSD maps acquired and presented in III.4.3 are shown in Table III.5. EBSD maps post-processing only concerned conventionally data cleaning.

Table III.5. Acquisition conditions of the maps presented in section III.4.3. The presented indexing rates, acquisition times per map and acquisition speeds of the maps are an average.

Acquisition conditions	Figure 22
Camera resolution (pixels)	156×128
Accelerating voltage [kV]	20
Step size [µm]	0.15
Exposure time [ms]	0.5
Pattern averaging	-
Map size [µm]	56.3×42.3
Indexing method	Optimized TKD
Indexing rate [%]	86%
Acquisition time per map [min]	1
Acquisition speed [Hz]	1738

III.4.3.3 Results and discussion

Analysis of ferrite nucleation and growth

As mentioned above, first ferrite nucleation was observed at 850°C; this temperature is very high for a ferritic transformation but this is due to the decarburization effect that has been explained in III.3.5. Figure III.24 shows the nucleation and growth of ferrite during cooling together with the deviation from KS-OR of the α/γ interfaces.

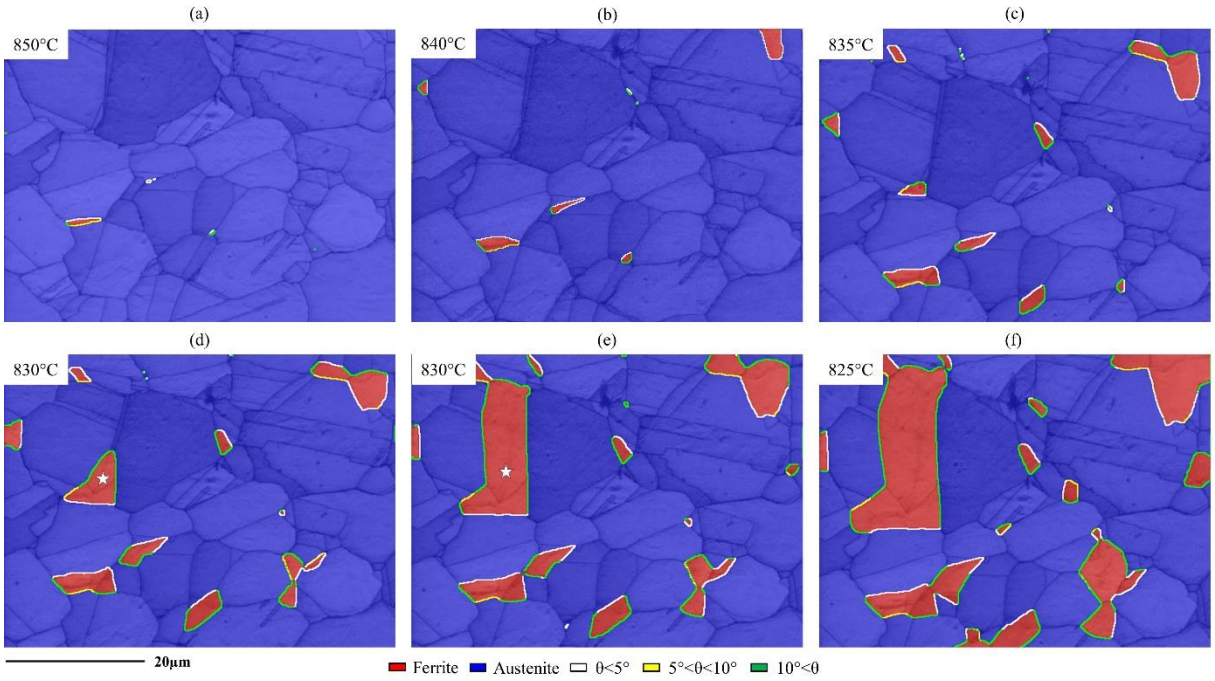

Figure III.24. Ferritic nucleation and growth during step-wise cooling. Deviation from KS-OR is plotted at the interfaces.

The first result shows that all the new nucleated grains (at any temperature) have as preferential nucleation sites triple points of the PAGs and they share a KS-OR with at least one of the neighboring PAGs. Once they nucleated, the initial growing stage is performed along the PAGBs until a new triple point is reached.

The second interesting result concerns the growth of the ferrite nucleus. The in-situ EBSD maps clearly shows that ferrite starts to grow inside one of the neighboring PAG, in particular into that with which it does not share the KS-OR. These two growing stages can also happen simultaneously, as in the example highlighted with stars in Figure III.24 (d) and (e), where the ferrite grain grows along the PAGB but also inside the neighboring PAGs with no KS-OR. Those boundaries with KS-OR have a much lower mobility and mainly remain static. This confirms the findings presented in pioneer in-situ heating EBSD studies about phase transformation in steels [91], [93], [94], [96] described in the literature review of Chapter I.

In order to combine in-situ heating experiments with the further post-mortem APT and EDX analysis to study the interactions between alloying elements (Fe-C-Mn) and the mobility of γ/α interfaces as in [121], it would be necessary to select an alloy with slower transformation kinetics and take into account the evolution of the sample surface chemistry in the interpretation of the results.

III.5 Conclusion and perspectives

A heating module adapted to perform EBSD has been purchased and successfully implemented in one of our SEMs. From the implementation details and feasibility tests, the following conclusions can be drawn:

- Concerning the module, the heating device is a resistive ceramic element with heating capacity up to 1050°C. The temperature is controlled by PID and measured with a Ni-NiCr thermocouple. We have tested a configuration where the sample is glued with a cement paste on a Mo cap placed over the heating element. The temperature was measured into the Mo cap.
- From the feasibility tests we can extract that the module has a maximum heating speed of 45°C/s (ΔT=870°C in 20s for the "Rapid Heating" mode) by accepting some overshoot and stabilization time. Heating with "PID control" mode provided an average heating speed of 3°C/s (ΔT=870°C in 5min). Maximum cooling speed attained by turning off the power supply was 3°C/s (ΔT=500°C in 3min). It must be noted that all the temperatures refer to the one measured by the thermocouple but we have evidenced a difference of some tens of °C with the actual temperature of the sample. It is also recommended to keep the sample size small with a reduced thickness to avoid an uneven distribution of the temperature.
- Concerning the microscope and EBSD acquisitions, the module is well adapted to perform EBSD experiments at high temperature. EBSD acquisition can be performed at a speed of almost 1800Hz with a high indexing rate above 85%. For a map of 111×85µm2, considering a step size was set to 0.5µm, the total acquisition time is around 20s. The best strategy to follow the transformation during heating and cooling was to slowly modify the temperature step-wise.
- Differences in the local chemistry of the sample have been found between the top surface and the material bulk and this has to be considered for the analysis of the phase transformation mechanisms. Indirect reconstruction can be performed to provide insights about the microstructure at the material bulk.

From the preliminary in-situ heating EBSD studies performed on different steels, we can extract the following conclusions:

- Study 1 confirmed that the successive austempering treatments refine the austenitic microstructure as previously shown by indirect reconstruction. In addition, in-situ analysis revealed a clear grain size heterogeneity that is not reduced by the cycling. As it was possible to capture the martensite transformation during cooling, indirect reconstructed parent austenite could be compared to the one obtained in-situ at high temperature. This confirmed that indirect reconstruction (here Merengue2 [7]) works very nicely.
- Study 2 evidenced by in-situ heating that the carbonitrided sample undergoes an austenitic grain refinement as it has been shown by indirect reconstruction. Additionally, we did not find a clear role of the CrN nitrides precipitated during carbonitriding enrichment in the refinement of the austenitic parent microstructure. However, we could determine that the nucleation of austenite during heating preferentially occurs inside the PAG with a KS-OR with the neighboring martensite and with the same orientation than the PAG. Some other austenite grains nucleated at the PAGBs with different orientations, being the origin of the grain refinement.

- Study 3 served to confirm several findings that have been already presented in the literature. During cooling, ferrite nucleation occurs preferentially in triple points. From the neighboring PAGs, at least one presents a KS-OR. Nucleated grains grow preferentially along the PAGBs and then inside the PAG with which they do not share a KS-OR.

Also, some perspectives can be drawn for each of the presented studies:

- Concerning the heating module, it would be interesting to keep testing different configurations to optimize the temperature control: clamp a second thermocouple closer to the sample in order to reduce the temperature gradient, place the sample directly on the heating element, find better PID values to optimize temperature regulation, etc.
- In study 1, it would be interesting to follow the austenitic evolution during heating in relation with the presence of chemical heterogeneities and local precipitations. This could help to better identify the nucleation sites and analyze the phase transformation mechanisms that result in the grain size refinement with strong grain size heterogeneities.
- In study 2, a perspective would be also to confirm if the carburized and nitrided samples also undergo an austenitic grain refinement during in-situ re-austenitization as the carbonitrided sample. Additionally, to assess the role of nanometric CrN in the austenitic grain refinement, in-situ TEM could be carried out.
- In study 3, it would be necessary to find an alloy with slower kinetics in order to follow the α/γ interface migration in desired conditions.

.

Chapter IV: **Literature review about artificial intelligence**

IV.1 Introduction

The term Artificial Intelligence (AI) was introduced as an academic discipline in 1956. At that time, the founders predicted that a machine would be intelligent as a human in no more than 20 years, generating high expectations. However, it was not until the 1990s that the field of AI started to be accepted to solve real life problems thanks to the increasing computer power and the available amount of data. From that moment on, AI has started to be applied in a large number of fields such as self-driving cars, medical diagnosis, speech recognition, among others.

In this respect, the field of materials science has not been the exception, where a vast number of studies has been published [122], [123]. The possibility of using AI to discover new materials, predict their properties or optimize their performance has highly attracted the attention of materials science researchers that started to invest in that direction. For instance, some studies have been dedicated to the prediction of fatigue crack growth [124], fatigue strength [125], fatigue failure initiation [126], damage formation [127], stress hot spot detection [128], detection and classification of defects [129], [130], microstructural design [131], among others.

One important application of AI in materials science is the phase detection and classification, necessary to carry out a complete microstructural characterization. Along this chapter we present the state-of-the art approaches dedicated to the microstructural characterization of steels using AI algorithms.

IV.2 Theoretical background about Artificial Intelligence

AI can be briefly defined as a science dedicated to simulate the cognitive capacities of the human brain in order to make predictions or take decisions with as little human intervention as possible. AI includes two main concepts such as Machine Learning (ML) and Deep Learning (DL) that will be described and detailed in the following sections.

IV.2.1 Machine Learning

ML is a subset of AI, that is basically dedicated to provide the ability to a computer program to perform a task from a provided dataset and improve with experience without being explicitly programmed to do so. ML uses algorithms, which are a set of statistical techniques used to learn patterns from the provided dataset and generates a model by training one of these algorithms.

First thing to do when trying to implement a ML approach is to clearly define the objective of the problem to solve i.e. answer the question what are we trying to predict? This will help us to better understand the kind of problem we are facing, such as classification, regression, clustering, segmentation, among others.

One of the most important steps to train a successful ML model is to prepare the dataset that will be used to make the model learn. This requires an exploratory analysis of the available data in order to

understand the patterns and trends that could be extracted to facilitate the learning stage. Here we define which of the features (or their combinations) are meaningful in order to be fed to the selected ML algorithm. From the defined features, we expect to find different values for the different classes we want to classify. This stage is called feature engineering and it is one of the most tedious and labor-intensive tasks when training a ML model.

The next step is to select the type of ML algorithm we are going to use to build our ML model based on the particular problem we are facing. Random Forests (RF) [132], Support Vector Machines (SVMs) [133], *k*-means clustering [134], are some famous algorithms that are often used in the literature.

The mentioned algorithms are fed with a dataset that contains, for each instance to classify, a particular value for each of the engineered features. This dataset is called training set, i.e. the data that our model uses to learn the specific task we are trying to achieve. In order to obtain a robust model, the entire dataset is usually split in training and validation sets with a standard 80-20 ratio. The validation set serves to evaluate the performance of the model on unseen data during the training process. Training is usually stopped when the performance on the validation dataset reach a steady state. Later on, once the model has been trained, its performance can be also evaluated on new testing data. The values of the features obtained for the testing data should not differ too much from those that the model learnt from the training set in order to obtain the best possible results.

Depending on the way our model learns, ML can be classified in two main types: supervised and unsupervised learning. Supervised learning is a technique where we teach the machine by providing the dataset together with its ground truth labeling. Inversely, unsupervised learning is the training of a machine that allows the algorithm to solve the problem without any guidance i.e. no labeled dataset is needed. Therefore, the machine has to understand the patterns and discover the output on its own by forming clusters based on the similarity of the features. As one can imagine, the supervision helps the machine to learn quicker and better as we guide it to the correct solution. However, labeling an entire dataset can sometimes demand huge amounts of time and effort, and this is why unsupervised approaches gain notoriety.

IV.2.2 Deep Learning

Deep Learning (DL) [135] can be basically defined as a subset of ML that uses Artificial Neural Networks (ANNs) to solve a complex problem. The main difference between ML and DL resides in the feature engineering step, where DL models are capable to extract the most meaningful features and patterns from the provided dataset by themselves, avoiding the need of the exploratory data step. Although this is a huge advantage, it must also be remarked that the features extracted by the ANNs are not always easy to interpret and sometimes lack of physical meaning. Thus, DL models may provide good results but we are not always sure about what they have focused on for learning.

DL is basically inspired in the human brain and how the neurons work. The fundamental structure of an ANN is a single neuron called perceptron in DL terms, whose main task is to receive an input (or a series of inputs), process it by performing some kind of calculation and provide an output. Once several neurons get connected to each other a neural network is formed as shown in Figure IV.1. This kind of neural network architecture is usually called fully connected neural network or multi-layer perceptron (MLP). It is composed by several layers of neurons where the first one is the input layer where we provide the data and the last one is the output layer that outputs a prediction from the input data with a certain associated probability. In between, we can find the so-called hidden layers, which perform the calculations required by our network to provide a prediction. The number of hidden layers and neurons per layer depends on the complexity of the problem to be solved; the deepest the architecture and the highest the number of neurons, the more complex features will be extracted from the input data.

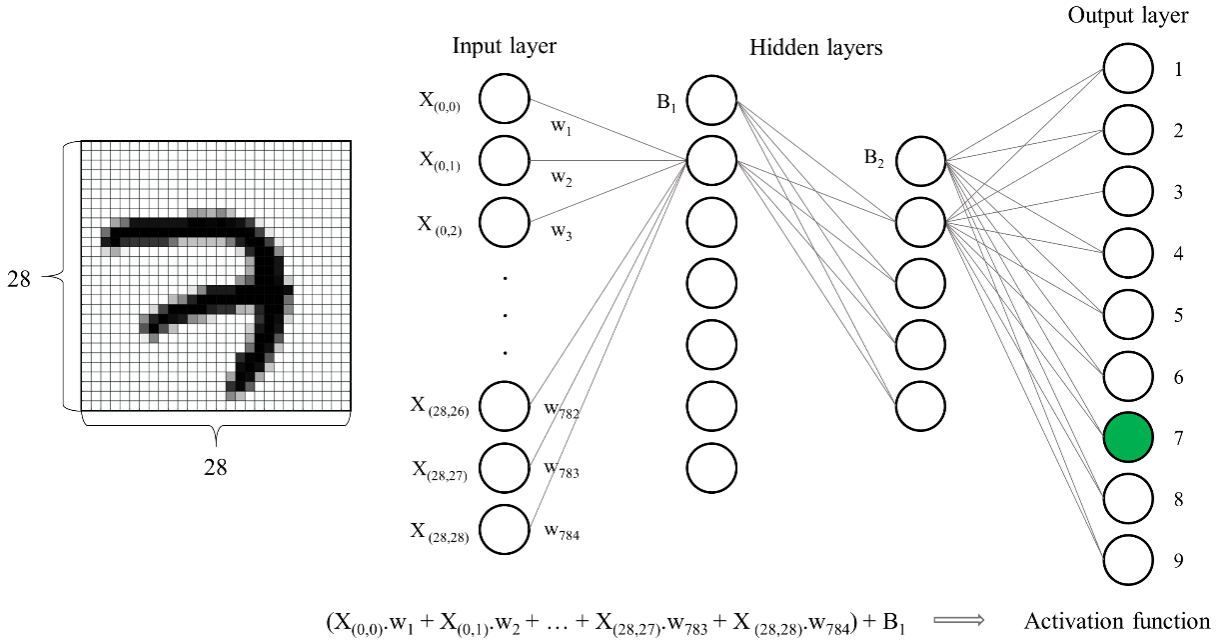

Figure IV.1. Scheme of a typical ANN dedicated to the classification of digits from 0 to 9.

To better explain how a neural network works, Figure IV.1 shows the example of a classification problem of 28×28-pixel images of digits from 0 to 9. The image is transformed into a vector of dimension 784 (28×28) and fed into the network in the input layer. Each input neuron is connected to all the neurons of the first hidden layer by "edges" and each edge has an associated numerical value called weight (w). The edges interconnect all the neurons in the network, but for simplicity, in Figure IV.1 only the connections of the neurons of the input layer with the first neuron of the hidden layer and so on are displayed. Often, each hidden layer is associated to another numerical value called bias (B) that can be seen as an additional neuron which is not connected to the previous layer. Fully connected neural networks have therefore as many parameters as edges and bias (i.e. for two consecutive layers: $n°\ of input\ neurons \times n°\ ouput\ neurons + 1$).

In order to know if a neuron gets activated or not, all the inputs arriving to a particular neuron are multiplied by their weights and summed, together with the neuron bias as shown in the equation of Figure IV.1 (for the case of a neuron of the first hidden layer). The result of this equation passes through an activation function that introduce non-linearity in the network and determine if the neuron gets activated or not. The neurons that get activated on the first hidden layer, serve as inputs to the second hidden layer, and this is repeated all along the network depth to the output layer, what is called forward propagation. The output neuron with the highest value (highest probability) is selected as the prediction, and this prediction is compared to the ground truth value by the loss function. The main idea of training a neural network is to reduce the value of the loss function (increase the similarity between the prediction and the ground truth) by applying the backpropagation, where the weights of the edges and the biases are adjusted. This forward and backpropagation cycle is iteratively repeated with multiple inputs in order to make the network predict well in most of the cases.

IV.2.2.1 Convolutional Neural Networks

Classic fully connected networks are limited for image classification problems. In those models, each pixel is represented by one (or several for color images) input neuron (s) and the number of parameters and training data required becomes quickly intractable. For example, typical micrographs of ~1000^2 pixels would imply about a million neurons in the input layer and several millions more in the hidden layers. This means a huge number of parameters to optimize what could take a long time and a lot of training data. For this reason, Convolutional Neural Networks (CNNs) have been developed [136].

CNNs are a subset of DL specially dedicated to work with images, where the main particularity is the application of convolution operations to an image in order to detect 2D-spatial features. The convolutions are applied with filters with a defined kernel size, and each filter is scanned all along the image to perform the feature extraction. In CNNs, filters are the equivalent to the neurons of an MLP, and they also have associated weights that collaborate in the activation of the filter. The concepts of activation function, loss function, forward- and back- propagation, etc. described for classic ANNs are valid for CNNs as well.

Figure IV.2 shows a scheme of a classic CNN to address an image classification task to discriminate images between horses, zebras or dogs. A first block of convolutional filters is applied to the input image through a kernel in order to extract first order features such as edges, lines, points, blobs, etc. Then, the image size is reduced and additional filters are applied to capture features at different scales. As we move deeper into the CNN, the filters detect increasingly complex features such as shapes or figures. At this point, the features detected for classifying the animals can be facial features such as the eyes, ears or muzzle.

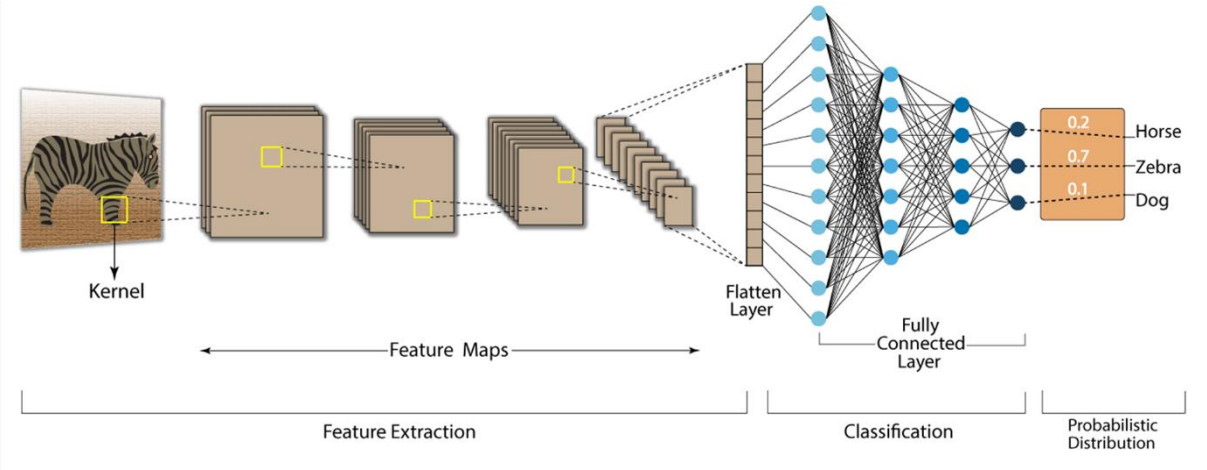

Figure IV.2. Scheme of a typical CNN dedicated to the classification of images into 3 classes namely horse, zebra and dog.

Once we reach the end point of the feature extraction with the CNN, the extracted feature maps are flattened into a vector which is fed into a fully connected neural network that will finally result in three possible outputs with an associated probability for each one. Nevertheless, this is not the only way to perform image classification, since the extracted features by the CNN can be exported and fed into any ML algorithm that can be trained to address the classification task. Thus, the CNN may only be used as a feature extractor but the final classification is performed by an MLP or any other ML algorithm. Some of the most widely known feature extraction CNNs are VGG [137], AlexNet [138], GoogLeNet [139], among others.

If the problem we want to solve evolves from a classification to a semantic segmentation (pixel-wise classification of an image), the so called Fully CNNs can be used. These neural networks keep the feature extraction part as described above but instead of transforming the features into a vector, they upsample the feature maps to recover the original image size and be able to classify each pixel. An example of such architecture is called U-Net [140] and is explained in detail in V.4.2, since it has been used during this thesis.

IV.3 AI applied to the microstructural characterization of steels

As it has been explained in the literature review of Chapter I, the microstructural characterization of steels is a complicated task that requires a wealth of expertise in the field due to its complexity. Additionally, it is very tedious as it becomes repetitive and time consuming. Last but not least, as it is an activity conventionally performed by humans, it is logic that each expert's opinion carries a high degree of subjectivity.

To alleviate these drawbacks, several authors have started to apply AI-based techniques to make work easier, quicker and aiming to find the most objective result as possible. From the 1990s to today, the growth in the number of articles that have combined AI and microstructural characterization of steels has increased exponentially as shown in Figure IV.3.

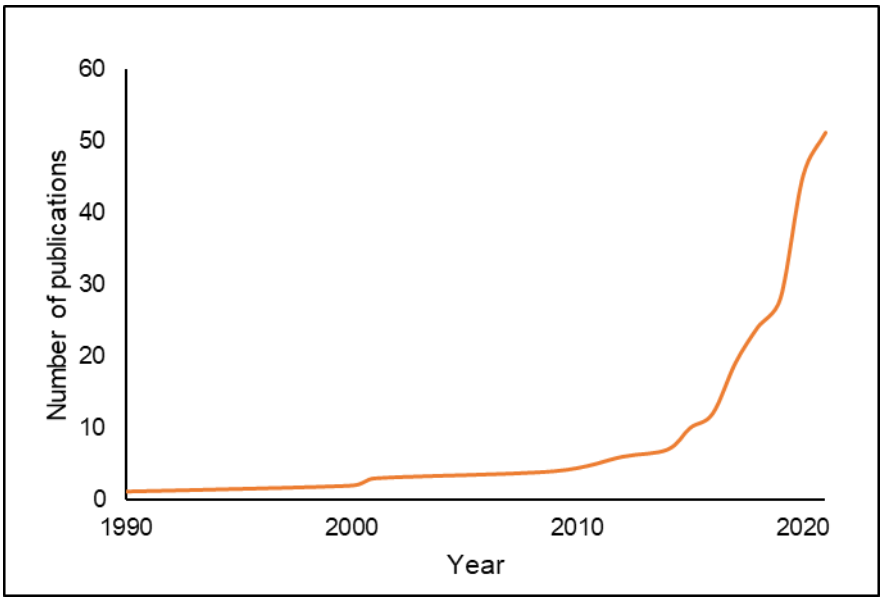

Figure IV.3. Evolution of the number of articles using AI for the characterization of steel microstructures.

Microstructural characterization of steels by means of AI has been approached in the literature from four main perspectives. First, considering the learning process, the greatest part of the authors has selected to work with supervised learning approaches as the implementation of such algorithms is well established and the attained performances can be higher since we guide them to the correct answers. However, the necessity of tedious and laborious labeling has forced few certain authors to start implementing unsupervised learning approaches. Second, taking a look at the data, several studies have been based on information obtained by LOM and SEM while only a limited number of articles have been focused on EBSD-based data. The main argument for this difference is that EBSD is an "expensive and time consuming" technique compared to classic LOM and SEM. However, last advances in EBSD allows to obtain large scanned areas in terms of minutes, what combined with the richer information both from the crystallography and microstructure, transform EBSD into an interesting option to couple with AI. Third, when looking at the algorithm types, several authors have trained ML models as they are easier to interpret by linking the results with the physical meaning of the features used for training. However, as mentioned in IV.2.1, the feature engineering step is highly laborious and that is the reason why DL models have also been trained to address this task. A last perspective is related to the information we can extract as a result from the trained model. While certain studies are focused on a classification problem, some others evolve to a bit more complex task as image segmentation. The latter allows us to have a real quantification of the micrograph we are looking at since the classification is performed pixel-wise.

IV.3.1 Supervised approaches

IV.3.1.1 Machine Learning applied to LOM and SEM micrographs

Classification

A great number of studies has been focused on the extraction of meaningful features from etched samples imaged under LOM or SEM in order to feed ML algorithms to perform a classification task. For instance, Arivazaghan et al. [141] proposed an image classification approach to categorize Nital-etched LOM micrographs into low, medium or high carbon classes. To accomplish this task, they have extracted textural features called Modified Alternate Local Ternary Pattern (MALTP) to feed different types of ML algorithms such as SVMs [133] and *k*-Nearest Neighbors (*k*-NN) [142]. In this case, the texture refers to the distribution of gray level pixels in the image. As the microstructures belonging to each class are very different from each other they reach a high classification accuracy above 98% for their testing dataset.

For their part, Gola et al. [143] suggested the classification of second phases contained in LOM and SEM micrographs of two-phase micrographs from low-carbon steels etched with a modified Beraha solution. The micrographs consisted of a ferritic matrix and either pearlite, martensite or bainite as second phase (Figure IV.4). To classify the phases, they have semi-manually segmented the second phases from the ferrite matrix and each segmented second phase contoured by ferrite was called object. From these objects, several morphological parameters as area, perimeter, diameter, ferret, among others, have been measured to feed an SVM algorithm. As a result, they obtained an average accuracy over the testing set above 87%, but showing better performances to classify martensite (94.2%) than pearlite and bainite (77.8% and 77.3% respectively). In order to improve their accuracies, they combined the morphological features with the so-called gray-level co-occurrence matrix (GLCM) features [144], also dedicated to analyze the gray-level texture of the image [13]. The SVM trained on these both input types, outperformed the morphological-based model by reaching testing accuracies above 96% for all the classes. Although very good results were obtained, the approach is limited by the initial segmentation step to separate second phases from ferrite.

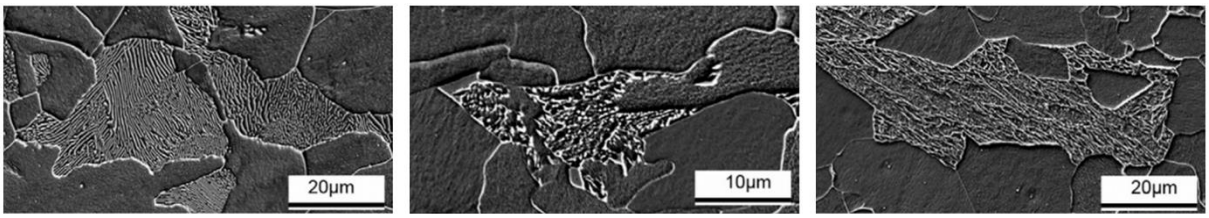

Figure IV.4. SEM micrographs of a ferritic matrix with (a) pearlite, (b) bainite and (c) martensite as second phases [143].

Müller et al. [145] considered that the GLCM together with local binary pattern (LBP) features [146] measured over Nital-etched SEM micrographs could be helpful to discriminate different types of bainite structures in 0.22%C steels. LBP features are as well gray-level texture descriptors. They trained an SVM to classify micrographs into one of six categories determined by the main constituent appearing

in the image: pearlite, granular bainite, degenerated upper bainite, upper bainite, lower bainite and martensite (Figure IV.5). The overall accuracy on the testing dataset is above 90% (showing its best performance for martensite of 97.14% and its lowest for upper bainite of 83.02%).

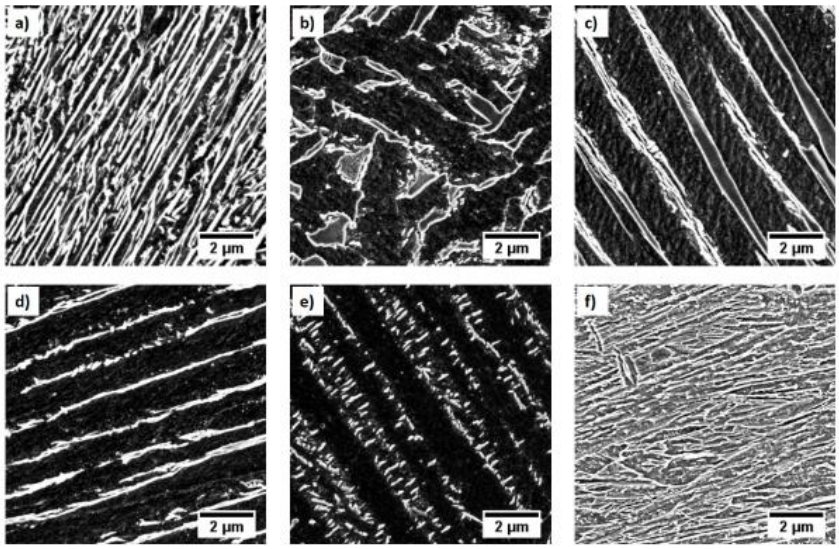

Figure IV.5. SEM micrographs of the six microstructure classes (a) pearlite, (b) granular bainite, (c) degenerated upper bainite, (d) upper bainite, (e) lower bainite, and (f) martensite [145].

A similar approach to that performed by Müller et al. [145] was proposed by Tsutsui et al. [147] by measuring GLCM features from SEM micrographs to carry out an image classification approach. They tried to classify microstructural images from a low-carbon steel into one of eight classes namely T1 to T8, being T1 fully upper bainite, T8 fully martensite and from T2 to T7 a phase mixture depending on the samples heat treatment (Figure IV.6). To this end they trained both random forest (RF) and gradient boosting machine (GBM) [148] algorithms. Their best result was obtained with GBM reaching an overall accuracy of only above 71%, with better performances for the single-phase micrographs than for those presenting a phase mixture. An important aspect of this study is that they trained two models with images coming from two different SEMs, namely FEG-SEM and W-SEM. They demonstrated that a model trained on FEG-SEM micrographs, but tested on W-SEM ones (or vice versa) provides very low accuracies even below 10%, showing that GLCM features highly vary depending on the microscope and acquisition conditions.

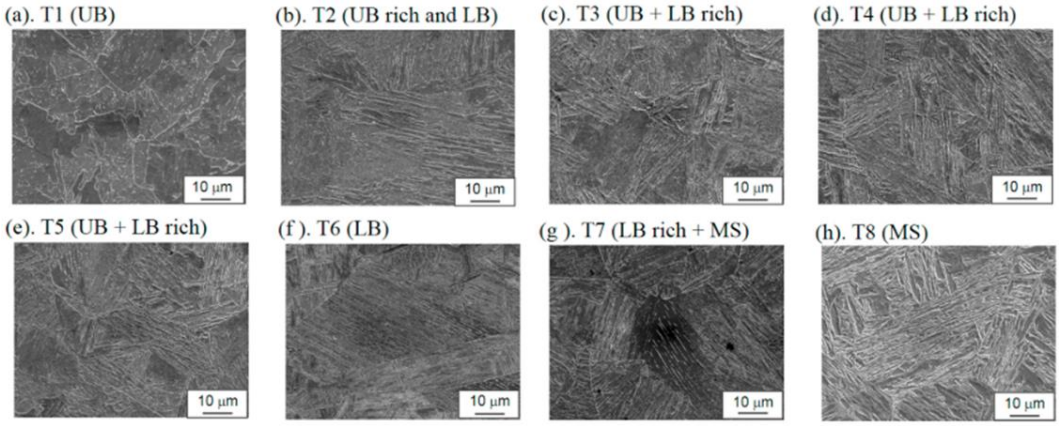

Figure IV.6. SEM images from (a) T1 to (h) T8. UB stands for upper bainite, LB lower bainite and MS martensite [147].

Segmentation

Some other studies tried to evolve into a more complex approach by characterizing a micrograph through a segmentation approach, i.e. a pixel-wise classification. Paul et al. [149] engineered gray level intensity features such as regional contour pattern and local entropy to be fed into a RF classifier and segment Nital etched LOM micrographs into ferrite, bainite and martensite. Although the testing accuracies are close to 90% for all three phases, they are calculated over a very small dataset and the segmentation results are only presented over three individual grains for each phase, i.e. they do not show an actual segmentation of an entire micrograph.

Bulgarevich et al. [150] proposed the pixel-wise segmentation of optical micrographs from a 0.15%C steel containing a multiphase ferrite, bainite and pearlite microstructure by applying various image filters (Gaussian blur, Sobel, Hessian, etc.) to extract features from the concerned microstructures. These features were then fed to train a RF classifier that provided very good agreements in terms of predicted phase fractions compared to a manual analysis. However, there is no accuracy calculation over the segmented micrograph, and although there seems to be a good visual agreement, it is difficult to assess up to which extent the model is performant (Figure IV.7).

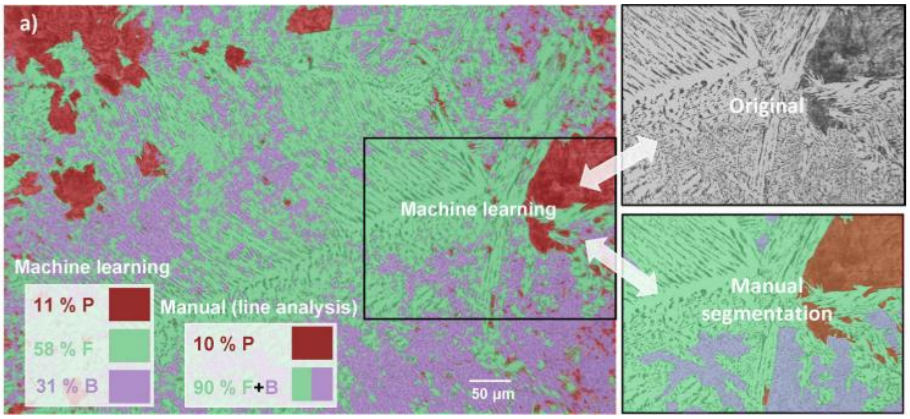

Figure IV.7. Segmentation result for the RF classifier. P stands for pearlite, F for ferrite and B for bainite [150].

For their part, Naik et al. [151] used the GLCM features to segment ferrite, pearlite and martensite contained in multiphase optical micrographs. They trained four different ML algorithms such as Naïve Bayes [152], k-NN, linear discriminant analysis (LDA) [153] and decision tree, that presented training accuracies above 90%. Nevertheless, once again there is no accuracy calculation for the testing dataset and only an approximative visual agreement can be observed between the segmentation result and the optical micrograph (Figure IV.8).

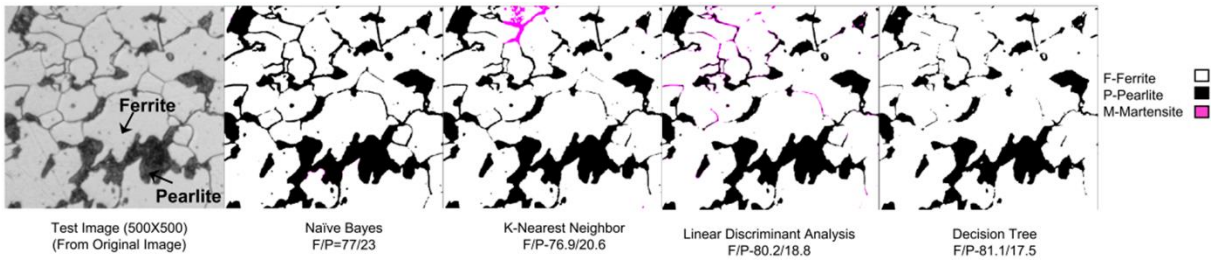

Figure IV.8. LOM micrograph of a dual phase ferrite-pearlite steel together with the segmentation results with all four tested algorithms [151].

IV.3.1.2 Deep Learning applied to LOM and SEM micrographs

There have been several authors that tried to perform the microstructural characterization of steels based on the feature extraction obtained from DL approaches, and in particular using CNNs. Here again, some have been focused on a classification approach while others addressed the segmentation problem.

Classification

Maemura et al. [154] proposed to solve the same task as Tsutsui et al. [147], SEM micrograph classification in categories from T1 to T8, but this time using a residual CNN called ResNet-50 [155] pretrained on the ImageNet dataset [156], to perform the feature extraction. They obtained accuracies above 94.1%. The main part of the errors comes from confusions between the T3 and T4 classes where a phase mixture can be found. An interesting point of this study is the interpretability evaluation of the CNN features using local interpretable model-agnostic explanations (LIME) [157]. LIME is able to highlight which part of an image increases the probability to be classified as the predicted class. Thus, they have found that a block boundary and a large carbide between laths was highlighted for T1 (upper bainite) (Figure IV.9 (a) and (d)), elongated thin blocks aligned parallel as if they would share the same habit plane were selected for T6 (mainly lower bainite) (Figure IV.9 (b) and (e)) and the packet and packet boundary were selected for T8 (martensite) (Figure IV.9 (c) and (f)).

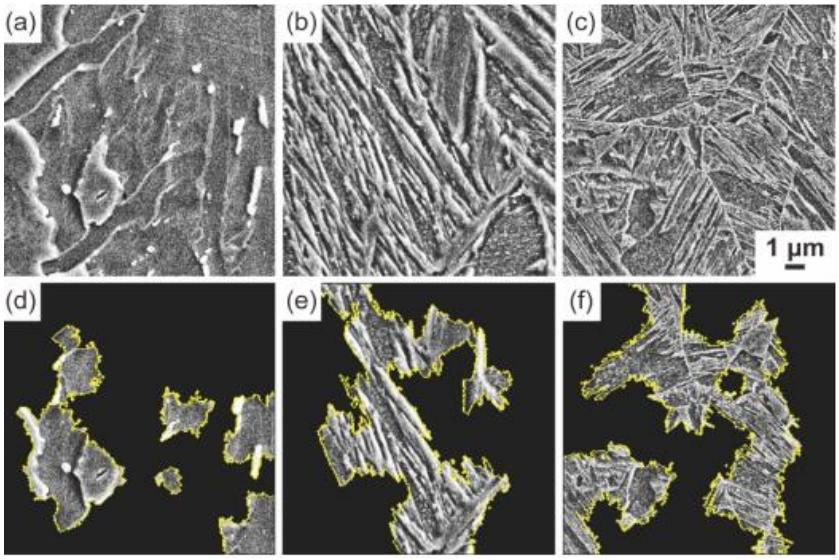

Figure IV.9. Upper row shows the input SEM micrographs and bottom row the LIME output images of (a) and (d) T1 (Upper Bainite), (b) and (e) T6 (Lower Bainite), and (c) and (f)T8 (Martensite)

Mulewicz et al. [158] employed the ResNet18 CNN pretrained on ImageNet dataset to carry out the classification of LOM micrographs coming from different steel grades and heat treatments. The classification was performed in a total of eight classes comprising bainite with carbide, granular bainite, columnar bainite, carbide free bainite, ferrite with grain boundaries, ferrite with grain boundaries and small islands of pearlite, martensite and pearlite. Each micrograph is formed by a single constituent e.g. 100% martensite. They obtained an overall testing accuracy above 96%, where the main part of the misclassifications corresponded to the different bainite types. However, no micrographs examples of the different classes are shown in the article to evaluate the complexity of the approach.

Larmuseau et al. [159] proposed an LOM micrograph classification approach to categorize a total of 60 materials coming from diverse chemical compositions and processing routes. Two tasks were addressed on two different datasets. First, they trained a model on a dataset containing LOM micrographs from 5 visually different groups whose classes are: austenitic matrix, martensitic with prior austenite grains, tempered martensitic, quenched martensitic and ferritic steels (Figure IV.10). To do so, they used the CNN ResNeXt50 to perform the feature extraction and an MLP that carry out a feature dimensionality reduction, as the idea is to construct low dimensional representations of microstructure images. To classify the images with the extracted features they have trained triplet networks, that allow to group an image with other images with similar characteristics and separate it from those that are different. The micrographs have been acquired with different step sizes ranging from 0.1 to 5µm (although the number of images for each step-size differs strongly). They have obtained high accuracies above 81% and 97% for the austenitic matrix and ferritic steels respectively, but the accuracies remained around 60% for the rest of the classes. In general, the model is robust to step size variations despite the fact that for some particular classes there are clear accuracy differences.

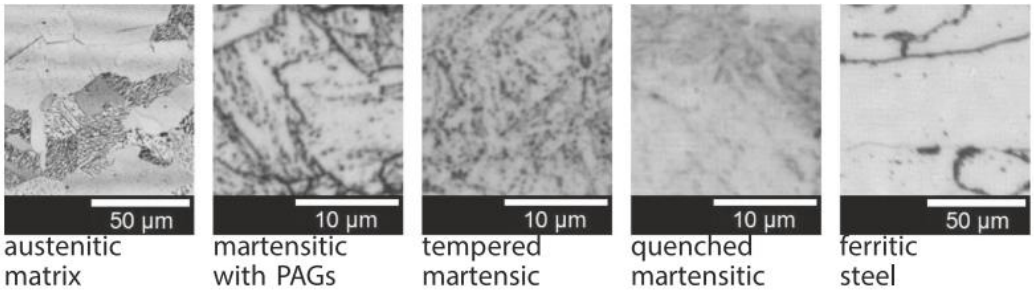

Figure IV.10. Crops of LOM micrographs belonging to the first dataset [159].

With the model trained on the first dataset, they tried to classify a second dataset containing 10 classes (Figure IV.11). One advantage of the triplet networks is that it only needs to know which images belong to the same class and which images do not, whereas classic CNNs need the particular label of each micrograph. This make it easier to extrapolate the trained models into new datasets. The model obtains a decent performance for all materials, but struggles most with materials that were not included in the original training set.

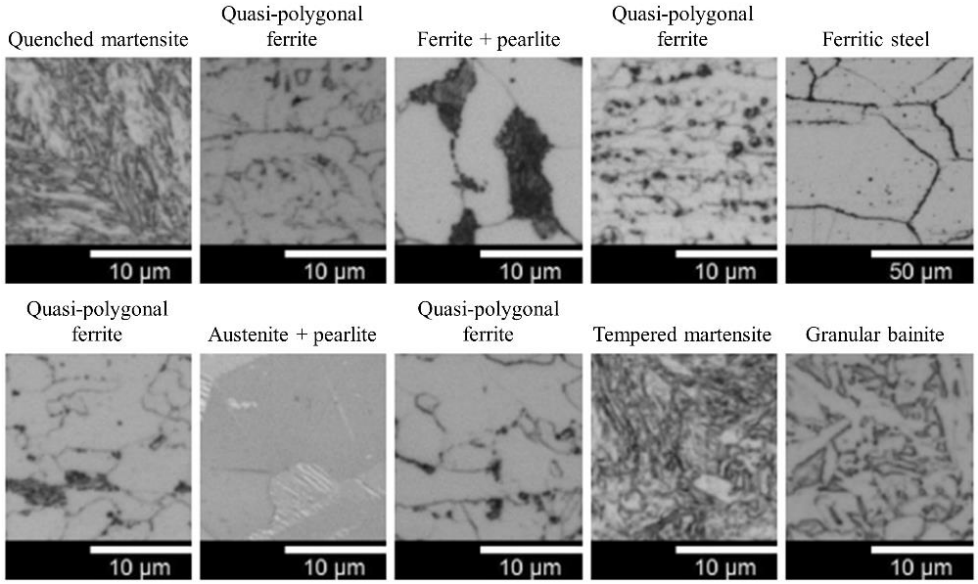

Figure IV.11. Crops of LOM micrographs belonging to the second dataset [159].

Based on the aforementioned study, Larmuseau et al. [160] proposed to compare the performance of their model to classify both LOM and SEM micrographs against human experts on the field. The model was able to overcome the experts' predictions. In this approach they add some particular modifications such as aggressive data augmentation, crops at different length scales and the explicit inclusion of the magnification as an additional input to the model.

Segmentation

When trying to solve the segmentation problem, Azimi et al. [12] were the first to implement a Fully Convolutional Neural Network (FCNN) for the pixel-wise classification of SEM micrographs into martensite, tempered martensite, bainite, pearlite and ferrite. The same set of ferritic matrix samples as in Gola et al. [143] has been used here. In particular, they used a pretrained VGG-16 CNN as feature

extractor and then performed upsampling operations to recover the original image size. They obtained an overall testing pixel accuracy of 93.94%, however this is due to the high accuracy obtained for the ferritic matrix (94.22%) because the rest of the phases reached much lower accuracies (79.85% for martensite, 72.62% for tempered martensite, 70.46% for pearlite and 37.32% for bainite). The authors explained that the very low accuracy obtained on bainite is due to the presence of a different type of bainite present in the testing set that has not been seen by the model during training. They have also tried to input LOM micrographs to train the FCNN model and although the pixel accuracy for the ferrite matrix is high (94.11%), the accuracies for the rest of the phases are way below than the SEM-based approach (50.11%, 58.36%, 19.35% and 5.21% for martensite, tempered martensite, pearlite and bainite respectively). Figure IV.12 shows some micrograph examples comparing the LOM and SEM segmentation.

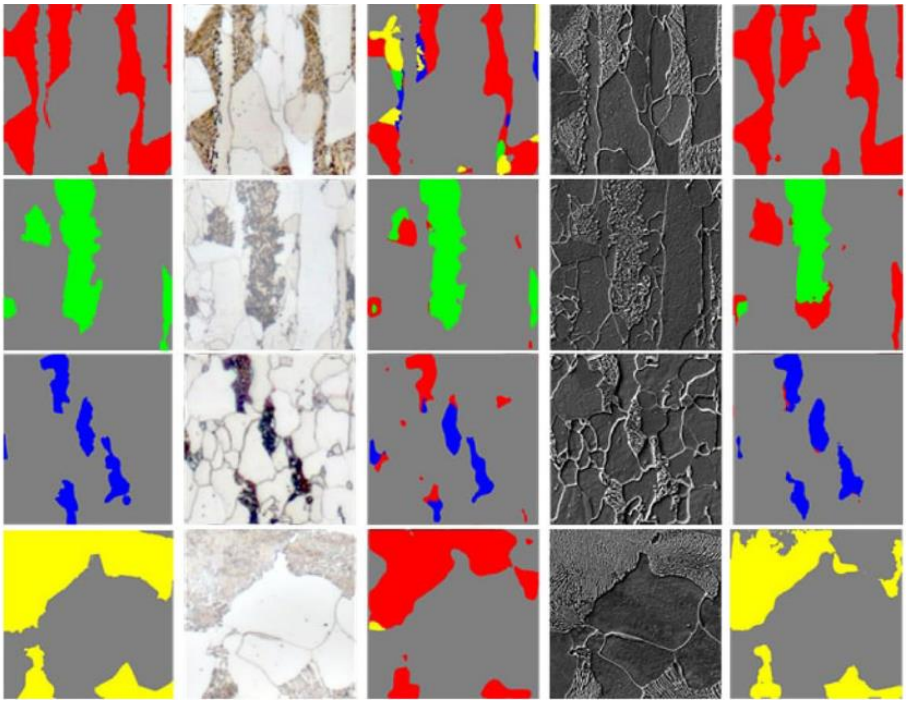

Figure IV.12. Comparison of LOM and SEM segmentation using FCNN network. Columns from left to right: Ground truth, LOM, LOM segmentation, SEM and SEM segmentation. The ground truth colors of martensite, tempered martensite, bainite and pearlite are red, green, blue, and yellow, respectively [12].

DeCost et al. [161] presented a DL method based on the application of a CNN architecture to carry out the pixel-wise classification ultra-high carbon steels into proeutectoid cementite network, fields of spheroidite particles, the ferritic matrix in the particle-free denuded zone near the network and Widmanstätten laths (Figure IV.13). The architecture chosen is PixelNet, formed by a VGG-16 feature extractor pretrained on the ImageNet dataset, an upsampling step to recover the original image size for segmentation and a last MLP to perform the pixel wise classification. They obtained an overall classification accuracy around 86.5%, showing better results for the cementite network and spheroidite particles but lower ones for the matrix and Widmanstätten laths.

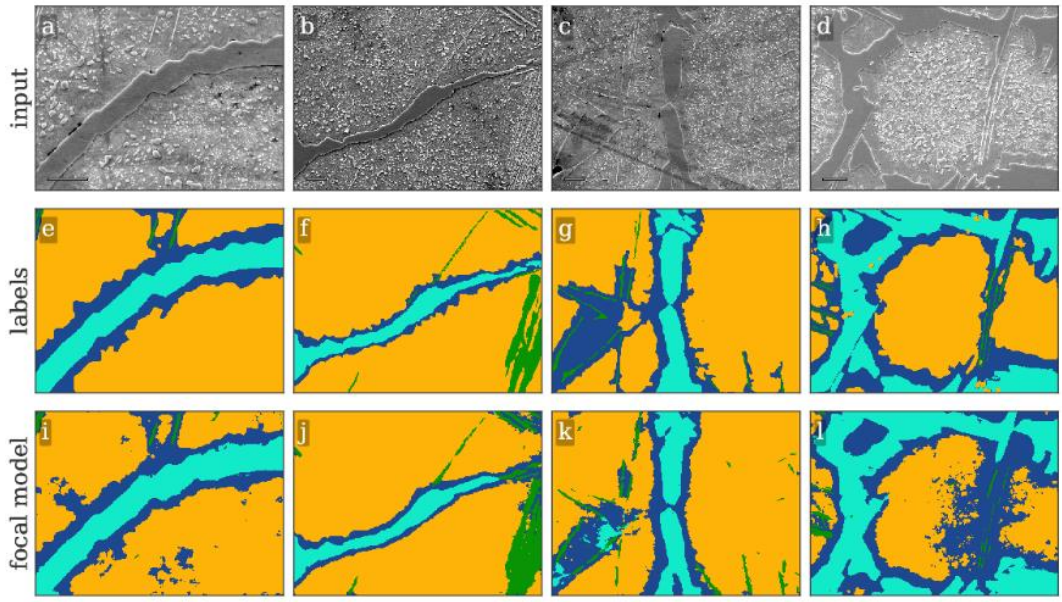

Figure IV.13. Segmentation of four example micrographs where microstructural constituents include proeutectoid grain boundary cementite (light blue), ferritic matrix (dark blue), spheroidite particles (yellow), and Widmanstätten cementite (green). Scale bars indicate 10μm.

Several authors have implemented the U-Net CNN architecture for the semantic segmentation of steel microstructures. For instance, Ajioka et al. [162] implemented U-Net to classify pixel-wise ferrite, martensite and grain boundaries within LOM micrographs (Figure IV.14). They obtained an overall accuracy above 95.1% with high performances for all three classes. Their approach was compared to other classic segmentation approaches such as gray-level intensity thresholding, Trainable Weka Segmentation (TWS) [163] or even another DL model such as SegNet [164], outperforming all of them.

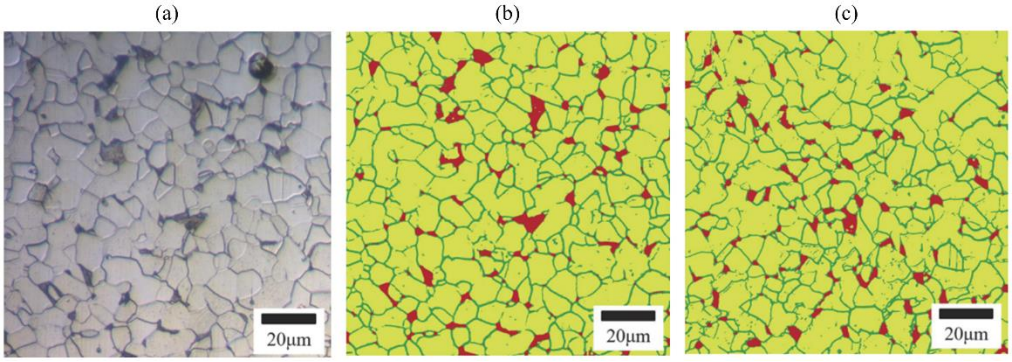

Figure IV.14. (a) LOM micrograph, (b) ground truth and (c) U-Net segmentation result. Ferrite, martensite and grain boundaries appear in yellow, red and green respectively.

For their part, Shen et al. [165] proposed the microstructure segmentation of both duplex (austenite and martensite) and Q&P (ferrite, martensite and residual austenite) steels from Backscatter Electron (BSE) and SE micrographs respectively using U-Net (Figure IV.15). One particularity of this study is that they have used EBSD for the ground truth labeling based on phase discrimination and pattern quality maps from the same regions of the SEM micrographs. They obtained overall testing pixel accuracies around 90% for the DP steel and around 85% for the Q&P steel. It is important to remark that, although the pixel accuracy is not perfect, they were able to correctly calculate the phase fractions of ferrite and

retained austenite from SE images which is a challenging task. Up to the authors, their model interprets the differences in morphology because it has a strong ability to extract image features by sensing the small differences in the contrast, grayscale, etc. Additionally, they tested the robustness of the model against the acquisition rate of the micrographs and the magnification over a large range of values. As a reference, they used an imaging rate of 100ns/pixel and a magnification of 2000x and tested over different imaging rates (100 ns/pixel, 200 ns/pixel and 500 ns/pixel) and magnifications (500x, 1000x and 4000x). It resulted that the model was more sensitive to imaging rates with a maximum overall accuracy drop of around 10% against 3% for magnification variations.

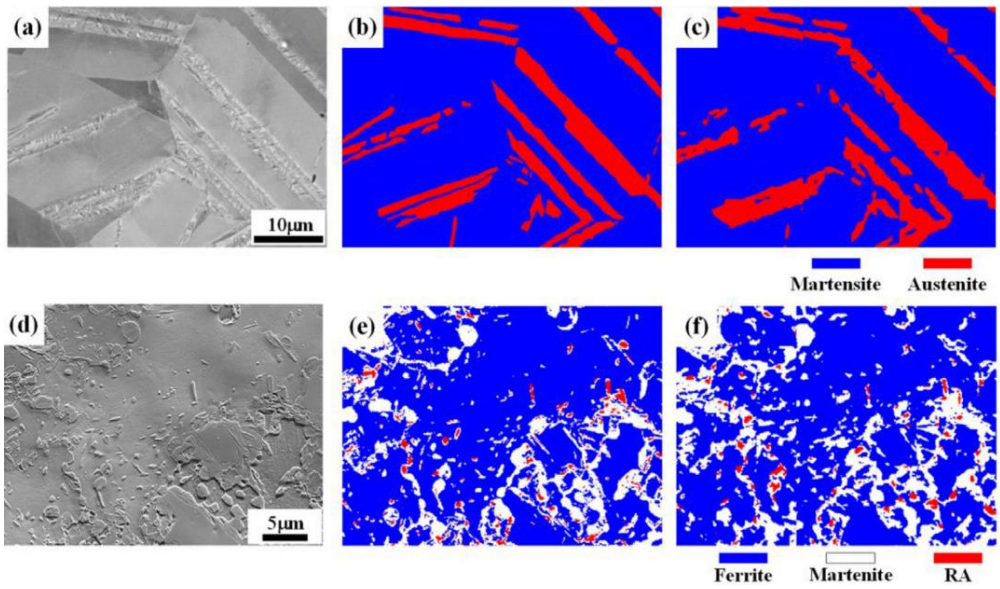

Figure IV.15. (a) BSE image, (b) EBSD phase map and (c) segmentation result of DP steel; (d) SE image, (e) EBSD phase map and (f) segmentation result of Q&P steel.

Same authors have also presented a data augmentation method to carry out the segmentation of SEM micrographs coming from DP steels with 0.17%C containing ferrite and martensite [166]. They trained a U-Net model with experimental micrographs of DP steels samples annealed at 750°C and 780°C. They observed that the change in the phase content was the main microstructural variation when the annealing temperature was changed. Therefore, they used the Thermo Calc software to simulate the potential phase fractions that would be present in the DP steel microstructure for annealing temperature ranging from 680°C to 840°C. With the phase fraction information, they performed the data augmentation by simulating microstructures with the desired phase fractions with an "image generator". This step is not deeply explained in the article and it remains unclear how the authors simulate the microstructures to carry out the data augmentation. The segmentation result shows a correct visual agreement with the SEM micrograph and the calculated phase fractions are consistent with the expectations. However, as these testing maps have not been labeled, there is no calculation of a pixel wise accuracy to know up to which extent the trained model is performant.

On their side, Durmaz et al. [167] proposed a binary segmentation approach of low-carbon CP steel to discriminate lath-shaped-bainite from a background class formed by polygonal and irregular ferrite with dispersed granular carbon-rich second phase. To accomplish this task, they implemented two different U-Net types (conventional and VGG16 U-Net) and they have evaluated and compared their performances when being fed with both LOM and SEM micrographs. To ensure the good quality of the ground truth labeling, EBSD maps were acquired in the same regions of the LOM and SEM micrographs. Conventional U-Net performed better when being fed with optical micrographs (90% pixel accuracy) while VGG16 U-Net provide a better performance with SEM ones (above 88%). However, the first has shown much better results for the segmentation of ferrite rather than bainite, whether the second one achieved similar accuracies for both phases, indicating that the SEM micrographs are richer in information to describe the bainite microstructure. Figure IV.16 shows some example results of the models' prediction. They have also demonstrated that pre-training the VGG16 U-Net with the ImageNet dataset is beneficial for the model's performance rather than training from scratch. In order to qualitatively explain how the models work, they have implemented both GradCam [168] and NetDissect [169] strategies. While the first enables the visualization of the most important regions of the input image to obtain the final prediction, the second helps to visualize the concepts that were learnt by individual filters in specific layers.

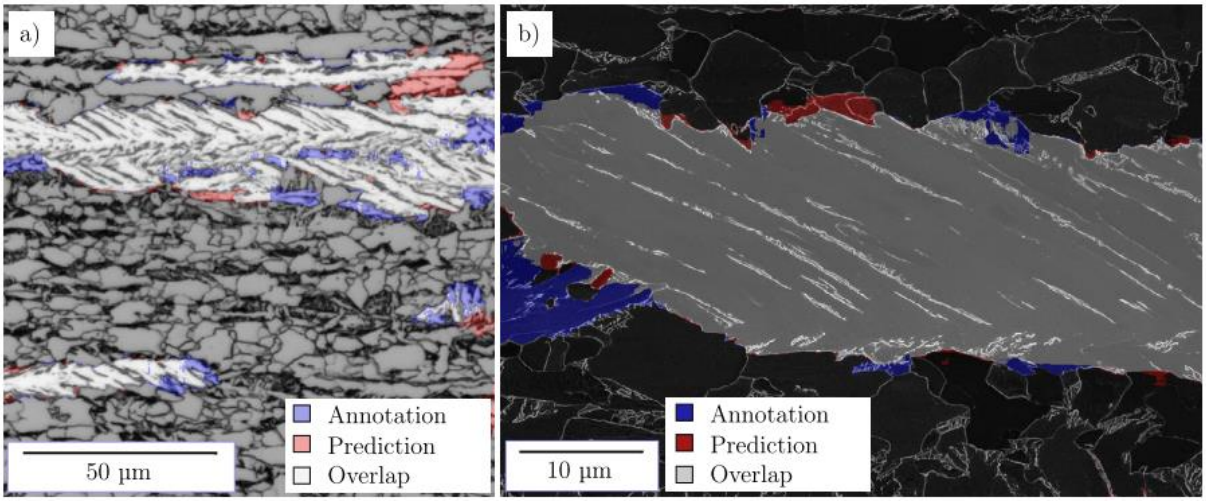

Figure IV.16. (a) LOM and (b) SEM micrographs superimposed with lath-bainite predictions of the conventional U-Net model trained from scratch, showing the comparison between model prediction (red) and manual expert annotation (blue). Overlap (gray) corresponds to the correctly classified regions according to the ground truth labeling.

IV.3.1.3 AI approaches based on EBSD data

Although all the described studies up to now present interesting and innovative points to consider, they are all based on LOM and SEM and for some particular cases the microstructural data alone is not enough to provide high-quality results. As it has been shown in [165], [167], certain studies use EBSD as a technique to increase the reliability of the ground truth labeling. Additionally, the chemical etching needed to observe the surface by classic LOM or SEM, may not always reveal all the meaningful features of a microstructure and also makes the approach sample preparation dependent.

The number of studies that train AI algorithms based on EBSD data for the microstructural characterization of steels is very limited. Certain authors considered some of the EBSD derived features described in I.4.1, such as pattern quality, KAM, spatial distribution of variants, etc., to address the task. For instance, Goulden et al. [170] proposed the pixel-wise segmentation of EBSD maps containing a dual phase ferrite and martensite microstructure. They implemented the pattern quality image BC as the input data to train a Nearest Neighbor ML algorithm. This approach has been implemented in the Aztec software and it is called Reclassify Phase. Recently, they have added the KAM as a second source of input data in order to improve the segmentation.

By their part, Tsutsui et al. [171] leveraged the organization of variants pairs and their density within PAGs, together with KAM to classify EBSD maps within seven different classes corresponding to microstructures obtained after a given heat treatment (T1 to T7). T1 corresponds to the microstructure class with a fully bainitic structure formed at high temperature, T2 is the bainite formed at low-temperature class, classes T3 to T6 are bainite-martensite mixed structures and T7 is a fully martensite class. This approach used conventional ML algorithms such as RF and SVM, and the best performance reached an accuracy above 88%. They have found out that the low-angle variant pair density of V1-V4 is a key feature for identifying the microstructures of low-carbon steels.

On the other hand, some studies have been performed using the EBSPs as the input data to the algorithm. Kaufmann et al. [76], [77] applied CNNs to EBSPs in order to identify their crystal symmetry and discriminate ferrite and martensite based on their subtle difference in lattice parameter variations. This results in a segmentation approach as each pattern corresponds to a pixel in the EBSD map. Nevertheless, no accuracies are calculated for the presented case although a good visual agreement can be seen when compared to the pattern quality map (Figure IV.17). The main limitation of this technique is the necessity to save the patterns, what needs a high storage capacity.

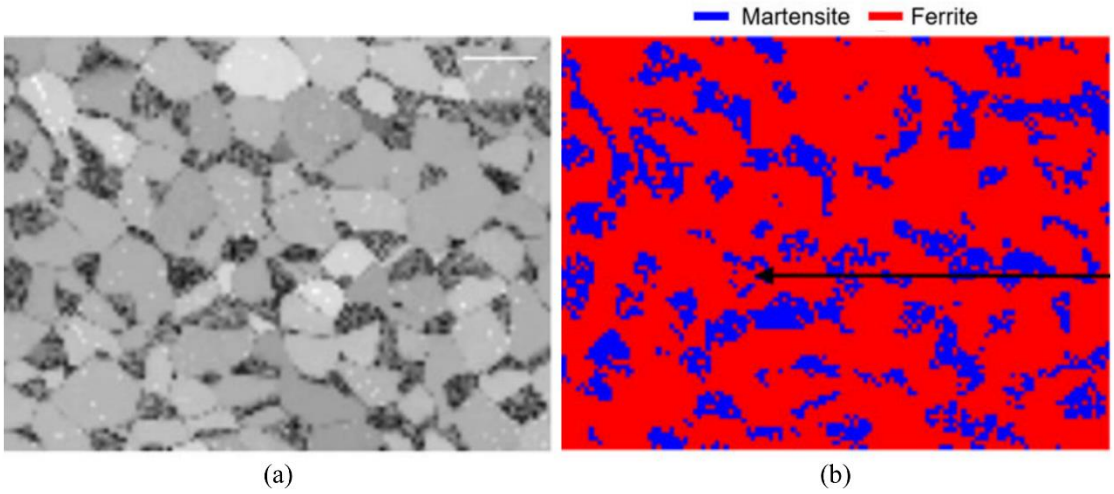

Figure IV.17. (a) Pattern quality map and (b) phase discrimination result.

Other authors addressed different tasks from EBSPs such as orientation determination. Liu et al. [172] proposed EBSD indexing using an EBSP as the input image of a CNN to predict the three Euler angles representing its orientation. However, they predicted each angle independently from each other with a separate CNN. In [173], [174] authors trained a single CNN to predict all three Euler angles together for both simulated and experimental EBSPs. Testing results indicate a reasonable indexing accuracy compared to both classic HT-based and DI. These approaches open a possibility for a new indexing method based on AI.

As it can be seen, very few authors have actually attempted to combine supervised AI techniques with EBSD for the microstructural characterization of steels. To the best of our knowledge, there are no approaches in the literature that use the raw orientation data obtained from EBSD indexing to feed an AI algorithm. Only EBSD maps colored with the Inverse Pole Figure (IPF) key (RGB images), have been fed into CNNs in the past for other applications [175] but, since the color in the IPF is determined from the projection of a macroscopic direction in the crystal reference frame, it intrinsically reduces the orientation information. For this reason, in Chapter V, we tested the ability of a CNN to extract features from raw orientation data in the form of quaternions in order to carry out a phase discrimination within the microstructures of dual phase steels.

IV.3.2 Unsupervised approaches

As described in IV.3, most AI approaches dedicated to the characterization of steel microstructures in the literature are supervised. Thus, a prior dataset labeling is needed to train the model and guide it during the learning process to the correct predictions. Given all the advanced ML and DL algorithms available today as open source and easy-to-use, the main bottleneck of their development is to obtain a large amount of accurately labeled data. To solve this issue, some authors initiated the development of open access segmented [176] and annotated [177] SEM micrograph databases that can be used and fed by other researchers. In addition, this would reduce the subjectivity of the labeling, since the opinion of several different experts can be aggregated to the database so it is as unbiased as possible.

Alternatively, a few studies suggested the use of unsupervised training strategies to both classify or segment the microstructure of steels. Kim et al. [178], [179] proposed unsupervised segmentation of LOM micrographs taken from an etched low-carbon steel sample using two different methods. In [178] the authors combine the training of a CNN with superpixel segmentation [180]. In short, the superpixel segmentation algorithm subdivides the image in small regions with identical contrast and texture characteristics and then apply convolutional filters, where the idea is to find the feature that gets the higher activation for each region. The regions whose highest activated feature is the same, are grouped in the same category. The CNN is trained to segment the image into a chosen number of classes. Although no accuracies are calculated, there seems to be a good visual agreement between the segmented image and the ground truth labeling for a multiphase microstructure containing martensite,

pearlite and ferrite (Figure IV.18). Since the number of classes to segment is defined by the user, the model can be trained to segment any microstructure containing any mixture of constituents.

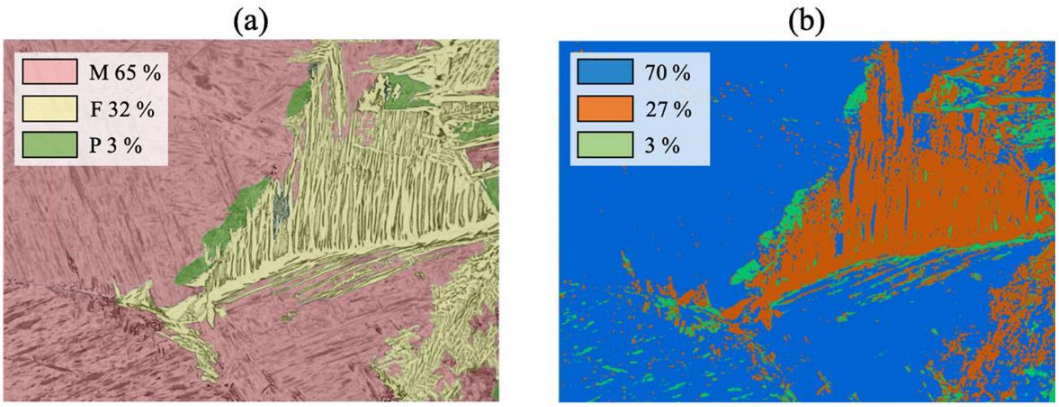

Figure IV.18. (a) LOM micrograph with the ground truth labeling overlaid. M stands for martensite, F for ferrite and P for pearlite. (b) Segmentation result.

In [179] instead, they applied convolutional filters such as mean, variance, energy, entropy, Gabor, among other filters to detect features from the microstructure. The obtained feature maps undergone a dimensionality reduction process using principal component analysis (PCA) [181] and then the pixels of the input images are clustered into the desired classes using a Bayesian Gaussian mixture model (BGMM) [182]. Segmentation results are presented over the same micrographs as in [178], and although once again there is no accuracy calculation, up to the authors, this approach outperforms the superpixel one for the same micrograph shown in Figure IV.18.

Goetz et al. [183] proposed the same segmentation task as in [167] but using an unsupervised approach, where the main idea is to train a CNN with a source dataset which is different from the target dataset they want to segment. For this task they use the AdaptSegNet [184], which is formed by a classic CNN for segmentation and a discriminator that is trained to discern if the segmentation result corresponds to an image of the source or the target dataset. For instance, they trained on an SEM source dataset and try to segment on two target datasets of SEM micrographs whose samples have undergone a different preparation that does not reveal the same features observable in the source dataset. In this case they got accuracies around 84% and 67% for each target. Another test was focused on using the same source dataset as before but change the target to LOM micrographs, where they obtained around 73% accuracy. Additionally, they trained a classic supervised CNN pre-trained on ImageNet and also a dataset containing SEM images from biological samples, fibers, films, coated surfaces, among others, where they demonstrated that the pre-training step is beneficial for the model's performance on microstructural data.

A single study has evaluated the possibility to couple unsupervised learning approaches with EBSD to characterize the microstructure of steels. Kim et al. [185] propose the quantification of phase fractions within six different multiphase steels containing ferrite, pearlite, bainite and martensite. To accomplish this task, they used EBSD-base features extracted from each detected grain and averaged over

neighboring grain. Especially grain features like average pattern quality, grain size, morphology, intragranular misorientation, grain boundary misorientation were considered. The data was fed to train an Information Maximizing Generative Adversarial Network (infoGAN) [186] and the results showed a small average error of 2.6% in the phase fractions prediction. They compared the performances of the infoGAN against classic unsupervised clustering approaches such as *k*-means, DBSCAN [187], etc. and it outperformed them all. An important aspect is the application of a technique called Layer-wise Relevance Propagation (LRP) [188] that is used to know which are the most relevant features that provides the prediction result. The negative point of this approach is that, although the phase fractions are correct if no segmentation is shown, we cannot be sure about the actual performance of the method.

IV.4 Conclusions

As we have seen along this chapter, AI has been used in numerous materials science related studies and in particular in the characterization of steel microstructures. The greatest part has been based on both LOM and SEM micrographs as there are the most established and simple techniques to perform materials characterization. However, it becomes very complicated in certain cases to establish with certainty which are the present phases in a microstructure based on these observations. Another important drawback is related to the necessity of a chemical etching to reveal the microstructural features, what may change from one sample preparation to the other hindering its reproducibility. For this reason, we propose to work with EBSD-based data, since no chemical etching is needed and the information that we can extract from the microstructure is much richer. Nowadays, EBSD technique has enormously progressed both in resolution and acquisition speed, making its use much more widely adopted for the characterization of microstructures. Only a few studies have been focused on the characterization of steels based on EBSD data, therefore we think it is of great interest to research in this direction.

In addition, thanks to the richness of the information obtained by EBSD, it is possible to have more elements to carry out the discrimination of more complex phases such as bainite. As we have seen throughout the literature, the discrimination of bainite from martensite and ferrite has not been achieved with sufficient success.

The main part of the presented studies has been performed on a supervised learning basis since it is the easiest way to make a model learn. For this reason, our first AI-based approach has been focused on teaching a CNN model to segment the phases within a microstructure in a supervised manner. Nevertheless, during the labeling procedure we have highly struggled in complicated situations and a huge amount of time has been dedicated to this task. For this reason, we propose an unsupervised learning approach too, as the number of studies in this field is still very limited.

It is important to remark that a great part of the presented studies proposed classification task but we think that the characterization is incomplete if we are not able to accurately localize the phases within

the acquired micrograph, for this reason our approaches are oriented to provide a segmentation result. Although some articles only provide a qualitative estimation of the results, we believe that it is necessary to quantitatively estimate the performance of the trained models. For this reason, all the results obtained are compared with manual labeling, in order to know how close the model is to a human segmentation.

Chapter V: **Supervised learning for phase discrimination in steels**

V.1 Introduction

This chapter presents the supervised learning approach we have implemented in order to characterize the microstructures of steels based on EBSD data. To this end, we propose a DL architecture called U-Net in order to perform a semantic segmentation of microstructures, i.e. assign each pixel of the image to the corresponding phase or microconstituent.

Two different tasks were proposed to be solved: the segmentation of Dual-Phase (DP) microstructures containing ferrite and martensite, and the segmentation of multiphase microstructures containing ferrite, upper bainite and martensite.

The first task served as a model application case since the binary discrimination of ferrite and martensite is relatively simple. The main idea was to apply DL algorithms to a simple case to be sure about the labeling and the obtained accuracy of our implementation. In this application, the focus was oriented on finding the best EBSD inputs to feed our U-Net architecture: EBSD-derived parameters such as pattern quality or KAM maps were used, as well as raw orientation data.

Since high accuracies were obtained for the DP microstructures, we decided to evolve into the more complex multiphase steel segmentation. It is important to remark that the microstructures we worked with came from industrial samples, thus we want to demonstrate the possibility to apply DL algorithms within the industry. This part of the work has been performed in collaboration with Industeel ArcelorMittal (Le Creusot, France) supported by the IRT M2P laboratory and is part of the post-doctoral work of Dr. Simon Breumier.

The chapter initially presents the samples and the EBSD acquisition conditions. Then, the most relevant EBSD features used by experts to discriminate phases are detailed and we explain how they have been used in order to label the microstructure. This is followed by an in-depth description of the DL strategy where the input data type, architecture parameters, training procedure, performance evaluation metrics, among others are described. Finally, the segmentation results for all microstructure types are presented.

V.2 Materials and EBSD acquisition

Two steel grades have been submitted to different heat treatments to generate desired microstructures for further analysis with supervised deep learning methods: (1) a model dual phase steel (DP-steel) containing different amounts of ferrite and martensite as main phases and a low amount of Widmanstätten ferrite and (2) two industrial multiphase steels (MP-steel) containing ferrite, martensite and upper bainite.

V.2.1 Dual phase steel

A total of three samples with a composition (wt%) 0.17% C and 1.5% Mn have been provided by ArcelorMittal Global R&D (Maizières-les-Metz, France). Each of them has been heat treated on a Bähr

dilatometer, as described Figure V.1. Figure V.2 shows a region of sample T3 containing the most representative features of the microstructures of the analyzed samples.

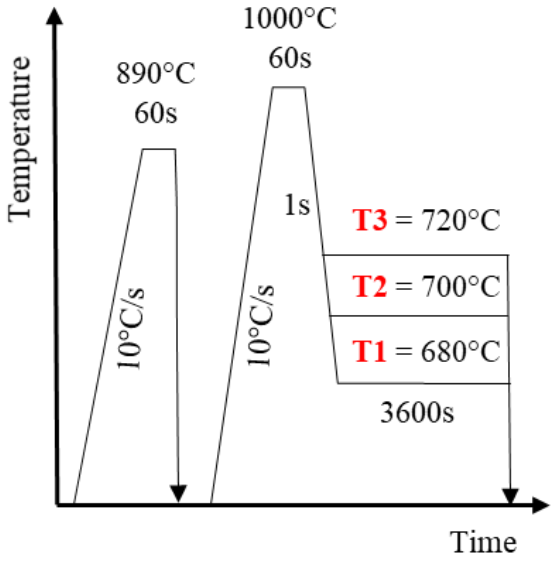

Figure V.1. Corresponding heat treatments of the DP-steel resulting in three samples called T1, T2, T3.

The heat treatments consisted in an austenitization at 1000°C for 60s followed by cooling down to different holding temperatures to form different amount of proeutectoid polygonal ferrite grains nucleating and growing from the PAGs by a diffusive mechanism [29]. The temperature was held during 3600s and then, quenching was performed below martensite start temperature (Ms = 430°C) what produced typically lath-like martensite formed by a displacive and diffusionless transformation. Some particular martensite domains showed a coarser convex shape, that may correspond in certain cases to auto-tempered martensite [189]. The resulting microstructures consisted in different ferrite-martensite fractions. From sample T1 to T3, the martensite fraction is increasing with the holding temperature. Whereas allotriomorph ferrite was observed at all temperatures, additional Widmanstätten ferrite was locally observed for T3. This ferrite type nucleates on allotriomorph ferrite and grows inside the PAG with which it is in orientation relationship (OR) with a plate or needle morphology [190]. Upon quenching, martensite precipitates alongside these Widmanstätten plates and shares nearly the same orientation.

The phase fractions detailed in Table V.1 have been obtained after labeling, as explained later in V.3.3.

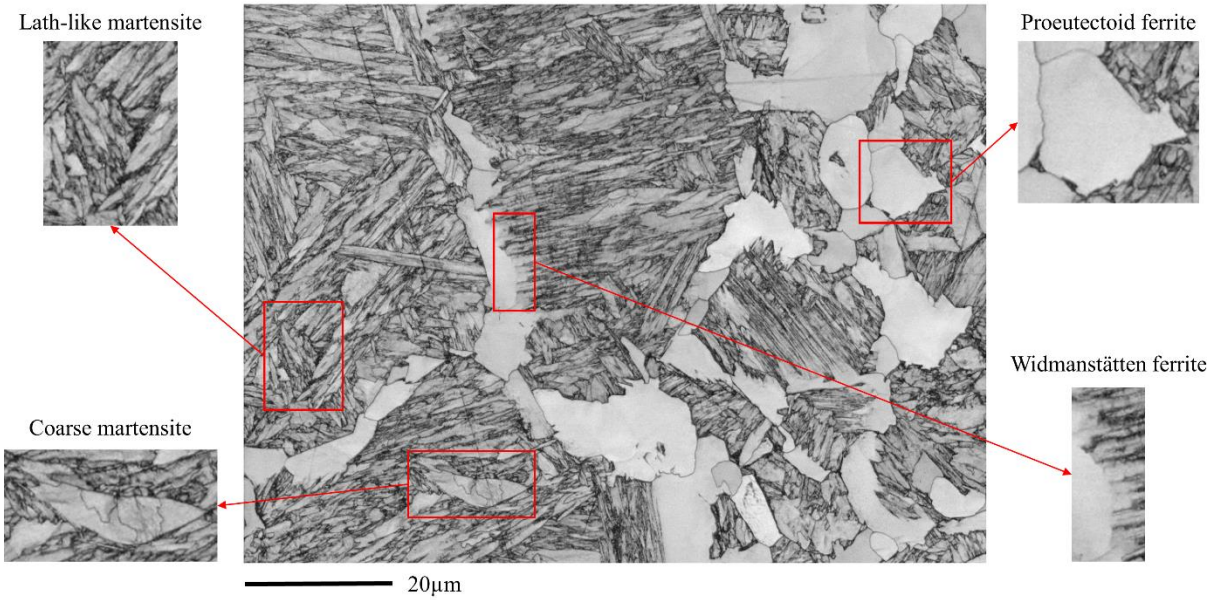

Figure V.2. Microstructure of T3 sample (revealed by the EBSD pattern quality).

Table V.1. Samples designation, corresponding heat treatments and phase fractions for DP-samples. F: ferrite and M: martensite.

Sample	Material	F/M fractions [%]
T1	DP-steel	57.2/42.8
T2	DP-steel	41.6/58.4
T3	DP-steel	33.7/66.3

The obtained DP microstructures can be considered as “easy” to segment by classical microstructural image analysis. That's why they were selected for our study. They act as “model” microstructures and are a good starting point to get in touch with DL algorithms to evaluate their application on EBSD data.

V.2.2 Multi-Phase steels

Contrary to the previous case, multiphase steels containing ferrite, bainite and martensite represent a greater challenge for the metallurgical industry to reliably identify each constituent. Indeed, their microstructural characterization is often very complicated and laborious using conventional methods. Therefore, this type of microstructure was used to demonstrate the application of DL algorithms based on EBSD data in an industrial context.

A total of six samples belonging to the SuperElso® 533 E and API5L X65QS PSL2 low-carbon steels has been provided by Industeel ArcelorMittal (Le Creusot, France). The first alloy has a major industrial interest since it is used in pressurized materials of the oil industry. The second one has a chemical composition close to API5L X65QS, but with a higher Nickel (Ni) content, thus the transformations during cooling are slower what offers a greater flexibility in the precipitation of reference phases. The nominal composition of both industrial alloys is presented in Table V.2. All samples were first heated above the austenitization temperature and then continuously cooled at different rates, detailed in Table

V.3. The phase fractions were provided by Industeel based on microscopic, hardness and dilatometry analysis.

Table V.2. Nominal composition (weight %) of each MP-steel sample.

Sample	C	Mn	P	S	Si	Cr	Mo	Ni	V	Other
SuperELso® 533 E	0.10	1.42	0.007	0.001	0.275	0.60	0.425	0.8	0.03	V+Nb 0.02
API5L X65QS	0.18	1.2	0.007	0.001	0.3	0.25	0.20	0.10	0.01	Nb 0.015

Table V.3. Samples' designation and corresponding heat treatment information and phase fractions for MP samples.

Sample	Material	Austenitization T [°C]	Cooling rate [°C/s]	Ms / Mf [°C]	F/UB/M fractions [%]
SA-1	SA533 E	980	0.28	430 / 305	60 / 40 / 0
API-1	API5L x65QS	975	2.8	400 / 300	50 / 50 / 0
API-2	API5L x65QS	975	2.8 to 620°C[2] + quench	400 / 300	Not provided
API-3	API5L x65QS	975	8.3	400 / 300	50 / 50 / 0
API-4	API5L x65QS	975	19.4	400 / 300	10 / 85 / 5
API-5	API5L x65QS	975	Quench (220)	400 / 300	0 / 0 / 100

Figure V.3 presents a region of the API-2 sample with the most representative features of the analyzed microstructure. The resulting microstructures are mixtures of ferrite/upper bainite/martensite and the amount of each transformation product depends on the cooling rate. The only sample presenting a single constituent is the API-5 as the direct quenching it has undergone gave place to a fully martensitic microstructure. The observed bainite is mostly upper bainite that nucleates and grows in the high temperature bainite range. It consists of coarse ferrite laths formed by a displacive transformation followed by a short range of carbon diffusion to form enriched austenite in the surrounding laths and finally cementite precipitates between laths [26]. Martensite/Austenite (M/A) islands can also be observed in most samples except in the mentioned API-5.

[2] Bainite start Temperature (Bs) estimated at 590°C

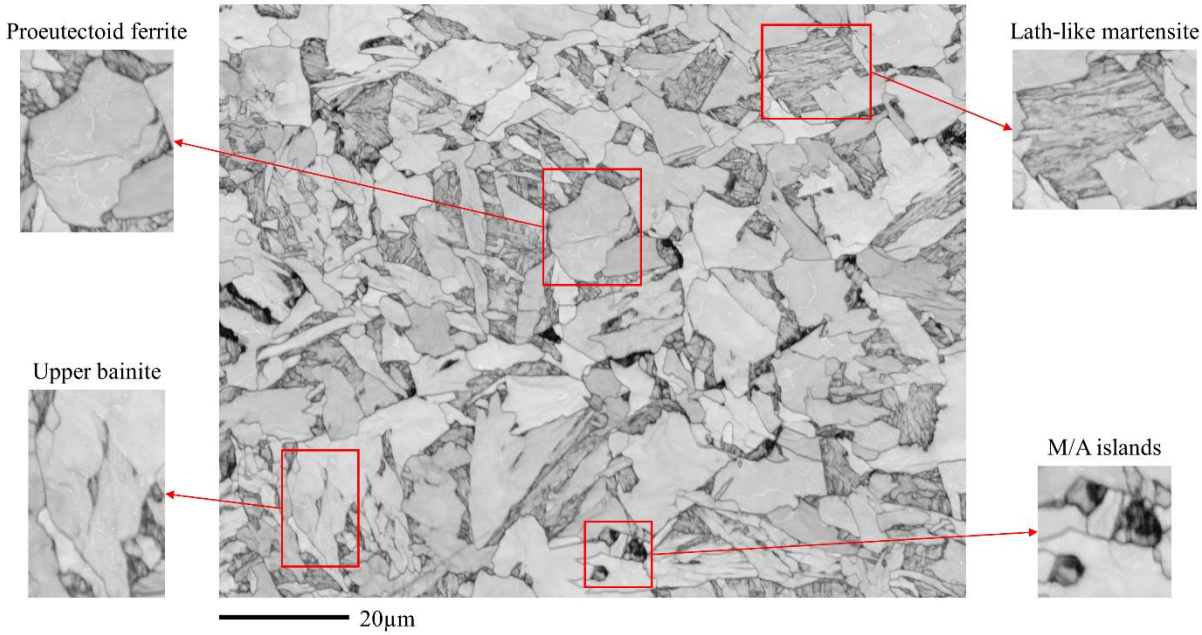

Figure V.3. Microstructure of the API-2 sample (revealed by the EBSD pattern quality).

V.2.3 EBSD acquisition

In order to obtain a well-prepared sample surface to perform EBSD, all described samples were mechanically polished with an initial step of SiC grit paper followed by successive steps of 9 and 3µm diamond suspension. The final step with a colloidal silica solution was with OP-U for the DP-samples and OP-S for the MP samples.

The acquisition conditions are detailed in Table V.4 and described hereafter. All DP samples were analyzed on a ZEISS Auriga 40 FIB–SEM microscope equipped with the Oxford Instruments CMOS Symmetry camera and AZtec acquisition software. A total of five maps of 114.1×85.6µm per sample has been acquired with a step size at 0.1µm and an accelerating voltage of 20 kV. The camera resolution was set to 156×128 pixels (i.e. 8×8 binning), the exposure time at 1ms and no pattern averaging was used. The raw maps were indexed as iron BCC and iron FCC using the Aztec "Optimized TKD" indexing method. The iron BCC phase includes the indexing of ferrite, bainite and martensite constituents as EBSD alone cannot discriminate them since their crystal structure is identical in low-carbon steels. A single map took around 15 minutes to be obtained, reaching an indexing rate around 90% (average values for the entire set of acquired maps). The remaining 10% of non-indexed patterns mainly belongs to highly dislocated martensite domains with poor pattern quality. The amount of indexed iron FCC is around 0.5% per map and was considered negligible. For DP-samples, the acquisition conditions have remained unchanged intentionally to focus on DL approach and get the best possible results for a simple case.

For MP-samples, an almost identical configuration was set but using a JEOL F100 SEM microscope also equipped with the Oxford Instruments CMOS Symmetry camera and AZtec acquisition software. Two maps of 252×189µm have been acquired per sample with a lower camera exposure time at 0.6ms.

A single map took around 90 minutes to be obtained, reaching an indexing rate close to 95% (average values for the entire set of acquired maps). Since the martensite fraction is lower than for DP-samples, the amount of non-indexed patterns decreases. In this case as well, the amount of indexed iron FCC (retained austenite) is below 0.1% per map and was considered negligible. This configuration is called Q_{ref}.

An additional configuration for the API-1 sample (Q_{alt}) was used in order to assess the robustness of the deep learning model against acquisition conditions variations. A single map was acquired with a camera resolution of 622×512 pixels (i.e. 2×2 binning), 3ms exposure time, 2 averaged patterns per point and the Aztec "Refined accuracy" indexing method. This map took around 11 hours to be obtained, reaching an indexing rate close to 97%.

Table V.4. Acquisition conditions for all the samples concerned in the chapter.

	DP samples	MP samples	API-1-High Quality
Microscope	Zeiss Auriga 40 FIB SEM	JEOL F100 SEM	JEOL F100 SEM
Camera resolution (binning)	156×128 (8×8)	156×128 (8×8)	622×512 (2×2)
Accelerating voltage [kV]	20	20	20
Step size [µm]	0.1	0.1	0.1
Exposure time [ms]	1	0.6	3
Pattern averaging	-	-	2
Map size [µm]	114.1×85.6	252×189	252×189
Indexing method	Optimized TKD	Optimized TKD	Refined Accuracy
Indexing rate [%]	90	95	97
Acquisition time per map (h)	0.25	1.5	11

V.3 EBSD-based phase discrimination

V.3.1 Important EBSD-based parameters for phase discrimination in steels

In order to perform a complete microstructural characterization, experts extract certain parameters from EBSD data that help to characterize and discriminate the present phases. One important parameter is the diffraction pattern quality, since the difference in dislocation density between the constituents may affect the diffraction signal varying its quality upon the scanned phase. The pattern quality can be expressed by the Band Contrast (BC) and Band Slope (BS) which are both indices available in AZtec. The BC corresponds to the brightness of the detected Kikuchi bands in the diffraction pattern and the BS evaluates the gradient of intensity at the edge of the bands [102]. These are expressed on a gray scale where white refers to the highest quality pattern and black means the worst possible quality. Low-quality patterns in several cases cannot be indexed producing the so-called non-indexed pixels. Thus, the constituent with higher dislocation density and lower pattern quality will also show a higher fraction of non-indexed pixels. One drawback of these indices is that their values may vary depending on the

acquisition conditions and sample preparation. This means that each EBSD map must be analyzed individually since it is very difficult to find a universal threshold based on the pattern quality.

Other important feature to consider is the intragranular misorientation induced by the dislocation network. It can be expressed by the Kernel Average Misorientation (KAM). The KAM is the average of the misorientation angles between the central pixel and all other pixels in a user defined kernel but excluding misorientations with an angle above a certain threshold. Since all constituents present different amounts of dislocation density, the KAM is a useful parameter to distinguish them. The only negative point of this parameter is its variability depending on the angular resolution of the EBSD data and the acquisition step size. If the step sizes are larger, the misorientation between pixels is also enlarged producing higher KAM values [191].

Another parameter that can be used, as described in I.3.2, is the existing orientation relationship (OR) between the parent and inherited phases during the phase transformation. In particular, bainite and martensite precipitate in OR within the PAG they transformed from, whereas it is not the case for proeutectoid ferrite. Even if in low-carbon steels, the parent austenite phase is no longer present at room temperature, it is possible to identify transformation products inherited with/without respecting an OR thanks to crystallographic reconstruction of the parent phase [7]. For example, ferrite can often be identified from the non-reconstructed areas.

Also, crystallographic domains inherited in the same PAG with respect to an OR are separated by specific boundary misorientations, as presented in I.3.4. Thus, it is helpful to plot these specific boundaries from the EBSD data. Low Angle Grain Boundaries (LAGBs) below 20° correspond to sub-block boundaries and are frequent for upper bainite. High Angle Grain Boundaries (HAGBs) above 45° correspond to packet boundaries and block boundaries, observed with a high frequency for lower bainite and martensite. Finally the random misorientations in between (from 20° to 45°) characterize the PAG boundaries and often ferrite boundaries [192]. As a consequence, the analysis of the arrangement of the transformed domains within PAGs in packets with high frequency of either blocks or sub-blocks has been reported to discriminate the transformation product [53], [54]. Of course, such analysis requires first to reconstruct the parent austenite map (using in-house software Merengue2 [7] for example).

V.3.1.1 Application to dual phase microstructures

As mentioned in V.2.1 ferrite and martensite can be easily discriminated based on microstructural image analysis and even more accurately on EBSD maps. Figure V.4 presents three maps, one coming from each type of DP-sample where the pattern quality (BS), the KAM and the specific misorientations maps are shown. Ferrite shows a bright pattern quality and a low content of intragranular deformation (low KAM values) while martensite presents mainly dark BS values and high KAM. The specific misorientation maps show a large fraction of high angle boundaries in martensite as expected. As mentioned in V.3.1, it can be confirmed that the BS is sensitive to sample preparation artifacts since

some scratches can be observed in the top left corner of the BS image of the T1 map in Figure V.4. These artifacts can be even observed in the KAM map if the scratch is deep enough to produce a deformation that can be captured by the misorientation calculation within the kernel.

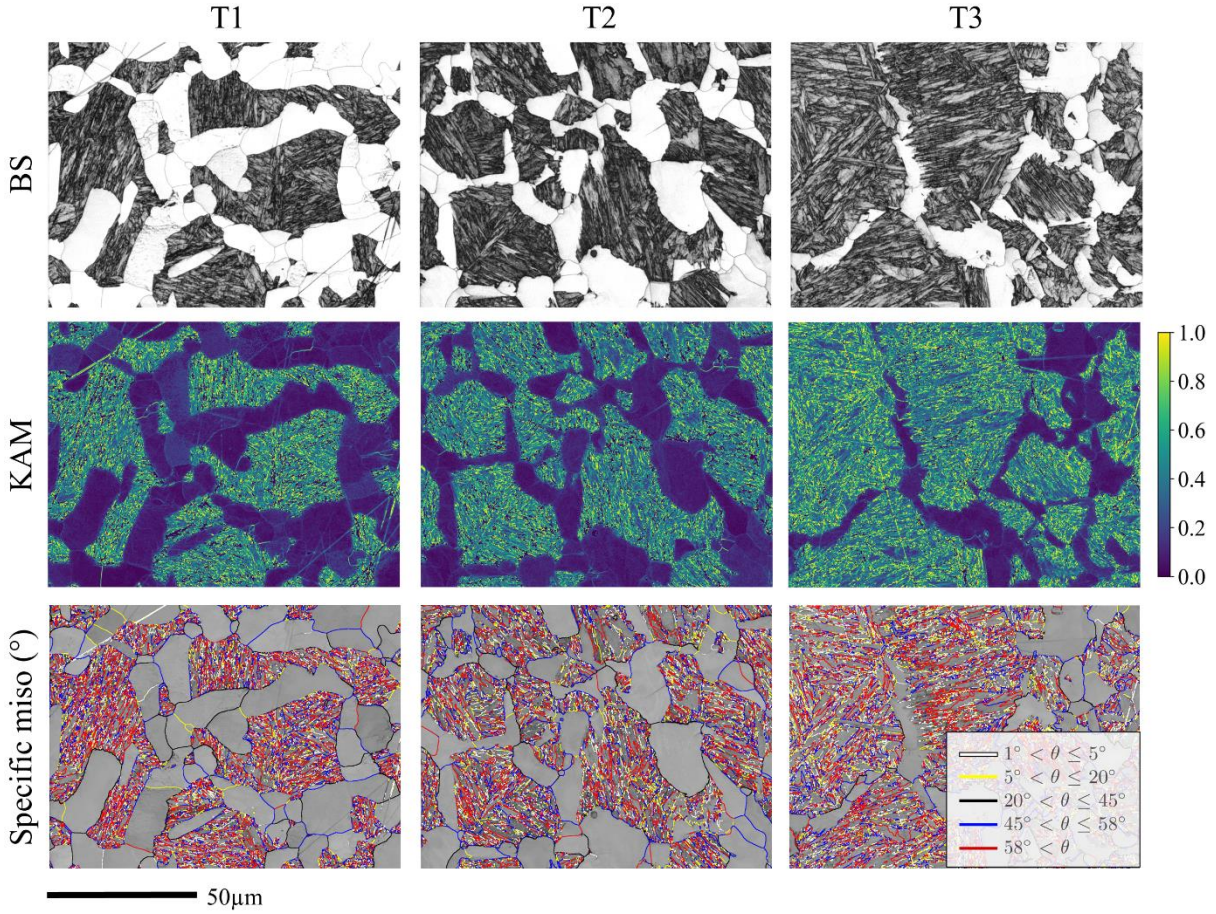

Figure V.4. BS, KAM and specific misorientation maps from each type of DP samples T1, T2 and T3. The KAM maps were computed using a 3×3 kernel ignoring misorientations greater than 3° and non-indexed pixels. The scale has been limited to 1° to better visualize the contrast between the different constituents.

Although the ferrite-martensite discrimination is relatively simple, there may exist certain complex cases. The mentioned coarser and convex martensite domains shown in Figure V.2 present a higher pattern quality and lower KAM than lath-like martensite, what may cause some hesitation to discriminate them from ferrite. Another complex discrimination case appears when trying to define the exact interphase boundary between martensite and Widmanstätten ferrite, as the later precipitates at the PAGB and grows progressively into martensite sharing nearly the same orientation.

The labeling method is detailed in V.3.3.1. Figure V.5 (a) and (b) present the resulting BS and KAM histograms for each constituent respectively. The BS and KAM distribution for both phases are clearly distinguished with limited overlapping. This confirms that those EBSD-based parameters are efficient to discriminate martensite and ferrite in DP steels.

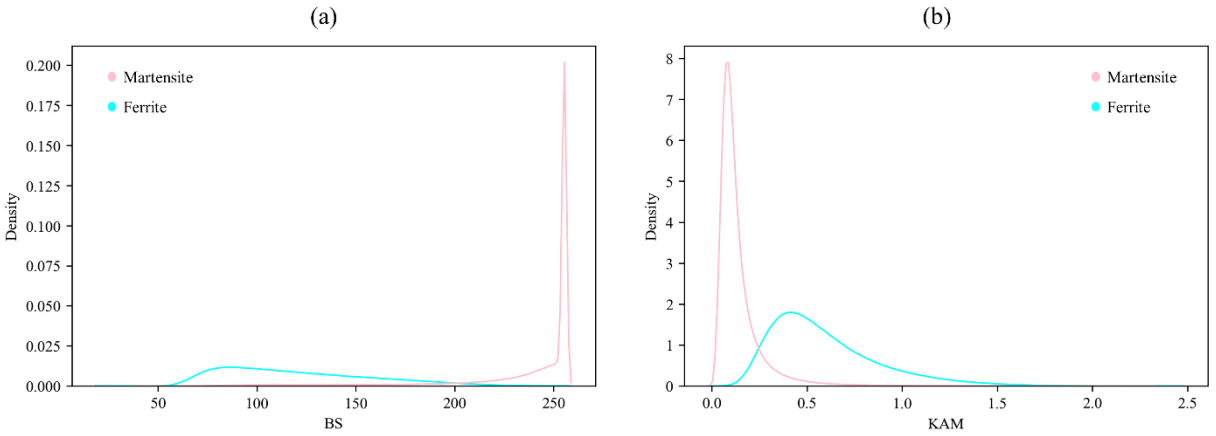

Figure V.5. (a) BS and (b) KAM values distributions for the labeled EBSD dataset acquired on DP samples.

V.3.2 Application to multiphase microstructures

In this case, the phase discrimination was not as straightforward as for the DP samples due to the presence of upper bainite that presents intermediate features between ferrite and martensite. The histograms of BC and KAM, obtained after labeling (as described in V.3.3) are presented in Figure V.6. The pronounced BC/KAM overlapping between the phases illustrates the complications when trying to use these parameters to distinguish the concerned phases.

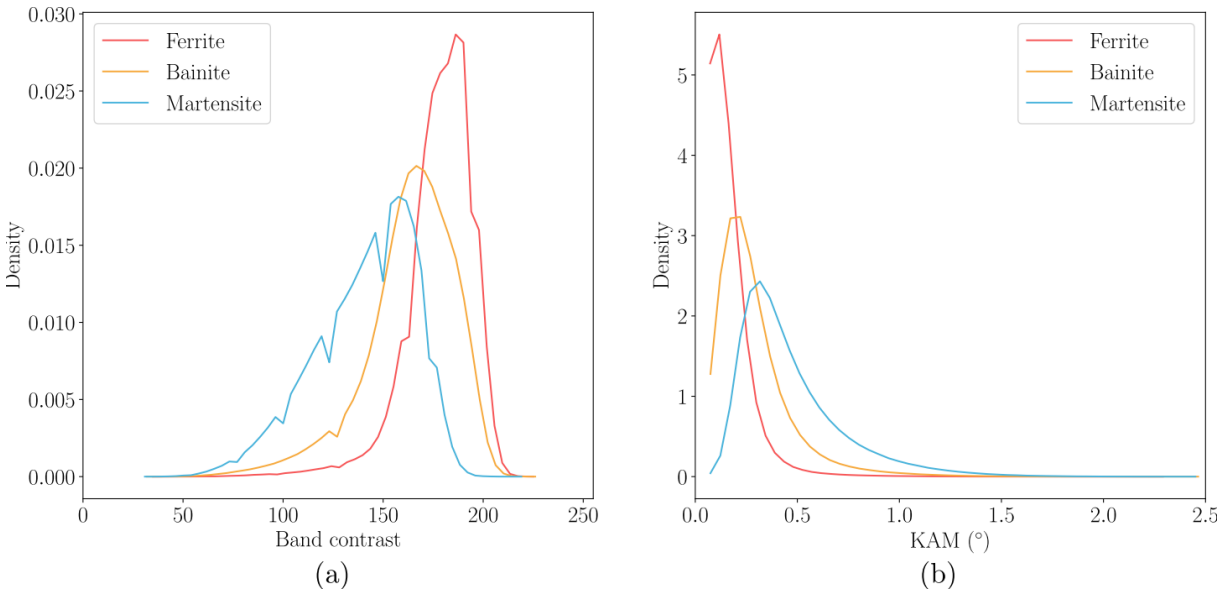

Figure V.6. (a) BC and (b) KAM values distributions for the labeled EBSD dataset acquired on the MP-samples.

Figure V.7 shows the crops of four representative maps from MP samples where the pattern quality (BC), the KAM and the specific misorientations images are presented. Martensite can be relatively well separated from the rest thanks to the much darker BC and the higher KAM values. The discrimination between ferrite and upper bainite appears to be more challenging. For example, both SA1 and API-1 microstructures are almost 50/50 mixed ferrite/upper bainite microstructures but looking at the BC, the gray level values are very similar for both. In terms of morphology, ferrite usually presents equiaxed grains whereas upper bainite ones are coarser, however this difference is not always clear. The most

pronounced difference appears for the SA1 sample using the KAM. Thanks to the increased density of dislocations inside upper bainite, the KAM may help in the discrimination with ferrite whose intragranular misorientation is very low. Unfortunately, the difference is less clear in the API-1 sample. The presence of a network of low angle boundaries between 0° and 5° as shown in the specific misorientation maps is a characteristic of upper bainite. Nevertheless, it may happen that certain grains present low KAM values and equiaxed shapes but with the presence of some low angle boundaries between 0° and 5°. Other ambiguous cases may be related to the interphase boundary, as there are grains that initially precipitate as ferrite and can then progress continuously into upper bainite during transformation, becoming difficult to establish where does exactly one phase gives place to the other.

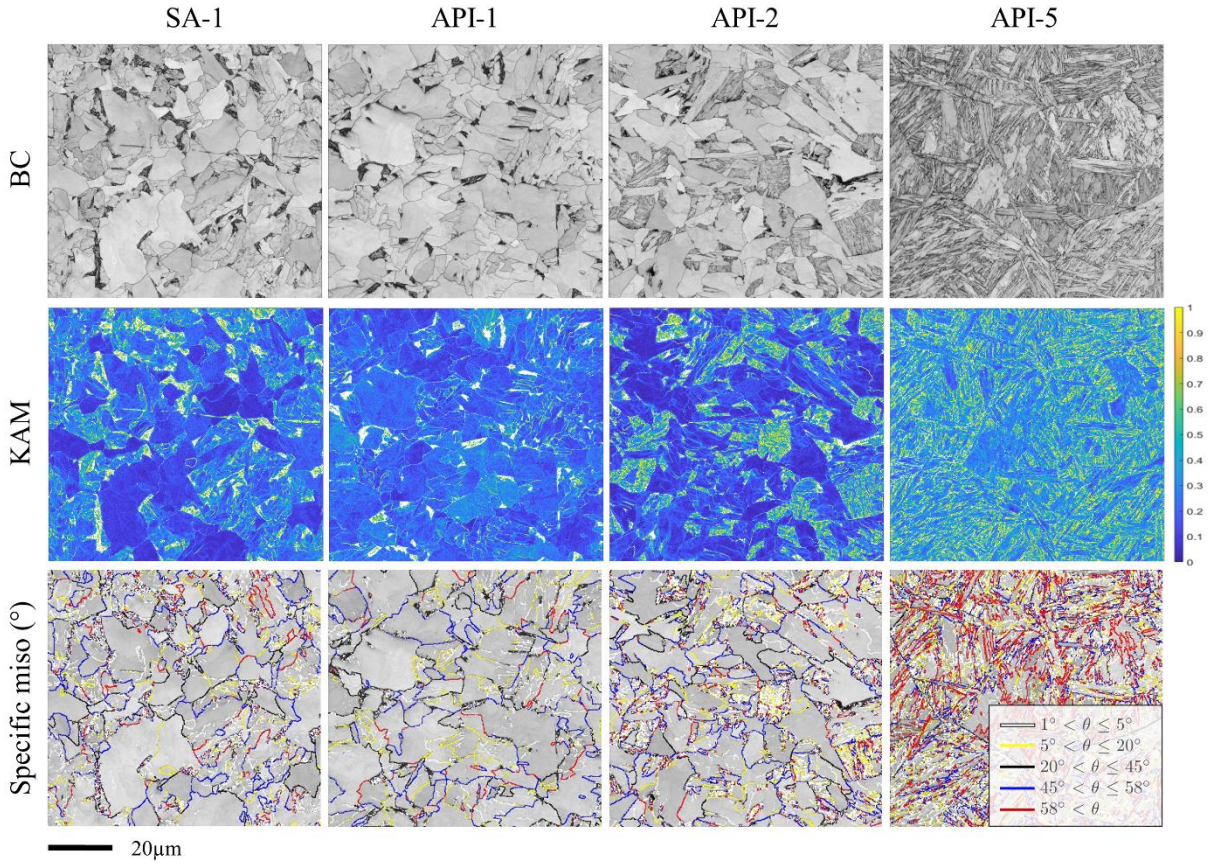

Figure V.7. Crops of the BC, KAM and specific misorientation maps from each of the MP samples labeled in the next section. The KAM maps were computed using a 3×3 kernel ignoring misorientations greater than 3° and non-indexed pixels. The KAM scale has been limited to 1 °to better visualize the contrast between the different constituents.

V.3.3 Labeling strategy

Supervised DL requires prior labeling. As explained in the literature review of Chapter IV, supervised approaches compare their results to the ground truth generated by humans in order to learn how to perform a task. The labeling stands for assigning to each pixel of an EBSD map the corresponding ground truth phase, namely ferrite, martensite or upper bainite. To do it so, we have used all the parameters described in the above section but also dilatometry curves and hardness measurements to have a rough estimate of the expected phases and their fractions.

On complex microstructures as in the case of the MP-steel, some particular grains were very challenging to label and we had hesitation to assign the ground truth phase. To overcome this difficulty, we have introduced an "unknown" class whose pixels are ignored during training. This makes the labeling process easier by not imposing a ground truth for ambiguous grains. As a consequence, these grains are not used to train the models what could be a drawback as some challenging configurations are not shown and therefore will not be explicitly learnt by the model during training. Thus, it is of interest to analyze the phase predictions proposed by the model over these complex cases and discuss their relevance (as detailed in V.6.1.3).

As one can imagine, this labeling task is not only very important, as the model learns from it, but also very complex and time consuming. It is important to remark that, although the labeling have been performed to the best of our abilities, the presence of mislabeling shall not be excluded.

V.3.3.1 Dual phase microstructure labeling

In this case, all the pixels in the maps have been assigned with the corresponding class "ferrite" or "martensite". The pixels identified as Widmanstätten ferrite have also been labeled as class "ferrite". The "unknown" class has not been needed for these less complex DP microstructures.

Our labeling strategy included three steps : (1) an automatic pre-labeling on pattern quality images using Trainable Weka Segmentation (TWS) [163], (2) labeling of indexed pixels using orientation based grain detection and manual corrections and (3) labeling of non-indexed pixels.

The pre-labeling using TWS was performed by training a classifier based on the BS images of the three maps shown in Figure V.4. The main idea of this tool is to manually label some regions that belong to ferrite and martensite which are then used to train a classification model (a Random Forest [132] classifier with all other settings left as default has been selected). This model has been applied to the entire dataset to obtain the pre-labeling and the result was applied on the whole set of EBSD data. Since this step does not rely on orientations, ferrite/martensite boundaries may not exactly match with grain boundaries as detected by EBSD.

Labeling of indexed pixels was carried out by performing first a grain detection and by allocating to each grain, the same label as the pre-label of the majority of its pixels (i.e. a grain with a majority of pixels pre-labeled ferrite was labeled as ferrite; martensite otherwise). This procedure allowed to adjust the pre-label interphase boundaries with orientation data. To handle also weakly misoriented interphase boundaries, the grain detection was performed using the AlGrID algorithm with a threshold angle of 2° and closing boundaries down to 0° [85]. Most of the remaining mislabeling concerned Widmanstätten ferrite / martensite interphase that could not be separated during grain detection even with AlGrID and manual corrections had to be performed. This makes Widmanstätten ferrite labeling somewhat subjective at the interphase boundary.

Although non-indexed pixels do not contain orientation data, we can infer to which phase they belong and label them. They were located either at the grain boundaries, in highly dislocated martensite or in M/A islands. In order to label the non-indexed pixels at the grain boundaries, a one-pixel closing operation (a dilatation followed by an erosion) was performed. Then, remaining non-indexed pixels were labeled into martensite. Some manual cleaning was performed afterwards to deal with non-indexed pixels appearing at ferrite grain boundaries but labeled as martensite because they were not eliminated by the dilate-erode operation. Another point to highlight is that non-indexed pixels are only labeled to generate the ground truth maps but they remain a non-indexed for the input data to train the model i.e. no cleaning of orientation data was performed.

In total, fifteen maps of 114.1×85.6µm (five from each sample) have been labeled for DP-samples with a fraction of 45% ferrite and 55% martensite in average. Figure V.8 shows the labeling obtained for the EBSD maps that have been presented in Figure V.4.

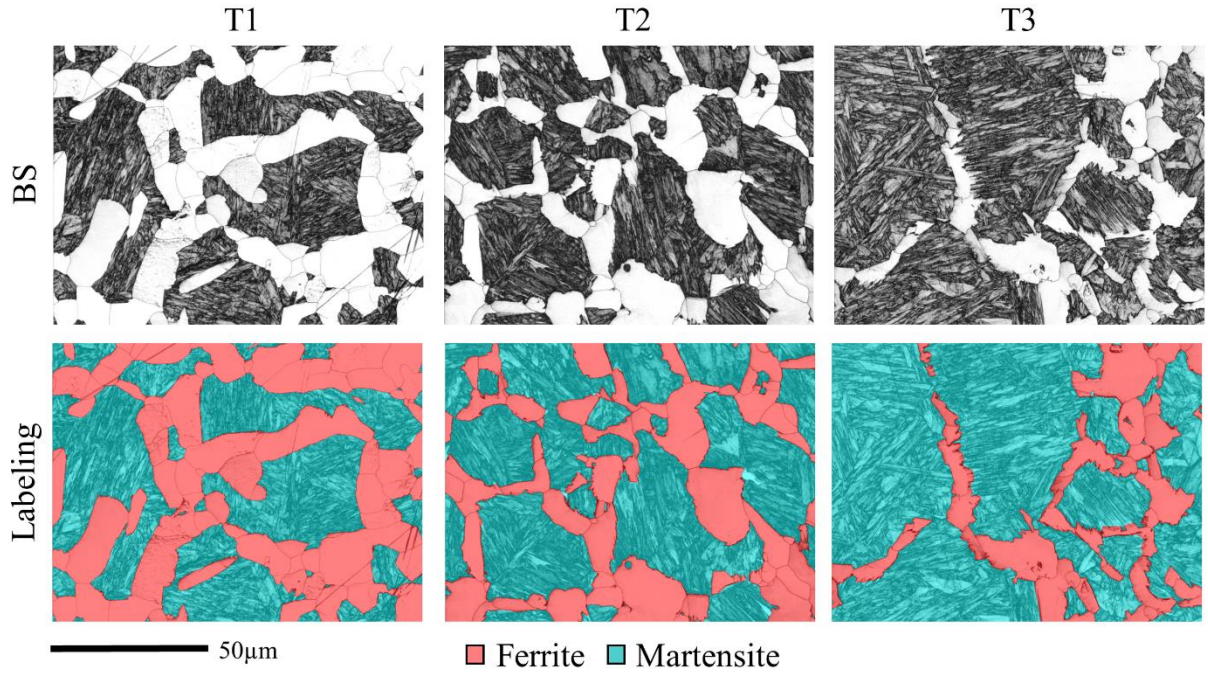

Figure V.8. BS and labeling images of three EBSD maps coming from each of DP samples (the same maps have been given in Figure V.4).

V.3.3.2 Multiphase microstructure labeling

In the case of MP samples, each pixel was labeled either as “ferrite”, “upper bainite”, “martensite” or “unknown” classes. As expected, the labeling complexity was higher than that of DP samples and manual corrections had to be performed at all steps. We started the labeling by thresholding the martensite grains based on their low BC values. Then using Merengue2 to reconstruct austenite allowed the identification of a significant fraction of ferrite grains that were not in OR with their surrounding grains (non-reconstructed grains in Merengue2). Finally, the KAM values were used to differentiate the remaining upper bainite from ferrite grains.

A final manual correction was performed based on grain morphology, KAM and amount of intragranular low angle boundaries. Pixels for which it was difficult to assess the ground-truth constituent were assigned to "unknown". These pixels belonged mainly to grains with intermediate features between ferrite and upper bainite. For instance, some equiaxed grains could be classed as ferrite but had a high density of low angle misorientations typical of upper bainite. Also, the difficulty of clearly defining some interphase boundaries was another reason to introduce the unknown phase. Non-indexed pixels have been treated exactly in the same way as described above for DP samples.

A total of eight 252×189µm maps (two maps from each SA-1, API-1, API-2 and API-5) were labeled and the resulting dataset was composed of 28% of ferrite, 25% of martensite, 44% of bainite and 3% of "unknown" pixels. Maps coming from API-3 and API-4 have not been labeled. Figure V.9 shows the labeling obtained for the crops of EBSD maps that have been presented in Figure V.7.

It must be noted that for both SA-1 and API-1 samples, the phase fractions provided by Industeel based on microscopy, hardness and dilatometry analysis (Table V.3) did not consider the presence of martensite. The possibility to work with EBSD data provides the advantage to better identify the present phases in the microstructure being possible to detect the small fraction of martensite present in these samples.

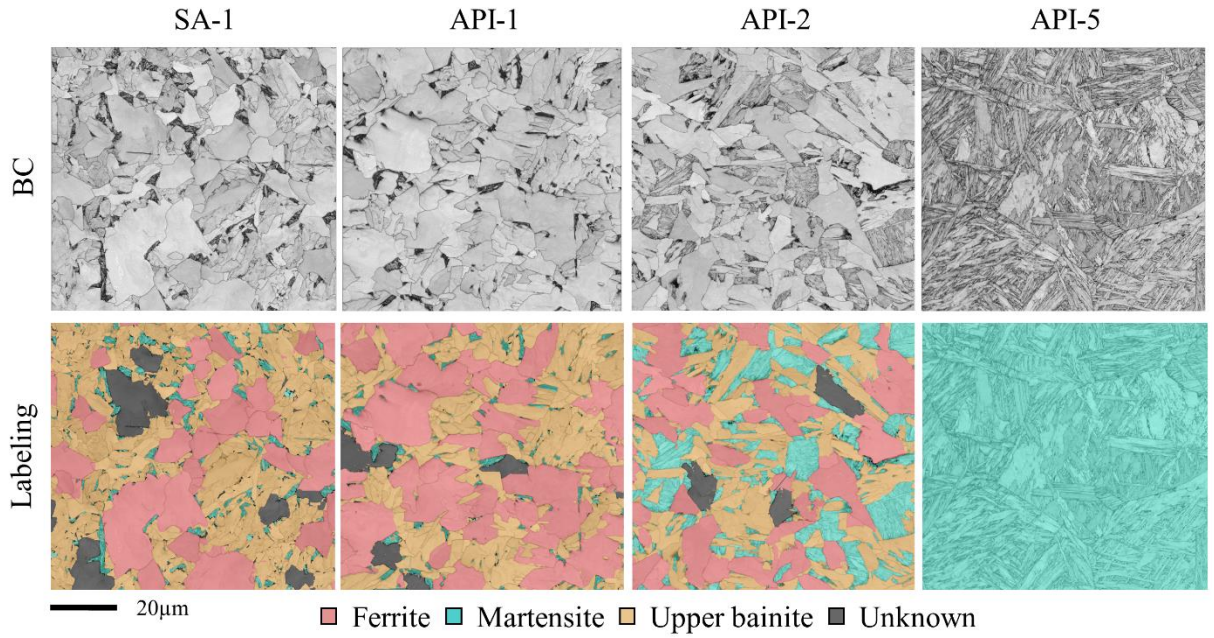

Figure V.9. Crops of BC maps and labeling images from each of the four MP labeled samples (the same crops have been presented in Figure V.7).

V.4 Deep learning strategy for semantic segmentation

As detailed in the literature review of Chapter IV, the aim of a semantic segmentation approach is to classify every single pixel of an image into a class and thus, be able to evaluate the phase fractions and the spatial distribution of the constituents that will affect the properties of the concerned steel.

V.4.1 Convolutional Neural Networks

The main idea of CNNs is to apply convolutional filters to an image in order to detect particular features that may help to discriminate the classes appearing in the image. Figure V.10 (a) shows the BS image of a T1 sample and Figure V.10 (b) and (c) present the 3x3 convolutional filters used to detect horizontal and vertical edges respectively, together with the feature images. Those filters show that many edges are located in the martensite domains compared to ferrite. These two features can be used by our network to discriminate both classes. It is important to remark that CNNs find these filters automatically during the learning process i.e. it adjusts the filter weights during back propagation. As a result, it converges toward filters that extract the most meaningful features that characterize the classes.

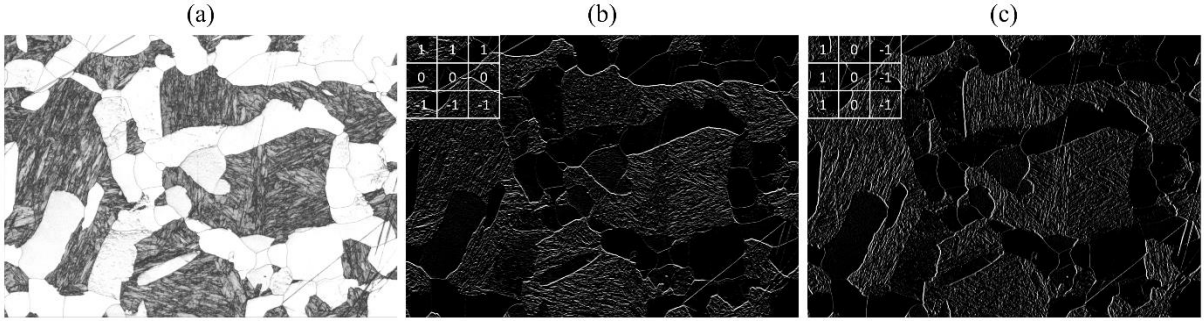

Figure V.10. (a) BS of a T1 sample map and feature maps together with the corresponding 3x3 convolutional filters for the detection of (b) horizontal edges and (c) vertical filters.

Something to consider when applying convolutional filters is how to handle the pixels at the borders for which the kernel goes beyond the image pixels. These are handled by adding a buffer of pixels all around the image this operation is called padding. The added pixels could be zeros, or could mirror the image. The strategy chosen here is called “padding same” and results in padding with zeros.

V.4.2 U-Net adapted to EBSD maps

We have selected a CNN with a U-Net architecture. This architecture has been developed by Weng et al. and was presented in 2015 to perform the segmentation of biomedical images [11]. As suggested by its name, it presents a U-shape with an initial contracting path called encoder followed by an expansive path called decoder. The encoder path serves as the feature extractor and the decoder is used to recover the original size of the input image what enables semantic segmentation. There is a main advantage of the U-Net compared to a similar architecture such as SegNet [164] and it is the presence of the so-called skip connections. These enable the combination of high-resolution features extracted from the encoder path with the expansive path to increase the resolution of the upsampled output.

In the encoder, two main operations are performed: 3×3 convolutions and 2×2 max pooling. The dropout is optional (but recommended) and will be explained in V.4.4.

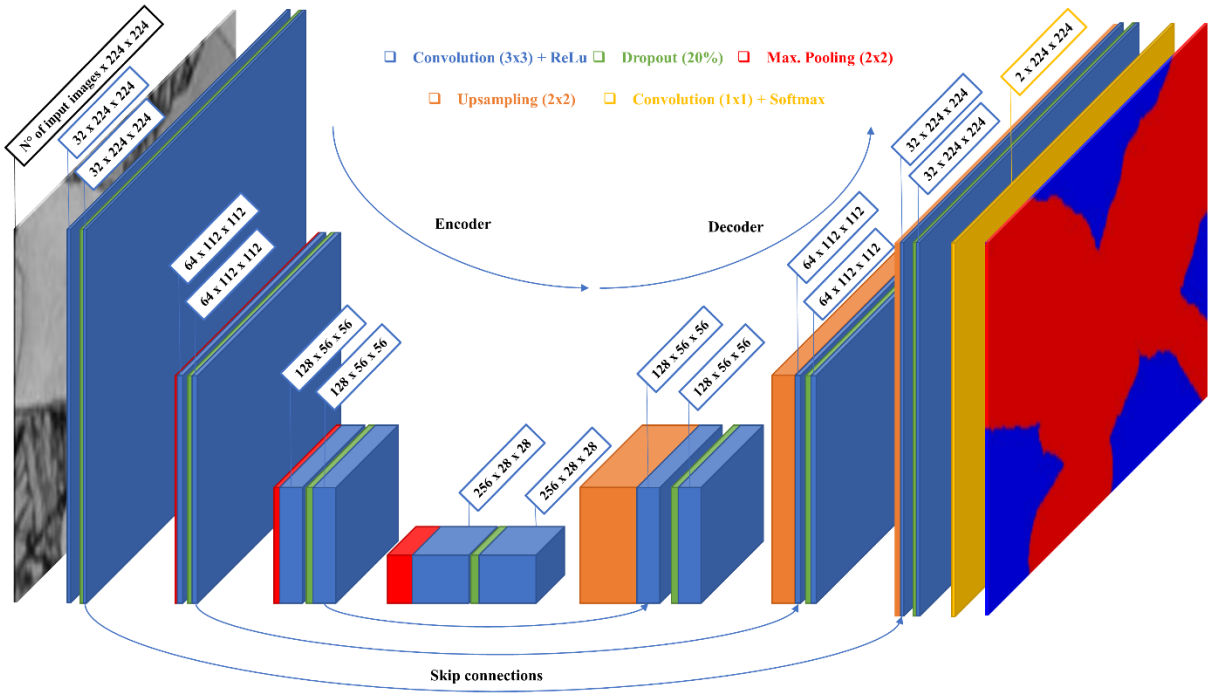

Figure V.11. Scheme of the U-Net architecture developed and implemented to segment DP samples.

V.4.2.1 Our UNET- architecture

Figure V.11 shows the schematic representation of the U-Net developed and implemented to segment our microstructures. This architecture has been adapted in order to enable the input of EBSD data. Initially, two layers of 32 convolutional filters of 3×3 pixels are applied over the input images of 224×224 pixels with a padding "same" strategy to the input images in order to detect low level features of the microstructure such as lines, edges, contours, among others. These filters are initially white noise and they are learnable parameters of the architecture, i.e. we do not predefine the filters values. The application of these two layers of convolutional filters provides 64 feature maps that will be max. pooled before being input to the next convolutional block. A max. pooling operation reduces the resolution of the feature maps by a factor of four, resulting in 64 feature maps of 112×112 pixels. Here two layers of 64 convolutional filters of 3×3 pixels are applied. As one can imagine, if the size of the convolutional filter is kept but the resolution of the feature maps is reduced, our filters will capture features from a larger neighborhood by combining the features detected beforehand. Therefore, as we move deeper into the architecture, the detected features become increasingly complex. This is the reason why we increase the number of filters after each convolutional block, so we can capture as many combinations of filters as possible to detect complex features. Once the central convolutional block is reached (256×28×28), the encoder path finishes and gives place to a symmetric decoder path where the max. pooling is replaced by upsampling i.e. the resolution of the feature maps is increased by a factor of two. Once the last convolution layer of the decoder is attained, a single pixel convolution is applied to map each 32-component feature vector to the desired number of classes, here ferrite and martensite. Finally, a Softmax layer is used to assign the predicted class to each pixel of the image by the highest probability,

it is a mathematical activation function that converts a vector of numbers into a vector of probabilities [193].

It is important to remark that not all the applied filters extract meaningful features and these are inhibited by an activation function that is placed after each convolutional layer. The selected activation function has been the rectified linear unit (ReLU) activation function, which is a linear function that outputs a zero if the input is negative (not meaningful filter) or outputs the input if the input is positive (meaningful filter) [194].

The scheme shown in Figure V.11 corresponds to the architecture developed for DP samples, formed by 7 convolutional blocks (4 blocks belonging to the contracting path while 3 to the expansive path). For MP samples, the number of blocks was increased to 11, where 6 belong to the contracting path and 5 to the expansive one.

V.4.2.2 EBSD maps as input data

This architecture has been adapted to enable inputting a stack of images, i.e. it is possible to load the BC map together with the corresponding KAM map to train a model based on two parameters. The only condition that the image must fulfill is that its sides must be multiple of 2^n, with n the number of max. pooling operations in the U-Net. In our case, 224×224 pixels image size has been selected, allowing a maximum of 5 max. pooling operations. This is the input size for the most known CNNs, enabling a high number of max. pooling operations but keeping a small size that allows saving memory during training. Another advantage of using crops is the shuffling of the data, as it allows to randomize the input so that the network does not see all similar microstructures at once.

Two different types of input data extracted from EBSD acquisition have been used to train our U-Net: EBSD-based parameters and raw orientation data.

EBSD-based parameters

Three EBSD parameters have been considered to train the models: BS, BC and KAM. All of them have been normalized so that their distribution over all maps was centered at 0 with a standard deviation of 1, since it has been demonstrated that it improves models training [195]. The KAM has been calculated with a 3×3 pixels kernel size and a threshold angle of 3° and non-indexed pixels were assigned with a zero KAM.

Raw orientation data

Additionally, we wanted to assess the ability of a CNN (here U-Net) to process raw orientation data and translate it into meaningful parameters analogous to those the experts use. For this reason, we have also use raw orientation data in the form of quaternions to train our U-Net. One advantage of using raw orientation data, against BS, BC or KAM, is lesser dependency to the acquisition conditions. Introducing such input data, one could expect the network being able to extract by itself the relevant orientation

information such as local misorientation, specific misorientation boundaries including angle and axes, etc.

Quaternions have been selected to express orientation data and they have been already defined in I.3.1. Several reasons have motivated the choice of quaternions: 1) their components are naturally in the range [−1,1], 2) quaternions-based computations (misorientation, averaging, etc.) involve only linear operations (products and additions), 3) they are very practical for high symmetry (cubic) computations [196] and 4) they are widely used by the EBSD community [8], [197]–[199]. Quaternions can be loaded to our U-Net with no issues since it has been adapted to receive a stack of any number of images.

One drawback when dealing with orientations is the presence of crystal symmetry. A cubic crystal has a total of 24 symmetries. This means that a single orientation can be defined by 24 different quaternions, each of them being a symmetric rotation of the other one. Therefore, it may happen that within a grain there exists two (or more) different quaternions that express the same orientation but that break the continuity of the orientation space across the detected grain. For this reason, all the quaternions contained in a grain have been rotated to be expressed with the same symmetry equivalent. Figure V.12 shows the difference in the q2 component map of a sample of T1 between raw quaternions and rotated quaternions with the same symmetry equivalent. The encircled ferritic grain is a clear example of the described problem. To perform the rotation, the first pixel of the detected grain acts as a reference and imposes its symmetry element for the rest of pixels forming the grain. Non-indexed pixels have been assigned with a quaternion whose components are all zero values.

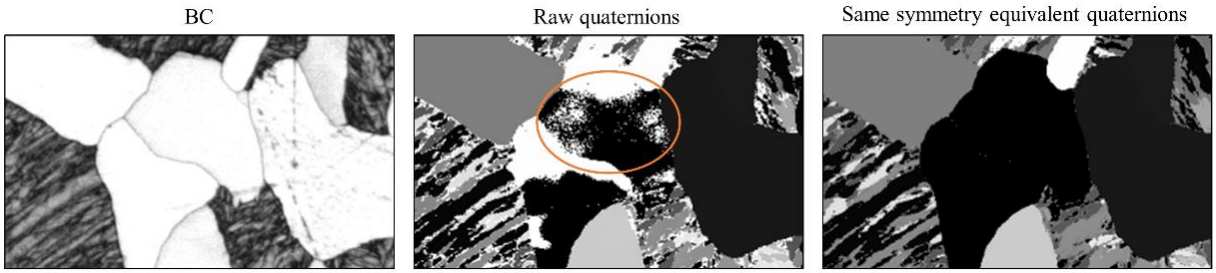

Figure V.12. Crop of an EBSD map from the T1 sample where the difference between expressing the raw quaternions and their rotation is highlighted.

The final result after quaternions preprocessing is shown in Figure V.13 for the example case of a T1 map. In q1 the non-indexed pixels are highlighted in black and it can be clearly seen that they correspond to the martensite domains. On the other hand, q2, q3 and q4 look relatively similar and they highlight the higher density of grain boundaries due to the lath like structure of martensite domains. Nevertheless, the discrimination between ferrite and martensite based only in the quaternions components does not appear to be as straightforward as using pattern quality or KAM.

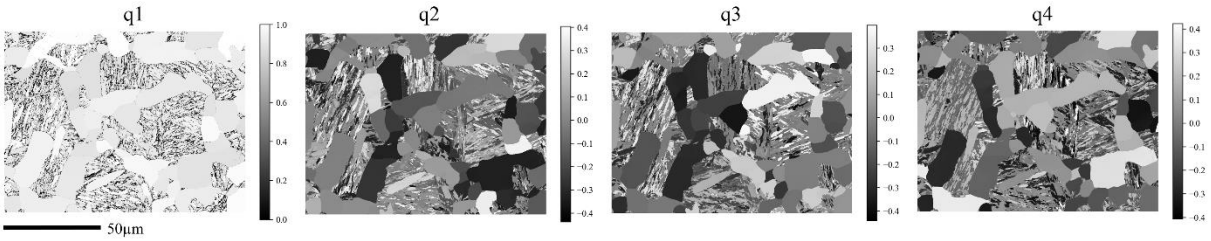

Figure V.13. Quaternions components as they are input to the U-Net (T1 map).

V.4.3 Robustness against the map step size

It has been stated in V.3.1, that the KAM is affected by the step size with which the EBSD map has been acquired. We would like our U-Net model to be robust against step size variations and for this reason we have applied a strategy in order to make the model aware about the acquisition step size of the input EBSD map. The strategy consists in adding one additional image to the stack of input images (BC, BS, KAM, etc.) containing the acquisition step size as the value of all the pixels in the image. The effect of this additional image has been evaluated for the case of MP-samples and will be detailed later in V.6.3.2. Such approach is similar to that performed by Facil et al. [200] to generalize a CNN prediction to different cameras, but to our knowledge, it is the first time that the pixel size is provided to a CNN in order to make it "aware" of the "scalebar" of the acquired map.

V.4.4 Training our U-Net

Figure V.14 shows a scheme of how a DL model is usually trained and the details concerning our U-Net are described below. First the training dataset is fed into the network to perform an initial classification. This result is compared against labeling to adjust the model's parameters. This step is called backpropagation learning and we have selected the stochastic gradient descent [201] method "adadelta" [202] to carry it out. The model performance is measured by a loss function, that measures how far an estimated value is from its true value, the smaller the loss, the higher the accuracy. We have selected the "Categorical Cross Entropy" loss function [203].

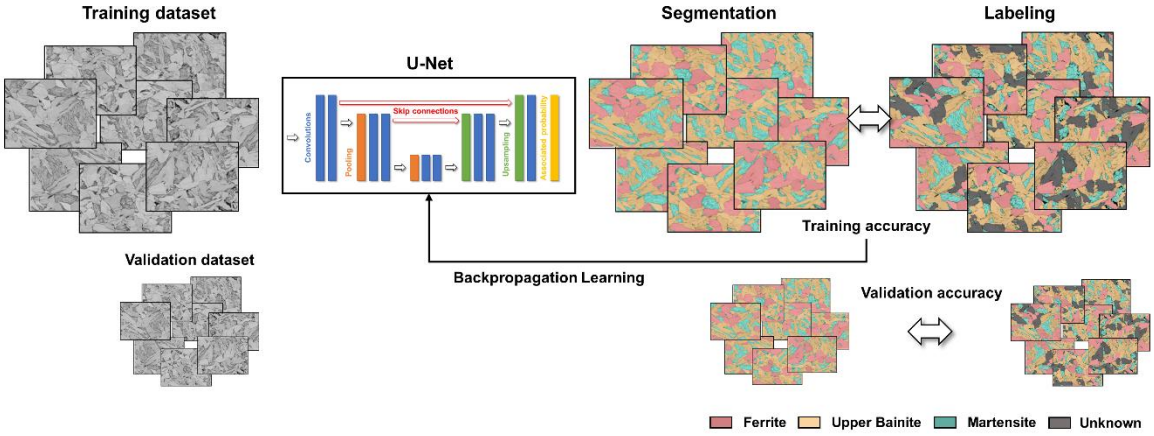

Figure V.14. Scheme of a classic U-Net training.

Once all the training dataset has been seen, the trained model is used to classify the validation dataset. This dataset was not shown during training but it is only used to evaluate the model's performance on unseen data and prevent overfitting. The validation dataset is usually a small fraction of the training one (training and validation ratio is usually 80-20). After one epoch of training, both the training and validation loss are very high. The number of epochs stands for the number of times the network has seen the entire training dataset. A network is trained for several epochs until the performance reach a steady state on the validation dataset.

As soon as a satisfactory accuracy is obtained, the final model is saved and its performance must be evaluated on a third dataset called testing. U-Net can be advantageously applied to any input size during testing and it is not constrained by the input size used during training. Thus, the entire testing map can be fed to the network. This avoids the need to perform the segmentation on several small 224×224 pixels crops and reconstruct the whole map afterwards, which induces a quality loss in the result due to border effects.

Once the training process has been explained, it makes sense to talk about the dropout layers presented in Figure V.11. Dropout is a regularization technique to improve the generalization ability of the network [204]. During training it may happen that some filters get high weights and conducts the model to reach local minimums where learning gets blocked. To avoid this issue, dropout is applied, where the idea is to randomly ignore or drop some filters i.e. temporarily remove them from the network, along with all the incoming and outgoing connections [204]. In our case, we have used a 20% dropout meaning that for each epoch 20% of the filters are randomly deactivated.

The U-Net implementation and training was coded in Python using Tensor Flow [205] and Keras [206] libraries. All the models have been trained on a desktop computer equipped with an Intel Core i5-8250U CPU @ 1.60GHz, 16Gb of RAM memory without using the graphic card. All the computation times expressed on this manuscript are relative to the aforementioned computer.

V.4.5 Dataset generation

V.4.5.1 Dual phase microstructure

For each of the three DP samples, two EBSD maps were randomly selected among the five available to build the training dataset. As stated in V.3.3.1, the dataset is balanced with nearly the same fraction of ferrite and martensite in the maps. Nine maps (three maps per sample) remained as testing set.

In order to increase the size of the training dataset, data augmentation techniques adapted to EBSD data were employed. Both BC and BS undergone classic data augmentation operations such as 90°, 180° and 270° rotations together with horizontal and vertical mirroring of the entire image. For the data augmentation of the orientation data, we have also applied the rotations quaternions-wise to keep the

coherency of the habit plane and special boundary traces. This makes orientation data augmentation a bit more complex.

The resulting maps, six original training maps plus their augmentations, have been cropped in 224×224 pixels crops and randomly shuffled. From this dataset, 80% of the crops have been used to train and 20% to validate.

V.4.5.2 Multiphase microstructure

For MP samples, each one of the eight labeled maps were cut in half horizontally. The top half was used as training dataset while the bottom half was kept for testing the model on unseen data. In this case, data per class was not as well balanced, with a higher percentage of upper bainite (44%) than ferrite and martensite (28% and 25% respectively). This is not recommended when training any ML or DL model and may affect the final result leading the algorithm to slightly overestimate upper. However, in our case this did not seem to introduce a measurable bias.

Data augmentation over the training dataset have been performed as described in V.4.5.1 for DP-samples. Additionally, in this case we have considered the variation of the KAM with the step size. For this reason, a resolution reduction of the maps was performed to mimic different step sizes and provide robustness to the trained model against step size variations. A resolution reduction by a factor of three was performed, resulting in input step sizes of 0.1 and 0.3µm.

The resulting maps were as well cropped in 224×224 pixels crops, randomly shuffled and split in training and validation dataset with an 80-20 ratio.

V.4.6 Performance evaluation metrics

A pixel-wise comparison between the ground truth labeling and the models' prediction was performed. A prediction per pixel was considered correct when it matched the assigned label. The pixel-wise accuracy is described as the fraction of correctly predicted pixels among the whole number of pixels within the considered dataset. When required, a confusion matrix has been plotted to allow an in-depth visualization of the misclassifications. For an explanation of what a confusion matrix is, see II.3.4. Additionally, the predicted phase fractions have been compared with those obtained after labeling.

V.5 Segmentation results on dual phase microstructures

V.5.1 Performance of the models trained on EBSD-based parameters

V.5.1.1 Training and validation datasets

Using the DP-samples, three models were initially trained based on BC, BS and KAM. The models' performances on the training and validation datasets are presented in Table V.5, showing accuracies above 98% in all the cases. The respective training and validation accuracies for each model are almost identical which indicates that the models did not overfit the training dataset.

Table V.5. Final accuracies [%] reached by the three models on the training and validation datasets – DP samples.

Dataset	BS	BC	KAM
Training	98.13	98.53	98.62
Validation	98.50	98.40	98.51

The training and validation accuracies have been evaluated during the entire training process to exactly know when it was necessary to stop the learning as described in V.4.4. Figure V.15 shows the training and validation accuracies against the number of epochs for the three models. High accuracies, above 90%, were achieved by all the models at early stages of the training process. At 15 epochs, both training and validation accuracies started to converge to the values presented in Table V.5, and at 30 epochs the learning procedure was stopped. Each epoch took ~700s to be completed.

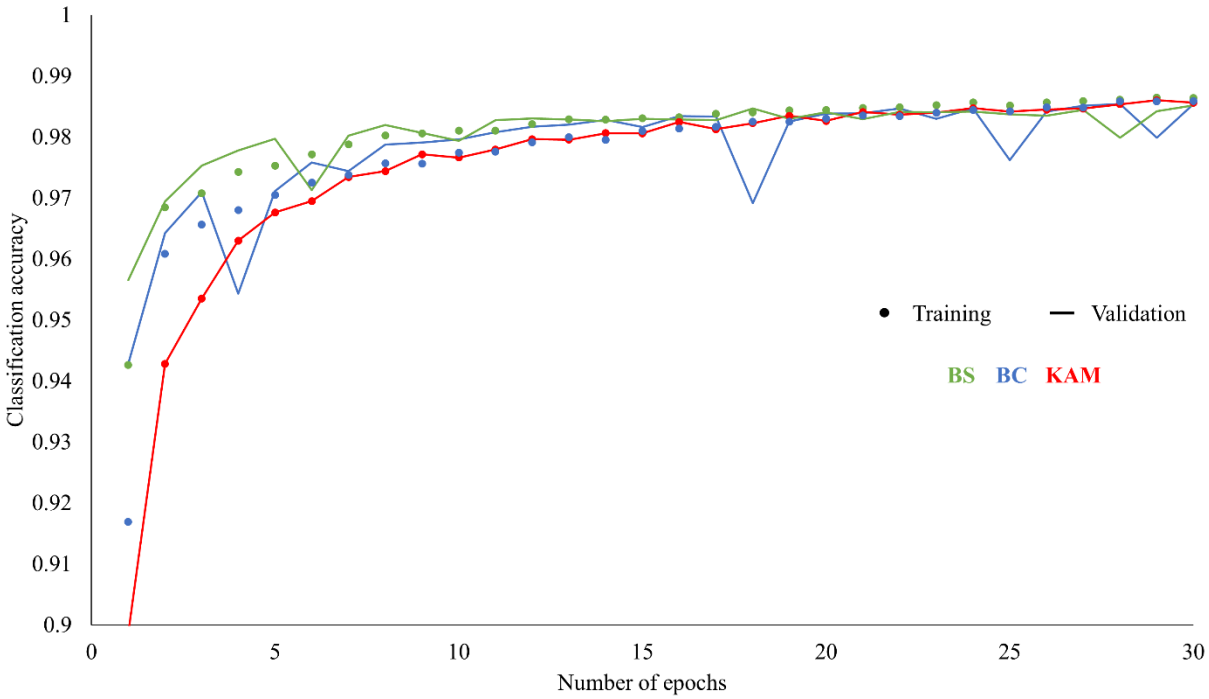

Figure V.15. Training and validation accuracies of the three trained models plotted against the number of epochs.

V.5.1.2 Testing dataset

The obtained models have been used to segment the testing dataset and the pixel-wise accuracies are visualized in the confusion matrices of Figure V.16. All the models are able to segment a testing EBSD map with an average accuracy above 98%. The computation time was of in the order of seconds once the desired model is loaded and the input image is available. The obtained accuracies are very close to those of the training and validation datasets presented in Table V.5 what highlights the robustness of the models since they can generalize to the new examples appearing in the testing dataset. For the BS and BC-based models, the greater part of false predicted pixels was found as false ferrite, indicating a higher complexity to correctly classify martensite than ferrite. The false predictions performed by the KAM-based model are equilibrated, what indicates that this model classifies martensite as good as it does for

ferrite. Although all three models reach excellent accuracies, the KAM-based one appears to be the best in average.

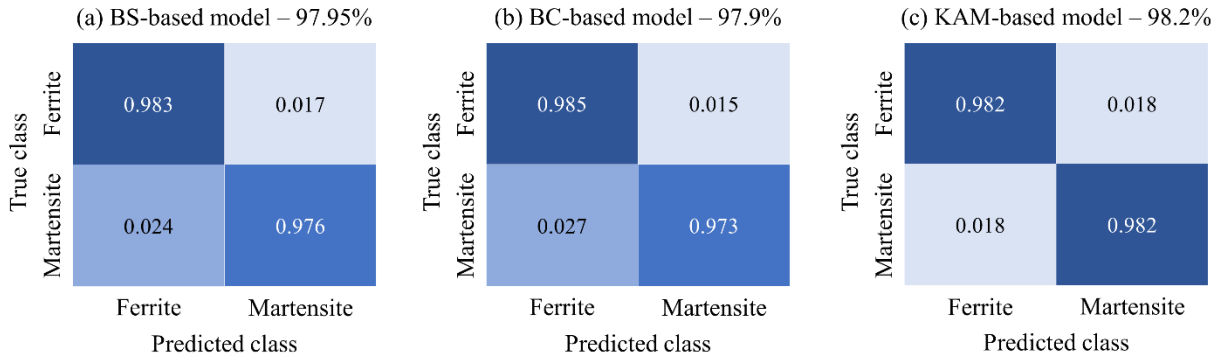

Figure V.16. Confusion matrices of the (a) BS-based model, (b) BC-based model and (c) KAM-based model over the testing dataset.

The accuracies and the misclassifications highlighted by the confusion matrices in Figure V.16 can be visualized in Figure V.17 on an example testing map belonging to the T3 sample. In the accuracy maps, correctly classified pixels are in white, false ferrite in cyan and false martensite in red. The obtained accuracies for all the models are in the order of those presented in Table V.5. For this particular map the KAM-based model slightly outperforms both the BS and BC-based ones. However, the greater fraction of errors for the KAM-based model corresponds to false ferrite and it is not equilibrated with false martensite as shown in Figure V.16 (c). It must be reminded that the misclassifications obtained on the confusion matrices are averaged along the entire dataset, thus each map is a particular case.

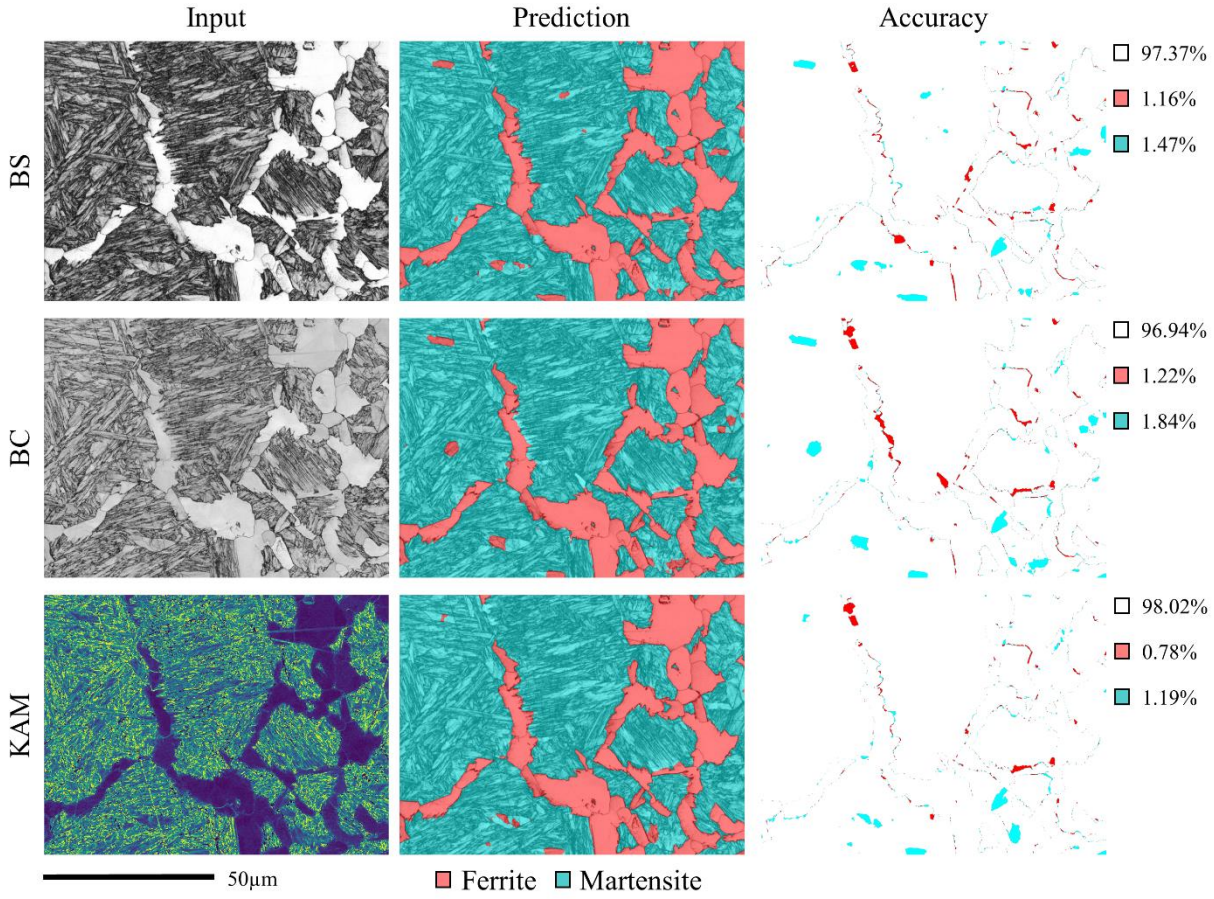

Figure V.17. Prediction and accuracy results for a map belonging to the T3 sample with the BS, BC and KAM-based models. In the accuracy maps, accurately predicted pixels are in white, false martensite in red, false ferrite in cyan.

V.5.1.3 Model trained on coupled inputs

Although the attained accuracies by the BS, BC and KAM-based models are high, one can ask if coupling inputs can still provide any further improvement. As BS and BC are same nature parameters, the BC was ignored in this assessment, thus a BS+KAM-based model has been trained. The testing accuracy and the misclassifications are shown by the confusion matrix in Figure V.18 (a). Although there is a little increment in the percentage of false martensite, a significant reduction of false ferrite is reached, making this model slightly better than its predecessors. This can be visually confirmed by comparing the accuracy images of the T3 map (Figure V.18 (b)) that has been already presented in Figure V.17.

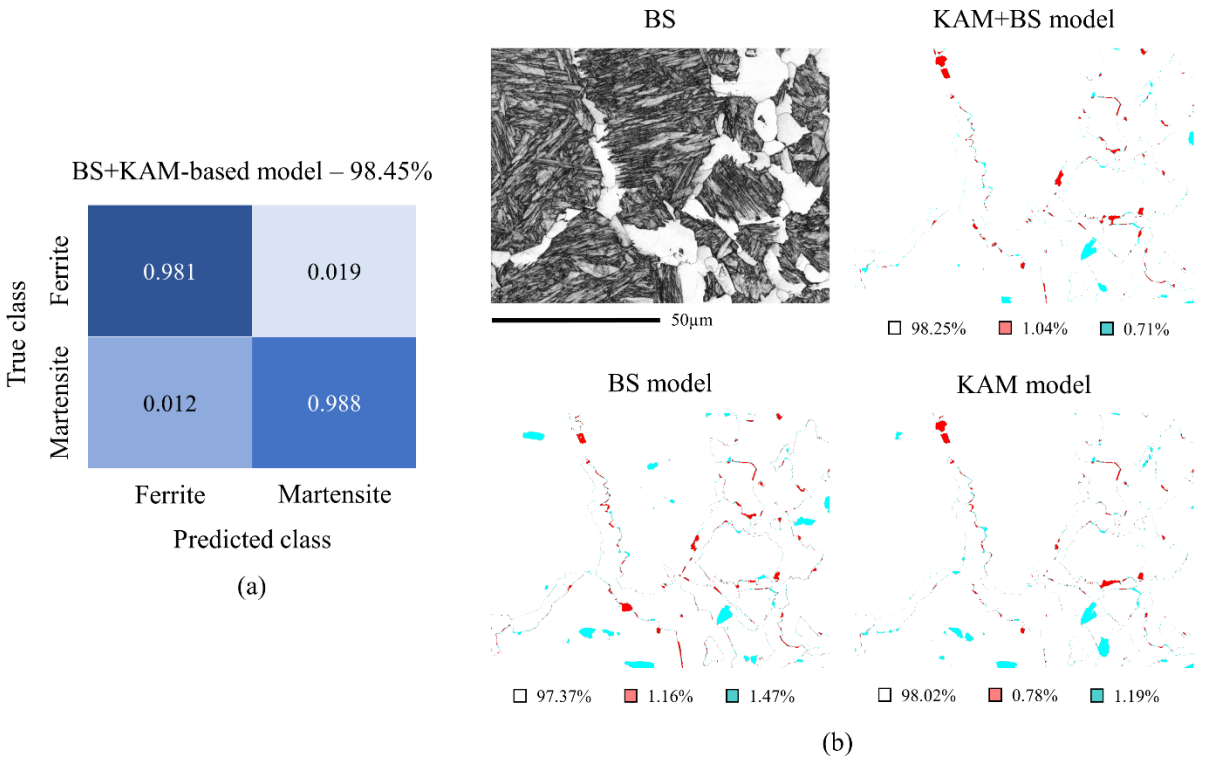

Figure V.18. (a) Confusion matrix over the testing dataset for the BS+KAM-based model. (b) Accuracy images over a T3 map for the BS, KAM and BS+KAM-based models. In the accuracy images, accurately predicted pixels are in white, false martensite in red, false ferrite in cyan.

This model has been used to calculate the phase fractions of the EBSD maps that comprise the testing dataset and the result has been compared to the ground truth labeling. As expected, the obtained phase fractions perfectly match the ground truth.

V.5.1.4 Effect of the microstructure's complexity

As presented in V.2.1, DP samples presented different fractions of ferrite and martensite upon the heat treatment they underwent. Additionally, T3 sample presented a particular form of ferrite called Widmanstätten ferrite whose discrimination from martensite is not so evident. This results in the complexity of segmenting the microstructures of the different samples not being exactly the same. Thus, the result obtained in Figure V.18 (a) will be broken down into the particular performance obtained for the BS+KAM-based model in each particular sample.

Table V.6 shows the accuracies per sample averaged over the three testing maps for the BS+KAM-based model. The highest accuracy was reached for T1, followed by T2 and T3. Cooling down to higher holding temperatures provided more complex microstructures with a higher fraction of martensite, that is more complex to classify than ferrite. As mentioned above, the difficulty to classify Widmanstätten ferrite also plays a role by increasing the complexity of T3 samples and reducing the attained accuracies.

Table V.6. Accuracies [%] per sample averaged over the three testing maps for BS+KAM-based models.

Sample	T1	T2	T3
Accuracy	99.43	98.92	97.39

Figure V.19 shows three EBSD maps, one for each DP sample together with the segmentation result obtained by the BS+KAM-based model. Starting with the T1 sample map (Figure V.19 (a)), the model reached an excellent accuracy (99.58%). Although this is a simple microstructure that could be easily segmented with classic approaches, it must be remarked that our model is robust to sample preparation artifacts as those scratches appearing in the top-left and bottom-right corners that are very visible with low BS and high KAM values.

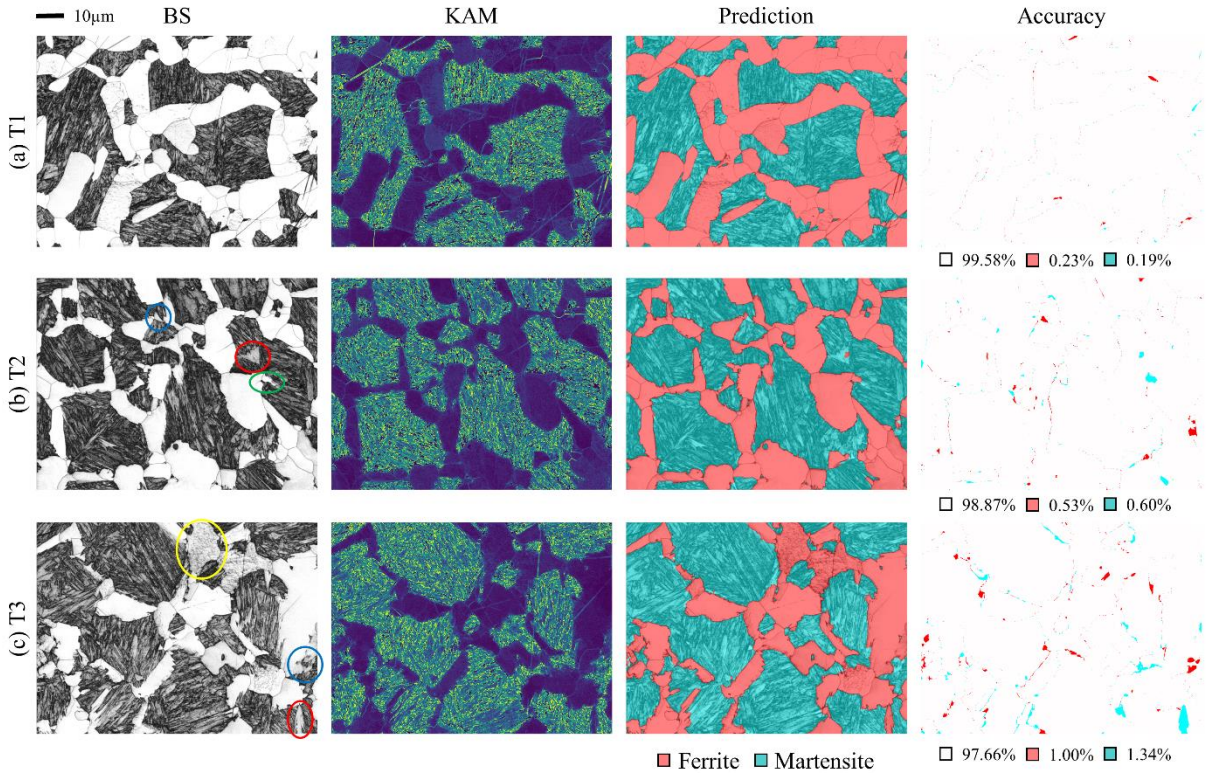

Figure V.19. Segmentation prediction and accuracy images obtained with the BS+KAM-based model over three EBSD maps belonging to each of the DP samples. In the accuracy images, accurately predicted pixels are in white, false martensite in red, false ferrite in cyan.

For the T2 sample map (Figure V.19 (b)), the accuracy remains very high (98.87%) but we can observe a microstructure with a higher fraction of martensite domains containing some coarse martensite grains differing from the classic lath like martensite. An example of these coarse grains is encircled in red in the BS image and it is one of the few areas where the model fails. Additionally, false martensite also appears (encircled in blue in the BS), in small ferrite grains neighboring martensite where the pattern quality gets lowered maybe due to due to pattern overlapping and higher dislocations density. However, there are other few regions, as the one encircled in green, where the model highlighted labeling errors. Interestingly, a model can sometimes outperform our labeling and help us to highlight labeling mistakes that can be corrected before retraining the model.

The map coming from sample T3 (Figure V.19 (c)) is the one showing the most complex features and therefore our model attained the lower accuracy compared to the above cases (97.66%). As for Figure V.19 (a), in this case the model is also robust to sample preparation artifacts here appearing as sample

surface deformation of certain ferrite grains (encircled in yellow). The main part of the errors comes from the irregular shape of the boundaries (affected by the precipitation of Widmanstätten ferrite), some coarse martensite grains as the one encircled in green in the bottom-right corner of the BS image and the false martensite cases already mentioned for Figure V.19 (b) (highlighted in blue).

A last source of errors appearing in every map is at the interphase boundaries and is visible as thin colored layers in the accuracy map. Since labeling was based on orientation data (grain detection) it is not surprising that the BC and BS-based models do not find the edge of the phases so accurately. In this respect, the KAM is a bit better as it considers a threshold angle based on the misorientation.

Performance on external sample

To evaluate how the trained model performs on another DP microstructure, we tested it with a map coming from a sample with the same composition detailed in V.2.1 but that has undergone a different heat treatment: austenitization to 905°C followed by cooling in 5s to 640°C and a final quenching to room temperature. The map was obtained under the same conditions described in V.2.3 for the DP samples and the BS map is shown in Figure V.20 (a).

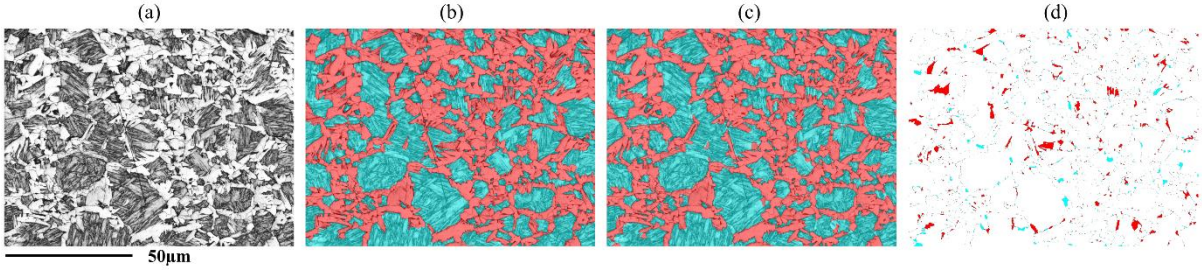

Figure V.20. (a) BS image and (b) ground truth labeling of a microstructure that does not belong to the original dataset. (c) BS + KAM-based model classification result and (d) accuracy map.

It can be observed a large fraction of martensite with complex lath shapes and different sizes, and in addition a great part of serrated ferrite/martensite interphases indicating a high fraction of Widmanstätten ferrite. This map looks rather different to what the model has been trained with and means an interesting challenge to segment. Labeling took over 2h to reach the final result shown in Figure V.20 (b). The segmentation result obtained by the BS+KAM-based model is presented in Figure V.20 (c) and the accuracy, over 95%, together with the misclassifications in Figure V.20 (d). The main fraction of wrong predictions are false martensite pixels (red clusters in Figure V.20 (d)). They come mainly from the wrongly classified Widmanstätten ferrite plates, since the models have not been trained enough on this kind of configuration. Although the result is not perfect, it is a very good approximation to the ground truth labeling.

V.5.1.5 Comparison to other state-of-the-art approaches

The results obtained by our U-Net have been compared to three other approaches proposed in the literature to address the phase discrimination of DP-samples. The first proposed method relies on finding a manual threshold that separates ferrite from martensite based on grain averaged pattern quality values

[61]. The second one is TWS, the method we have implemented to pre-label our microstructures. This approach has been proposed for optical micrographs segmentation in the past [162], [207]. The last method is the Reclassify Phase that appears as a functionality in the AZtec software [208] (already mentioned in the literature review of Chapter IV).

BS has been selected as the parameter to work with these methods. They have been applied on the three maps presented in Figure V.19 and the accuracies reached by each one are presented in Figure V.21. The best results on average over all three maps are achieved by our U-Net model (98.35%). Even in the more complex microstructure of T3 sample, our model outperforms the rest of the methods.

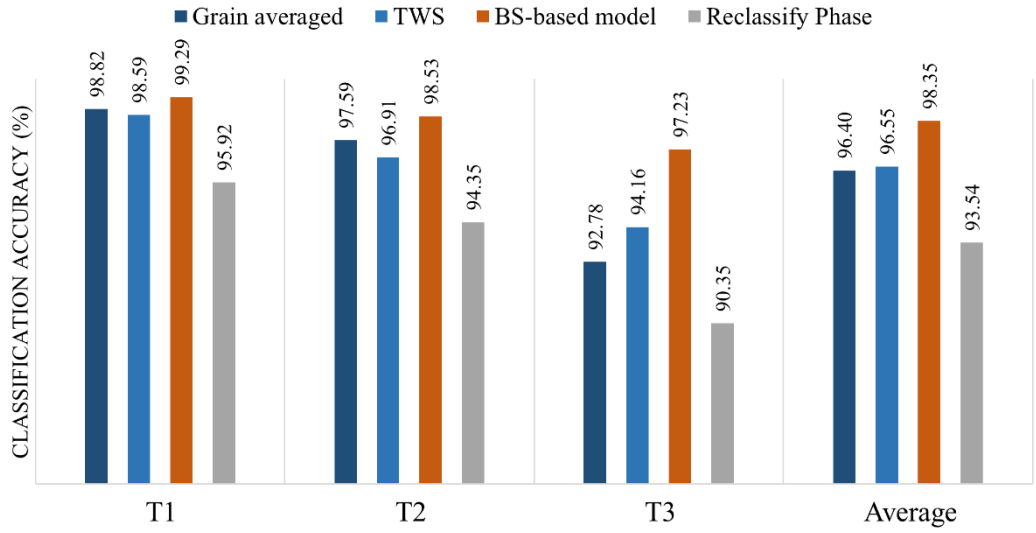

Figure V.21. Classification accuracies reached by our BS-based model and other state of the art methods over 3 representative microstructures of the testing set.

Additionally, it must be noted that for all three methods (grain average, TWS and Reclassify Phase), each map was treated individually what required time and effort to find the most suitable phase discrimination, while our approach segments all the maps with the same trained model. TWS offers the possibility to train a model that can be saved to be applied on new maps without the need to relabel, but the model's loading can take several minutes depending on the trained model's size. In our approach, the models are instantly loaded and are able to segment a map in terms of seconds without the need of any user input.

V.5.1.6 Models stability

The obtained results are subjected to the variability of the learning process and also to the accuracy with which the ground truth segmentation (labeling) has been obtained. The first one is related to the random initialization of the filters and the stochastic nature of backpropagation learning, what may cause that two models that have been trained in the exact same way do not precisely arrive to the same result. To account for the models training variability, 5 BS-based models presenting the training data exactly in the same order have been trained from scratch. The accuracies over the testing dataset presented a

standard deviation of σ = 0.075% resulting in an uncertainty of ±0.1% (calculated as $3 \times \sigma/\sqrt{N}$ with N=5 being the number of trained models). This indicates that accuracy variations below this value are not considered as meaningful.

In second instance, the effect of labeling errors has been assessed. For this purpose, a technique called data poisoning has been implemented, where the main idea is to intentionally mislabel a fraction of the training data. Hence, the model will be trained on some examples where the labeling is explicitly wrong. To introduce the data poisoning, a grain detection has been performed with a threshold angle of 3°. From all the detected grains of the training dataset, a total of 1% of the ferrite grains has been mislabeled as martensite and 1% of martensite grains as ferrite, resulting in a total of 2% mislabeled data. A BS-based model trained with the "poisoned" dataset has attained an accuracy over the testing dataset of 97.3%, showing a 0.65% difference with the testing accuracy reached by the original BS-based model (97.95%) presented in Figure V.16. Although intentional mislabeling was added, the model remains robust and does not drastically reduce its performance. This highlights that errors that could be introduced during labeling by the expert (usually less than 2% for such microstructures) would only marginally affect the models' performance.

V.5.2 Performance of the model trained on raw orientation data expressed as quaternions

It has been demonstrated that training models based on orientation-derived parameters such as pattern quality or KAM images provide excellent results for the segmentation of dual phase steels microstructures. Even better results have been obtained by coupling both input types. Therefore, there still remains an open question: can a CNN (here U-Net) leverage raw orientation data to extract significant features and perform an accurate phase discrimination as that obtained with BS, BC and KAM?

To answer this question, a quaternions-based model has been trained by inputting the quaternions as a stack of images formed by the q1, q2, q3 and q4 components as shown in Figure V.13. Figure V.22 shows the training and validation accuracies against the number of epochs equivalent to the plot in Figure V.15. At 25 epochs, the training accuracy of the quaternions-based model kept showing an upward trend while the validation accuracy remained constant, what indicates overfitting. Thus, the model trained at epoch 25 was selected as the final one. Table V.7 shows the final training and validation accuracies.

Table V.7. Final accuracies [%] reached by the quaternions-based model on the training and validation datasets.

Model	Training	Validation
Quaternions-based	96.76	96.61

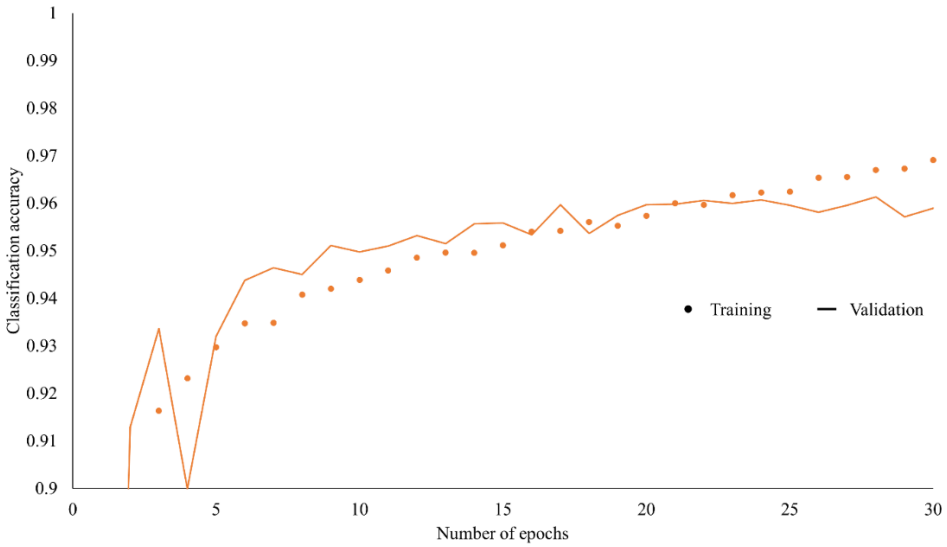

Figure V.22. Training and validation accuracies of the quaternions-based model plotted against the number of epochs.

The accuracy attained and the misclassifications produced by the quaternions-based model on the testing dataset can be seen in the confusion matrix of Figure V.23. The accuracy above 96% can be considered as a very good result when compared to classic phase discrimination approaches. However, the models obtained in V.5.1 outperform the quaternions-based model by around 2%. As for the BS and BC-based models, the greatest part of errors comes from false ferrite but here the trend is even more evident. This indicates that the quaternions-based model struggles to classify martensite more than any other trained model.

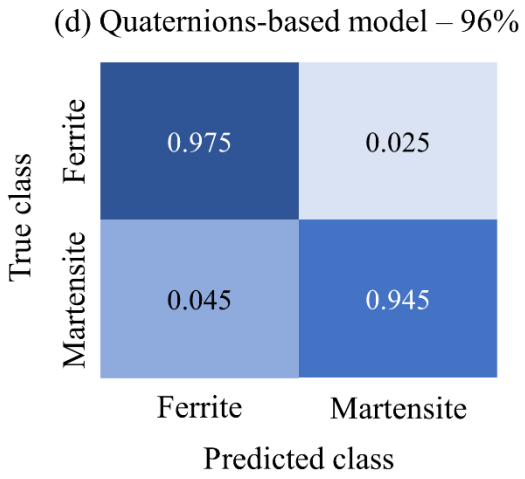

Figure V.23. Confusion matrix of the quaternions-based model over the testing dataset.

In this context, it is expected that if the accuracy is analyzed sample-wise, better results will be obtained for sample T1 than for sample T3 due to the higher martensite fraction in the latter. Table V.8 presents these results and they are compared with the BS, BC and KAM-based models. The accuracy shown by the quaternions-based model for T1 sample (98.49%) is excellent, and only 0.77% away from the best performing model (KAM-based one). However, when the complexity of the microstructure gets higher,

the accuracy of the quaternions-based model gets highly dropped (93.75%), being outperformed by the rest of the models by around 3% for the T3 sample.

Table V.8. Accuracies [%] per sample averaged over the three testing maps for the BS, BC, KAM and quaternions-based models.

Sample	BS	BC	KAM	Quaternions
T1	99.15	99.13	99.26	98.49
T2	98.4	98.27	98.58	95.5
T3	96.74	96.67	97.04	93.75

To better understand the performances attained on Table V.8, the maps already presented in Figure V.19 have been segmented by the quaternions-based model and the segmentation results are shown in Figure V.24. Looking at the EBSD map of the T1 sample (Figure V.24 (a)), one can rightly state that the accuracy achieved is very good (98.47%). However, a substantially accuracy drop can be seen once the segmentations are performed on the EBSD maps of T2 and T3 samples (96.03% and 94.26% respectively). As shown in the confusion matrix of Figure V.23, the main part of the errors come from false ferrite. These errors correspond to the coarse martensite grains that do not show a lath like structure and the model confuse as equiaxed ferrite grains. As expected, the fraction of false ferrite increases with the complexity of the microstructure as a higher fraction of martensite is present.

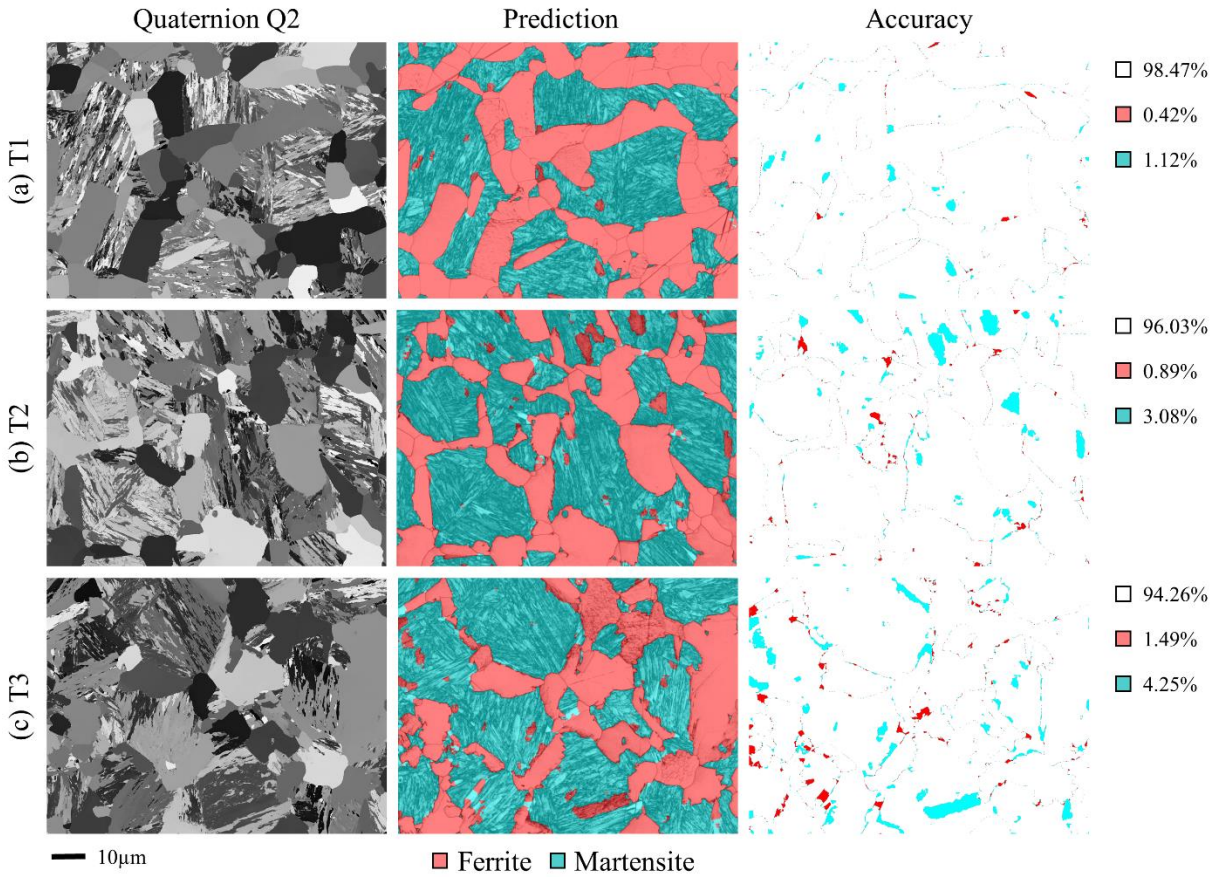

Figure V.24. Segmentation prediction and accuracy images obtained with the quaternions-based model over three EBSD maps belonging to each of the type (1) samples. In the accuracy images, accurately predicted pixels are in white, false martensite in red, false ferrite in cyan.

V.5.2.1 Quaternions-based model interpretation

The results presented in V.5.1 showed that, in general, the models are able to learn that domains with low BS, low BC, high KAM or a high density of non-indexed pixels correspond to martensite and reversely to ferrite. Based on this features, BS, BC and KAM models reached very high accuracies for all DP samples. However, the quaternions-based model struggle more than the rest and shows a lower performance. As shown in Figure V.13, the quaternions data do not look as contrasted as BS, BC or KAM to discriminate ferrite from martensite, thus the model is forced to perform a more complex feature extraction to find specific characteristics to the classes in question.

Since it is not clear what kind of features the quaternions-based model exactly extracts, a reverse engineering process was applied by testing the model on two new datasets: maps with averaged orientations per grain and maps where non-indexed pixels were cleaned. Cleaning was performed by a simple interpolation between nearest neighbors. The orientation averaged map was classified with a high accuracy, meaning that the trained model does not look only at the small orientation variations within the grain to perform its classification. We can conclude that the network does not extract features similar to KAM from the quaternions, although the KAM is a kind of convolution calculated from orientation data. The result on the cleaned maps showed very low accuracies, what means that the model uses the

non-indexed pixels to carry out the classification. However, trained with mixed data (raw and corrected), the model could achieve similar results as previously. Therefore, the features that the quaternions-based model uses to segment the microstructures are related to the high density of grain boundaries and the lath-like shapes characterizing martensite and the large equiaxed grains corresponding to ferrite (Figure V.13). This indicates that the implemented U-Net architecture can find some basic correlations but it is not able to exploit the advanced properties of raw orientation data in the form of quaternions in a proper way to characterize the constituents appearing in steels.

V.6 Segmentation results on multiphase steel microstructures

V.6.1 Model's performance to segment the labeled dataset

The model to segment MP samples has been trained based on BC and KAM inputs. In this case, BC has been selected over BS for three main reasons: 1) we have obtained similar accuracies for both BC and BS-based models in DP steels, 2) BC is a more universal parameter that can be obtained with any EBSD manufacturer rather than BS that is only available for Oxford Instruments users and 3) the BS maps of the MP samples were too much saturated. Initially, the results have been only evaluated on the four labeled MP samples, SA-1, API-1, API-2 and API-5, as presented in V.3.3.2.

An image crop belonging to the API-2 sample has been selected to visualize the segmentation performance of the trained model (Figure V.25). In general, the model classifies grains with few local misorientations as ferrite, grains with subgrain boundaries and tortuous grain boundaries or coarse laths as bainite and small laths with high KAM values and a dark BC as martensite. This can be confirmed by the BC and KAM distributions obtained by the model for each of the constituents on the labeled dataset (Figure V.26).

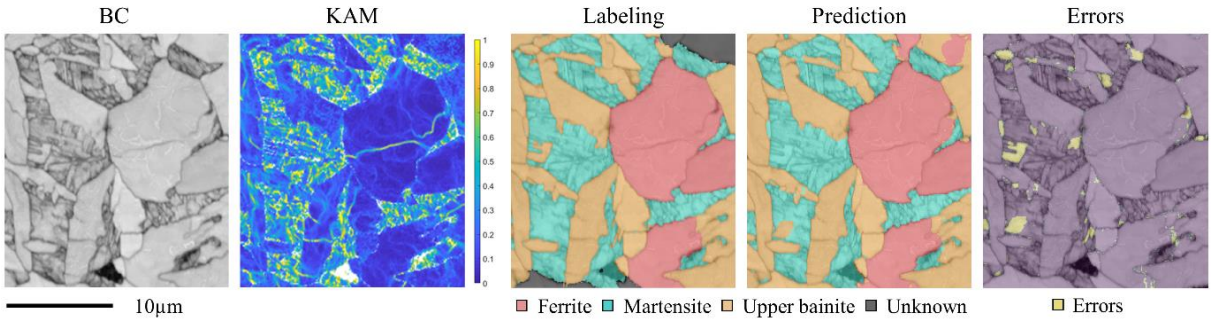

Figure V.25. Crop of a Model prediction example on an API-2 test map. The errors image expresses the difference between labeling and prediction.

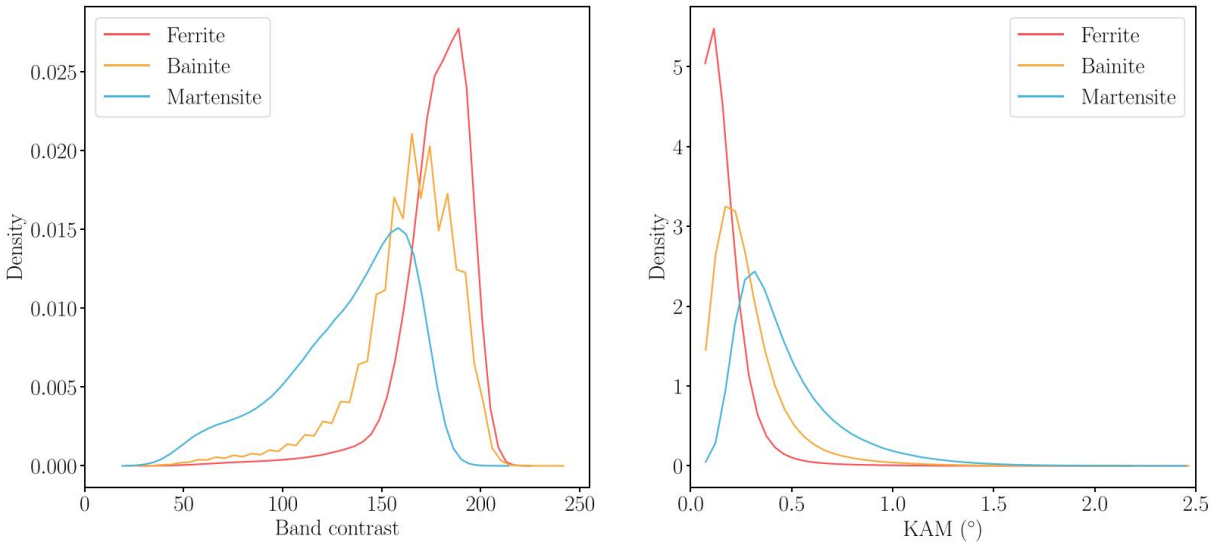

Figure V.26. Distribution of the BC and KAM values over all the labeled samples for each predicted constituent.

V.6.1.1 Effect of the microstructure's complexity

Table V.9 shows the accuracies of the model per sample over the training and testing datasets. In this case, the accuracies over the validation dataset are not shown as it was used only to determine the number of epochs that should be performed to maximize the model accuracy without overfitting the training dataset. Once the number of epochs was defined at 100, the training dataset (80%) was combined with the validation dataset (20%) resulting in a single dataset used to carry out the training. This was done in order to increase the number of training examples seen by the model.

Table V.9. Final accuracies reached by the model on the training and testing datasets per labeled sample. F: ferrite, UB: upper bainite, M: martensite and U: unknown.

Sample	Material	Training accuracy [%]	Testing accuracy [%]
SA-1	SA533 E	96.2	94.6
API-1	API5L x65QS	93.0	87.2
API-2	API5L x65QS	91.3	86.6
API-5	API5L x65QS	100	99.9

Testing accuracies reached are in the order of the training ones, indicating no overfitting. However, the training-testing accuracy gap is larger than that obtained for the DP samples. As the API-5 sample contained only martensite, it was therefore easier to segment reaching an excellent testing accuracy. The multiphase microstructures containing ferrite, upper bainite and martensite (SA-1, API-1 and API-2) have been classified with testing accuracies above 86%. These are excellent quality results when compared with state-of-the-art approaches. Few authors made the distinction between upper bainite and ferrite [13], [149]. However, most of these models were only assigning a single class to a whole EBSD map and were not performing a segmentation of the analyzed microstructure. Azimi et al. [12] performed pixel-wise segmentation of bainite using LOM pictures. However, they only obtained a 37.32% pixel-wise accuracy for the bainite class.

In particular, the SA-1 sample presented the most pronounced KAM contrast between upper bainite and ferrite, what helped the model to reach a high testing accuracy (94.6%) for such microstructure type. The API-1 sample was more difficult to label, as distinction between upper bainite and ferrite was often more ambiguous. The model accuracy was accordingly lower than for the SA1 sample (87.2%). The API-2 sample contained a larger proportion of martensite than that of the two first samples. It therefore represented a greater challenge both for labeling and prediction. However, the average accuracy for this sample was similar to that of the API-1 sample (86.6%). Examples of these microstructures and their respective labeling to check the phase fractions have been presented in Figure V.7 and Figure V.9.

V.6.1.2 Segmentation errors performed by the model

The confusion matrix on Figure V.27 shows the pixel-wise accuracy over the labeled testing dataset. The confusion between martensite and the other classes is negligible while the largest errors are found between ferrite and upper bainite. Indeed, 15% of the pixels labeled as ferrite were misclassified as bainite by the model. Inversely, around 7% of the pixels labeled as bainite were misclassified as ferrite. A higher error rate is therefore found for ferrite rather than bainite. This could result from the dataset which is not perfectly balanced and contains more upper bainite examples than ferrite. It could also be a consequence of labeling mistakes, as, despite introducing the "unknown" class, the difference between the two constituents was often ambiguous. However, when compared with the results for bainite segmentation obtained in [12], our model outperforms its accuracy.

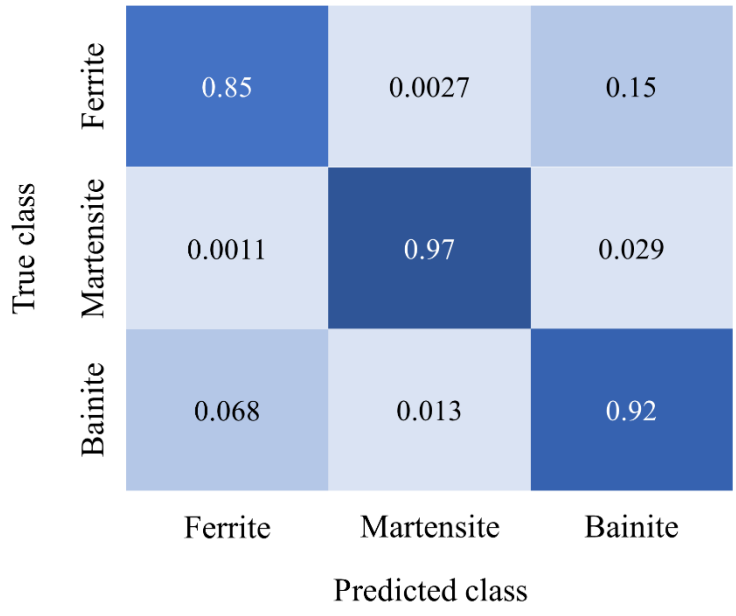

Figure V.27. Confusion matrix over the entire labeled testing dataset.

An insight about the errors highlighted by the confusion matrix in Figure V.27 is presented in Figure V.28 (a) together with the corresponding KAM image (Figure V.28 (b)) for the API-2 sample. Main part of the errors is colored with yellow or violet, concerning the ferrite-upper bainite phases. Some small or non-equiaxed ferrite grains surrounded by bainite or martensite grains or presenting few intragranular

misorientations were predicted as bainite. Large bainite grains surrounded by ferrite grains were inversely often misclassified as ferrite. However, it can be seen that some errors do not concern an entire grain but only a fragment as shown in the highlighted grain in Figure V.28 (a). This is an actual ferrite grain whose upper part has been misclassified as bainite, what may happen due to the presence of the low angle grain boundary highlighted in the KAM map of Figure V.28 (b). This result shows that our U-Net does not classify the grains as a single entity i.e. it does not classify all the pixels contained in a region closed by grain boundaries as a single class.

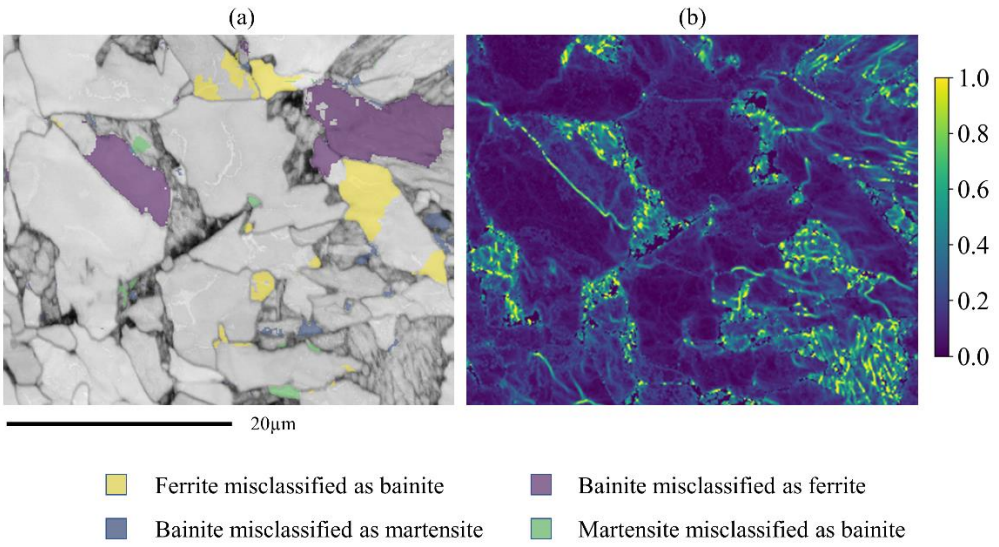

Figure V.28. (a) Example of local misclassification in the API-2 sample EBSD map overlap on BC and (b) the associated KAM map.

V.6.1.3 Model's performance on unknown-labeled domains

As explained in V.3.3, there were certain ambiguous cases where it was difficult to assign a class with certainty. For this reason, we have introduced the unknown class in order to ease the labeling task and avoid introducing errors that could bias the model. Clearly, these unknown domains have not been used to train the models but they have been introduced within the testing dataset to evaluate the performance of the model in such ambiguous cases. Two particular cases appearing on a map belonging to the API-2 sample have been selected and both are presented in Figure V.29.

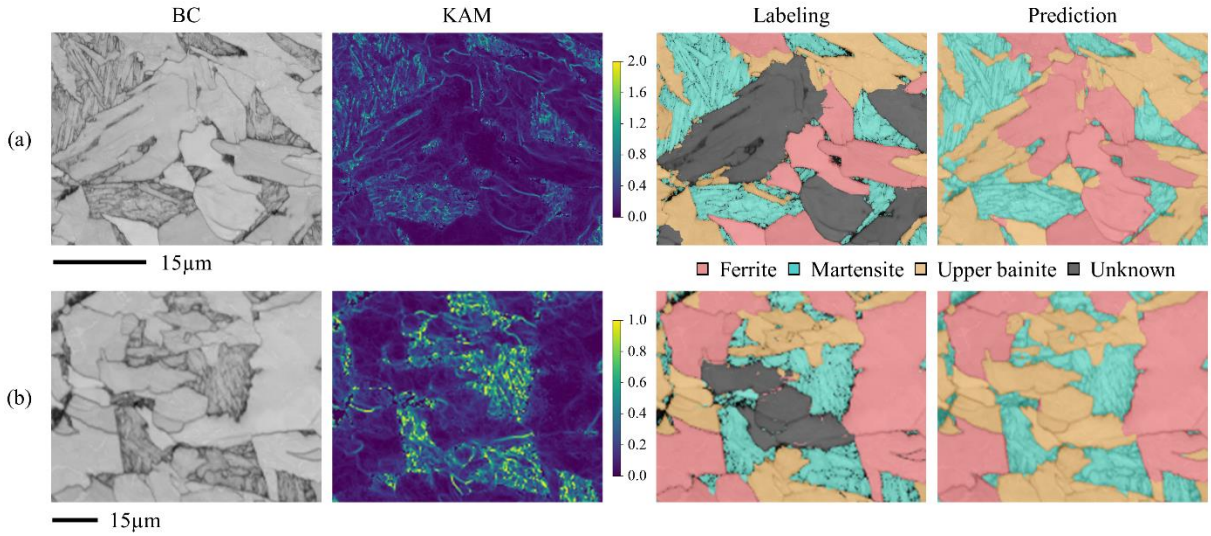

Figure V.29. Prediction of the model on grains labeled as "unknown" on an API-2 map.

Figure V.29 (a) shows the BC, KAM, labeling and prediction of a map crop containing a ferrite grain which continuously transformed into bainite during cooling. If we would have labeled this "unknown" grain, we would have divided it into a ferrite part containing a large equiaxed zone with very few intragranular misorientations and a bainite part corresponding to a lath like structure with a slightly higher intragranular misorientation density. Due to the continuous nature of this transformation, no clear boundary can be identified between those two parts neither on the KAM nor on the BC map. The model's prediction has correctly identified the dual nature of the grain, but it traced an interphase boundary without physical meaning as the bainitic lath-like structure has not been correctly represented. This is probably because the model was fed with only few labeled examples of such transitions, due to the difficulty to label them.

The case presented in Figure V.29 (b) shows certain "unknown" grains with an intermediate value of KAM between upper bainite and ferrite, which were the two options that we have hesitated to assign during labeling. The predicted result by the model is upper bainite, what is coherent as the model predicts one of the two phases that the human had considered during labeling.

V.6.2 Model's performance to segment unlabeled data

In the above section, the testing dataset belonged to the same samples as the training dataset. Here, we will evaluate the performance on different samples, API-3 and API-4, that have not been labeled. These samples presented a similar microstructure as that of SA-1 and API-1 but with a higher upper bainite fraction as a result of the heat treatment presented in Table V.3. Figure V.30 (a) and (c) shows the model segmentations while Figure V.30 (b) and (d) their respective KAM images for the API-3 and API-4 samples respectively. Ferrite was predicted on large zones with few misorientations while upper bainite was assigned to zones with a higher misorientation density and more tortuous grain boundaries. The M/A islands were also qualitatively well identified by the model as martensite. Some coarser bainite laths containing very few intragranular misorientations were misclassified as ferrite, as can be seen for

instance in the dotted frame in Figure V.30 (c). This results from the absence of such microstructures in the training dataset, what remarks the importance of providing the model with a broad set of different microstructures to help it generalize.

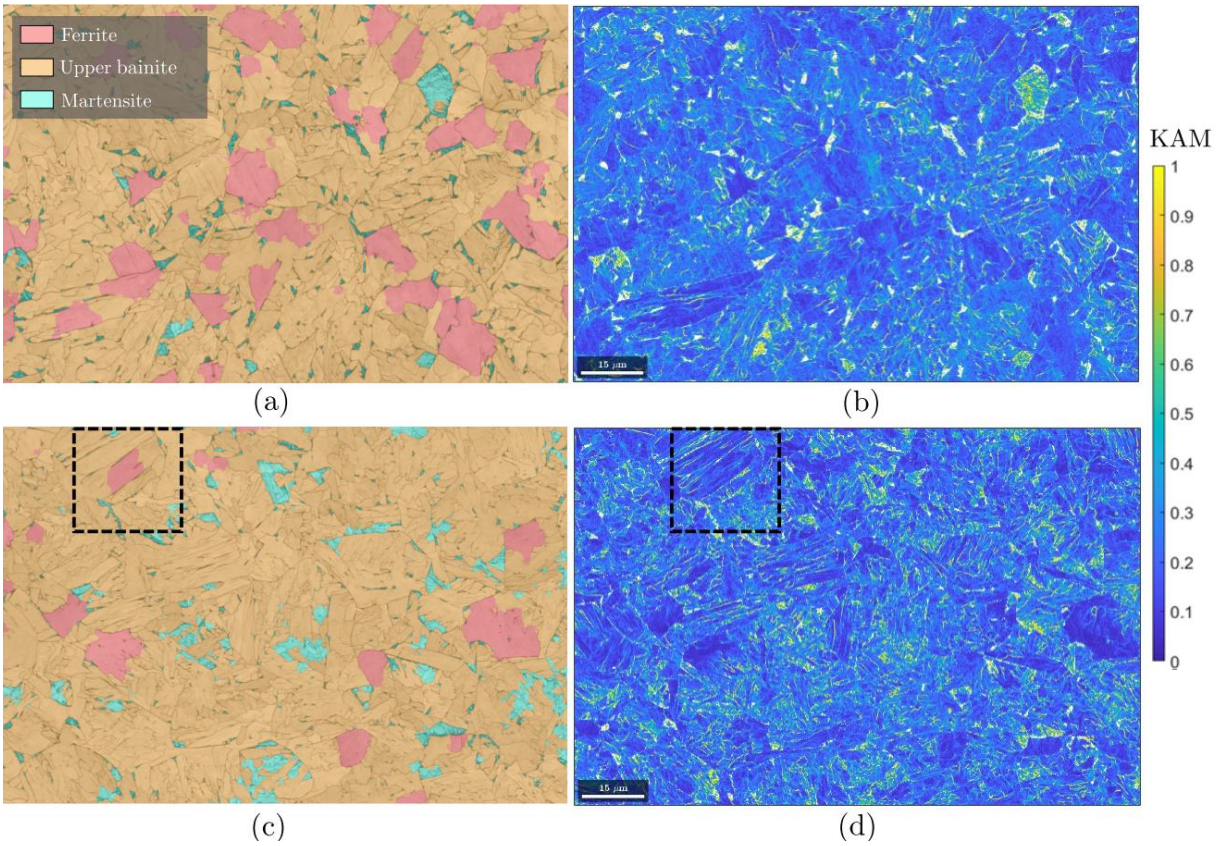

Figure V.30. (a) and (c) Model segmentations on two unlabeled maps corresponding to API-3 and API-4 samples respectively. (b) and (d) Associated KAM maps. The dotted frame highlights coarse bainite laths misclassified as ferrite as they contained few KAM variations.

Table V.10 presents the predicted constituents' fractions for the labeled API-1 and unlabeled API-3 and API-4 samples to confirm the physical consistency of the model predictions over different cooling rates. The higher the cooling rate is, the lower the ferrite fraction and the higher the bainite and martensite fractions are, as expected from the transformation mechanism of these constituents. These results reveal that the model generalizes well to microstructures of the same steel grade, with similar features as those seen during training but with different constituent fractions resulting from different heat treatments.

Table V.10. Predicted constituent fraction for MP samples transformed with different cooling rates.

Sample	Heat treatment	Ferrite [%]	Upper bainite [%]	Martensite [%]
API-1	2.8°C/s	50.0	45.9	4.1
API-3	8.3°C/s	26.2	70.1	3.7
API-4	19.4°C/s	3.9	89.5	6.6

V.6.3 Effect of the input data

V.6.3.1 Data quantity and diversity

In order to train a robust U-Net model, a significant amount of training data must be provided. To know if the provided amount is sufficient to get the best results, several models have been trained with different datasets. Figure V.31 shows the evolution of the model testing accuracy with the number of 224×224 pixels crops used for training. Each point represents the average of five successive trainings using the same input data and hyper parameters but with different initial weights. The testing accuracy saturates around 1000 crops. As the whole dataset was used for the final training, a sufficient amount of data was therefore given to the model to reach the optimal accuracy. Also, the model accuracy varies by 1% over five successive trainings. This results from the stochastic nature of the backpropagation learning as well as the random weight initialization. The network will therefore not necessarily converge systematically toward the same local equilibrium.

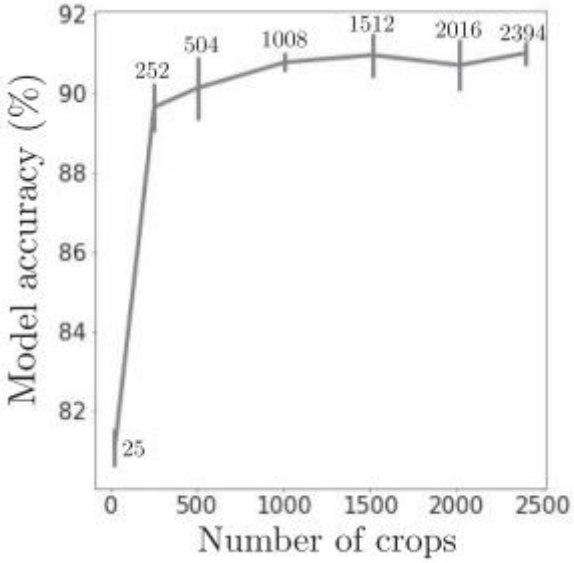

Figure V.31. Evolution of the testing accuracy with the number of 224×224 crops used for training. The number of crops used is displayed next to each evaluation point for better readability.

The performance of the model on segmenting the testing dataset was satisfactory but what if less data was provided to the model? To assess this point, an additional model has been trained without including maps from the API-5 sample (fully martensitic microstructure). In this case, the resulting training dataset contained only an amount of 9% martensite and there is no microstructure with a large martensite content; the API-2 sample contained only 21% of martensite and regarding the API-1 and SA-1 samples, martensite appeared only within M/A islands (5% and 3% respectively).

Table V.11 presents the testing accuracy of the concerned model compared to the original model presented in Table V.9. Although the accuracy on the SA-1, API-1 and API-2 samples has been only marginally impacted, the performance on the API-5 sample is drastically reduced. Figure V.32 shows the prediction of the model trained without (a) and with (b) the API-5 map, on a crop of an API-5 map.

The model trained without any quenched sample maps predicted a higher fraction of upper bainite as it is the phase that resembles martensite the most. Therefore, the data diversity on the training dataset has a great impact in the model's performance.

Table V.11. Accuracies on the labeled testing dataset per sample for a model trained with and without the API-5 sample.

Sample	Without API-5	With API-5
SA-1	93.8	94.6
API-1	87.4	87.2
API-2	86.2	86.6
API-5	69.2	99.9

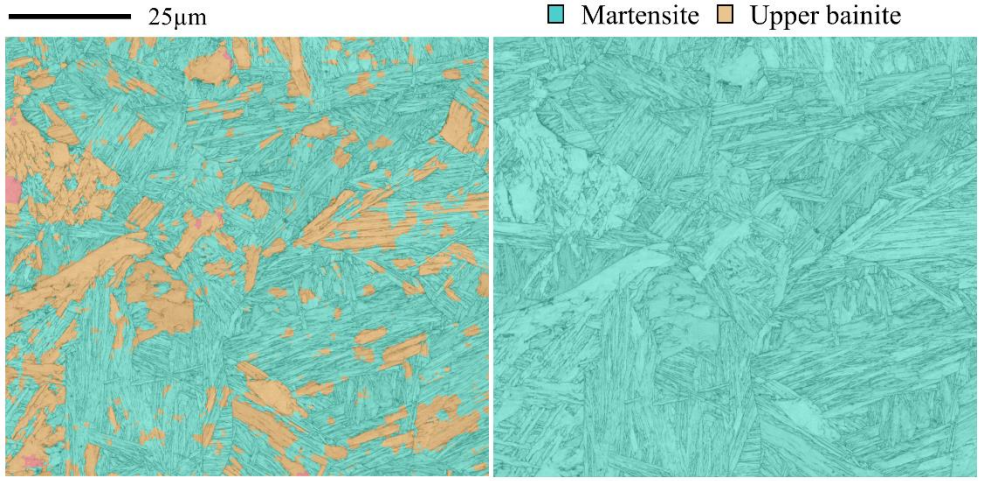

Figure V.32. Model prediction on an API-5 map with a model trained (a) without and (b) with API-5 maps.

V.6.3.2 Acquisition conditions

As mentioned in V.2.3, two different acquisition conditions were used on the API-1 sample (Q_{ref} and Q_{alt}) to investigate the influence on the model's performance. Figure V.33 shows the KAM distribution for each constituent on the maps for the two conditions. A slightly higher misorientation contrast can be observed between the constituents on the Q_{alt} map than on the Q_{ref} map. Table V.12 compares the accuracies of two models trained with and without the map obtained with acquisition condition Q_{alt}. A 2% difference in accuracy can be observed between the API-1 (Q_{ref}) and (Q_{alt}) maps. This is of the same order than the intrinsic variability due to random weight initialization and to the stochastic nature of the backpropagation learning. Therefore, the model reached similar classification accuracies on both maps, even when the higher quality map (Q_{alt}) was not used during training.

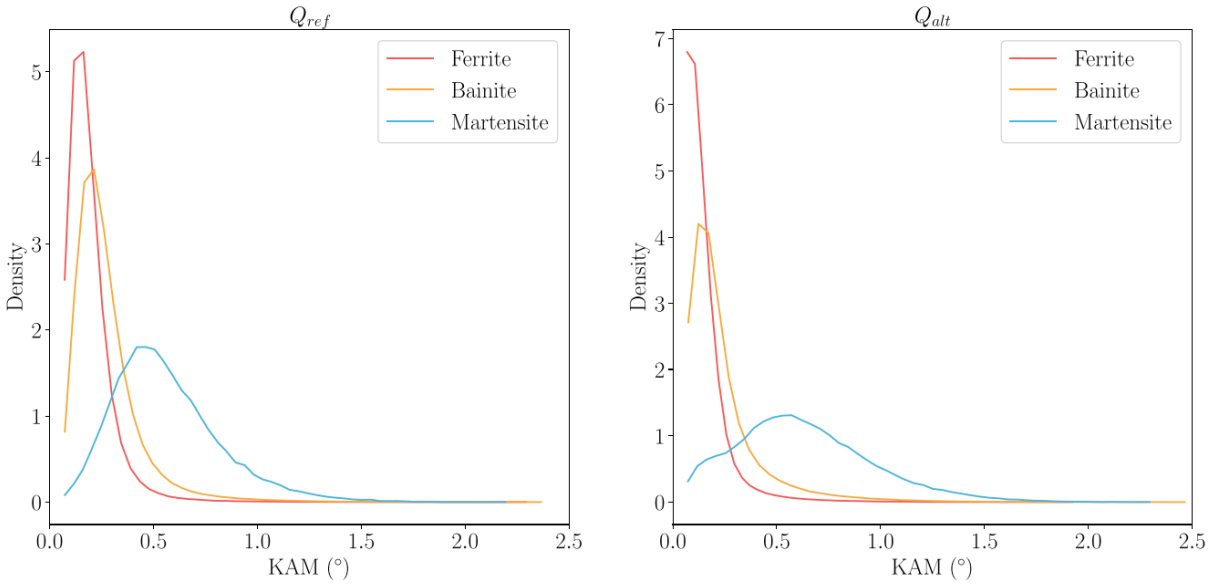

Figure V.33. KAM distribution for each of the labeled constituents on the EBSD map acquired with conditions Q_{ref} and Q_{alt}.

Table V.12. Testing accuracy of the models trained with and without the map acquired with Q_{alt}.

Sample	Training with Q_{alt}	Training without Q_{alt}
SA-1	94.6	95.8
API-1 (Q_{alt})	87.6	87.6
API-1 (Q_{ref})	86.8	85.2
API-2	86.6	85.4

A robust model should also have the ability to correctly segment EBSD maps acquired at different step sizes and resolutions. This is the reason why we have introduced the step size as an additional input to our U-Net architecture as explained in V.4.2. Here we will evaluate how this strategy impacts the quality of the result by considering three training situations: (1) training our U-Net without the additional input and dataset containing maps acquired at a single step size of 0.1µm, (2) training our U-Net without the additional input and dataset containing maps acquired at 0.1µm and 0.3µm step sizes and (3) training our U-Net with the additional input and a dataset containing maps acquired at 0.1µm and 0.3µm step sizes.

Figure V.34 shows the prediction results on a crop of a map from the API-2 sample with all three strategies for different acquisition step sizes. Strategy (1) showed a good accuracy on segmenting maps acquired at 0.1µm but its performance dropped with step sizes not seen during training. The larger the step size, the lower the model's accuracy is over the whole API-2 map as ferrite is completely misclassified as bainite. Increasing the step size produces a global increase of the KAM values and an apparent "thickening" of the subgrain boundaries as there are less pixels on the maps. This model could therefore confuse ferrite grains with upper bainite as the density of sub-grain boundaries appears greater. Note that the martensite prediction remains relatively constant for the different steps as the model may rely on the BC value to discriminate this constituent from the others, which does not vary much with the

step size. Strategy (2) demonstrates that, while the different step sizes are explicitly shown to the model during training, the model will be able to correctly segment such cases. However, it fails to classify maps with unseen acquisition step sizes. The model trained with strategy (3) reaches higher accuracies for the 0.2µm and 0.4µm step size maps, which were not shown during training. This reveals that the step size input image helps to better interpolate and extrapolate to acquisition steps not seen during training. However, lower accuracies are reached when compared to step sizes provided during training.

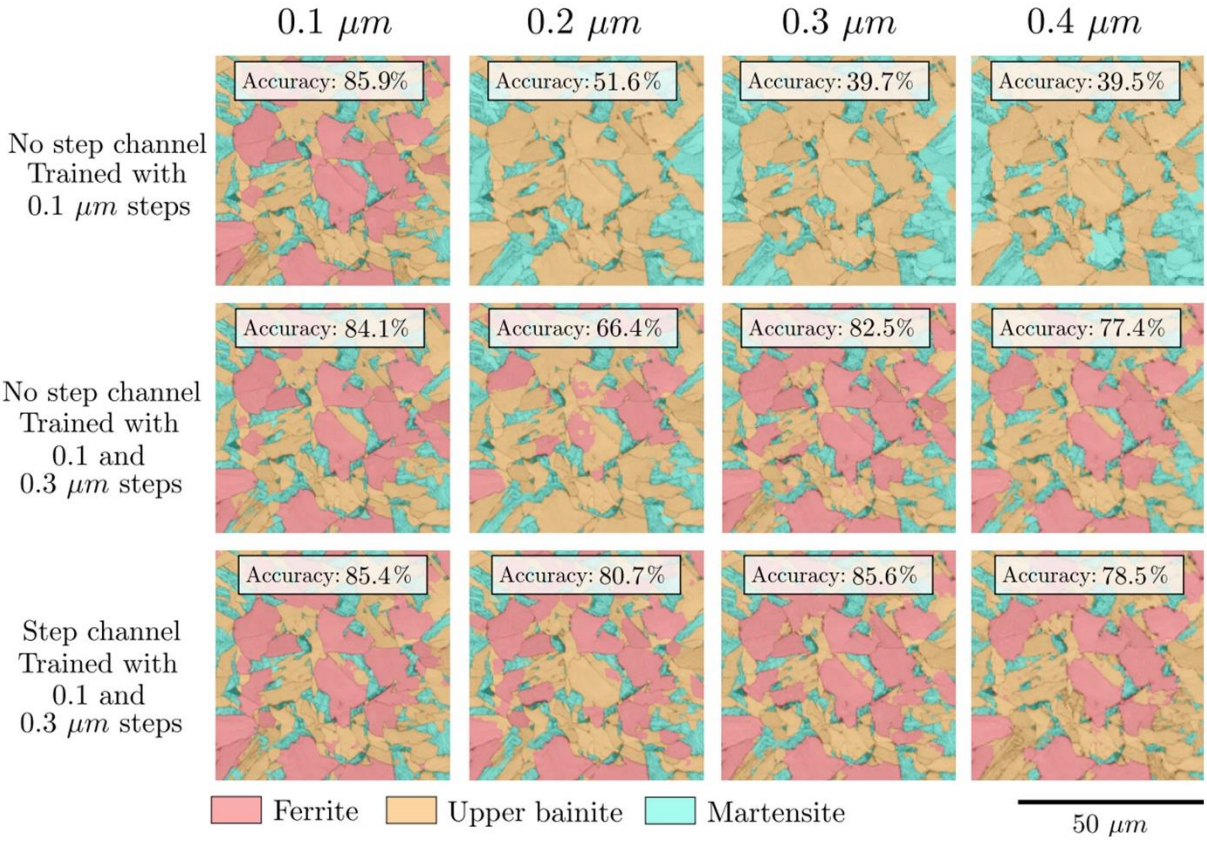

Figure V.34. Comparison of predictions on an API-2 maps crop with three different models, for an acquisition step of 0.1µm, 0.2µm, 0.3µm and 0.4µm.

V.6.3.3 Model's performance according to the pixel location in the map

The influence of the border was also investigated because grains at the border of the crop are cut out and padding take care of the missing information. The size, intragranular misorientation content or the neighborhood of those grains are therefore inaccessible which makes their constituent difficult to assess, even during manual labeling.

Figure V.35 shows the prediction of the model on API-2 crops of different sizes and the same central position. The figure reveals that the network predictions are rather consistent for the different crop sizes, especially for grains at the middle of the crop. Some grains, such as the one highlighted in frames 1 and 2 are predicted differently for the different crop sizes. In Figure V.35 (d), only a third of the grain in frame 1 can be seen. It is therefore misclassified as ferrite. The grain is nevertheless rightly classified in larger crops where it is fully represented.

The grain in frame 2 is partially misclassified as ferrite, even in Figure V.35 (c) where it is fully present in the crop. Figure V.35 (b) however shows that this grain is rightly classified as bainite, once it is situated in the middle of the crop. This results from the various pooling and padding operations performed in the different layers of the network. Due to such operations, the morphology of the cropped features as well as the gradient of information may change. The pixel position in the crop has therefore some importance for constituent fraction estimation using a U-Net model.

This effect is however minimized here for two reasons. First, the model was trained on a large number of small crops extracted from larger maps. The grains at the border of those crops were therefore rightly labeled. The model could have learned to adapt its decision parameters depending on the position of the grain on the crop. Also, the influence of padding is the strongest on the deepest layers of the network, for which only low-level features are detected. This border effect should therefore not impact too much the detection of high-level features (such as the presence of low-angle boundaries) and their use in the constituent prediction.

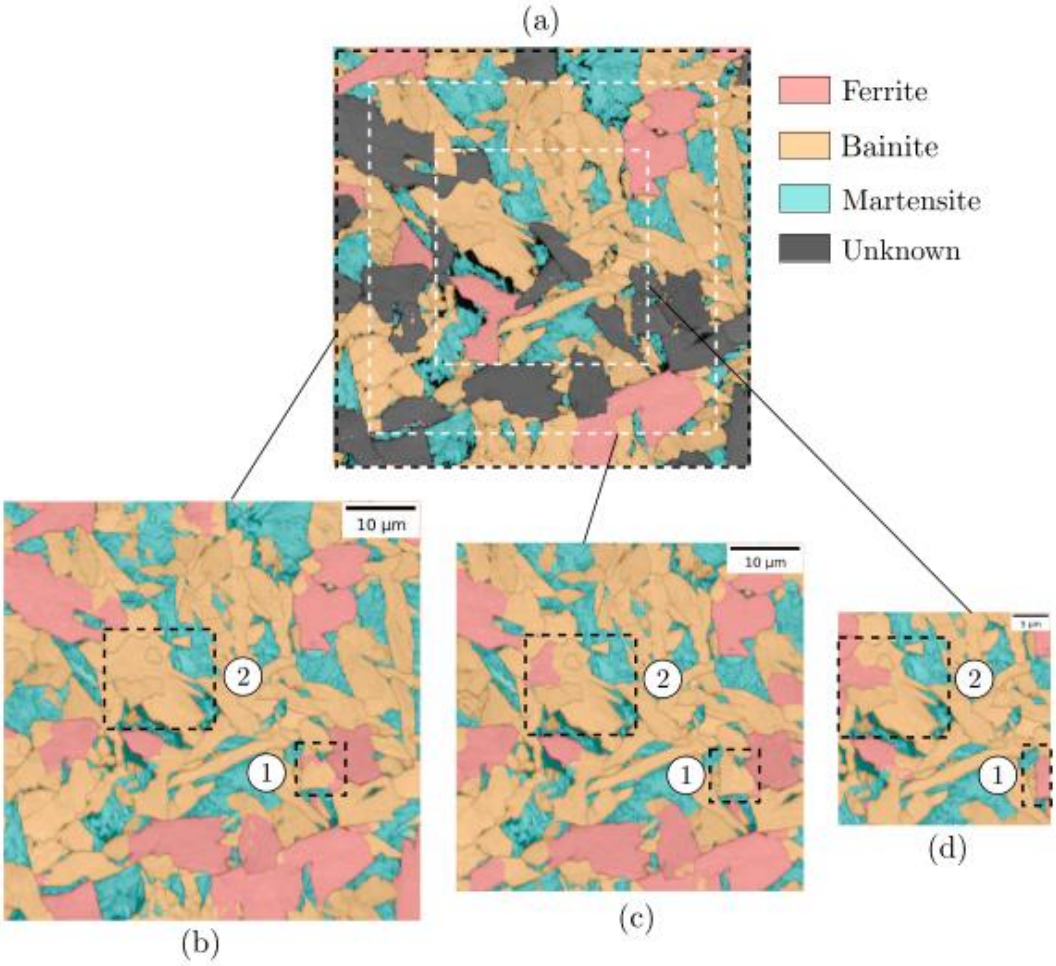

Figure V.35. Model predictions on an API-2 crop with different definitions (a) Labels (b) 300×300 pixels, (c) 400×400 pixels (d) 600×600 pixels.

V.7 Conclusions and perspectives

A DL method based on the implementation of the CNN U-Net architecture has been successfully developed to automatically segment the phase transformation products within complex steel microstructures using EBSD-based data.

Initially, a model dual phase steel microstructure has been selected to work with since its labeling is relatively simple compared to multiphase microstructures. The main idea was to get in closer touch with artificial intelligence techniques, to question what is the most suitable type of EBSD data to feed our network and to evaluate their capabilities to perform a microstructural characterization based on EBSD data. The method developed on the model microstructures was the successfully applied on multiphase industrial microstructures presenting ferrite, upper bainite and martensite.

From the findings and results presented along the current chapter, the following conclusions can be drawn:

- Excellent accuracies around 98% have been obtained to segment dual phase microstructures with models trained on BS, BC and KAM images as inputs. It has been proven that coupling inputs such as BS and KAM, the performance of the model trained model is further improved. This validates the ability of CNNs to handle EBSD data and perform a correct segmentation.
- Raw orientation data has also been provided to our U-Net in the shape of quaternions to evaluate if it was capable to derive features from orientation (similar to the KAM, specific misorientations, habit planes, etc.) to discriminate the phases ferrite from martensite. However, we concluded that, the implemented architecture fed with quaternions as input data was not well adapted to perform this task. It must be noted that this was the first time that raw orientation data was provided to a CNN in order to carry out phase discrimination.
- From this first experience BC+KAM was chosen to train the model dedicated to segment the multiphase industrial microstructures. The accuracies attained by this model range from 86% to 99% and this variation responds to the complexity of the specific microstructure to segment. It is important to mention that this is the first model in the literature to perform pixel-wise segmentation of ferrite, upper bainite and martensite based on EBSD data.
- One of the main strengths of this approach is the short time needed to obtain a result. Once the trained model is loaded and the inputs are available, the segmentation of an entire map as those presented in this chapter takes a few seconds.
- It has been shown that providing the acquisition step size as an input to the model helped it to generalize well to different acquisition steps. To the author knowledge, explicitly providing acquisition parameters as an input to a U-Net model had never been applied to the segmentation of microstructures.

- It has been shown that the model is able to generalize and correctly segment microstructures that have not been present in the labeled dataset, but that show similar features than those the model learnt. However, it has been also demonstrated that the variability of the training dataset is a major asset to consider. It needs to include all possible configurations that we would like to segment since it cannot generalize to new microstructures showing new features.
- Undoubtedly, the greater drawback of this method is the need to label the training dataset. In this respect, in order to ease this challenging task, the minimum amount of training data needed to train a performing model has been assessed. However, we have demonstrated that the dataset variability is a very important point to consider. Additionally, introducing the "unknown" class, ignored by the model during training, eased this process by allowing the exclusion of certain ambiguous cases from the training.

Also, we present some perspectives:

- We have shown that providing the raw orientation data in the form of quaternions has not been well adapted for our U-Net to correctly learn the desired features. It would be important to continue investigating how artificial intelligence algorithms could directly exploit raw orientation data in order to automatically extract meaningful features.
- We have trained our U-Net from scratch to segment both DP and MP samples. However, since the results obtained for DP are excellent, we could pre-train the network on DP in order to optimize the weights on a similar task, and later train it on MP to treat more complex microstructures.
- As the labeling is a challenging task, we have thus started to build a first labeled EBSD database, which can be enriched by future labeling performed by different experts on a wider range of microstructures, by integrating the variabilities induced by the acquisition conditions and the expert's subjectivity to label.
- Another idea that we have started to work with and can be useful to limit the amount of data to label is the introduction of synthetic EBSD data, that can be generated by respecting the main features characterizing the different steel constituents. In Chapter VI we present a software that is able to generate the orientation of synthetic EBSD maps. However, our U-Net has been fed with pattern quality and KAM, that our software does not simulate. Thus, the application of innovative networks such as Generative Adversarial Networks (GANs) [209] are very interesting for this task as they are able to simulate fake data that resembles real data.
- Nevertheless, avoiding labeling is a main challenge to overcome in order to speed up the training of the models. This could be performed using unsupervised learning approaches that are presented in Chapter VI.

Chapter VI: **Unsupervised learning for phase discrimination in steels**

VI.1 Introduction

As we have seen in Chapter V, good results can be obtained by means of supervised CNNs for the segmentation of both DP and MP samples. Accuracies reaching above 85% are in the order of those obtained by human experts but with the advantage of being automatically predicted by the trained model. However, the main issue with supervised learning approaches resides in the need of labeling a dataset to train our model. As we have repeated several times, this is a task that we would like to avoid or at least, to reduce to the minimum effort and time consumption as possible.

This chapter, where we want to investigate different strategies to both ease the labeling procedure or directly avoid it by working with unsupervised learning algorithms, is divided in three main parts.

In first instance, we present a microstructure generation software (Orientation Map Generator) that allows creating EBSD maps containing desired steel microconstituents with controlled features. This is an original way of facilitating labeling as we can generate synthetic and labeled data that resembles experimental data in order to train any supervised or unsupervised learning approach.

Secondly, we try to segment a microstructure containing upper and lower bainite (UB and LB respectively) by using a classic unsupervised clustering algorithm like *k*-means. For this, we work with both synthetic maps obtained with the Orientation Map Generator and also experimental EBSD maps. The main idea of the method is to use EBSD-derived features of two neighboring grains in order to classify their interface into four different classes namely UB/UB, LB/LB, UB/LB and LB/UB. For this, a feature engineering procedure was performed to find the most suitable parameters characterizing both grains. Once all the interfaces are classified, a final step assigns the class to each detected grain according to its classified interfaces. This part of the work follows the post-doctoral work of Dr. Simon Breumier which has been performed in collaboration with Industeel ArcelorMittal (Le Creusot, France) supported by the IRT M2P. During this work, Dr. Breumier and I tested the same strategy described above but with a different unsupervised algorithm called InfoGAN [186]. The obtained results are not presented in this thesis and will be part of an upcoming publication.

Last, as both *k*-means and InfoGAN approaches need feature engineering, but we wanted to try an unsupervised approach based on CNN feature extraction coupled with superpixel segmentation to segment the DP and MP samples presented in Chapter V. The main goal of this method, that is called U-CNN (Unsupervised CNN) along this chapter, is to extract features that characterize different regions of the microstructure and let the model train itself to segment the regions with the same activated features in the same class.

VI.2 Orientation Map Generator

Designing synthetic EBSD maps allows labeled maps with well separated features to be obtained quickly in order to reduce the need of labeling. Additionally, working with these synthetic maps is a good way

to rapidly evidence the challenges to train any ML or DL model and represent a simpler validation problem before addressing the more complex real microstructures.

The microstructure generation algorithm has been embedded in a software called "Orientation Map Generator" and it was designed to generate multiphase maps with different transformation products such as ferrite, upper bainite, lower bainite and martensite [210]. The characteristic features of upper bainite, lower bainite and martensite were inspired by the work of Takayama et al. [55]. All parameters needed to generate a synthetic microstructure are listed in Table VI.1 and explained below.

Table VI.1. Parameters used for the synthetic EBSD map generation with the Orientation Map Generator.

Parameters	**Symbols (unit)**	**Set values**
Width and height of the map in pixels	w × h (pixel)	-
1. Prior austenite microstructure		
Prior austenite crystallographic texture	$f(g_\gamma)$	-
Number of austenite Voronoi seeds	S	
Austenite elongation ratio	c/a	-
Fraction of austenite coherent twins	f_{Twin} (%)	-
Gaussian width distribution of the twins	$\Theta_{TwinWidth}$ / $\sigma_{TwinWidth}$	-
2. Allotriomorph ferrite microstructure		
Fraction of triple point for nucleation	f_{TP} (%)	-
Fraction of Euclidean growth of allotriomorph grain	f_{EG} (%)	-
Fraction of potts growth	f_{PG} (%)	-
Gaussian halfwidth of the orientation noise	HW_{AF} (°)	-
3. Upper bainite microstructure		
Fraction of upper bainite	f_{UB} (%)	50
Sheaf width	w_{Sheaf} (pixel)	100
Sub-unit diameters of the ellipses	a, b (pixel)	40, 6
Sub-unit seeds density	$f_{Sheaves}$ *(%)*	5
Orientation relation of upper bainite	OR_{UB} (°)	4.3, 46.7, 5.43
Gaussian halfwidth of the orientation noise	HW_{UB} (°)	0.4
4. Lower bainite microstructure		
Fraction of upper bainite	f_{LB} (%)	50
Packet width	w_{packet} (pixel)	100
Width of the blocks	w_{block} (pixel)	20
Sub-block surface	$A_{sub\text{-}block}$(pixel)	100
Anisotropy ratio of the sub-block tessellation	R	10
Orientation relation of lower bainite	OR_{LB} (°)	3.6, 46.41, 6.3
Gaussian halfwidth of the orientation noise	HW_{LB} (°)	0.4
5. Martensite microstructure		
Fraction of martensite	f_M (%)	-
Packet width	w_{packet} (pixel)	
Width of the blocks	w_{block} (pixel)	
Sub-block surface	$A_{sub\text{-}block}$(pixel)	
Anisotropy ratio of the sub-block tessellation	R	
Orientation relation of lower bainite	OR_{LB} (°)	
Gaussian halfwidth of the orientation noise	HW_{LB} (°)	

The first step is the creation of the prior austenite microtexture. Once the size $w \times h$ of the desired EBSD map is defined, a Voronoi tessellation is used to create the parent austenite grains. The user inputs either the number of seeds, S, or the average grain area $\frac{w \times h}{S}$ and can introduce a global anisotropy by giving a direction and an aspect ratio. The orientation of the grains can present a defined texture or be randomly selected. Coherent twins can be introduced in f_{Twin} of the parent grains. The twins pass through a random point in the grain and are materialized by a band whose width follows a chosen gaussian distribution. The twin variant is randomly selected and the twin inclination is the common (111) plane trace.

The following step is the generation of allotriomorph ferrite growing from austenite triple points (Figure VI.1 (a)), where the user defines the fraction of triple points (f_{TP}) where ferrite nucleates. The nucleated ferrite grains are in KS-OR with at least one of the grains sharing the triple point and grow in two steps: first an Euclidean growth is performed but only in the non-KS-related grains [211]. This growth is stopped when the ferrite fraction reaches a user-defined threshold fraction (f_{EG}) (Figure VI.1 (b)). Second, in order to provide a realistic shape to the grains, a Potts model is applied and stopped when the final ferrite fraction (f_{PG}) is reached [212] (Figure VI.1 (c)). Some orientation noise can be added to the ferrite pixels as rotation around a random axis by an angle following a gaussian distribution with a given half width (HW_{AF}).

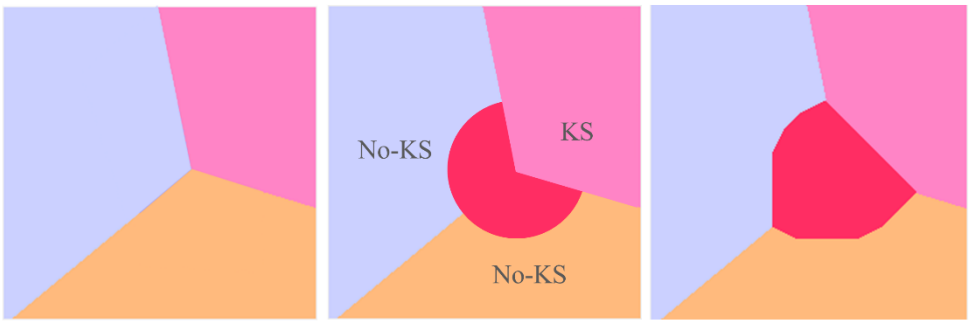

Figure VI.1. Process of generating synthetic allotriomorph ferrite from a triple point in austenite. For the austenite generation S=3, f_{Twin}=0 and the rest of the parameters for austenite and allotriomorph ferrite were set as in Table VI.1.

Then, UB is generated in the remaining austenite grains in two steps: 1) bainite "sheaves" nucleation and 2) sub-units introduction. One bainite sheave is generated at the time until a fraction f_{UB} of upper bainite is reached. Nucleation starts by choosing a nucleation point at a γ/γ or a γ/UB interface. Then a main variant is selected to respect the lowest deviation to the double-KS condition [213]. The symmetry element of the parent is switched so that the selected main variant corresponds to V1 in the variant list [55]. In this reference frame, the habit plane trace is assumed to be (111). The bainite sheaf is a band of width w_{Sheaf}. In each sheaf some sub-units are introduced by choosing a random point and a variant according to these probabilities: V2: 10%, V8: 10% V1:80%. Then the variant is inserted in the sheaf as an ellipse of length a and width b, elongated along the {111} habit plane (note that the habit plane differs for the V8 variant which has to be calculated separately). The number of sub-units is chosen as

a function of the size of the considered sheaf so that the density ($f_{Sheaves}$) stays constant over the microstructure. Figure VI.2 (b) shows the generated UB from an austenitic microstructure (Figure VI.2 (a)) where no allotriomorph ferrite was previously generated.

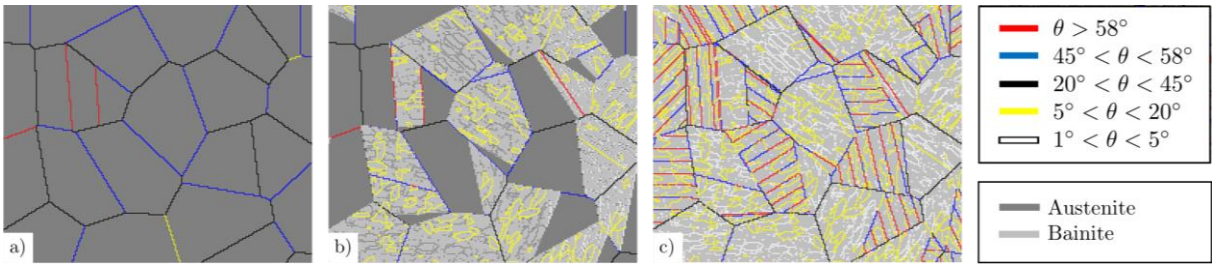

Figure VI.2. Steps of synthetic microstructure generation a) twined austenite, b) upper bainite sheaves and sub-units, c) lower bainite packets/block/sub-blocks. For the generation of austenite, UB and LB the parameters were set as in Table VI.1.

All the remaining pixels are finally transformed into lower bainite or martensite depending on the selected fractions by repeating the following three steps: 1) packet nucleation, 2) blocks division and 3) sub-blocks introduction (lower bainite and martensite share the same features). Packet nucleation starts by selecting a nucleation point following the double-KS condition at a γ/γ or a γ/bainite interface. A side effect of this variant selection is that adjacent packets nucleating at the same boundary are the same. The packet is a band with a width, w_{packet}, inclined along the habit plane of the selected variant. The packet is divided into blocks having a fixed width, w_{block}, and alternating regularly. Finally, blocks are divided into sub-blocks by an anisotropic Voronoi tessellation where each Voronoi cell is randomly allocated to sub-block 1 or 2. The density of Voronoi seeds is set to match the user-chosen average sub-block area ($A_{sub\text{-}block}$) and an anisotropy is introduced in the Euclidian distance computation so that the distances are R times shorter along the habit plane direction as in the perpendicular direction. For the case of Figure VI.2 (c), the remaining austenite was transformed only into LB and no martensite fraction was added.

The bainite and martensite orientations of the pixel are obtained from the austenite orientations, the orientation relationship of the transformed product (OR_{UB} or OR_{LB}) and the symmetry operator corresponding to the variant. Some orientation noise can be also added as rotation around a random axis by an angle following a 0-centered gaussian distribution with a given half width (HW_{UB} and HW_{LB}).

VI.3 Automatic segmentation of upper and lower bainite

VI.3.1 Data for testing and validation

Initially, a synthetic map containing 50% UB and 50% LB has been generated with the parameters described in the column “Set value” in Table VI.1. The strategy has been tested on such synthetic microstructures as a simpler validation problem before addressing the more complex real microstructures.

The experimental EBSD map comes from the SuperElso® 533 E low carbon steel sample, whose chemical composition has been presented in V.2.2. This sample was austenitized and then cooled to form upper bainite down to 450°C. The sample was then maintained 15min above Ms at 450°C to transform the remaining austenite into lower bainite. Finally, an helium quenching was performed, resulting in a two-phase microstructure showing upper and lower bainite. To differentiate this sample from the ones presented in Chapter V, we call it B sample along this chapter.

The sample was mechanically polished using P1000 SiC grit paper, a 9 μm and 3 μm diamond suspension and a colloidal silica solution finish. EBSD acquisitions were performed using an Oxford Instruments Symmetry camera in a JEOL F100 SEM. A single 252×189 μm map was acquired with a 0.1 μm step, 20 kV accelerating voltage, 8×8 binning, 0.6ms integration time and no pattern averaging. No austenite was indexed in the map and the attained indexing rate was 98.3%.

VI.3.2 Important EBSD-based parameters to discriminate upper and lower bainite

Figure VI.3 (a) shows Band Contrast (BC) of the experimental map with the specific misorientations while Figure VI.3 (b) presents a manual labeling that has been performed based on the parameters that will be described below. Both constituents can be observed: (1) Upper bainite (UB) characterized by irregular grains presenting boundaries with low misorientation angles and sometimes forming coarse laths and (2) Lower bainite (LB) presenting a lath-like structure with high inter-granular misorientation angle values greater than 45°.

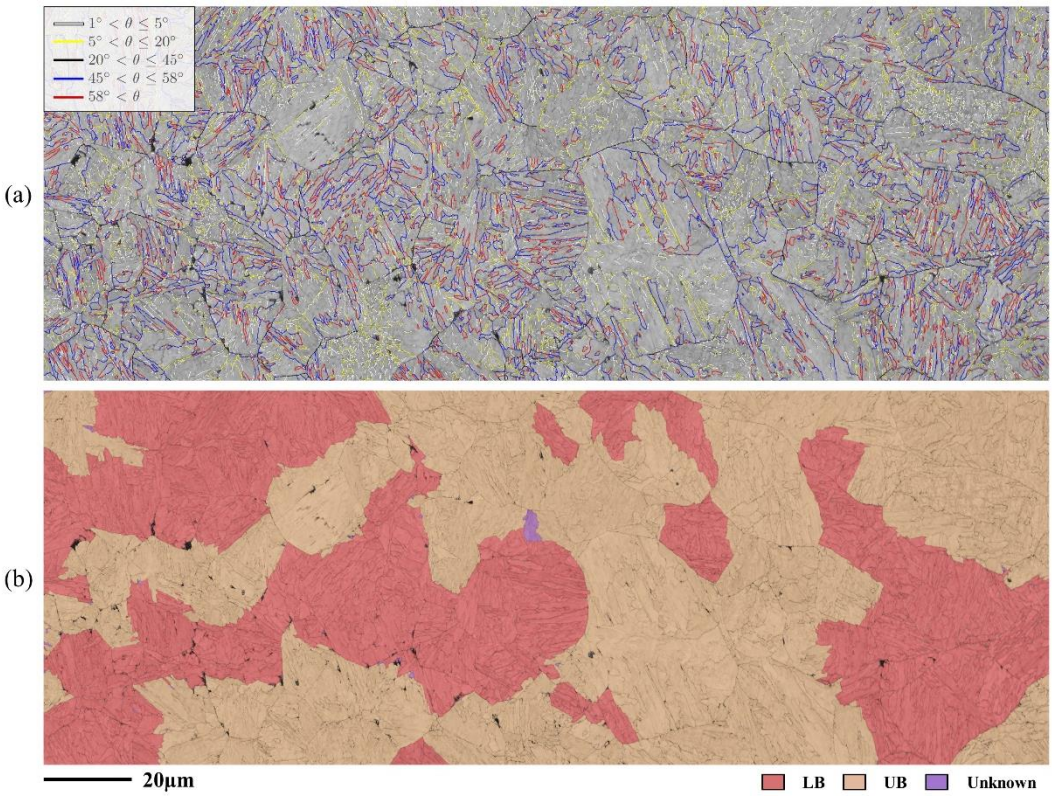

Figure VI.3. (a) Specific misorientations and (b) labeling of the acquired map on the B sample.

These two constituents present distinct variant organizations within their prior austenite grains that could help to differentiate them. Parent grain reconstruction was performed using Merengue2 software [7]. In a first step, crystallographic domains were detected with a 3° threshold angle using AlGrId method down to 0° to close remaining open contours [85]. Then fragments of austenite grains were identified with a 3° threshold and enlarged with a 4° threshold. The orientation relationship used was refined with XABX method ($\phi_1 = 3.384, \Phi = 46.293, \phi_2 = 5.797$) [214]. These parameters made it possible to reconstruct 93.6% of the parent map.

Figure VI.4 shows the reconstructed parent grains on a crop, along with the packets, blocks and sub-blocks (variants) of two parent austenite grains. The top grain represents typical UB, it contains two packets that also represent two blocks, and these blocks contain one or two sub-blocks. On the other hand, the bottom parent grain is representative of LB. It contains several packets which are subdivided in several block and sub-blocks, which is representative of an LB or martensite variant organization [192]. The misorientation distribution inside each packet in such microstructure therefore seems to be an interesting indicator to distinguish those two constituents.

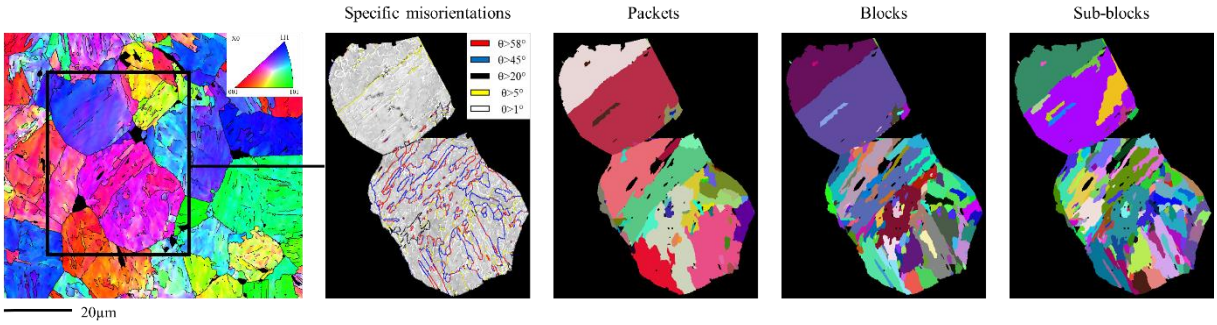

Figure VI.4. Reconstructed austenite grains, specific misorientations and the packet/block/sub-block organization of two specific parent grains. Each of the colors on the packet/block/sub-block plot indicates a different packet, Bain group or variant respectively.

Figure VI.5 presents the (a) specific misorientations and (b) labeling of the generated synthetic microstructure where the characteristics described above for an experimental microstructure can be found.

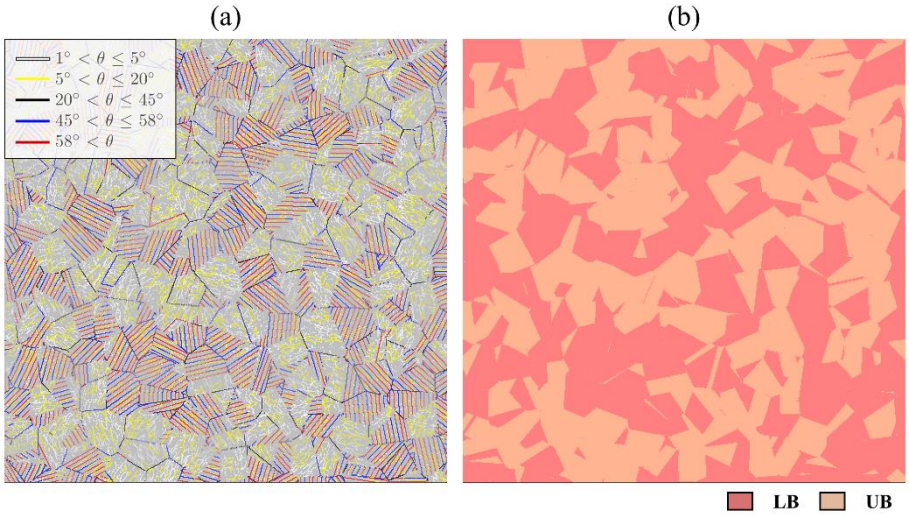

Figure VI.5. (a) Specific misorientations and (b) labeling of the generated synthetic microstructure.

VI.3.3 Methods

VI.3.3.1 *k*-means clustering principle

k-means is a classic clustering approach that has been used across a large range of application areas in many different fields. The k-means algorithm divides a set of n samples *x* into *k* disjoint clusters of equal variances, each described by the mean μ_j of the samples in the cluster [215]. The means are commonly called the cluster "centroids". The centroids are selected in order to minimize the inertia criteria known as:

$$\left(\sum_{i=0}^{n} \min\left(\|x_i - \mu_j\|^2\right)\right)$$

To better explain its principle, we observe Figure VI.6 where we consider a 2D dataset. Firstly, the centroids are randomly initialized (denoted by the crosses in Figure VI.6 a). In general, the centroids do not belong to the dataset *x* but live in the same space. The number of centroids is defined by the user by setting *k*. Once centroids are initialized, the Euclidean distances from the centroids to all the data points are measured and the data points are assigned to the cluster with the closest centroid (Figure VI.6 (b)). Once the clusters are formed, the mean of the data points forming the cluster is calculated and the centroid is repositioned in order to optimize the clustering (Figure VI.6 (c)). Centroid optimization and cluster assignment are iteratively repeated until the centroids stop changing their positions and become static, where the algorithm is considered to reach convergence.

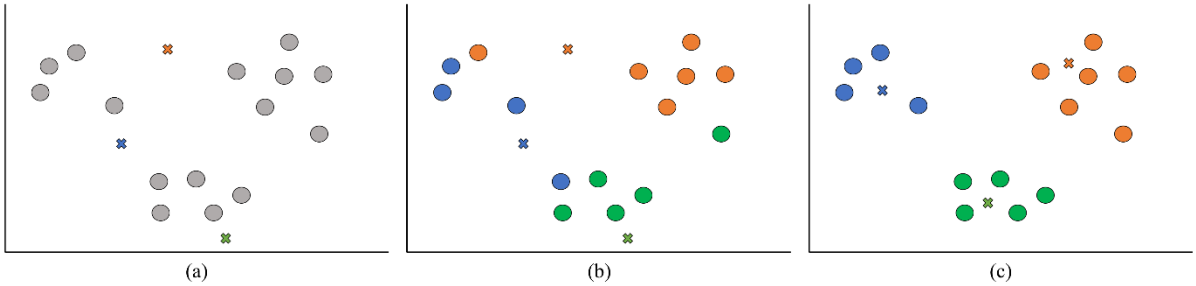

Figure VI.6. (a) Random centroid initialization, (b) cluster assignment and (c) centroid optimization and cluster assignment.

However, the convergence highly depends on the centroids' random initialization. It is possible to obtain two different results after two successive clustering. For this reason, *k*-means is applied several times to the same data set (the number of times is defined by the user), and the selected clustering is the one that mostly reduces the resulting clusters' variance.

The *k*-means implementation available in the Python package scikit learn has been used in this work [216]. The number of clusters k has been set to 4 (four interfaces to classify UB/UB, LB/LB, UB/LB and LB/UB).

VI.3.3.2 Feature extraction and processing

Table VI.2 lists the EBSD-based features that have been used to carry out the classification of the interfaces after a feature engineering process. Apart from the interface average misorientation angle, the remaining features refer to each of the neighboring grains.

Table VI.2. List of features used to feed the k-Means.

Symbol	Feature name
θ	Interface average misorientation angle (°)
Θ_{Grain1}	Packet mean kernel maximum misorientation for Grain 1 (°)
Θ_{Grain2}	Packet mean kernel maximum misorientation for Grain 2 (°)
Σ_{Grain1}	Packet kernel maximum misorientation standard deviation of Grain 1 (°)
Σ_{Grain2}	Packet kernel maximum misorientation standard deviation for Grain 2 (°)

The grains were obtained by a classical grain detection that clusters pixels misoriented one to the next below a user-defined threshold angle. UB usually presents a lot of sub-blocks with low angle boundaries. Therefore, a classical grain detection threshold (3-5°) clusters most of the UB sub-blocks in larger UB grains (blocks). Reducing the threshold angle to 1° allowed the detection of more grains for the UB phase resulting in a more balanced dataset. Note that despite being small, this threshold is still above the acquisition angular precision (estimated around 0.4°). The interface misorientation angle was obtained by averaging the misorientations along the interface as described here [217].

The organization inside the packets can help to differentiate the two constituents. LB usually presents several blocks per packet while UB forms one block divided in sub-blocks [55], [213]. The packet each grain was assigned to was found by performing a parent grain reconstruction using Merengue2 software

[7] following the methodology described in VI.3.2. The grains for which the parent grain orientation could not be reconstructed were removed from the dataset. A kernel maximum misorientation map was computed as a way to characterize the average and standard deviation of the misorientation angle inside each packet. In such a map, one assigns to each pixel the maximum angle of the misorientation with its first 8 neighboring pixels. The average (Θ) and standard deviation (Σ) of this angle is then calculated inside each packet and is used as a feature because it was thought to be sensitive to variant pairing (number and type of blocks and sub-blocks).

These features were extracted from both the synthetic and experimental EBSD maps. The smallest grains (area $< 2\ \mu m^2$) were removed from the dataset. Those grains are mostly low angle misoriented clusters introduced by the 1° grain detection. Their constituent can easily be obtained by neighbors' extrapolation after segmentation. To balance the dataset, data with $\Theta_{Grain1} = \Theta_{Grain2}$ and $\Sigma_{Grain1} = \Sigma_{Grain2}$ have been ignored. This increase drastically the ratio UB/LB + LB/UB over UB/UB + LB/LB boundaries but reduce also the intra-packet boundaries. Before being fed, each feature data was normalized so that the distribution of the whole dataset was centered in 0 with a standard deviation of 1.

VI.3.3.3 Grain constituent segmentation

The clustering yields the constituent of the grain at each side of the interface. However, since the clustering is not 100% accurate, some errors must be tolerated in the grain interface classification. Thus, the final segmentation is obtained by computing the probability $P_i(j)$ of the grain (i) to belong to a constituent (j) as:

$$P_i(j) = \frac{\sum_{p=0}^{N} l_{ip}\,\delta\big(C(x_{ip}), j\big)}{\sum_p l_{ip}}$$

where δ is the Kronecker function, $c(x_{ip})$ represents the classifier prediction for features x of the interface between grains (i) and (p) , l_{ip} is the length of the interface and N is the number of interfaces of the grain. The grain is considered to belong to the constituent (j) if $P_i(j)$ is over 51%. Otherwise, the grain is considered ambiguous and is not classified.

VI.3.3.4 Performance evaluation metrics

Although most of the unsupervised learning approaches seen in the literature do not compare their results to human labeling, we think that it is the only way to evaluate to which extent the segmentation of the microstructure provided by our method is correct or at least close to our expectations. Therefore, the map acquired for the B sample has been labeled based on the criteria described in VI.3.2 and performing manual corrections. As in the case of MP samples presented in Chapter V, ambiguous grains were labeled as 'unknown' and were not used to estimate the accuracy of the method.

To calculate the accuracy of the result, the obtained segmentation and the labeling have been compared pixel-wise using the F1 score explained in II.3.4.

VI.3.4 Segmentation results

VI.3.4.1 Performance on synthetic microstructures

Figure VI.7 presents the distribution of the datapoints observing the four features described in Table VI.2 that have been used to carry out the clustering. The colors separate the *k* clusters found. It must be noted that once the clusters are found by the *k*-means algorithm, it does not know to which of the classes each cluster belongs, i.e. we have to assign the classes to the obtained clusters based on our experience. Four clear clusters have been found:

The cyan class showing low mean misorientation angle with low standard deviation, associated to the UB/UB interface and inversely the violet class presenting high mean misorientation angle with high standard deviation associated to the LB/LB interface. Thus, the yellow cluster refers to the UB/LB interfaces while the red one corresponds to the LB/UB. It must be noted that these 2D scatter plots do not allow to see the real distribution in the 4D space observed by the *k*-means algorithms and some information can be lost in the analysis.

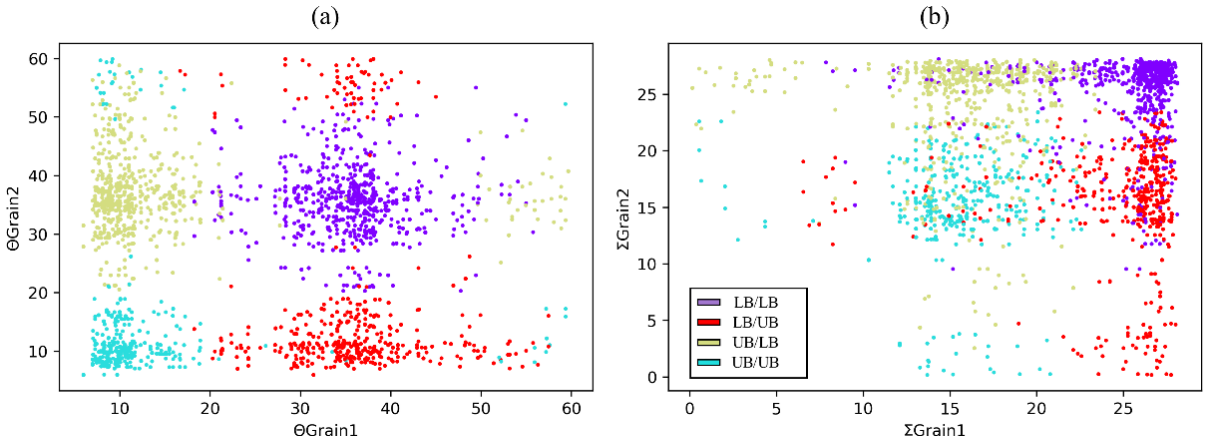

Figure VI.7. Datapoints distribution observing (a) ΘGrain1 vs. ΘGrain2 and (b) ΣGrain1 vs. ΣGrain2. The colors represent the k clusters found.

Figure VI.8 presents the synthetic map where (a) shows the specific misorientation angle distribution, (b) the labeling, (c) the *k*-means interfaces classification and (d) the grain segmentation obtained after the process detailed in VI.3.3.3. An excellent correlation between the segmentations and the labeling was found, overcoming 99%-pixel accuracy (ignoring the pixels that were not classified during clustering).

Grains in white and in purple in Figure VI.8 (d) represent respectively grains that were too small to be classified (1.6% of the map), and grains that were considered "ambiguous" as defined in (0.24% of the map). Ambiguous grains were either single UB grains surrounded by LB or small LB packets surrounded by UB. Such grains presented different characteristics from the other grains of the same constituent. Their constituent was therefore more challenging to assess.

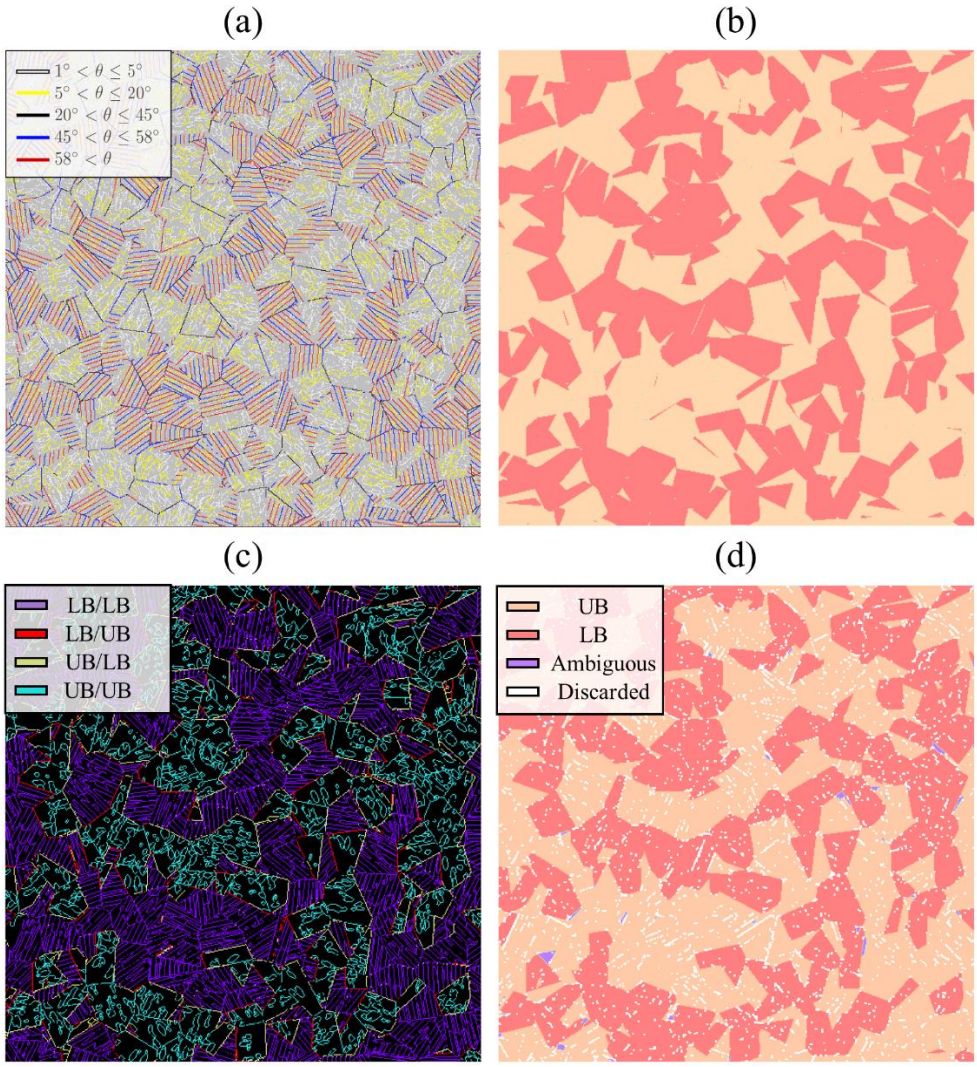

Figure VI.8. Synthetic map where (a) specific misorientation angle distribution, (b) labeling, (c) k-means interfaces classification and (d) grain segmentation.

VI.3.4.2 Performance on experimental microstructures

Once we demonstrated the validity of the strategy on synthetic microstructures, we assessed the ability of our approach to segment real microstructures showing UB and LB. Figure VI.9 presents the distribution of the datapoints observing the four features described in Table VI.2 that have been used to carry out the clustering. Although the clusters found in Figure VI.9 are not so well separated as in Figure VI.7, the same trend has been found.

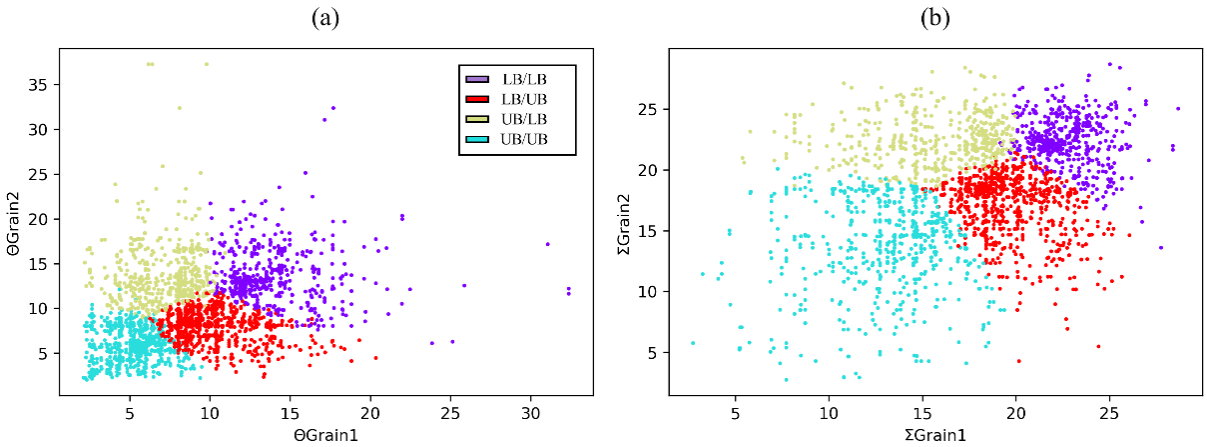

Figure VI.9. Datapoints distribution observing (a) ΘGrain1 vs. ΘGrain2 and (b) ΣGrain1 vs. ΣGrain2. The colors represent the k clusters found.

Figure VI.10 presents a crop of the experimental map presented in Figure VI.3 where (a) shows the specific misorientation angle distribution, (b) the *k*-means interfaces classification, (c) the labeling and (d) the grain segmentation. A general visual agreement can be found when comparing the labeling (Figure VI.10 (c)) and the segmentation result (Figure VI.10 (d)).

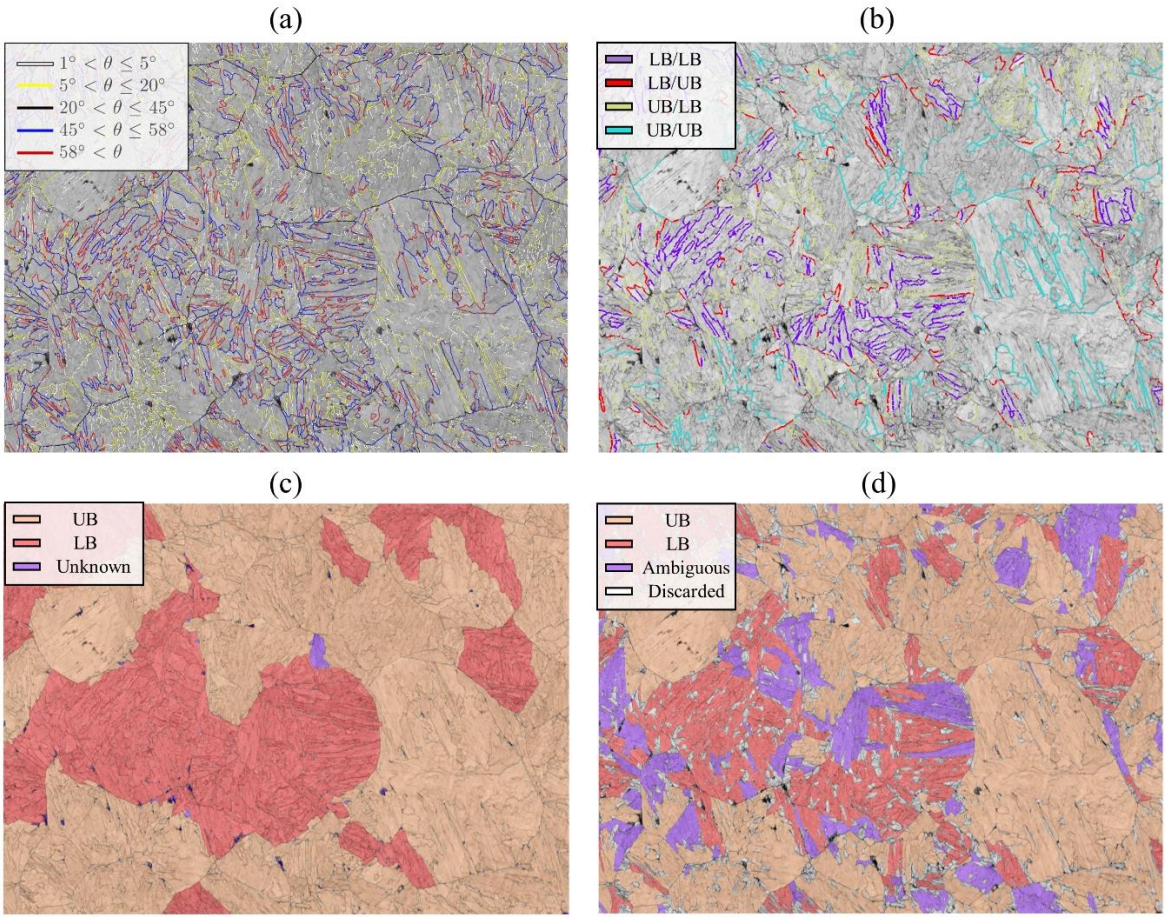

Figure VI.10. Crop of the experimental map where (a) shows the specific misorientation angle distribution, (b) the labeling, (c) the k*-means interfaces classification and (d) the grain segmentation.*

The quantitative results are presented in Table VI.3. Even if Figure VI.10 only shows a crop of the acquired map, the quantitative results presented below have been calculated across the entire map. It

must be noted that the calculation of the general accuracy, together with both F1 scores do not consider the discarded nor unknown/ambiguous pixels. A general accuracy above 93% can be considered as a good result regarding the complexity of the microstructure and the unsupervised nature of the approach. Additionally, this accuracy is well funded since the F1 scores of both phases reached high values.

Table VI.3. Evaluation of the pixel-wise performance of the method.

General accuracy [%]	F1 score UB	F1 score LB	Ambiguous pixels [%]	Discarded pixels [%]
93.23	0.91	0.82	15.05	13.95

VI.3.4.3 Importance of feature engineering

The features presented in Table VI.2, are the result of a feature engineering process where the most suitable features to separate UB and LB have been researched. However, there exists other features that can be easily obtained from EBSD such as BC, KAM, grain size, among others (Table VI.4).

Table VI.4. Classic EBSD derived features.

Symbol	Feature name
A_{Grain1}	Grain 1 area (μm^2)
A_{Grain2}	Grain 2 area (μm^2)
BC_{Grain1}	Grain 1 Band Contrast mean
BC_{Grain2}	Grain 2 Band Contrast mean
GAM_{Grain1}	Grain 1 Grain Average Misorientation (°)
GAM_{Grain2}	Grain 2 Grain Average Misorientation (°)

The GAM has been obtained by calculating the mean of the KAM with a threshold angle of 3° and a kernel size of 3x3 within each detected grain. Features such as BC and KAM have been very useful in the discrimination of the DP and MP microstructures presented in Chapter V, thus a *k*-means clustering has been applied to such parameters and the result is presented in Figure VI.11 (a) together with the labeling (Figure VI.11 (b)).

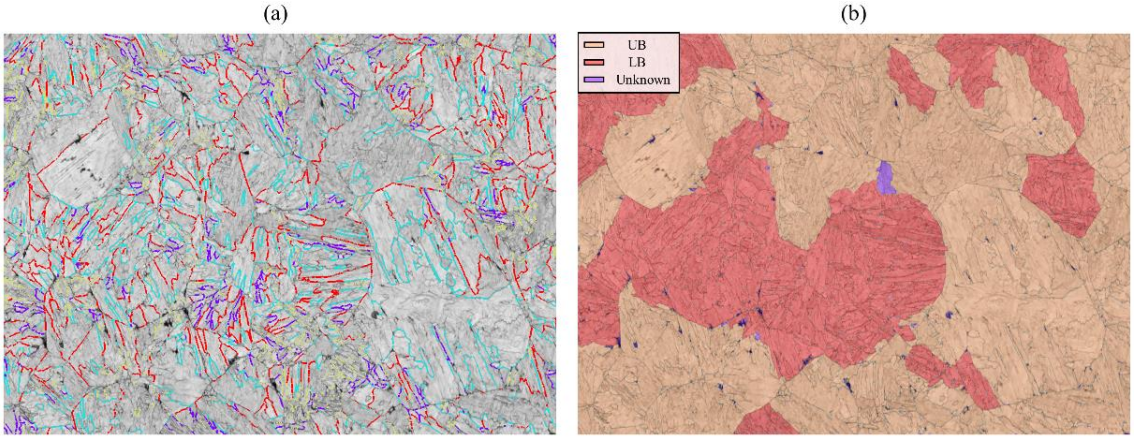

Figure VI.11. (a) k-means interfaces classification using the features of Table VI.4 and (b) labeling.

From the result presented in Figure VI.11 (a) it becomes complicated to assign with high confidence what color correspond to what interface type as the classification looks random. This is related to the fact that the features in Table VI.4 do not present values that discriminate significantly UB from LB.

Although the information obtained at the level of the packets needs prior analyses like parent reconstruction, it provides very important and discriminative features for the characterization of UB and LB. It must be noted that the interface average misorientation angle has been added to Table VI.2 since it slightly improved the segmentation in terms of general accuracy and F1 scores, however the real game changers to get high quality results seem to be packet related features.

VI.4 U-CNN approach

Inversely to methods based on feature engineering to find the best characteristics that describe the desired classes to discriminate, the U-CNN approach performs feature extraction by itself. As we want to segment the DP and MP samples presented in Chapter V, the method is fed with the same EBSD-based images (BS and KAM) as U-Net.

VI.4.1 Description of the method

Figure VI.12 shows a scheme of the proposed method. It has been initially developed by Kanezaki [218] for the segmentation of images coming from the Berkeley Segmentation Dataset and Benchmark (BSDS500) [219], [220] and later implemented by Kim et al. [178] and adapted for the segmentation of LOM micrographs.

The main idea behind the method is basically divided in three steps. First the input image is separated into small regions of interest using a superpixel algorithm that subdivides the image into clusters of pixels sharing similar characteristics in terms of color and spatial proximity. Then, features characterizing each of the clusters are searched by introducing the input image into a CNN. The clusters that are characterized by the same features are likely to be classified with the same label producing a refined image of the CNN output. In the following, details about each of the steps considered in the method are given.

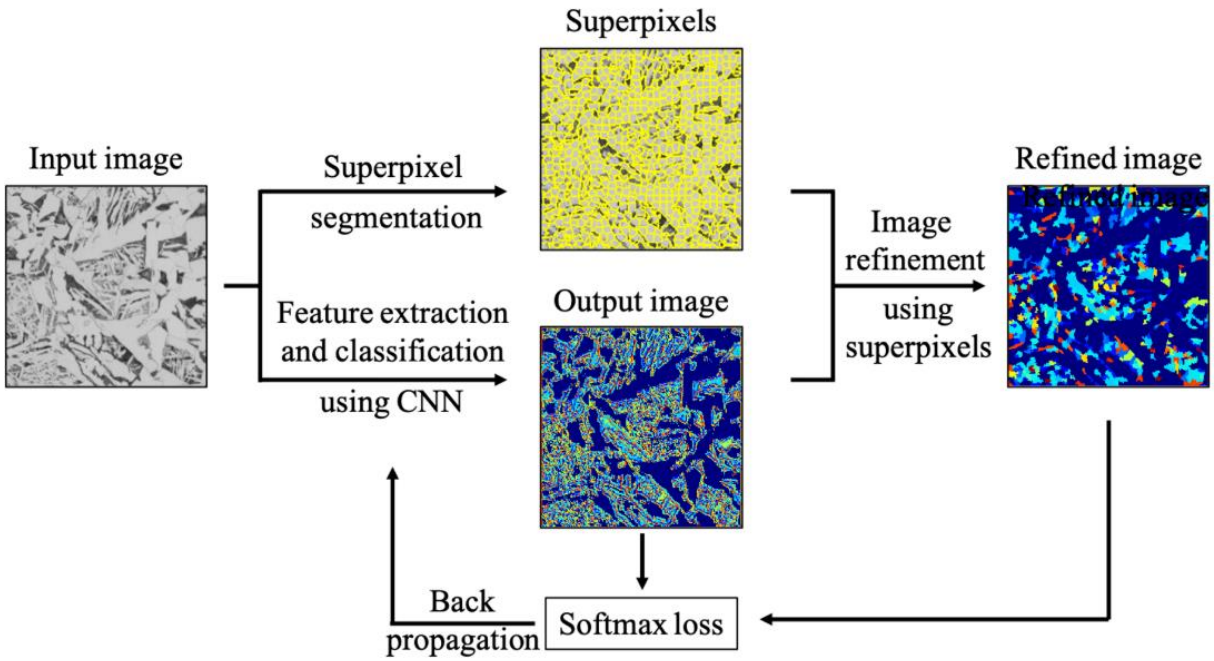

Figure VI.12. Schematic illustration of the applied algorithm composed of CNN and a superpixel algorithm. Image extracted from [178].

VI.4.1.1 CNN feature extraction and classification

The CNN is used as a feature extractor and pixel classifier. The architecture used in [178] is presented in Figure VI.13. Basically, it presents several hidden convolutional layers where feature extraction is performed. After each layer, a ReLU activation function is employed. A batch normalization is applied after each activation function [221] where the idea is to normalize the outputs of the activation function so that a subsequent convolutional layer can receive an image having zero mean and unit variance. It has been shown that rescaling the image before inputting allows a faster, efficient, and more stable learning [222].

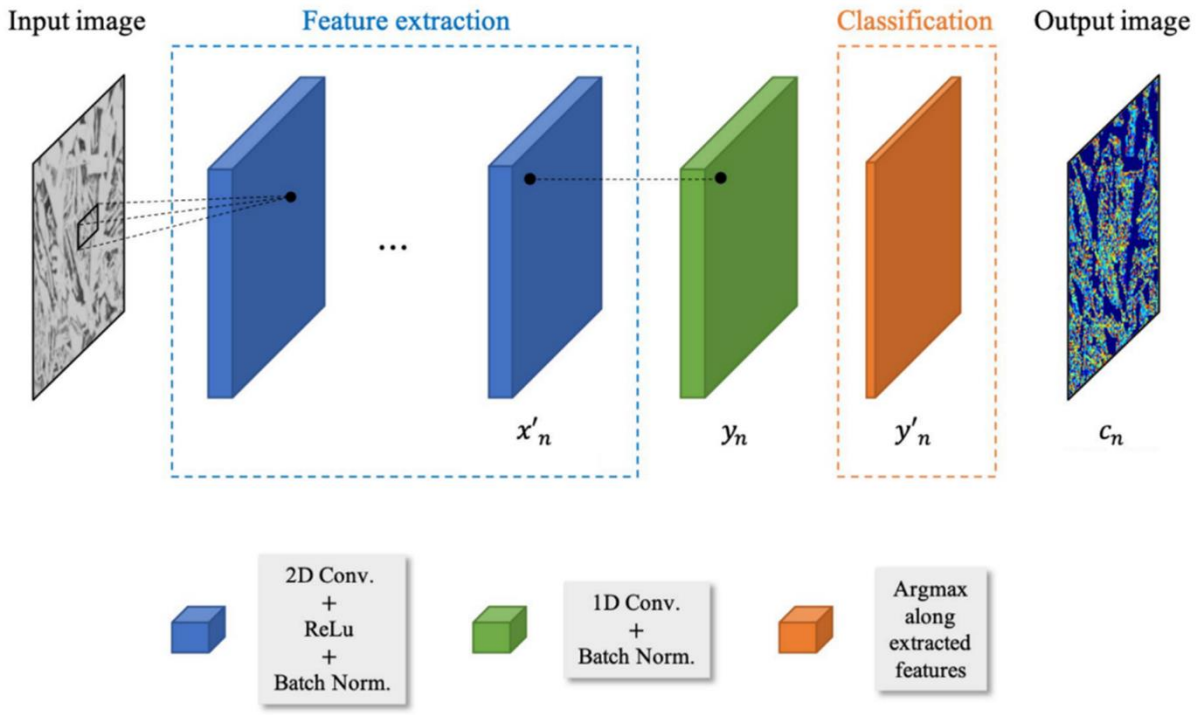

Figure VI.13. Scheme of the algorithm's architecture. Image extracted from [178].

After the hidden layers, a 1D convolution is applied in order to obtain the feature vectors characterizing each pixel of the image and the batch normalization is also implemented here. The final classification to assign each pixel with a class is carried out by an Argmax function (finds the class with the largest predicted probability). Thus, the final output of the CNN is a segmented image where each pixel is assigned to a class, and this class depends on the feature that most activates that pixel. If two pixels get a high activation with the same feature, then they will likely belong to the same class.

The hyperparameters of the CNN have been selected after trial and error but the final values are 4 hidden layers, 50 filters per hidden layer with a kernel of 3x3 pixels.

VI.4.1.2 Superpixel segmentation: SLIC

The superpixel algorithm used in [178], [218] was the simple linear iterative clustering (SLIC) [180]. This algorithm performs a local clustering of pixels in a 5D space [*labxy*], where [*lab*] are the components L, a and b of the CIELAB color space and [*xy*] are the pixel position. Therefore, it clusters pixels by their color similarity and spatial proximity.

In order to cluster pixels in this 5D space, it is not possible to use Euclidean distances as the possible distance between two colors in the CIELAB space is limited and the spatial distance in the *xy* plane depends on the image size. Therefore, a new distance measure that considers the superpixel size must be introduced.

The algorithm takes as input a desired number of approximately equally-sized superpixels *K*. Considering an image of *N* pixels, the size of each superpixel is *N/K* and there would be a superpixel

center at every grid interval $S = \sqrt{N/K}$. Euclidean distances in CIELAB color space are perceptually meaningful for small distances. If spatial pixel distances exceed this perceptual color distance limit, then they begin to outweigh pixel color similarities. Thus, the new distance measure is defined as follows:

$$D_s = d_{lab} + \frac{m}{S} d_{xy}$$

Where d_{lab} and d_{xy} are the Euclidean distances in the CIELAB color space and *xy* space respectively, defined as:

$$d_{lab} = \sqrt{(l_k - l_i)^2 + (a_k - a_i)^2 + (b_k - b_i)^2}$$

$$d_{xy} = \sqrt{(x_k - x_i)^2 + (y_k - y_i)^2}$$

In the equation of D_s, the Euclidean distance of the *xy* space is normalized by the grid interval *S* and a variable *m* is introduced to control the compactness of a superpixel. The greater the value of *m*, the more spatial proximity is emphasized, otherwise the color proximity gains more relevance. Figure VI.14 shows an example of the effect of varying both *K* and m parameters for a random RGB image.

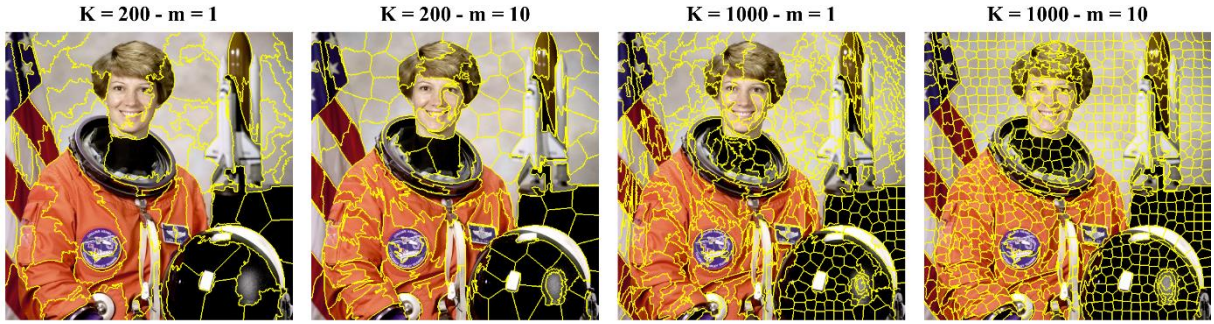

Figure VI.14. Effects of the number of superpixels K and the compactness m on the superpixel segmentation. The image of the astronaut has been extracted from the Python scikit-learn library [216].

VI.4.1.3 Image refinement and CNN training

Once the image is fed to the CNN, it undergoes the corresponding convolutions and after the first epoch it will provide a first labeling result called output image in Figure VI.12. As a reminder, the number of epochs is equals to the number of times the network has seen the entire training dataset, in this case, the image we want to segment. Each pixel of this output image has been classified with a class according to the filter from the 1D convolution that most activates the particular pixel. Thus, if a total of 50 filters have been applied in the 1D convolution, the maximum number of classes that the output image can have is equal to 50 (after the first epoch).

The output image is extracted and refined using the image segmented with the superpixel approach. Each superpixel is formed by a set of pixels each one with an assigned class after the CNN classification. Therefore, the superpixel will be assigned to the class that the higher fraction of its forming pixels has been assigned after CNN classification. This results in finding features that characterize the superpixels.

In order to train the CNN, the refined image is used to calculate the loss function with the output image of the CNN. Like this, the number of classes starts to get reduced after each epoch. The training comes to an end when the desired number of classes set by the user are segmented in the image.

The backpropagation learning is performed using the stochastic gradient descent (SGD) optimization algorithm and the selected loss function is the cross entropy, although in Figure VI.12 the Softmax loss is indicated.

VI.4.2 Segmentation results

VI.4.2.1 Performance on DP samples

Figure VI.15 shows the segmentation results for the EBSD maps presented in V.5. The obtained accuracies are very high and in the order of those obtained by the U-Net supervised approach for the same maps. The main part of the errors observed in the accuracy maps are located at the ferrite-martensite interphase as a result of a martensite size overestimation (false martensite = red pixels).

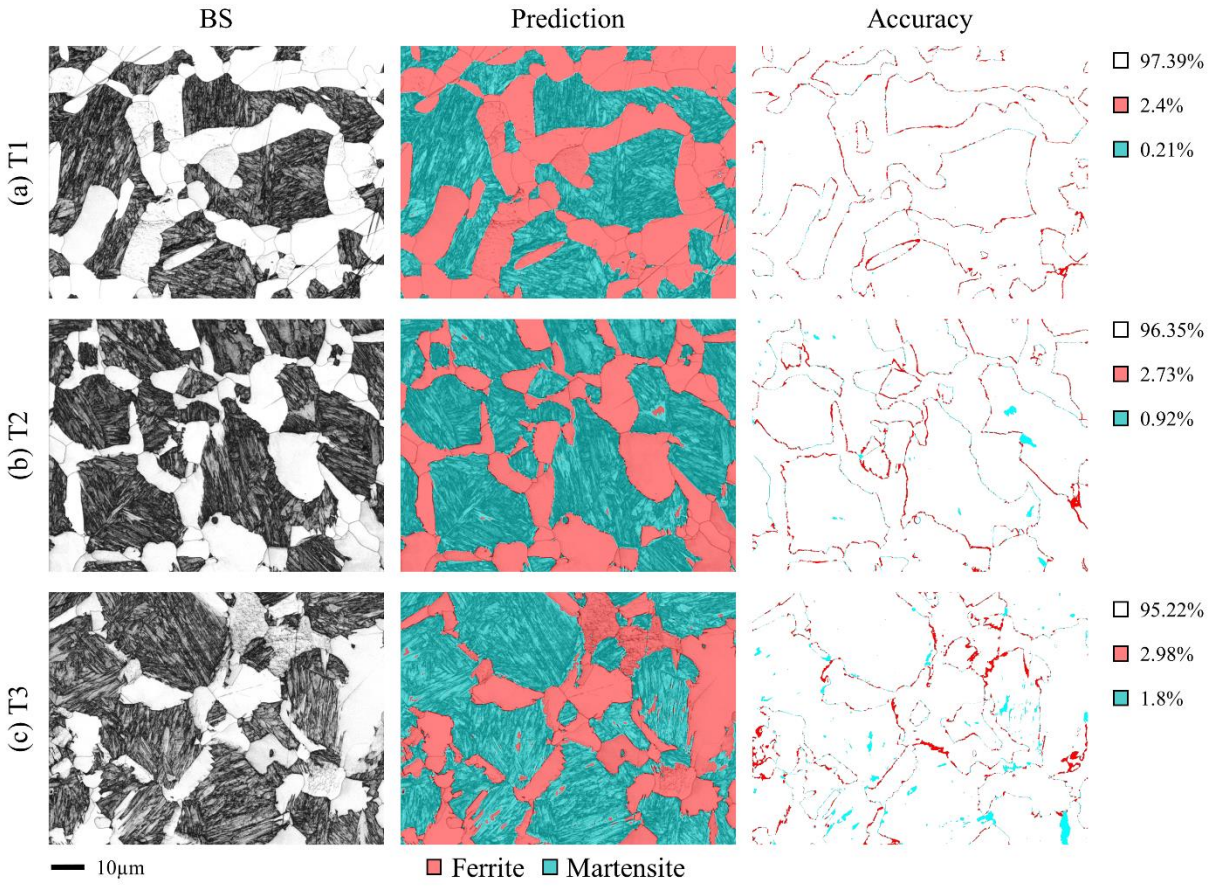

Figure VI.15. Segmentation prediction and accuracy images obtained over three EBSD maps belonging to each of the DP samples.

These results have been obtained by setting the *K* and *m* SLIC parameters to 5000 and 1 respectively and using the BS map as input image (Figure VI.16 (a)). It can be seen that in the regions where the color similarity is high, the superpixels remain mainly squared increasing the compactness and giving relevance to the spatial proximity. However, when we approach the interphases where there is a great

change in color, then the superpixels get an irregular shape what allows to gives importance to the color similarity. It must be noted that although the lowest possible compactness parameter has been provided (m=1), the shapes of the superpixels are not so irregular as in the example shown in Figure VI.14. If an m=10 would be used to segment our DP BS map, almost no irregularities in the superpixels shape are allowed and the clusters are almost perfectly squared (Figure VI.16 (b)).

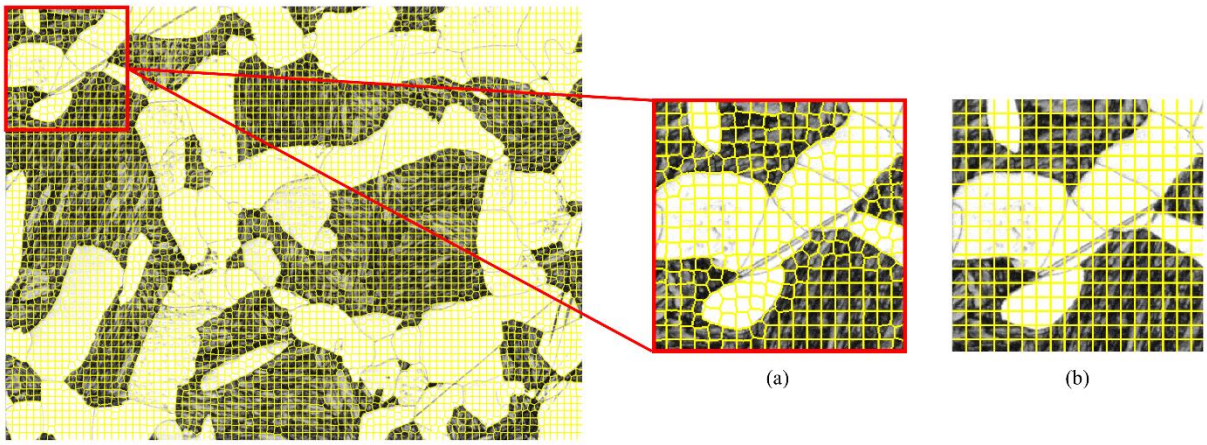

Figure VI.16. Superpixel segmentation of the T1 sample using (a) K=5000 and m=1 and (b) K=5000 and m=10.

VI.4.2.2 Performance on MP samples

Figure VI.17 (a) and (b) show a crop of the BS map and the labeling of the API-1 sample presented in Chapter V respectively. Figure VI.17 (c) presents the segmentation result. As in the case of the DP samples, the *K* and *m* SLIC parameters have been set to 5000 and 1 respectively and the BS map was used as the input image.

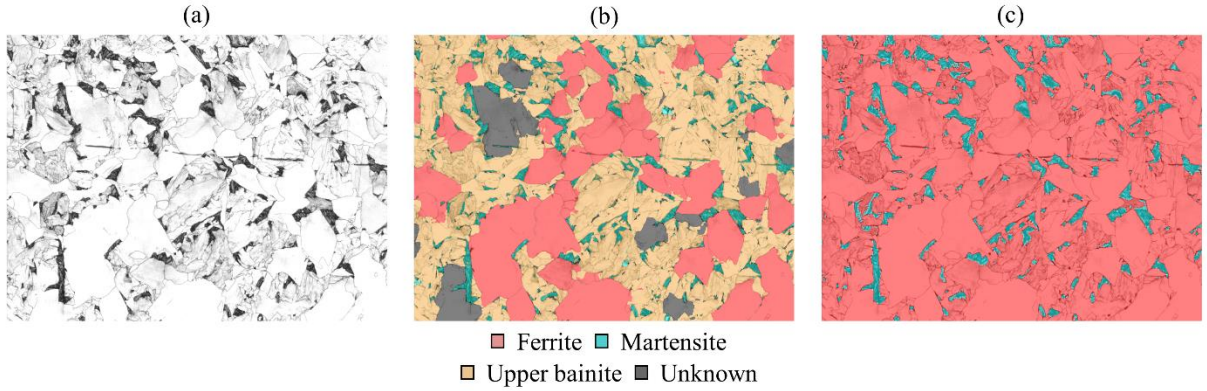

Figure VI.17. (a) BS, (b) labeling and (c) segmentation result with a model trained on BS for a crop of the API-1 sample.

Although three classes (ferrite, upper bainite and martensite) are present in the API-1 sample, the segmentation result of Figure VI.17 (c) shows that the model found two main classes: red and cyan. The cyan class can be clearly associated to martensite, as in the case of DP samples, and the red class is a mixture of ferrite and upper bainite. Therefore, by providing the BS only, the segmentation result is not satisfactory as it cannot even find the number of present phases. However, the F1 score on the martensite segmentation reached 0.79, a high value considering the unsupervised nature of this approach.

As in the case of the U-Net architecture presented in Chapter V, the CNN can be fed with any number of inputs. Thus, it is possible to provide EBSD-derived features such as KAM together with the BS. Figure VI.18 (a) and (b) show the KAM map and the labeling of the API-1 sample and Figure VI.18 (c) presents the segmentation result obtained with a model trained on both BS+KAM inputs. In this case, three classes are clearly detected by the model, cyan (martensite), red (ferrite) and orange (upper bainite). Even if the result does not look perfect, the model is able to correctly find the regions of the map associated to each of the present phases.

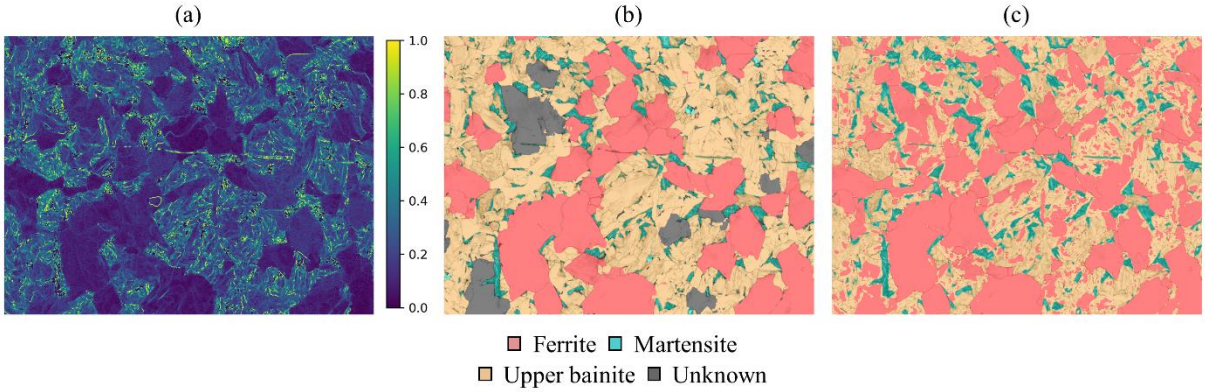

Figure VI.18. (a) KAM, (b) labeling and (c) segmentation result with a model trained on BS+KAM for a crop of the API-1 sample.

Figure VI.19 presents the confusion matrix together with the F1 scores for each of the phases. Reaching F1 scores around 0.8 for the classification of such multiphase microstructure is a very good result considering the unsupervised nature of the approach. As seen from the confusion matrix, the highest fraction of errors comes from false ferrite predicted in actual upper bainite. It is logic that the model struggles in such situation since it is the most difficult configuration even for experts. Although the segmentation of martensite visually matches the labeling, there exist a slight size overestimation that reduces its F1 score.

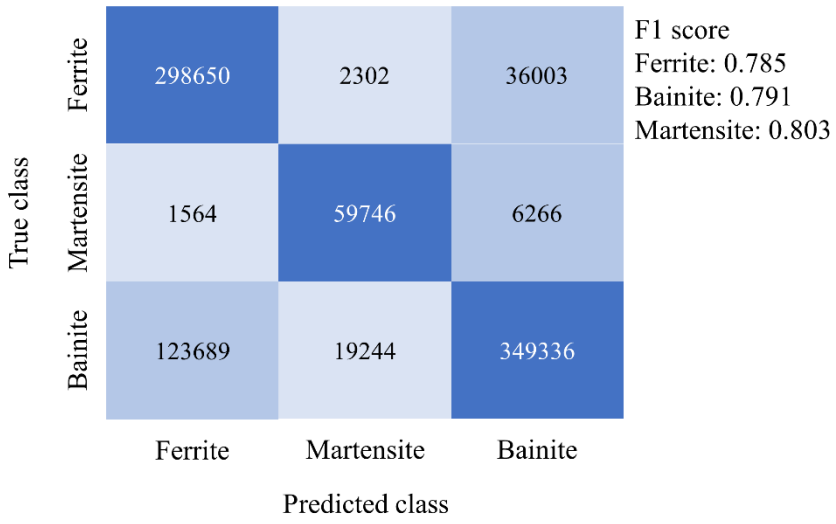

Figure VI.19. Confusion matrix and F1 scores for each present phase in the API-1 sample.

The method worked relatively well on the API-1 sample, but it did not on another MP sample such as the API-2. Figure VI.20 shows the (a) BS, (b) KAM, (c) labeling and (d) segmentation result using a model trained on BS+KAM for a crop of the API-2 sample. It can be observed that the martensite phase is mainly well segmented (F1 0.79) due to the high contrast existing with ferrite and upper bainite in terms of BS and KAM. However, there is no clear contrast between ferrite and upper bainite in both BS and KAM maps, what results in a single class that segments both phases. This example shows that for the model to work properly and provide accurate results, the inputs must show enough contrast in their microstructural features.

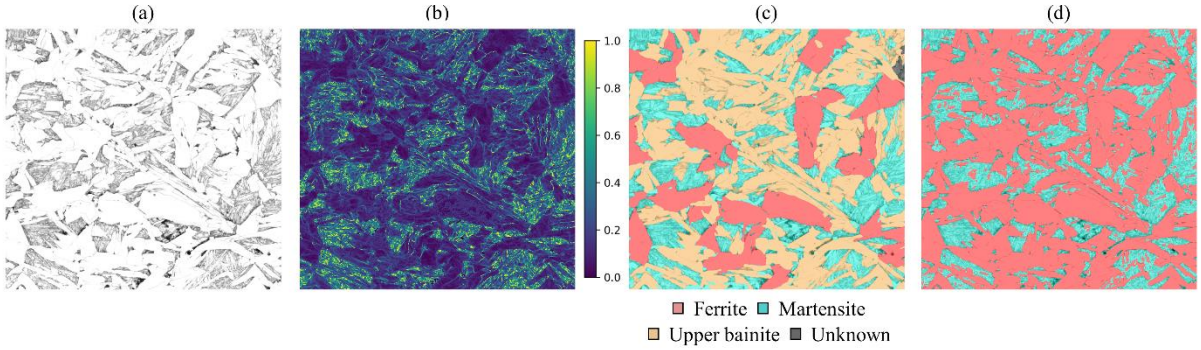

Figure VI.20. (a) BS, (b) KAM, (c) labeling and (d) segmentation result with a model trained on BS+KAM for a crop of the API-2 map. The KAM scale has been limited to 1° to better visualize the contrast between the different constituents

VI.4.2.3 Variability of the result

Due to the random initialization of the CNN and the stochastic nature of the backpropagation learning it is possible that the segmentation results obtained after two successive trainings may be different. For instance, the segmentation results for the API-1 sample after two successive trainings based on BS+KAM look like those shown in Figure VI.21 (b) and (c). While in (b) there is an overestimation of the upper bainite fraction, in (c) inversely we can observe an underestimation. The model struggles to correctly classify ferrite and upper bainite while martensite is classified mainly homogeneously after successive trainings.

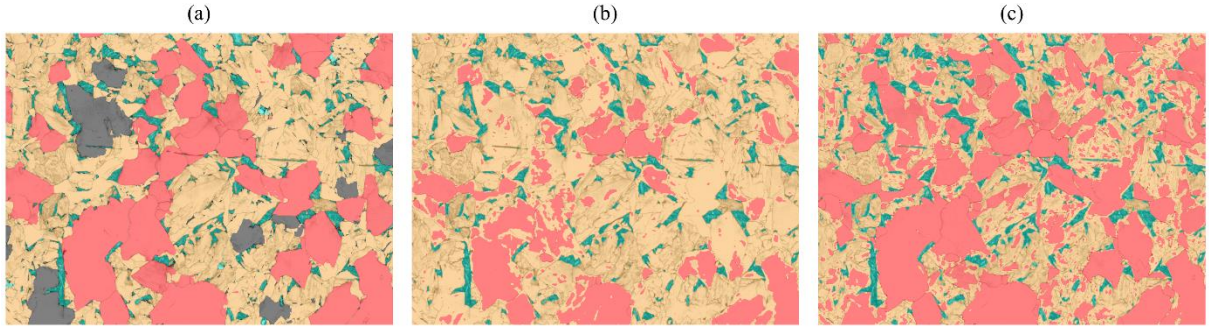

Figure VI.21. (a) Labeling, (b) and (c) segmentation results for two successive trainings.

VI.5 Conclusions and perspectives

Three interesting preliminary axes have been addressed in the search of progressively integrate unsupervised learning approaches to the characterization of steel microstructures. From the findings and results presented along the current chapter, the following conclusions and perspectives can be drawn:

- It has been shown that the Orientation Map Generator software has the ability to simulate crystallographic features of the phase transformation products obtained in steel. Although it has not been fully exploited during this thesis, this tool has a huge potential to train or pre-train any AI-related algorithm avoiding or reducing the need of an experimental dataset generation. Additionally, the fact of generating microstructures with controlled and desired features serves as an ideal validation problem before evolving to a more complex classification or segmentation task involving real microstructures.
- Regarding the *k*-means clustering approach, we have found that features obtained from the packets are interesting to separate UB and LB. Classic EBSD-derived features such as pattern quality or KAM failed to distinguish these two phases being necessary to engineer new features obtained after indirect reconstruction.
- One of the main limitations of the proposed method is that the number of interfaces to classify increases exponentially as we increase the number of considered classes. For instance, if we would like to segment an EBSD map with UB, LB and ferrite, then we have to classify 9 interfaces.
- As a perspective, in order to avoid the interfaces classification, a similar approach could be applied but classifying the packets as an entity, instead of classifying the interfaces and then the grains. Features as those used here, coupled with the number of blocks and subblocks within the packet, their morphology, among others, could be interesting to separate the phases.
- The U-CNN approach has demonstrated an excellent ability to separate ferrite from martensite from the DP-samples. The results are in the order of those obtained by the supervised U-Net. For the MP-samples the results were good only for some particular microstructures showing a clear difference between the phases in terms of pattern quality or KAM. The obtained results for the supervised U-Net were much better in this case.
- In order to improve the quality of the results, it would be possible to initialize the unsupervised CNN with the trained weights of a supervised CNN trained to perform a similar task.
- The main advantage of the U-CNN approach compared to *k*-means is the lack of feature engineering, we only need to provide the input image and let the algorithm work. On the contrary, the input image must present enough discriminating features to find the desired classes.

It must be noted that the presented work in this chapter is preliminary. We have tried to test different paths in order to get in contact with unsupervised approaches and assess the potential of this tool for future works. The obtained results are promising and open opportunities to further research in this direction.

General conclusions and perspectives

Throughout this thesis we have analyzed and studied the contribution of some of the latest developments in the field of acquisition and post-processing of EBSD data for the characterization of steel microstructures inherited from phase transformation. The manuscript has been divided in two main sections: 1) the application of advanced EBSD-based orientation microscopy for the analysis of steel microstructures and 2) the contribution of Artificial Intelligence (AI) algorithms for the discrimination of phase transformation products in steels. The conclusions and perspectives are drawn for each section below.

Section 1 contains two parts:1) the contribution of last generation EBSD cameras and new pattern indexing methods (Hough-based and Pattern Matching) to improve the characterization of multiphase steels and 2) the contribution of high temperature EBSD experiments to analyze the transformation mechanisms and inherited microstructure while heating and cooling, in complementarity with indirect parent reconstruction.

For the first part, we have demonstrated that in order to improve the data quality in terms of indexing rate and the discrimination of phases with similar crystal symmetry, the selected indexing methods plays an important role. Classic Hough Transform (HT) indexing could be further improved by optimizing the list of considered reflectors per phase for indexing. Indeed, HT-based methods do not correlate the actual intensity of the Kikuchi band with its theoretical intensity.

Other indexing methods such as Refined Accuracy (RA) and Dictionary Indexing (DI) have shown their ability to take the band width into account to discriminate phases with the exact same list of reflectors and a difference in the lattice parameter of 0.73Å for both methods, although DI demonstrated a better performance than RA in average.

The quality metric used for phase discrimination with DI also plays a role. Two metrics are usually employed: Normalized Dot Product (NDP) and the Normalized Cross Correlation (NCC). The use of the NCC metric appears to be more robust outperforming NDP in most phase discrimination tasks.

The selection of one indexing method or another is closely related to the desired quality as well as the available time. DI has been tested on different microstructures and the accuracies obtained were the best among all indexing methods. However, its main weakness is the needed preprocessing before indexing that includes pattern saving and dictionary generation, making this technique time consuming. On the other hand, both classic HT-based and RA allow on-the-fly indexing, but in order to exploit its full potential, RA needs to index on high quality patterns what makes it more time consuming than classic HT.

Some perspectives can be drawn from this axis of study. For any HT-based indexing, it would be important to develop a method that considers also the intensity of the detected bands in coherence with their theoretical intensity. In order to optimize time and data quality, ongoing optimized implementation of "on-the-fly Pattern Matching" in acquisition software sounds promising and should be further tested for phase discrimination in steels.

The other main axis of study in section 1 was related to the application of in-situ heat treatments EBSD in complement with indirect reconstruction techniques. Here we have presented a heating module used to carry in-situ experiments. The module can reach 1050°C and has been specifically designed to fit our microscope and be able to perform EBSD in optimal conditions. Preliminary tests of feasibility highlighted maximum heating speeds of 45°C/s and maximum cooling speed of 3°C/s. High quality EBSD maps could be easily and quickly acquired at a speed of 1800Hz and indexing rates above 85%, resulting in acquisition times per map of 30s. Temperature gradients between the temperature measured by the thermocouple and the real temperature of the region of analysis at the surface were evidenced by following the phase transformation. Also, free surface effects such as local chemistry variations like decarburization have been observed in low-alloy steels. Thus, the interpretation of in-situ analyses must consider these aspects of local chemistry variations. More generally, the observation on the free surface must to be verified in the material bulk, which is possible with the help of indirect reconstruction.

Three preliminary in-situ heating experiments on different steel samples were successfully performed. They allowed us firstly to confirm the evolution of the high temperature austenite microstructure obtained on post mortem analysis and indirect reconstruction and secondly to provide new data with more statistics and to propose hypotheses on the mechanisms of transformation. We confirmed that the indirect reconstruction algorithm we use (Merengue2) provides a reliable evaluation of the high temperature austenite phase and their results can be trusted. These preliminary studies open doors to several interesting perspectives where the main focus is on taking advantage of the high quality and acquisition speed of last generation EBSD cameras in order to follow dynamic processes during phase transformation events.

Section 2 was dedicated to the discrimination of phase transformation products in steels microstructures by means of AI algorithms. First, we proposed a supervised semantic segmentation approach with U-Net CNN being fed with EBSD-derived data such as pattern quality and KAM, and considering the step size as an important factor. We were able to reach accuracies above 98% to segment dual phase (ferrite and martensite) microstructures and accuracies ranging from 86% to 99% to segment multi-phase (ferrite, upper bainite and martensite) microstructures. It is important to mention that this is the first model in the literature to perform pixel-wise segmentation of ferrite, upper bainite and martensite based on EBSD data.

To make our model more robust and to generalize its performance, it would be interesting to train it with microstructures coming from different steel grades so that it can work on a wider spectrum of microstructures. Additionally, it would be very useful to generate a database with the labeling results from different users in order to train the model and reduce the subjectivity associated with each of the experts. In order to reduce the need of labeling, working with synthetic maps could be a valid option. A software that generates synthetic orientation EBSD maps containing steel phase transformation products has been developed and could be used to train or pre-train any AI-related algorithm without the need to acquire experimental data and also to confirm the validity of a model before working on real microstructures. Last, it would be important to continue investigating how artificial intelligence algorithms could directly exploit raw orientation data in order to automatically extract meaningful features.

Undoubtedly, the greater drawback of supervised methods is the need of labeling which is very challenging for steel microstructures. Therefore, we have also started to investigate the contribution of unsupervised learning methods. A *k*-means clustering approach has been proposed for the segmentation of upper and lower bainite. Here the interfaces between grains are classified and then the class of each grain is found by a voting scheme considering all its interfaces. In this case, it was necessary to carry out a feature engineering process. We have shown that some features obtained after indirect reconstruction, such as the misorientation within a packet, are good to discriminate upper and lower bainite. The main drawback of this method is that the number of interfaces to classify increases exponentially as we increase the number of considered classes (phases). As a perspective, in order to avoid the interfaces classification, a similar approach could be applied but classifying the packets as an entity by considering the number of blocks and subblocks within the packet, their morphology, among others that may come out of a deeper feature engineering process. This would allow us to classify more phases with no limitation.

Additionally, we have presented an unsupervised CNN coupled with a superpixel clustering algorithm that has been trained on pattern quality and KAM. It demonstrated an excellent ability to segment dual phase (ferrite and martensite) microstructures but it struggled to separate ferrite, upper bainite and martensite from the multi-phase microstructures. The main advantage of this method is the absence of feature engineering (only the input image is needed). Considering the unsupervised nature of this approach and the minimum effort needed, the provided results are satisfactory and can be applied to get a pre-labeling that can be further improved with postprocessing. In order to enhance the quality of the results, it would be possible to initialize the unsupervised CNN with the trained weights of a supervised CNN trained to perform a similar task.

It must be noted that the unsupervised approaches tested in this thesis are preliminary and there is still a lot of work to do in this direction. As important points, we have detected that, although it is labor

intensive, the feature engineering process has a major impact in the performance of a model. This is even more critical in unsupervised methods as they do not have the labeling to guide them. For this reason, if the features are sufficiently distinctive, classification will be much easier. For the clustering we have used a basic *k*-means method to test the feasibility of the approach but there is a large number of more complex algorithms that could be tested.

References

[1] T. Martinez Ostormujof, R. R. P. Purushottam Raj Purohit, S. Breumier, N. Gey, M. Salib, and L. Germain, “Deep Learning for automated phase segmentation in EBSD maps. A case study in Dual Phase steel microstructures,” *Mater. Charact.*, vol. 184, p. 111638, Feb. 2022.

[2] S. Breumier *et al.*, “Leveraging EBSD data by deep learning for bainite, ferrite and martensite segmentation,” *Mater. Charact.*, vol. 186, p. 111805, Apr. 2022.

[3] “Advanced High-Strength Steel (AHSS) Definitions.” [Online]. Available: https://www.worldautosteel.org/steel-basics/automotive-advanced-high-strength-steel-ahss-definitions/. [Accessed: 20-Oct-2022].

[4] J. Goulden, P. Trimby, and A. Bewick, “The Benefits and Applications of a CMOS-based EBSD Detector,” *Microsc. Microanal.*, vol. 24, no. S1, pp. 1128–1129, 2018.

[5] K. Thomsen, N. H. Schmidt, A. Bewick, K. Larsen, and J. Goulden, “Improving the Accuracy of Orientation Measurements using EBSD,” *Microsc. Microanal.*, vol. 19, no. S2, pp. 724–725, Aug. 2013.

[6] Y. H. Chen *et al.*, “A Dictionary Approach to Electron Backscatter Diffraction Indexing,” *Microsc. Microanal.*, vol. 21, no. 3, pp. 739–752, 2015.

[7] L. Germain, N. Gey, R. Mercier, P. Blaineau, and M. Humbert, “An advanced approach to reconstructing parent orientation maps in the case of approximate orientation relations: Application to steels,” *Acta Mater.*, vol. 60, no. 11, pp. 4551–4562, 2012.

[8] F. Bachmann, R. Hielscher, and H. Schaeben, “Texture analysis with MTEX- Free and open source software toolbox,” in *Solid State Phenomena*, 2010, vol. 160, pp. 63–68.

[9] R. Hielscher, T. Nyyssönen, F. Niessen, and A. A. Gazder, “The variant graph approach to improved parent grain reconstruction,” *Materialia*, vol. 22, May 2022.

[10] H. S. Ubhi, J. Parsons, N. Othen, S. Campbell, R. Poole, and A. Gholinia, “In-situ EBSD phase transformation and recrystallisation,” *J. Phys. Conf. Ser.*, vol. 522, no. 1, 2014.

[11] A. Taniyama, T. Amino, K. Hata, and J. Miki, “Development of in-situ orientation mapping and microstructure observation system for ferrite/austenite and martensitic transformations in steel,” *ISIJ Int.*, vol. 60, no. 4, pp. 714–720, 2020.

[12] S. M. Azimi, D. Britz, M. Engstler, M. Fritz, and F. Mücklich, “Advanced steel microstructural classification by deep learning methods,” *Sci. Rep.*, vol. 8, no. 1, pp. 1–14, 2018.

[13] J. Gola *et al.*, “Objective microstructure classification by support vector machine (SVM) using

a combination of morphological parameters and textural features for low carbon steels," *Comput. Mater. Sci.*, vol. 160, pp. 186–196, 2019.

[14] M. M. Nowell and S. I. Wright, "Phase differentiation via combined EBSD and XEDS," *J. Microsc.*, vol. 213, no. 3, pp. 296–305, 2004.

[15] T. B. Britton and J. L. R. Hickey, "Understanding deformation with high angular resolution electron backscatter diffraction (HR-EBSD)," *IOP Conf. Ser. Mater. Sci. Eng.*, vol. 304, no. 1, p. 012003, Jan. 2018.

[16] M. A. Crimp, B. A. Simkin, and B. C. Ng, "Demonstration of the g·b × u = 0 edge dislocation invisibility criterion for electron channelling contrast imaging," *Philos. Mag. Lett.*, vol. 81, no. 12, pp. 833–837, Dec. 2001.

[17] S. Zaefferer and N. N. Elhami, "Theory and application of electron channelling contrast imaging under controlled diffraction conditions," *Acta Mater.*, vol. 75, pp. 20–50, Aug. 2014.

[18] H. Mansour, J. Guyon, M. A. Crimp, N. Gey, B. Beausir, and N. Maloufi, "Accurate electron channeling contrast analysis of dislocations in fine grained bulk materials," *Scr. Mater.*, vol. 84–85, pp. 11–14, Aug. 2014.

[19] P. W. Trimby, "Orientation mapping of nanostructured materials using transmission Kikuchi diffraction in the scanning electron microscope," *Ultramicroscopy*, vol. 120, pp. 16–24, Sep. 2012.

[20] E. Brodu, E. Bouzy, J. J. Fundenberger, J. Guyon, A. Guitton, and Y. Zhang, "On-axis TKD for orientation mapping of nanocrystalline materials in SEM," *Mater. Charact.*, vol. 130, pp. 92–96, Aug. 2017.

[21] M. A. Groeber, B. K. Haley, M. D. Uchic, D. M. Dimiduk, and S. Ghosh, "3D reconstruction and characterization of polycrystalline microstructures using a FIB-SEM system," *Mater. Charact.*, vol. 57, no. 4–5, pp. 259–273, Dec. 2006.

[22] S. Zaefferer, S. Wright, and D. Raabe, "3D-Orientation Microscopy in a FIB SEM: A New Dimension of Microstructure Characterization," *Microsc. Microanal.*, vol. 13, no. S02, pp. 1508–1509, Aug. 2007.

[23] H. K. D. H. Bhadeshia, "Metallography of Steels." [Online]. Available: http://www.phase-trans.msm.cam.ac.uk/2008/Steel_Microstructure/SM.html. [Accessed: 21-Jul-2022].

[24] R. L. Bodnar and S. S. Hansen, "Effects of austenite grain size and cooling rate on Widmanstätten ferrite formation in low-alloy steels," *Metall. Mater. Trans. A*, vol. 25, no. 4, pp. 665–675, Apr. 1994.

[25] G. Murry, *Transformations dans les aciers, Techniques de l'ingénieur*. 1998.

[26] H. Bhadeshia, *Bainite in steels: theory and practice*, Third edition. Maney Publishing.

[27] H. I. Aaronson, W. T. Reynolds, G. J. Shiflet, and G. Spanos, "Bainite viewed three different ways," *Metall. Trans. A*, vol. 21, no. 6, pp. 1343–1380, Jun. 1990.

[28] S. Zajac, V. Schwinn, and K. H. Tacke, "Characterisation and quantification of complex bainitic microstructures in high and ultra-high strength linepipe steels," *Mater. Sci. Forum*, vol. 500–501, pp. 387–394, 2005.

[29] D. A. Porter and K. E. Easterling, *Phase Transformations in Metals and Alloys*, Third edit. CRC Press, 2009.

[30] V. Bordereau, "Quantitative relationships between chemical composition, microstructure and mechanical properties for bainitic steels.," PhD thesis, Ecole Nationale Supérieure des Mines de Paris, 2015.

[31] T. Wvjadlowski, "Etude des sulfures dans des alliages de fer de haute pureté," PhD thesis, Université de Paris VI, 1973.

[32] B. L. Adams, S. I. Wright, and K. Kunze, "Orientation imaging: The emergence of a new microscopy," *Metall. Trans. A*, vol. 24, no. 4, pp. 819–831, 1993.

[33] H.-J. Bunge, *Texture Analysis in Materials Science*. 1982.

[34] M. Humbert, F. Wagner, H. Moustahfid, and C. Esling, "Determination of the Orientation of a Parent β Grain from the Orientations of the Inherited α Plates in the Phase Transformation from Body-Centred Cubic to Hexagonal Close Packed," *J. Appl. Crystallogr.*, vol. 28, no. 5, pp. 571–576, Oct. 1995.

[35] D. Rowenhorst *et al.*, "Consistent representations of and conversions between 3D rotations," *Model. Simul. Mater. Sci. Eng.*, vol. 23, no. 8, p. 083501, Oct. 2015.

[36] E. C. Bain and N. Y. Dunkirk, "The nature of martensite," *Trans. AIME*, vol. 70(1), pp. 25–47, 1924.

[37] G. Kurdjumow and G. Sachs, "Über den Mechanismus der Stahlhärtung," *Zeitschrift für Phys.*, vol. 64, no. 5–6, pp. 325–343, May 1930.

[38] Z. Nishiyama, "X-Ray investigation of the mechanism of the transformation from the face-centered cubic lattice to body-centered cubic," *Sci. Rep. Tohoku Imp*, vol. Vol. 23, pp. 637–664, 1934.

[39] W. Pitsch, "The martensite transformation in thin foils of iron-nitrogen alloys," *Philos. Mag.*,

vol. 4, no. 41, pp. 577–584, 1959.

[40] A. B. Greninger and A. R. Troiano, "The mechanism of Martensite formation," *JOM*, vol. 1, no. 9, pp. 590–598, Dec. 1949.

[41] A. F. Gourgues-Lorenzon, "Application of electron backscatter diffraction to the study of phase transformations," *Int. Mater. Rev.*, vol. 52, no. 2, pp. 65–128, Mar. 2007.

[42] S. Lubin, "Etude des mécanismes de la transformation de phase bainitique dans les aciers bas carbone," PhD thesis, École nationale supérieure des mines de Paris, 2009.

[43] G. Nolze, "Irrational orientation relationship derived from rational orientation relationships using EBSD data," *Cryst. Res. Technol.*, vol. 43, no. 1, pp. 61–73, Jan. 2008.

[44] G. Miyamoto, N. Takayama, and T. Furuhara, "Accurate measurement of the orientation relationship of lath martensite and bainite by electron backscatter diffraction analysis," *Scr. Mater.*, vol. 60, no. 12, pp. 1113–1116, Jun. 2009.

[45] M. Humbert, P. Blaineau, L. Germain, and N. Gey, "Refinement of orientation relations occurring in phase transformation based on considering only the orientations of the variants," *Scr. Mater.*, vol. 64, no. 2, pp. 114–117, Jan. 2011.

[46] N. Y. Zolotorevsky, S. N. Panpurin, A. A. Zisman, and S. N. Petrov, "Effect of ausforming and cooling condition on the orientation relationship in martensite and bainite of low carbon steels," *Mater. Charact.*, vol. 107, pp. 278–282, Sep. 2015.

[47] R. J. Dippenaar and R. W. K. Honeycombe, "The crystallography and nucleation of pearlite," *Proc. R. Soc. London. A. Math. Phys. Sci.*, vol. 333, no. 1595, pp. 455–467, Jun. 1973.

[48] J. R. Yang and H. K. D. H. Bhadeshia, "Acicular ferrite transformation in alloy-steel weld metals," *J. Mater. Sci. 1991 263*, vol. 26, no. 3, pp. 839–845, Jan. 1991.

[49] W. L. Fink and E. D. M. Campbell, *Influence of heat treatment and carbon content on the structure of pure iron carbon alloys*. 1925.

[50] M. A. Jaswon and J. A. Wheeler, "Atomic displacements in the austenite–martensite transformation," *Acta Crystallogr.*, vol. 1, no. 4, pp. 216–224, Sep. 1948.

[51] A. Lambert-Perlade, A. F. Gourgues, and A. Pineau, "Austenite to bainite phase transformation in the heat-affected zone of a high strength low alloy steel," *Acta Mater.*, vol. 52, no. 8, pp. 2337–2348, May 2004.

[52] C. P. Luo and J. Liu, "Crystallography of lath martensite and lower bainite in alloy steels," *Mater. Sci. Eng. A*, vol. 438–440, pp. 149–152, Nov. 2006.

[53] S. Morito, H. Tanaka, R. Konishi, T. Furuhara, and T. Maki, "The morphology and crystallography of lath martensite in Fe-C alloys," *Acta Mater.*, vol. 51, no. 6, pp. 1789–1799, 2003.

[54] T. Furuhara, H. Kawata, S. Morito, and T. Maki, "Crystallography of upper bainite in Fe-Ni-C alloys," *Mater. Sci. Eng. A*, vol. 431, no. 1–2, pp. 228–236, 2006.

[55] N. Takayama, G. Miyamoto, and T. Furuhara, "Effects of transformation temperature on variant pairing of bainitic ferrite in low carbon steel," *Acta Mater.*, vol. 60, no. 5, pp. 2387–2396, 2012.

[56] A. F. Gourgues, H. M. Flower, and T. C. Lindley, "Electron backscattering diffraction study of acicular ferrite, bainite, and martensite steel microstructures," *Mater. Sci. Technol.*, vol. 16, no. 1, pp. 26–40, 2000.

[57] L. Ryde, "Application of EBSD to analysis of microstructures in commercial steels," *Mater. Sci. Technol.*, vol. 22, no. 11, pp. 1297–1306, 2006.

[58] S. Zaefferer, P. Romano, and F. Friedel, "EBSD as a tool to identify and quantify bainite and ferrite in low-alloyed Al-TRIP steels," in *Journal of Microscopy*, 2008, vol. 230, no. 3, pp. 499–508.

[59] J. Y. Kang *et al.*, "Phase analysis of steels by grain-averaged EBSD functions," *ISIJ Int.*, vol. 51, no. 1, pp. 130–136, 2011.

[60] J. Y. Kang, S. J. Park, and M. B. Moon, "Phase analysis on dual-phase steel using band slope of electron backscatter diffraction pattern," *Microsc. Microanal.*, vol. 19, no. SUPPL. 5, pp. 13–16, 2013.

[61] K. Zhu, D. Barbier, and T. Iung, "Characterization and quantification methods of complex BCC matrix microstructures in advanced high strength steels," *J. Mater. Sci.*, vol. 48, no. 1, pp. 413–423, 2013.

[62] S. L. Shrestha, A. J. Breen, P. Trimby, G. Proust, S. P. Ringer, and J. M. Cairney, "An automated method of quantifying ferrite microstructures using electron backscatter diffraction (EBSD) data," *Ultramicroscopy*, vol. 137, pp. 40–47, 2014.

[63] J. Laigo, F. Christien, R. Le Gall, F. Tancret, and J. Furtado, "SEM, EDS, EPMA-WDS and EBSD characterization of carbides in HP type heat resistant alloys," *Mater. Charact.*, vol. 59, no. 11, pp. 1580–1586, 2008.

[64] M. Fazarinc and M. Terc, "Transformation and Precipitation Kinetics in 30Cr10Ni Duplex Stainless Steel," vol. 41, no. September, pp. 0–10, 2010.

[65] G. Daniel, "Full characterization of a tool steel texture and microstructure by using fast

simultaneous EBSD / EDS measurements," vol. 174, pp. 1290–1295, 2011.

[66] A. J. Schwartz, M. Kumar, B. L. Adams, and D. P. Field, "Electron backscatter diffraction in materials science," *Electron Backscatter Diffr. Mater. Sci.*, pp. 1–403, 2009.

[67] E. J. Payton and G. Nolze, "The backscatter electron signal as an additional tool for phase segmentation in electron backscatter diffraction," *Microsc. Microanal.*, vol. 19, no. 4, pp. 929–941, 2013.

[68] S. I. Wright, M. M. Nowell, R. De Kloe, P. Camus, and T. Rampton, "Electron imaging with an EBSD detector," *Ultramicroscopy*, 2015.

[69] M. Afshar, "Phase discrimination by pattern brightness in EBSD mappings," *Mater. Charact.*, vol. 132, no. September, pp. 405–412, 2017.

[70] J. Sharma, A. Nicolaÿ, M. De Graef, and N. Bozzolo, "Phase discrimination between δ and η phases in the new nickel-based superalloy VDM Alloy 780 using EBSD," *Mater. Charact.*, vol. 176, p. 111105, Jun. 2021.

[71] G. Nolze, A. Winkelmann, and A. P. Boyle, "Pattern matching approach to pseudosymmetry problems in electron backscatter diffraction," *Ultramicroscopy*, vol. 160, pp. 146–154, 2016.

[72] A. Foden, D. M. Collins, A. J. Wilkinson, and T. B. Britton, "Indexing electron backscatter diffraction patterns with a refined template matching approach," *Ultramicroscopy*, vol. 207, no. July 2018, p. 112845, 2019.

[73] F. Ram and M. De Graef, "Phase differentiation by electron backscatter diffraction using the dictionary indexing approach," *Acta Mater.*, vol. 144, pp. 352–364, 2018.

[74] G. Nolze, A. Winkelmann, G. Cios, and T. Tokarski, "Tetragonality mapping of martensite in a high-carbon steel by EBSD," *Mater. Charact.*, vol. 175, p. 111040, May 2021.

[75] T. Tanaka, N. Maruyama, N. Nakamura, and A. J. Wilkinson, "Tetragonality of Fe-C martensite – a pattern matching electron backscatter diffraction analysis compared to X-ray diffraction," *Acta Mater.*, vol. 195, pp. 728–738, Aug. 2020.

[76] K. Kaufmann *et al.*, "Crystal symmetry determination in electron diffraction using machine learning," vol. 568, pp. 564–568, 2020.

[77] K. Kaufmann, C. Zhu, A. S. Rosengarten, D. Maryanovsky, H. Wang, and K. S. Vecchio, "Phase Mapping in EBSD Using Convolutional Neural Networks," *Microsc. Microanal.*, pp. 1–11, 2020.

[78] S. Zaefferer, J. Ohlert, and W. Bleck, "A study of microstructure, transformation mechanisms

and correlation between microstructure and mechanical properties of a low alloyed TRIP steel," *Acta Mater.*, vol. 52, no. 9, pp. 2765–2778, May 2004.

[79] M. Humbert, H. Moustahfid, F. Wagner, and M. J. Philippe, "Evaluation of the high temperature texture of the β phase of a TA6V sample from the individual orientations of grains of the low temperature α phase," *Scr. Metall. Mater.*, vol. 30, no. 3, pp. 377–382, Feb. 1994.

[80] M. Abbasi, T. W. Nelson, C. D. Sorensen, and L. Wei, "An approach to prior austenite reconstruction," *Mater. Charact.*, vol. 66, pp. 1–8, 2012.

[81] V. Tari, A. D. Rollett, and H. Beladi, "Back calculation of parent austenite orientation using a clustering approach," *J. Appl. Crystallogr.*, vol. 46, no. 1, pp. 210–215, 2013.

[82] M. J. Holzweissig, D. Canadinc, and H. J. Maier, "Computation of parent austenite grain orientation from product grain orientations upon displacive phase transformations," *Model. Simul. Mater. Sci. Eng.*, vol. 21, no. 8, p. 085009, Oct. 2013.

[83] N. Bernier, L. Bracke, L. Malet, and S. Godet, "An alternative to the crystallographic reconstruction of austenite in steels," *Mater. Charact.*, vol. 89, pp. 23–32, 2014.

[84] G. Miyamoto, N. Iwata, N. Takayama, and T. Furuhara, "Mapping the parent austenite orientation reconstructed from the orientation of martensite by EBSD and its application to ausformed martensite," *Acta Mater.*, vol. 58, no. 19, pp. 6393–6403, 2010.

[85] L. Germain, D. Kratsch, M. Salib, and N. Gey, "Identification of sub-grains and low angle boundaries beyond the angular resolution of EBSD maps," *Mater. Charact.*, vol. 98, pp. 66–72, Dec. 2014.

[86] L. Germain, N. Gey, and M. Humbert, "Reliability of reconstructed β-orientation maps in titanium alloys," *Ultramicroscopy*, vol. 107, no. 12, pp. 1129–1135, Nov. 2007.

[87] C. Cayron, B. Artaud, and L. Briottet, "Reconstruction of parent grains from EBSD data," *Mater. Charact.*, vol. 57, no. 4–5, pp. 386–401, 2006.

[88] C. Y. Huang, H. C. Ni, and H. W. Yen, "New protocol for orientation reconstruction from martensite to austenite in steels," *Materialia*, vol. 9, p. 100554, Dec. 2020.

[89] E. G. De Araujo, H. Pirgazi, M. Sanjari, M. Mohammadi, and L. A. I. Kestensa, "Automated reconstruction of parent austenite phase based on the optimum orientation relationship," *J. Appl. Crystallogr.*, vol. 54, no. 2, pp. 569–579, Mar. 2021.

[90] G. G. E. Seward, S. Celotto, D. J. Prior, J. Wheeler, and R. C. Pond, "In situ SEM-EBSD observations of the hcp to bcc phase transformation in commercially pure titanium," *Acta Mater.*, vol. 52, no. 4, pp. 821–832, 2004.

[91] I. Lischewski, D. M. Kirch, A. Ziemons, and G. Gottstein, “Investigation of the α-γ-α phase transformation in steel: High-temperature in situ EBSD measurements,” *Texture, Stress. Microstruct.*, 2008.

[92] T. Fukino and S. Tsurekawa, “In-Situ SEM/EBSD observation of α/γ phase transformation in Fe-Ni Alloy,” *Mater. Trans.*, vol. 49, no. 12, pp. 2770–2775, 2008.

[93] K. Hata *et al.*, “In situ EBSD analysis on the crystal orientation relationship between ferrite and austenite during reverse transformation of an Fe-Mn-C Alloy,” *Mater. Trans.*, vol. 57, no. 9, pp. 1514–1519, 2016.

[94] G. Zijlstra, M. S. B. van Daalen, D. I. Vainchtein, V. Ocelík, and J. T. M. De Hosson, “Interphase boundary motion elucidated through in-situ high temperature electron back-scatter diffraction,” *Mater. Des.*, vol. 132, pp. 138–147, 2017.

[95] A. Hoang Pham, S. Morito, T. Ohba, and T. Hayashi, “In situ ebsd observation of pearlite-austenite reverse transformation in eutectoid steel,” *Mater. Sci. Forum*, vol. 985, pp. 42–47, 2020.

[96] H. Farahani, G. Zijlstra, M. G. Mecozzi, V. Ocelík, J. T. M. De Hosson, and S. Van Der Zwaag, “In Situ High-Temperature EBSD and 3D Phase Field Studies of the Austenite-Ferrite Transformation in a Medium Mn Steel,” *Microsc. Microanal.*, pp. 1–17, 2019.

[97] Y. Tomota, N. Sekido, S. Harjo, T. Kawasaki, W. Gong, and A. Taniyama, “In situ observations of transformation behavior upon heating for a 1.5Mn-1.5Si-0.2C steel-comparison between neutron diffraction, XRD, EBSD and dilatometry-,” *ISIJ Int.*, vol. 57, no. 12, pp. 2237–2244, 2017.

[98] R. A. Schwarzer, “Automated crystal lattice orientation mapping using a computer-controlled sem,” *Micron*, vol. 28, no. 3, pp. 249–265, 1997.

[99] S. Kikuchi, “Diffraction of Cathode Rays by Mica,” *Proc. Imp. Acad.*, vol. 4, pp. 271–274, 1928.

[100] J. A. Venables and C. J. Harland, “Electron back-scattering patterns—a new technique for obtaining crystallographic information in the scanning electron microscope,” *Philos. Mag.*, vol. 27, no. 5, pp. 1193–1200, 1973.

[101] N. H. Schmidt, J. B. Bilde-Sørensen, D. Juul Jensen, D. Juul, N. Schmidt, and J. Bilde-Sl, “Band Positions Used for On-Line Crystallographic Orientation Determination from Electron Back Scattering Patterns,” *Scanning Microsc.*, vol. 5, no. 3, pp. 637–643, 1991.

[102] L. Ryde, “Application of EBSD to analysis of microstructures in commercial steels,” *Mater. Sci. Technol.*, vol. 22, no. 11, pp. 1297–1306, Nov. 2006.

[103] N. C. Krieger Lassen, "Automated Determination of Crystal Orientations from Electron Backscattering Patterns," PhD thesis, Dänische Technische Universität Lyngby, 1994.

[104] P. G. Callahan and M. De Graef, "Dynamical electron backscatter diffraction patterns. Part I: Pattern simulations," *Microsc. Microanal.*, vol. 19, no. 5, pp. 1255–1265, 2013.

[105] M. De Graef, "GitHub - EMsoft-org/EMsoft: Public EMsoft repository." [Online]. Available: https://github.com/EMsoft-org/EMsoft. [Accessed: 12-Jul-2022].

[106] A. Tellier, "Evolutions microstructurales lors de la Compression Isostatique à Chaud (CIC) d'un acier à haute teneur en carbone et influence sur les propriétés d'usage : de la poudre au produit fritté," PhD thesis, Université Bourgogne Franche-Comté, 2020.

[107] Ånes H and Bergh T, "GitHub - pyxem/kikuchipy: Processing, simulating and analyzing electron backscatter diffraction (EBSD) patterns in Python." [Online]. Available: https://github.com/pyxem/kikuchipy. [Accessed: 12-Jul-2022].

[108] A. E. Davis *et al.*, "Optimising large-area crystal orientation mapping of nanoscale β phase in α + β titanium alloys using EBSD," *Mater. Charact.*, vol. 194, p. 112371, Dec. 2022.

[109] S. I. Wright, M. M. Nowell, S. P. Lindeman, P. P. Camus, M. De Graef, and M. A. Jackson, "Introduction and comparison of new EBSD post-processing methodologies," *Ultramicroscopy*, vol. 159, no. P1, pp. 81–94, Dec. 2015.

[110] P. Trimby, K. Larsen, M. Hjelmstad, A. Winkelmann, and K. Mehnert, "Improving Data from Electron Backscatter Diffraction Experiments using Pattern Matching Techniques," *Microsc. Microanal.*, vol. 28, no. S1, pp. 3182–3183, Aug. 2022.

[111] D. M. Kirch *et al.*, "Laser powered heating stage in a scanning electron microscope for microstructural investigations at elevated temperatures," *Rev. Sci. Instrum.*, vol. 79, no. 4, 2008.

[112] S. Morito, H. Yoshida, T. Maki, and X. Huang, "Effect of block size on the strength of lath martensite in low carbon steels," *Mater. Sci. Eng. A*, vol. 438–440, pp. 237–240, Nov. 2006.

[113] Livia Cupertino Malheiros, "Study of Structure, Hydrogen Diffusion and Trapping, Plasticity and Fracture towards the Comprehension of Hydrogen-Assisted Cracking of High-Strength Low-Alloy Martensitic Steels," PhD thesis, La Rochelle, 2020.

[114] L. Cupertino Malheiros *et al.*, "Local fracture criterion for quasi-cleavage hydrogen-assisted cracking of tempered martensitic steels," *Mater. Sci. Eng. A*, vol. 847, p. 143213, Jul. 2022.

[115] A. Laureys, T. Depover, R. Petrov, and K. Verbeken, "Microstructural characterization of hydrogen induced cracking in TRIP-assisted steel by EBSD," *Mater. Charact.*, vol. 112, pp. 169–179, Feb. 2016.

[116] S. D. Catteau *et al.*, "Carbon and nitrogen effects on microstructure and kinetics associated with bainitic transformation in a low-alloyed steel," *J. Alloys Compd.*, vol. 658, pp. 832–838, Feb. 2016.

[117] S. D. Catteau, "Effets du Carbone et de l'Azote sur les Cinétiques de Décomposition de l'Austénite dans un Acier Faiblement Allié-Étude Expérimentale et Modélisation," PhD thesis, Université de Lorraine, 2017.

[118] H. P. Van Landeghem *et al.*, "Isothermal decomposition of carbon and nitrogen-enriched austenite in 23MnCrMo5 low-alloy steel," *Acta Mater.*, vol. 148, pp. 363–373, Apr. 2018.

[119] M. Mandal, J. da C. Teixeira, N. Gey, L. Germain, F. Lebel, and S. Denis, "Microstructure refinement after nitrogen enrichment and austenite decomposition in a low-alloyed steel studied by EBSD and Laser Confocal Scanning Microscopy," in *PTM2022 - 8th International Conference on solid→solid Phase Transformations in inorganic Materials*, 2022.

[120] O. Nakonechna, "Etude à l'échelle nanométrique des interfaces de transformations austénite/ferrite dans Fe-Mn-C à différentes températures intercritiques," PhD thesis, Université de Rouen, 2022.

[121] F. Danoix, X. Sauvage, D. Huin, L. Germain, and M. Gouné, "A direct evidence of solute interactions with a moving ferrite/austenite interface in a model Fe-C-Mn alloy," *Scr. Mater.*, vol. 121, pp. 61–65, Aug. 2016.

[122] E. A. Holm *et al.*, "Overview: Computer Vision and Machine Learning for Microstructural Characterization and Analysis," *Metall. Mater. Trans. A Phys. Metall. Mater. Sci.*, vol. 51, no. 12, pp. 5985–5999, Dec. 2020.

[123] K. Choudhary *et al.*, "Recent advances and applications of deep learning methods in materials science," *npj Computational Materials*, vol. 8, no. 1. Nature Publishing Group, pp. 1–26, 05-Apr-2022.

[124] H. Wang, W. Zhang, F. Sun, and W. Zhang, "A comparison study of machine learning based algorithms for fatigue crack growth calculation," *Materials (Basel).*, vol. 10, no. 5, p. 543, May 2017.

[125] A. Agrawal and A. Choudhary, "A fatigue strength predictor for steels using ensemble data mining," in *International Conference on Information and Knowledge Management, Proceedings*, 2016, vol. 24–28, pp. 2497–2500.

[126] C. Kantzos, J. Lao, and A. Rollett, "Design of an interpretable Convolutional Neural Network for stress concentration prediction in rough surfaces," *Mater. Charact.*, vol. 158, p. 109961, Dec. 2019.

[127] C. Kusche, T. Reclik, M. Freund, T. Al-Samman, U. Kerzel, and S. Korte-Kerzel, "Large-area, high-resolution characterisation and classification of damage mechanisms in dual-phase steel using deep learning," *PLoS One*, vol. 14, no. 5, p. e0216493, May 2019.

[128] A. Mangal and E. A. Holm, "Applied machine learning to predict stress hotspots I: Face centered cubic materials," *Int. J. Plast.*, vol. 111, pp. 122–134, Dec. 2018.

[129] A. R. Kitahara and E. A. Holm, "Microstructure Cluster Analysis with Transfer Learning and Unsupervised Learning," *Integr. Mater. Manuf. Innov.*, vol. 7, no. 3, pp. 148–156, Sep. 2018.

[130] W. Li, K. G. Field, and D. Morgan, "Automated defect analysis in electron microscopic images," *npj Comput. Mater.*, vol. 4, no. 1, pp. 1–9, Jul. 2018.

[131] H. Xu, R. Liu, A. Choudhary, and W. Chen, "A machine learning-based design representation method for designing heterogeneous microstructures," in *Proceedings of the ASME Design Engineering Technical Conference*, 2014, vol. 2B, no. 5.

[132] L. Breiman, "Random forests," *Mach. Learn.*, vol. 45, no. 1, pp. 5–32, Oct. 2001.

[133] C. Cortes and V. Vapnik, "Support-Vector Networks," *Mach. Learn.*, vol. 20, pp. 273–297, 1995.

[134] K. P. Sinaga and M. S. Yang, "Unsupervised K-means clustering algorithm," *IEEE Access*, vol. 8, pp. 80716–80727, 2020.

[135] M. Nielsen, "Neural networks and deep learning." [Online]. Available: http://neuralnetworksanddeeplearning.com/. [Accessed: 07-Aug-2022].

[136] Y. Bengio and Y. Lecun, "Convolutional Networks for Images, Speech, and Time-Series," in *The handbook of brain theory and neural networks*, 1995, vol. 3361, pp. 1–14.

[137] K. Simonyan and A. Zisserman, "Very deep convolutional networks for large-scale image recognition," in *3rd International Conference on Learning Representations, ICLR 2015 - Conference Track Proceedings*, 2015.

[138] A. Krizhevsky, I. Sutskever, and G. E. Hinton, "ImageNet classification with deep convolutional neural networks," *Commun. ACM*, vol. 60, no. 6, pp. 84–90, 2017.

[139] C. Szegedy *et al.*, "Going deeper with convolutions," in *Proceedings of the IEEE Computer Society Conference on Computer Vision and Pattern Recognition*, 2015, vol. 07-12-June, pp. 1–9.

[140] W. Weng and X. Zhu, "UNet: Convolutional Networks for Biomedical Image Segmentation," *IEEE Access*, vol. 9, pp. 16591–16603, 2015.

[141] S. Arivazhagan, J. J. Tracia, and N. Selvakumar, "Classification of steel microstructures using

Modified Alternate Local Ternary Pattern," *Mater. Res. Express*, vol. 6, no. 9, 2019.

[142] E. Fix and J. L. Hodges, "Discriminatory Analysis. Nonparametric Discrimination: Consistency Properties," *Int. Stat. Rev. / Rev. Int. Stat.*, vol. 57, no. 3, pp. 238–247, Dec. 1989.

[143] J. Gola *et al.*, "Advanced microstructure classification by data mining methods," *Comput. Mater. Sci.*, vol. 148, pp. 324–335, 2018.

[144] R. M. Haralick, I. Dinstein, and K. Shanmugam, "Textural Features for Image Classification," *IEEE Trans. Syst. Man Cybern.*, vol. SMC-3, no. 6, pp. 610–621, 1973.

[145] M. Müller, D. Britz, L. Ulrich, T. Staudt, and F. Mücklich, "Classification of bainitic structures using textural parameters and machine learning techniques," *Metals (Basel).*, vol. 10, no. 5, pp. 1–19, 2020.

[146] T. Ojala, M. Pietikäinen, and T. Mäenpää, "Multiresolution gray-scale and rotation invariant texture classification with local binary patterns," *IEEE Trans. Pattern Anal. Mach. Intell.*, vol. 24, no. 7, pp. 971–987, Jul. 2002.

[147] K. Tsutsui *et al.*, "A methodology of steel microstructure recognition using SEM images by machine learning based on textural analysis," *Mater. Today Commun.*, vol. 25, no. July, 2020.

[148] J. H. Friedman, "Greedy function approximation: A gradient boosting machine," *Ann. Stat.*, vol. 29, no. 5, pp. 1189–1232, 2001.

[149] A. Paul, A. Gangopadhyay, A. R. Chintha, D. P. Mukherjee, P. Das, and S. Kundu, "Calculation of phase fraction in steel microstructure images using random forest classifier," *IET Image Process.*, vol. 12, no. 8, pp. 1370–1377, 2018.

[150] D. S. Bulgarevich, S. Tsukamoto, T. Kasuya, M. Demura, and M. Watanabe, "Pattern recognition with machine learning on optical microscopy images of typical metallurgical microstructures," *Sci. Rep.*, vol. 8, no. 1, pp. 1–8, Feb. 2018.

[151] D. L. Naik, H. U. Sajid, and R. Kiran, "Texture-based metallurgical phase identification in structural steels: A supervised machine learning approach," *Metals (Basel).*, vol. 9, no. 5, May 2019.

[152] G. I. Webb, "Naïve Bayes," in *Encyclopedia of Machine Learning and Data Mining*, 2016, pp. 1–2.

[153] A. J. Izenman, "Linear Discriminant Analysis," Springer, New York, NY, 2013, pp. 237–280.

[154] T. Maemura *et al.*, "Interpretability of Deep Learning Classification for Low-Carbon Steel Microstructures," *Mater. Trans.*, vol. 61, no. 8, pp. 1584–1592, Aug. 2020.

[155] K. He, X. Zhang, S. Ren, and J. Sun, "Deep residual learning for image recognition," in *Proceedings of the IEEE Computer Society Conference on Computer Vision and Pattern Recognition*, 2016, pp. 770–778.

[156] "ImageNet." [Online]. Available: https://web.archive.org/web/20200907124944/http://image-net.org/about-overview. [Accessed: 23-Oct-2022].

[157] M. T. Ribeiro, S. Singh, and C. Guestrin, "'Why should I trust you?' Explaining the predictions of any classifier," in *Proceedings of the ACM SIGKDD International Conference on Knowledge Discovery and Data Mining*, 2016, vol. 13-17-Augu, pp. 1135–1144.

[158] M. Bartłomiej, K. Grzegorz, K. Jan, and P. Ulrich, "Autonomous Interpretation of the Microstructure of Steels and Special Alloys," 2019.

[159] M. Larmuseau, M. Sluydts, K. Theuwissen, L. Duprez, T. Dhaene, and S. Cottenier, "Compact representations of microstructure images using triplet networks," *npj Comput. Mater.*, vol. 6, no. 1, 2020.

[160] M. Larmuseau, M. Sluydts, K. Theuwissen, L. Duprez, T. Dhaene, and S. Cottenier, "Race against the Machine: can deep learning recognize microstructures as well as the trained human eye?," *Scr. Mater.*, vol. 193, pp. 33–37, 2021.

[161] B. L. DeCost, B. Lei, T. Francis, and E. A. Holm, "High throughput quantitative metallography for complex microstructures using deep learning: A case study in ultrahigh carbon steel," *Microsc. Microanal.*, vol. 25, no. 1, pp. 21–29, 2019.

[162] F. Ajioka, Z. L. Wang, T. Ogawa, and Y. Adachi, "Development of high accuracy segmentation model for microstructure of steel by deep learning," *ISIJ Int.*, vol. 60, no. 5, pp. 954–959, 2020.

[163] I. Arganda-Carreras *et al.*, "Trainable Weka Segmentation: A machine learning tool for microscopy pixel classification," *Bioinformatics*, vol. 33, no. 15, pp. 2424–2426, Aug. 2017.

[164] V. Badrinarayanan, A. Kendall, and R. Cipolla, "SegNet: A Deep Convolutional Encoder-Decoder Architecture for Image Segmentation," *IEEE Trans. Pattern Anal. Mach. Intell.*, vol. 39, no. 12, pp. 2481–2495, Dec. 2017.

[165] C. Shen *et al.*, "A generic high-throughput microstructure classification and quantification method for regular SEM images of complex steel microstructures combining EBSD labeling and deep learning," *Artic. J. Mater. Sci. Technol.*, vol. 93, pp. 191–204, 2021.

[166] C. Shen, X. Wei, C. Wang, and W. Xu, "A deep learning method for extensible microstructural quantification of DP steel enhanced by physical metallurgy-guided data augmentation," *Mater. Charact.*, vol. 180, p. 111392, Oct. 2021.

[167] A. R. Durmaz *et al.*, "A deep learning approach for complex microstructure inference," *Nat. Commun.*, vol. 12, no. 1, pp. 1–15, Nov. 2021.

[168] R. R. Selvaraju, M. Cogswell, A. Das, R. Vedantam, D. Parikh, and D. Batra, "Grad-CAM: Visual Explanations from Deep Networks via Gradient-Based Localization," *Int. J. Comput. Vis.*, vol. 128, no. 2, pp. 336–359, 2020.

[169] D. Bau, B. Zhou, A. Khosla, A. Oliva, and A. Torralba, "Network dissection: Quantifying interpretability of deep visual representations," in *Proceedings - 30th IEEE Conference on Computer Vision and Pattern Recognition, CVPR 2017*, 2017, vol. 2017-Janua, pp. 3319–3327.

[170] J. Goulden, K. Mehnert, K. Thomsen, and H. Jiang, "A Method for Separating Crystallograpically Similar Phases in Steels using EBSD and Machine Learning," *Microsc. Microanal.*, vol. 23, no. S1, pp. 110–111, 2017.

[171] K. Tsutsui, H. Terasaki, T. Maemura, K. Hayashi, K. Moriguchi, and S. Morito, "Microstructural diagram for steel based on crystallography with machine learning," *Comput. Mater. Sci.*, vol. 159, no. December 2018, pp. 403–411, 2019.

[172] R. Liu, A. Agrawal, W. Liao, A. Choudhary, and M. De Graef, "Materials discovery: Understanding polycrystals from large-scale electron patterns.," in *IEEE International Conference on Big Data (Big Data), 2261–2269*, 2016.

[173] D. Jha *et al.*, "Extracting grain orientations from EBSD patterns of polycrystalline materials using convolutional neural networks," *Microsc. Microanal.*, vol. 24, no. 5, pp. 497–502, Oct. 2018.

[174] Z. Ding, E. Pascal, and M. De Graef, "Indexing of electron back-scatter diffraction patterns using a convolutional neural network," *Acta Mater.*, vol. 199, pp. 370–382, 2020.

[175] Y. Han, R. J. Griffiths, H. Z. Yu, and Y. Zhu, "Quantitative microstructure analysis for solid-state metal additive manufacturing via deep learning," *J. Mater. Res.*, vol. 35, no. 15, pp. 1936–1948, 2020.

[176] B. L. DeCost, M. D. Hecht, T. Francis, B. A. Webler, Y. N. Picard, and E. A. Holm, "UHCSDB: UltraHigh Carbon Steel Micrograph DataBase," *Integr. Mater. Manuf. Innov. 2017 62*, vol. 6, no. 2, pp. 197–205, May 2017.

[177] D. Iren *et al.*, "Aachen-Heerlen annotated steel microstructure dataset," *Sci. Data 2021 81*, vol. 8, no. 1, pp. 1–9, May 2021.

[178] H. Kim, J. Inoue, and T. Kasuya, "Unsupervised microstructure segmentation by mimicking metallurgists' approach to pattern recognition," *Sci. Rep.*, vol. 10, no. 1, p. 17835, 2020.

[179] H. Kim, Y. Arisato, and J. Inoue, "Unsupervised segmentation of microstructural images of steel using data mining methods," *Comput. Mater. Sci.*, vol. 201, no. July 2021, 2022.

[180] R. Achanta, A. Shaji, K. Smith, A. Lucchi, P. Fua, and S. Süsstrunk, "SLIC superpixels compared to state-of-the-art superpixel methods," *IEEE Trans. Pattern Anal. Mach. Intell.*, vol. 34, no. 11, pp. 2274–2281, 2012.

[181] H. Abdi and L. J. Williams, "Principal component analysis," *Wiley Interdisciplinary Reviews: Computational Statistics*, vol. 2, no. 4. John Wiley & Sons, Ltd, pp. 433–459, 01-Jul-2010.

[182] D. M. Blei and M. I. Jordan, "Variational inference for Dirichlet process mixtures," *Bayesian Anal.*, vol. 1, no. 1 A, pp. 121–144, Mar. 2006.

[183] A. Goetz *et al.*, "Addressing materials' microstructure diversity using transfer learning," *npj Comput. Mater.*, vol. 8, no. 1, pp. 1–13, 2022.

[184] Y. H. Tsai, W. C. Hung, S. Schulter, K. Sohn, M. H. Yang, and M. Chandraker, "Learning to Adapt Structured Output Space for Semantic Segmentation," in *Proceedings of the IEEE Computer Society Conference on Computer Vision and Pattern Recognition*, 2018, pp. 7472–7481.

[185] S. W. Kim, S. H. Kang, S. J. Kim, and S. Lee, "Estimating the phase volume fraction of multi-phase steel via unsupervised deep learning," *Sci. Rep.*, vol. 11, no. 1, p. 5902, 2021.

[186] X. Chen, Y. Duan, R. Houthooft, J. Schulman, I. Sutskever, and P. Abbeel, "InfoGAN: Interpretable Representation Learning by Information Maximizing Generative Adversarial Nets," *Adv. Neural Inf. Process. Syst.*, pp. 2180–2188, Jun. 2016.

[187] M. Ester, H.-P. Kriegel, J. Sander, and X. Xu, "A Density-Based Algorithm for Discovering Clusters in Large Spatial Databases with Noise," in *Proceedings of the 2nd International Conference on Knowledge Discovery and Data Mining*, 1996, pp. 226–231.

[188] W. Samek and K. R. Müller, "Towards Explainable Artificial Intelligence," in *Lecture Notes in Computer Science (including subseries Lecture Notes in Artificial Intelligence and Lecture Notes in Bioinformatics)*, vol. 11700 LNCS, Springer Verlag, 2019, pp. 5–22.

[189] L. Morsdorf, C. C. Tasan, D. Ponge, and D. Raabe, "3D structural and atomic-scale analysis of lath martensite: Effect of the transformation sequence," *Acta Mater.*, vol. 95, pp. 366–377, Jun. 2015.

[190] D. Phelan, N. Stanford, and R. Dippenaar, "In situ observations of Widmanstätten ferrite formation in a low-carbon steel," *Mater. Sci. Eng. A*, vol. 407, no. 1–2, pp. 127–134, Oct. 2005.

[191] M. Kamaya, "Assessment of local deformation using EBSD: Quantification of accuracy of

measurement and definition of local gradient," *Ultramicroscopy*, vol. 111, no. 8, pp. 1189–1199, Jul. 2011.

[192] M. B. H. Slama, N. Gey, L. Germain, K. Zhu, and S. Allain, "Key parameters to promote granularization of lath-like bainite/martensite in FeNiC alloys during isothermal holding," *Materials (Basel).*, vol. 11, no. 10, pp. 1–13, 2018.

[193] "Softmax Function Definition | DeepAI." [Online]. Available: https://deepai.org/machine-learning-glossary-and-terms/softmax-layer. [Accessed: 02-Jun-2022].

[194] "ReLu Definition | DeepAI." [Online]. Available: https://deepai.org/machine-learning-glossary-and-terms/relu. [Accessed: 02-Jun-2022].

[195] D. K. Dhana Sree and C. Shoba Bindu, "Data Analytics: Why Data Normalization," *Int. J. Eng. Technol.*, vol. 7, no. 6, pp. 209–213, 2018.

[196] H. Grimmer, "Disorientations and coincidence rotations for cubic lattices," *Acta Crystallogr. Sect. A*, vol. 30, no. 6, pp. 685–688, Nov. 1974.

[197] P. J. Konijnenberg, S. Zaefferer, S. B. Lee, A. D. Rollett, G. S. Rohrer, and D. Raabe, "Advanced methods and tools for reconstruction and analysis of grain boundaries from 3D-EBSD data sets," in *Materials Science Forum*, 2012, vol. 702–703, pp. 475–478.

[198] D. Rowenhorst *et al.*, "Consistent representations of and conversions between 3D rotations," *Model. Simul. Mater. Sci. Eng.*, vol. 23, no. 8, p. 083501, Oct. 2015.

[199] M. A. Groeber and M. A. Jackson, "DREAM.3D: A Digital Representation Environment for the Analysis of Microstructure in 3D," *Integr. Mater. Manuf. Innov.*, vol. 3, no. 1, pp. 56–72, Dec. 2014.

[200] J. M. Facil, B. Ummenhofer, H. Zhou, L. Montesano, T. Brox, and J. Civera, "CAM-Convs: Camera-Aware Multi-Scale Convolutions for Single-View Depth," *Proc. IEEE Comput. Soc. Conf. Comput. Vis. Pattern Recognit.*, vol. 2019-June, pp. 11818–11827, Apr. 2019.

[201] L. Bottou, "Stochastic Gradient Learning in Neural Networks," *Proc. Neuro-Nımes*, vol. 91, no. 8, p. 12, 1991.

[202] M. D. Zeiler, "ADADELTA: An Adaptive Learning Rate Method," *arXiv Prepr. arXiv1212.5701.*, Dec. 2012.

[203] K. E. Koech, "Cross-Entropy Loss Function." [Online]. Available: https://towardsdatascience.com/cross-entropy-loss-function-f38c4ec8643e. [Accessed: 02-Jun-2022].

[204] N. Srivastava, G. Hinton, A. Krizhevsky, I. Sutskever, and R. Salakhutdinov, "Dropout: A simple way to prevent neural networks from overfitting," *J. Mach. Learn. Res.*, vol. 15, pp. 1929–1958, 2014.

[205] M. Abadi *et al.*, "TensorFlow: A system for large-scale machine learning," in *Proceedings of the 12th USENIX Symposium on Operating Systems Design and Implementation, OSDI 2016*, 2016, pp. 265–283.

[206] F. Chollet, "Keras, GitHub repository," 2015. [Online]. Available: https://www.scirp.org/(S(351jmbntvnsjt1aadkposzje))/reference/ReferencesPapers.aspx?ReferenceID=1887532. [Accessed: 04-Jun-2021].

[207] D. S. Bulgarevich, S. Tsukamoto, T. Kasuya, M. Demura, and M. Watanabe, "Automatic steel labeling on certain microstructural constituents with image processing and machine learning tools," *Sci. Technol. Adv. Mater.*, vol. 20, no. 1, pp. 532–542, 2019.

[208] O. Instruments, "AZtec ® Reclassify Phase: Discriminating phases in steels."

[209] I. Tolstikhin *et al.*, "Generative Adversarial Networks," *Lect. Notes Comput. Sci. (including Subser. Lect. Notes Artif. Intell. Lect. Notes Bioinformatics)*, vol. 11046 LNCS, no. NeurIPS, pp. 1–9, Jun. 2014.

[210] L. Germain, "EBSD Software - Lionel GERMAIN repository for EBSD data analysers and utilities." [Online]. Available: http://lionelgermain.free.fr/. [Accessed: 11-Mar-2022].

[211] A. D. King and T. Bell, "Crystallography of grain boundary proeutectoid ferrite," *Metall. Trans. A*, vol. 6, no. 7, pp. 1419–1429, Jul. 1975.

[212] D. J. Srolovitz, G. S. Grest, and M. P. Anderson, "Computer simulation of grain growth-V. Abnormal grain growth," *Acta Metall.*, vol. 33, no. 12, pp. 2233–2247, Dec. 1985.

[213] T. Furuhara, H. Kawata, S. Morito, G. Miyamoto, and T. Maki, "Variant selection in grain boundary nucleation of upper bainite," in *Metallurgical and Materials Transactions A: Physical Metallurgy and Materials Science*, 2008, vol. 39 A, no. 5, pp. 1003–1013.

[214] M. Humbert, L. Germain, N. Gey, and E. Boucard, "Evaluation of the orientation relations from misorientation between inherited variants: Application to ausformed martensite," *Acta Mater.*, vol. 82, pp. 137–144, Jan. 2015.

[215] S. Mannor *et al.*, "K-Means Clustering," in *Encyclopedia of Machine Learning*, Springer, Boston, MA, 2011, pp. 563–564.

[216] F. Pedregosa *et al.*, "Scikit-learn: Machine Learning in Python," *J. Mach. Learn. Res.*, vol. 12, pp. 2825–2830, 2011.

[217] M. Humbert, N. Gey, J. Muller, and C. Esling, “Determination of a Mean Orientation from a Cloud of Orientations. Application to Electron Back-Scattering Pattern Measurements,” *J. Appl. Crystallogr.*, vol. 29, no. 6, pp. 662–666, Dec. 1996.

[218] A. Kanezaki, “Unsupervised image segmentation by backpropagation,” in *ICASSP, IEEE International Conference on Acoustics, Speech and Signal Processing - Proceedings*, 2018, vol. 2018-April, pp. 1543–1547.

[219] D. Martin, C. Fowlkes, D. Tal, and J. Malik, “A database of human segmented natural images and its application to evaluating segmentation algorithms and measuring ecological statistics,” *Proc. IEEE Int. Conf. Comput. Vis.*, vol. 2, pp. 416–423, 2001.

[220] P. Arbeláez, M. Maire, C. Fowlkes, and J. Malik, “Contour detection and hierarchical image segmentation,” *IEEE Trans. Pattern Anal. Mach. Intell.*, vol. 33, no. 5, pp. 898–916, 2011.

[221] S. Ioffe and C. Szegedy, “Batch normalization: Accelerating deep network training by reducing internal covariate shift,” in *32nd International Conference on Machine Learning, ICML 2015*, 2015, vol. 1, pp. 448–456.

[222] S. Santurkar, D. Tsipras, A. Ilyas, and A. Madry, “How does batch normalization help optimization?,” in *Advances in Neural Information Processing Systems*, 2018, pp. 2483–2493.